
Characterization and Quantification of Offshore Methane Emissions using Airborne in situ Measurements of Methane, Ethane and Methane Isotopologues

Flugzeuggestützte Charakterisierung und Quantifizierung von Offshore-Methanemissionen mittels in-situ Messungen von Methan, Ethan und Methanisotopologen

Magdalena Maria Theresia Pühl



München 2024

**Characterization and Quantification of Offshore
Methane Emissions using Airborne in situ
Measurements of Methane, Ethane and
Methane Isotopologues**

**Flugzeuggestützte Charakterisierung und Quantifizierung
von Offshore-Methanemissionen mittels in-situ Messungen
von Methan, Ethan und Methanisotopologen**

Magdalena Maria Theresia Pühl

Dissertation
an der Fakultät für Physik
der Ludwig-Maximilians-Universität
München

vorgelegt von
Magdalena Maria Theresia Pühl
aus Weiden i. d. Opf.

München, den 10. Oktober 2024

Erstgutachter: Prof. Dr. Markus Rapp

Zweitgutachter: Prof. Dr. James Lee

Tag der mündlichen Prüfung: 22. November 2024

Zusammenfassung

Methan (CH_4) ist nach Kohlendioxid das zweitwichtigste anthropogene Treibhausgas und wegen seiner kurzen Lebenszeit von etwa einer Dekade besonders interessant für kurzfristig wirkende Mitigationsstrategien. Atmosphärische CH_4 Konzentrationen haben sich seit der industriellen Revolution jedoch fast verdreifacht. Seit 2007 erfährt CH_4 zudem einen beschleunigten Anstieg, wobei parallel ein Absinken des Verhältnisses der Methanisotopologe $^{13}\text{CH}_4/^{12}\text{CH}_4$, ausgedrückt als $\delta^{13}\text{C}(\text{CH}_4)$, zu beobachten ist. Dies deutet auf eine Veränderung der Zusammensetzung der Methanquellen und/oder Senken hin, da diese sich in ihren $\delta^{13}\text{C}(\text{CH}_4)$ Signaturen unterscheiden. Das unzureichende Detailverständnis des Methanbudgets erschwert sowohl die Priorisierung von Mitigationsmaßnahmen als auch zuverlässige Prognosen des zukünftigen Methantrends.

Das Ziel dieser Dissertation ist eine detailliertere Charakterisierung anthropogener Methanemissionen mittels flugzeuggestützter in-situ Messmethoden. Der Fokus liegt dabei auf dem bisher unzureichend untersuchten Sektor der Offshore-Öl- und Gasproduktion. Um die Hypothese zu untersuchen, dass Emissionskataster Offshore-Emissionen mittels generischer Methoden nur unzureichend abschätzen, werden flugzeuggestützte Messungen von Offshore-Anlagen ausgewertet und die berechneten Emissionen mit Angaben in Emissionskatastern verglichen. Darüber hinaus ist die Adaption als auch der flugzeuggetragene Einsatz von Laser-Absorptionsspektroskopie zur hochaufgelösten und kontinuierlichen Messung der Tracer C_2H_6 und $\delta^{13}\text{C}(\text{CH}_4)$ ein weiteres Ziel dieser Arbeit, um Offshore-Emissionen besser zu charakterisieren.

Der erste Teil beschäftigt sich mit der Analyse der Daten einer Flugzeugmesskampagne, die 2019 in der südlichen Nordsee vom British Antarctic Service (BAS) durchgeführt wurde. Mit der etablierten Massenbilanzmethode wurden CH_4 -Emissionsraten von Gasplattformen bestimmt. Diese wurden mit Betreiberdaten, als auch mit verschiedenen regionalen und einem globalen Emissionskataster verglichen. Letzteres nutzt Emissionen, die von Ländern aufgrund der Klimarahmenkonvention der Vereinten Nationen (UNFCCC) berichtet werden, um diese mittels Infrastrukturdaten räumlich zu verteilen. Die Emissionskataster unterschätzen die aus den Messungen abgeleiteten Emissionen deutlich um Faktoren zwischen 6 und 279, wobei das globale Kataster die größte Abweichung zeigt. Direkt gemeldete Betreiberdaten für den jeweiligen Messtag zeigen die beste Übereinstimmung mit den Messungen, die um den Faktor 0.64 abweichen. Die hier diskutierten Messungen und ein Vergleich mit Messungen in anderen Offshore-Regionen zeigt, dass die beobachteten Emissionen nicht linear mit Öl- oder Gasproduktionsraten korrelieren, wie typischerweise für Emissionsabschätzungen von Katastern angenommen.

Der zweite Teil der Arbeit umfasst die Adaptierung und Charakterisierung des DLR-Laser-Absorptionsspektrometers (DLR-QCLS) für die schnelle und hochaufgelöste Messung der Tracer C_2H_6 und $\delta^{13}\text{C}(\text{CH}_4)$, um isotopische Quellsignaturen von Offshore-Punktquellen abzuleiten. Laborversuche mit der neuen Laserkonfiguration zeigen, dass Quellsignaturen qualitativ detektiert werden können. Bei der höchsten instrumentellen Auflösung (0.86‰ (1σ , 2 Hz)) ist eine Detektion von fossilen Quellen mit Methanerhöhungen von mehr als 250 ppb, abhängig von der individuellen Quellsignatur, möglich. Das DLR-QCLS wurde bei zwei Flugzeugmesskampagnen zur Messung von $\delta^{13}\text{C}(\text{CH}_4)$ und C_2H_6 eingesetzt. Dabei wurden Emissionen von Offshore-Ölplattformen detektiert und deren charakteristische C_2H_6 zu CH_4 Verhältnisse und Quellsignaturen bestimmt. Die in dieser Arbeit durchgeführten Analysen zeigen, dass das DLR-QCLS für eine quantitative Messung von Quellsignaturen bei in-situ Messungen und vorbereitend im Labor weiter optimiert werden muss, um eine bessere Übereinstimmung von Quellsignaturen zu erhalten.

Abstract

Methane (CH_4) is the second-most important long-lived anthropogenic greenhouse gas after carbon dioxide and, because of its short lifetime, is an attractive target for rapid emission reduction. Atmospheric CH_4 mole fractions have almost tripled since pre-industrial times due to human activity. A concurrent decline in the $^{13}\text{CH}_4/^{12}\text{CH}_4$ isotopic ratio of CH_4 (expressed as $\delta^{13}\text{C}(\text{CH}_4)$) since 2007 points to a significant change in CH_4 sources and sinks, since those vary in their $\delta^{13}\text{C}(\text{CH}_4)$ signatures. So far, the understanding of the underlying drivers is insufficient, which hampers both prioritizing mitigation actions and predicting future CH_4 trends.

This dissertation aims at a more detailed characterization of anthropogenic CH_4 emissions using airborne in situ measurement methods. Thereby, the focus is on the sector of offshore fossil fuel production, which is understudied so far. Driven by the hypothesis that emission inventories using generic scaling methods are not able to estimate emissions with sufficient accuracy, airborne measurement data gathered around offshore installations is analyzed and compared with different inventory data. Moreover, it is investigated, whether emissions can be better characterized by using the latest airborne laser spectroscopy methods. To this end, an existing direct laser absorption spectrometer is adapted for the high-resolution and continuous airborne measurement of the tracers C_2H_6 and $\delta^{13}\text{C}(\text{CH}_4)$, and deployed on research aircraft to study offshore emissions.

The first part presents the analyses of an airborne study conducted by the British Antarctic Service (BAS) in the southern North Sea in 2019. CH_4 emission rates from offshore gas installations were derived by applying the well-established mass balance method. They were then compared with direct operator-reporting, estimates from regional point source inventories and a globally gridded inventory, which uses national reported emissions in the framework of the United Nations Framework Convention on Climate Change (UNFCCC) and infrastructure data for a spatial downscaling. The findings reveal significant deviations between the derived emission rates and the estimates in the existing inventories. The inventories underestimate emissions by factors from 6 to 279, with the global inventory deviating the most. Notably, the operator-based facility-level reporting corresponds with the calculated flux, which only deviates by a factor of 0.64. The comparison with estimates from airborne measurements in other offshore regions shows that CH_4 emission rates are comparable and do not depend on oil- and gasproduction rates, which are typically used for emission estimates in inventories.

The second part of the thesis describes the characterization and adaptation of the DLR-QCLS, a fast and precise Quantum-cascade and Interband-cascade laser spectrometer, enabling it to measure the tracers C_2H_6 and isotopic CH_4 ($^{13}\text{C}(\text{CH}_4)$; $^{12}\text{C}(\text{CH}_4)$), to then use the isotopic ratio $\delta^{13}\text{C}(\text{CH}_4)$ to derive source signatures from offshore point sources. The laboratory characterization shows that, given the instrument precision (0.86‰ (1σ , 2 Hz)), source detection is feasible for strong fossil fuel plumes larger than approximately 250 ppb CH_4 , depending on the individual source signature. Furthermore, the qualitative detection of source signatures is demonstrated. During two aircraft campaigns the DLR-QCLS detected C_2H_6 and $\delta^{13}\text{C}(\text{CH}_4)$ signals from offshore oil installations, from which characteristic C_2H_6 to CH_4 ratios and source signatures were calculated. Nonetheless, it is necessary to refine the methodology both in laboratory settings and during field operations in order to achieve a better correspondence between the quantitative measurement of $\delta^{13}\text{C}(\text{CH}_4)$ and estimated source signatures.

Contents

Zusammenfassung	iii
Abstract	v
1 Introduction	1
2 Theoretical and methodological background	7
2.1 The Earth's atmosphere	7
2.1.1 Layers of the atmosphere	7
2.1.2 Atmospheric composition	9
2.1.3 Earth's energy budget and greenhouse effect	9
2.2 The greenhouse gas methane and tracers isotopic ratio $\delta^{13}\text{C}(\text{CH}_4)$ and ethane C_2H_6	11
2.3 Mass balance method for top-down CH_4 flux estimation	21
2.4 In situ measurement techniques for CH_4 , C_2H_6 and $\delta^{13}\text{C}(\text{CH}_4)$	23
2.4.1 Flasks (GC-IRMS)	24
2.4.2 Cavity ring-down spectroscopy	24
2.4.3 Tunable laser absorption spectroscopy	25
3 Quantification of CH_4 emissions from fossil fuel production in the southern North Sea	29
3.1 Types of emissions on offshore installations	30
3.2 Airborne field campaign in the southern North Sea	30
3.3 Method for top-down CH_4 flux estimation of offshore installations	32
3.4 Calculated Top-down CH_4 fluxes for UK and NL offshore installations	34
3.4.1 Comparison with bottom-up inventories	34
3.4.2 Correlations of CH_4 with C_2H_6 and CO_2	40
3.4.3 CH_4 loss rates	43
3.4.4 Comparison with CH_4 emissions from other offshore regions	43
3.5 Summary Chapter 3	45
4 Modifying the DLR-QCLS for the measurement of $\delta^{13}\text{C}(\text{CH}_4)$	49
4.1 Precision requirements for the study of CH_4 isotopic source signatures	50
4.2 Instrument description: The DLR-Quantum Cascade Laser Spectrometer (DLR-Quantum Cascade Laser Spectrometer (DLR-QCLS))	53
4.3 Adaptations for the measurement of $\delta^{13}\text{C}(\text{CH}_4)$	55
4.3.1 Selection of a new laser for the measurement of $^{13}\text{CH}_4$	55

4.3.2	Adaptation of the data retrieval	56
4.3.3	Calibration strategy	59
4.4	Laboratory characterization of the new DLR-QCLS laser configuration	62
4.4.1	Stability	62
4.4.2	Linearity	63
4.4.3	Water correction	67
4.4.4	Comparison with the Picarro Isotope Analyser (G2210i)	72
4.5	Summary Chapter 4	77
5	Instrument deployment during MAGIC and MTGA	79
5.1	Monitoring of Atmospheric composition and Greenhouse gases through multi-Instruments Campaign (MAGIC) campaign	80
5.1.1	MAGIC objectives, airborne payload and flight pattern	80
5.1.2	DLR-QCLS performance during MAGIC	81
5.1.3	Comparison with flask samples	86
5.2	METHANE-To-Go Africa (MTGA) campaign	89
5.2.1	MTGA objectives, airborne payload and flight strategy	89
5.2.2	Changes applied to the DLR-QCLS after MAGIC	89
5.2.3	DLR-QCLS performance during MTGA	91
5.2.4	Source signatures and C ₂ :C ₁ ratios for selected plumes	97
5.3	Summary Chapter 5	100
6	Summary and Outlook	103
A	Additional information on Chapter 3	109
B	Additional information on Chapter 5	113
C	Publications	115
	List of figures	118
	List of tables	119
	Acronyms	121
	Danksagung (Acknowledgements)	137

Chapter 1

Introduction

The global mean temperature increase since the start of the industrialization is remarkable. The last decade was warmer than any multi-century period since the last interglacial 125.000 years ago (Intergovernmental Panel on Climate Change (IPCC) 6th Assessment Report, 2021). Each year since 2015, the global mean surface temperature has surpassed pre-industrial levels from 1850-1900 by 1 °C. In 2023, a 1.48 °C higher level was reached with almost 50% of days already warmer than 1.5 °C (ECMWF (09 January 2024)).

As illustrated in Figure 1.1, climate model simulations demonstrate that the observed global surface temperature change is caused by anthropogenic activity, mainly due to emissions of greenhouse gases such as carbon dioxide (CO₂) and methane (CH₄). After CO₂, CH₄ is nowadays the second most important anthropogenic greenhouse gas. With a factor of 80-83 times stronger global warming potential (GWP) over a 20-year time horizon compared to CO₂, it contributes 16 (12-21)% to the abundance-based effective radiative forcing (ERF) or 32 (22-43)% to the emission-based ERF of well-mixed greenhouse gases over 1750-2019 (Forster et al. (2021), Szopa et al. (2021)). CH₄ is not only a greenhouse gas but also indirectly affects the air quality by its sink reactions, e. g. leading to the production of tropospheric ozone (O₃). According to Staniaszek et al. (2022), by 2050 1 °C of warming and 690.000 premature deaths per year can be attributed to anthropogenic CH₄ emissions in one of the IPCC projections for future climate (Shared Socioeconomic Pathway (SSP) SSP3-7.0), which predicts a global temperature increase of 4.4 °C by 2100. As shown in Figure 1.2(a), the currently observed CH₄ trend approaches the IPCC SSP4-6.0 scenario predicting a global temperature increase of 3.2-3.3 °C (Saunio et al. (2020), Lan et al. (2023)).

Atmospheric CH₄ mole fractions have strongly increased since 1750 due to human activity and continue to rise (Saunio et al. (2020)). The upper panel in Figure 1.2(b) depicts the atmospheric CH₄ mole fractions measured at the remote marine surface site Mauna Loa from 1998 to 2022 within the framework of the Global Monitoring Laboratory (GML) of the National Oceanic and Atmospheric Administration (NOAA). Since the beginning of the measurements in 1984, atmospheric CH₄ is continuously increasing with a plateau between 2000-2006 and a re-newed accelerating increase from 2007 onwards. Globally-averaged atmospheric CH₄ has experienced the highest annual increases between 2020 and 2022, on average +15.4 parts per billion (ppb) yr⁻¹, reaching 1930 ppb in March 2024 (Lan et al. (2023)).

Climate change and its impacts are accelerating, highlighting the need for urgent action. Within the United Nations Framework Convention on Climate Change (UNFCCC), the Paris

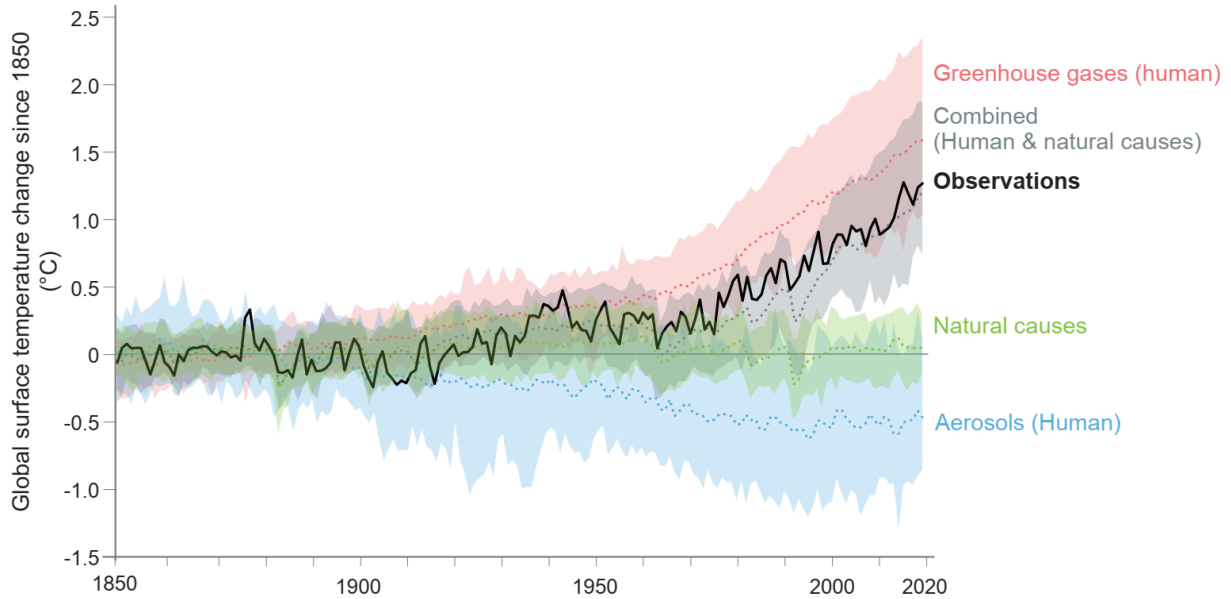


Figure 1.1: Global surface temperature change from 1850 to 2020 relative to 1850-1900 temperatures: Observations in black along with climate model simulations of the temperature responses due to greenhouse gas emissions only (red), from aerosols and other human influences (blue), natural drivers only (green) and combined human and natural forcings (gray). Solid lines show the multi-model mean and coloured bands the 5-95% range of simulations. (from Sixth Assessment Report of the IPCC, Eyring et al. (2021))

Agreement in 2015 set the goal of limiting the global average temperature increase to 1.5°C or at least well below 2°C above pre-industrial levels. Due to its relatively short atmospheric lifetime compared to CO_2 of around a decade, reduction in CH_4 emissions bears a high potential for mitigation strategies with fast impact (Nisbet et al. (2020)). CH_4 is emitted from a variety of sources. The natural sources are dominated by wetlands, which account for approximately 31% of all emissions. The largest anthropogenic CH_4 source is the agricultural and waste sector (approximately 38%), followed by fossil fuel emissions contributing with approximately 19% to total emissions (measurements averaged over 2008-2017, Saunio et al. (2020)). Reducing CH_4 emissions is often easily feasible and also economically interesting, especially from fossil fuel sources (e.g. leakages) (International Energy Agency (IEA) (2023)), and would have rapid impact on the global CH_4 burden (Nisbet et al. (2023)). To keep the Paris Agreement within reach, in November 2021 155 countries representing 50% of global anthropogenic CH_4 emissions including the European Union and the UK, joined the Global Methane Pledge with the aim to cut global CH_4 emissions by at least 30% from 2020 levels by 2030 (UNEP (2023)).

For the development of effective reduction strategies and to prioritize actions, CH_4 emissions, their distribution, their variability as well as their contribution to the overall budget must be well constrained. There are two different approaches to estimate emissions, the bottom-up and the top-down approach. Bottom-up inventories report emissions, which are estimated by multiplying activity data (e.g. amount of gas/oil production) with emission factors (e.g. CH_4 emissions per gas/oil produced), and allow to construct sector-specific global maps of emissions (Saunio

et al. (2020)). However, estimates are, especially on a regional and local scale, highly uncertain, because of local characteristics of emissions, which are not well represented by generic emission factors.

Contrary, top-down emission estimates are based on independent measurements. CH₄ emissions are estimated using ground-based, airborne or satellite observations of atmospheric CH₄. While top-down estimates allow for independent emission quantification, they are often expensive, complex and only represent snap-shot measurements. Nevertheless, top-down measurements are key to evaluate inventories and can help to resolve discrepancies between inventories.

The sustained CH₄ growth since 2007 is accompanied by a simultaneous negative shift in the ¹³C/¹²C isotopic ratio of CH₄, expressed as $\delta^{13}\text{C}(\text{CH}_4)$ (see lower panel in Figure 1.2(b)). This indicates that the CH₄ budget of sources and sinks is undergoing a profound change, since $\delta^{13}\text{C}(\text{CH}_4)$ varies depending on the source type and sink due to different CH₄ formation and removal processes. The underlying drivers and their relative contributions is subject of debate among scientists. An increase in biogenic CH₄ emissions, such as from wetlands and livestock, could contribute to the observed trend, since it is relatively more depleted in ¹³CH₄ compared to the atmospheric background (e.g. Zhang et al. (2023), Nisbet et al. (2023)). Thermogenic CH₄ from fossil fuel sources, for example from natural gas leaks, is usually relatively closer to background $\delta^{13}\text{C}(\text{CH}_4)$, but also suspected to contribute to the growth because of the parallel increase in atmospheric ethane (C₂H₆), which is a tracer especially for fossil fuel sources (e.g. Hausmann et al. (2016)). The third category of CH₄ sources is pyrogenic CH₄, which is rich in ¹³CH₄ and emitted from burning organic matter, for example in wildfires or burning biofuels. Next to the tracer C₂H₆ for thermogenic CH₄ sources, ¹³CH₄ or $\delta^{13}\text{C}(\text{CH}_4)$ serves as a tracer for CH₄ sources as it identifies their source category (biogenic, thermogenic, pyrogenic).

Fossil fuel CH₄ emissions are estimated to significantly contribute to the total anthropogenic CH₄ emissions, but measurements indicate large underestimations by bottom-up inventories (e.g. Gorchov Negrón et al. (2020), Johnson et al. (2017), Schwietzke et al. (2016)). In particular, offshore oil and gas installations are understudied but presumably important emission sources. Emissions originate from venting or flaring of natural gas and from unintended leaks. After CH₄, C₂H₆ is the second-most abundant component of natural gas and released simultaneously with CH₄. Therefore, C₂H₆ is widely used as a tracer for fossil fuel emissions. Satellite measurements have revealed large onshore super-emitters (Schuit et al. (2023), Thorpe et al. (2023), Varon et al. (2019), Pandey et al. (2019)). Offshore installations, however, are more difficult to detect for satellites due to their location next to water (International Energy Agency (IEA) (2023)). Shipborne measurements of offshore installations rely on an additional plume model for the estimation of the vertical plume extent, which is necessary for the quantification of emissions (Yacovitch et al. (2020), Riddick et al. (2019)). In contrast, the mobility of airborne platforms allows to cover the vertical and horizontal extent of selected CH₄ plumes, independent of e.g. the wind direction. Furthermore, the range of aircrafts enables the coverage of larger regions within short time frames. Airborne offshore measurements have been conducted in the Northern Gulf of Mexico, Central North Sea, Norwegian Sea and Southeast Asia (Foulds et al. (2022), Gorchov Negrón et al. (2020), Lee et al. (2018), Roiger et al. (2015), Nara et al. (2014)). Numerous in situ airborne measurements successfully used C₂H₆ as a tracer for fossil fuel CH₄ emissions (e.g. Peischl et al. (2018), Johnson et al. (2017)).

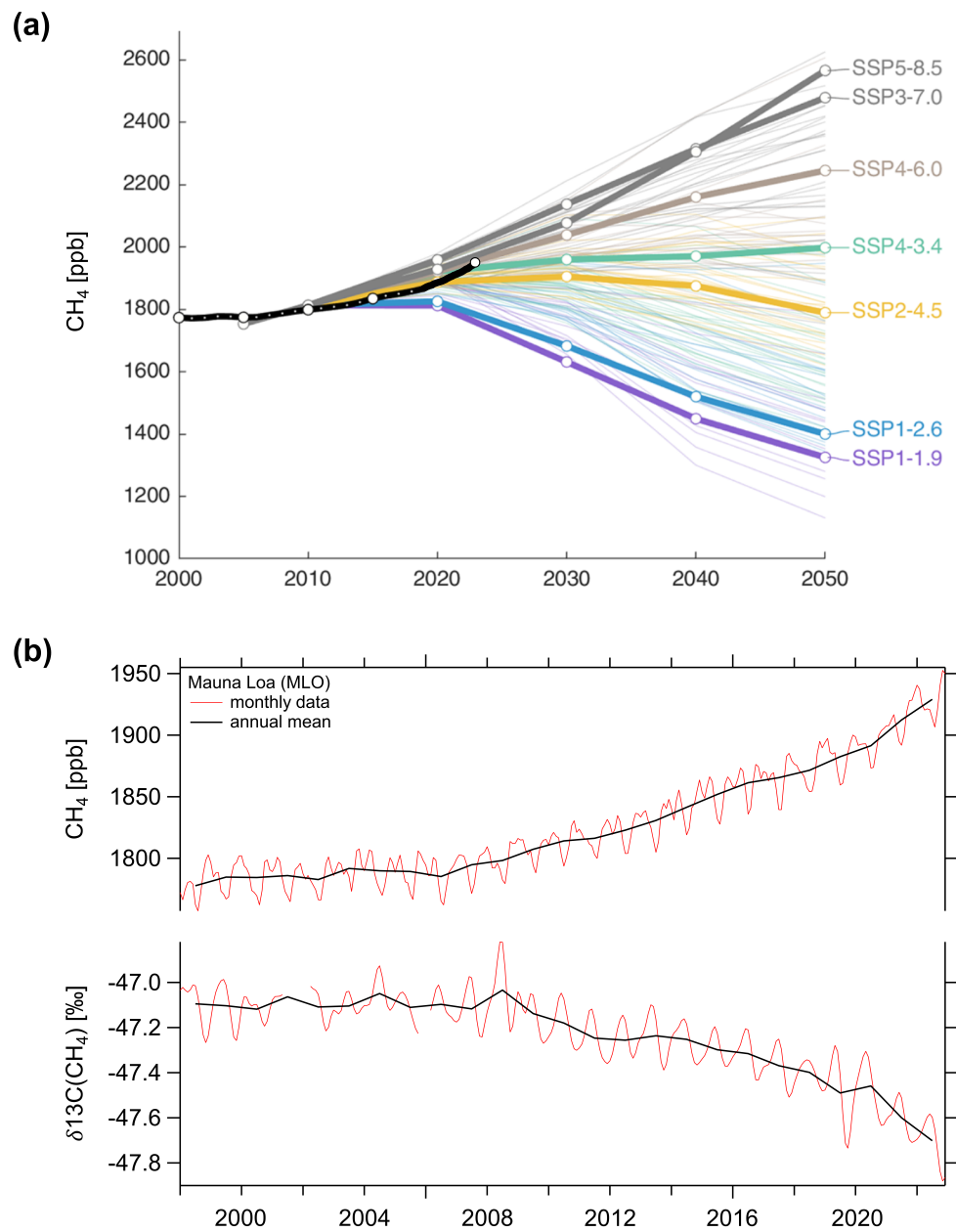


Figure 1.2: (a) Atmospheric CH_4 mole fractions (black) for NOAA surface sites along with projections based on Shared Socioeconomic Pathways (SSPs) (Figure adapted from Saunio et al. (2020)). (b) Atmospheric CH_4 mole fractions and $\delta^{13}\text{C}(\text{CH}_4)$ measured at the NOAA remote marine surface site Mauna Loa (MLO) from 1998 to 2022 (data taken from the NOAA Global Monitoring Laboratory (GML), Michel et al. (2023), Lan et al. (2023)).

Motivated by the need to better constrain offshore fossil fuel CH₄ emissions and their contribution to the current trend in atmospheric CH₄ and $\delta^{13}\text{C}(\text{CH}_4)$, this thesis focuses on the study of offshore fossil fuel sources by applying airborne measurement methods. For the airborne study of point source emissions, which often display sharp enhancements, a continuous measurement technique for $\delta^{13}\text{C}(\text{CH}_4)$ is beneficial to derive isotopic CH₄ source signatures. Therefore, this thesis investigates the potential of the continuous airborne measurement of the tracer $\delta^{13}\text{C}(\text{CH}_4)$ and its use to characterize offshore emissions from point sources (oil and gas installations). The following hypothesis is set:

"Generic emission reporting methods used in global inventories and for UNFCCC reporting do not correctly reflect offshore emissions. Recent developments and improvements of laser absorption spectroscopy allow for continuous airborne measurements of the two tracers $\delta^{13}\text{C}(\text{CH}_4)$ and C₂H₆ to support the characterization of offshore fossil fuel emissions."

To test this hypothesis, the offshore regions in the southern North Sea and western Central Africa are studied. In Europe, after Norway, the United Kingdom and the Netherlands with their offshore installations located in the southern North Sea are the leading producers of natural gas (Eurostat (2020)). The Angolan and Gabonese oil and gas industry at the western Central African coast is estimated to contribute with 18.5% to the African oil production (bp (2022)), but is especially understudied. Thus, these are important target regions for the measurement of fossil fuel CH₄ emissions. The Deutsches Zentrum für Luft- und Raumfahrt (DLR)-Quantum Cascade Laser Absorption Spectrometer (DLR-QCLS) is a fast and precise instrument and has been already used for several aircraft campaigns in the past. It provides the means to establish the continuous measurement of $\delta^{13}\text{C}(\text{CH}_4)$ for the fast airborne sampling of point sources such as offshore installations.

This thesis is guided by the following research questions:

RQ 1: How high and variable are top-down derived CH₄ emission estimates and C₂H₆ to CH₄ (C₂:C₁) ratios for offshore fossil fuel installations in the southern North Sea?

RQ 2: How do the top-down CH₄ emission estimates in the southern North Sea compare with bottom-up inventory estimates?

RQ 3: How do the top-down CH₄ emission estimates in the southern North Sea compare with top-down studies in other offshore regions?

RQ 4: How well can we measure important tracers for CH₄ source attribution ($\delta^{13}\text{C}(\text{CH}_4)$, C₂H₆) using airborne laser-based absorption spectroscopy?

RQ 5: How well do the observational-based C₂H₆ to CH₄ (C₂:C₁) ratios and $\delta^{13}\text{C}(\text{CH}_4)$ source signatures of Angolan and Gabonese offshore oil installations agree with data from the literature?

RQ 6: What are the challenges of airborne $\delta^{13}\text{C}(\text{CH}_4)$ measurements and what are necessary improvements?

The first part of this work (**RQ 1-3**) is the analysis of an airborne study that had been conducted 2019 in the southern North Sea by the British Antarctic Service (BAS) to assess CH₄ emissions from British and Dutch offshore natural gas installations (France et al. (2021)). In

this work, the data was used to calculate CH₄ top-down emission fluxes for eleven targeted gas installations. These were compared with different bottom-up estimates, including a globally gridded inventory, two national point source inventories, and operator-based facility-level reporting. Further, C₂H₆ measurements were used as a tracer to identify fossil fuel plumes. C₂H₆ to CH₄ ratios were derived, which are characteristic for the respective gas fields. Emission fluxes and loss rates (emissions normalized to production rates) are set into a wider context in a regional comparison with two other regions, the Norwegian Sea and the Northern Gulf of Mexico.

The second part (**RQ 4-6**) involves the adaptation of the fast (2 Hz time resolution) DLR-QCLS (original manufacturer Aerodyne Research Inc., Billerica (USA)) for the continuous measurement of methane isotopologues (¹³CH₄ and ¹²CH₄) to then use the isotopic ratio $\delta^{13}\text{C}(\text{CH}_4)$ for a better understanding and differentiation of CH₄ sources. To this end, a laser was selected in a suitable wavelength range based on relevant criteria such as ¹³CH₄ and ¹²CH₄ absorption line strengths and separation of absorption lines from other gases typically abundant in the atmosphere. The instrument was extensively characterized in the laboratory with the new laser configuration in preparation of the DLR MTGA field campaign in September 2022. The campaign aimed at studying fossil fuel CH₄ emissions from offshore oil installations at the coasts of Angola and Gabon. An additional field campaign in Northern Sweden and Finland (MAGIC) in 2021 was used to test the airborne performance and to allow for improvements for the MTGA campaign.

This thesis is structured as follows: In Chapter 2 the theoretical background is given including a brief description of the structure of the Earth's Atmosphere, followed by a detailed explanation of the role of CH₄ and the tracers $\delta^{13}\text{C}(\text{CH}_4)$ and C₂H₆. Further, the mass balance method for emission quantification is explained along with measurement techniques used for CH₄, $\delta^{13}\text{C}(\text{CH}_4)$ and C₂H₆. Chapter 3 presents the study of fossil fuel CH₄ emissions of offshore gas installations in the southern North Sea. Chapter 4 treats the adaptation and characterization of the DLR-QCLS with the new isotopic laser configuration in the laboratory. In Chapter 5, the airborne performance of the DLR-QCLS with the new configuration is evaluated for the MAGIC and the MTGA campaign. Finally, in Chapter 6 the main findings of this thesis are summarized including an outlook for future improvements and studies.

Chapter 2

Theoretical and methodological background

In this first chapter, an overview of the theoretical and methodological background is given. First, the structure of the Earth's Atmosphere and the influence of its atmospheric constituents is described in Section 2.1. In Section 2.2 a more detailed description of the greenhouse gas methane CH_4 and its tracers methane isotopologue $^{13}\text{CH}_4$ and ethane C_2H_6 is given. Furthermore, the method for CH_4 flux estimation as applied in this work is described in Section 2.3, followed by the explanation of common in situ measurement techniques in Section 2.4.

2.1 The Earth's atmosphere

This section is based on textbooks by Seinfeld and Pandis (2016), Petty (2006) and Roedel and Wagner (2017), if not otherwise specified.

2.1.1 Layers of the atmosphere

The Earth's atmosphere is subdivided into five layers depending on the average temperature profile of the atmosphere as depicted in Figure 2.1. In this work, the focus is on the study of CH_4 emissions from point sources on the ground. Therefore, the lowest part of the atmosphere, namely the planetary boundary layer within the troposphere, where all emissions from the surface are directly mixed into, is most important.

The **troposphere** contains roughly 85-90% of the total mass of the Earth's atmosphere. Heated up by energy transfer from the surface, the temperature in the troposphere decreases up to approximately 10 km altitude at an average lapse rate of 6.5 K per km. The upper troposphere temperature minimum with temperatures as low as -50 to -80 °C is called the tropopause. The tropopause is defined as the lowest level at which the lapse rate decreases to 2 K per km or less (World Meteorological Organisation (WMO (1957))). There also exist other definitions like a substantial increase in stratospheric ozone or decrease in tropospheric water vapor (Connolly et al. (2024)). The height of the tropopause depends on latitude and time of the year, whereby in warm tropical regions the tropopause is higher (~16 km) than in cold polar regions (~9 km) (Gulev et al. (2021)). Driven by decreasing temperatures with increasing altitude, convection

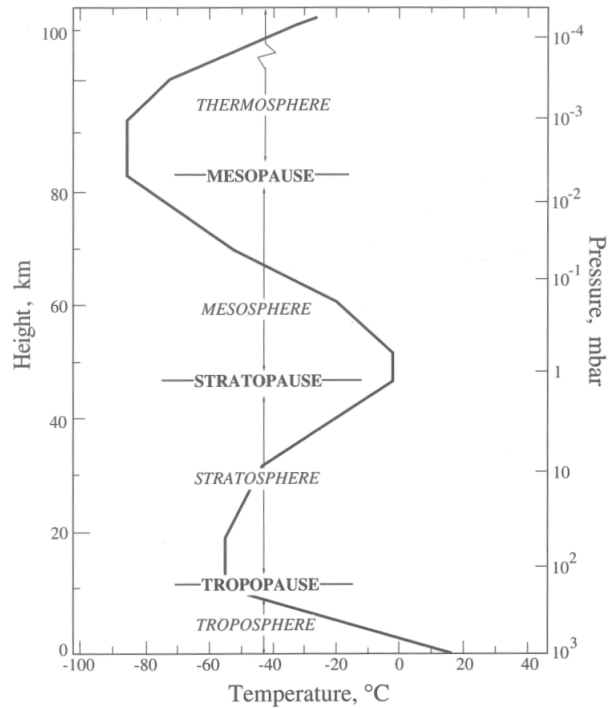


Figure 2.1: Mean temperature profile of the atmosphere with height and pressure. The atmosphere is subdivided into layers according to the temperature profile (from Seinfeld and Pandis (2016)).

and turbulence sets in and together with horizontal wind and frontal systems the troposphere is the layer, where the primary turbulent mixing of the atmosphere takes place.

The troposphere can be divided into the **planetary boundary layer (PBL)**, which directly couples to the Earth's surface and extends up to 0.1-3 km, and the upper free troposphere.

The PBL is directly affected by surface forcings such as heat transfer and friction making it a highly turbulent layer. In the lowest ~ 100 m of the PBL (Prandtl-layer) the influence of surface friction is highest. As the influence decreases with increasing height, usually an increase in horizontal wind speed is observed. The layer above the Prandtl-layer, where surface friction is less relevant, is called the Ekman-Layer. In this layer, horizontal wind speed is relatively constant, while wind direction typically changes and approximates the prevailing geostrophic wind (parallel to isobars) of the upper free troposphere at middle and high latitudes.

The PBL builds up during the day due to solar irradiance, which induces turbulent convection. Within the PBL, variables such as wind, temperature, water vapor and trace gases show great variability. Air masses containing emissions and evaporated water from the ground rapidly mix and surface emissions can reach the upper free troposphere within only a few hours. The PBL reaches its maximum height in early afternoon, but is usually lower over water compared to over land due to the higher heat capacity of water. When the Earth's surface cools down at night, the residual PBL is more stable and only has a few hundred meters height. The height of the PBL (boundary layer height (BLH)) is defined by a positive gradient in potential temperature (temperature of an air parcel when adiabatically moved to the ground) indicating the transition to

the more stable upper free troposphere. Still, in a thin transition zone or entrainment zone, some exchange between the PBL and the free troposphere occurs. When studying surface emissions with in situ airborne measurements, it is favorable measuring at fair weather conditions in the afternoon, when the PBL has reached its maximum height. Then the PBL is well-mixed and emissions are most uniformly distributed in the vertical.

For the sake of completeness, a short description of the upper layers is given in the following. The **stratosphere** is the atmospheric layer above the tropopause extending up to the stratopause at 45-55 km altitude. The atmospheric temperature increases with altitude makes this layer much more stable and slower in vertical mixing compared to the troposphere. The temperature increase is a result from the absorption of solar ultraviolet (UV) radiation by ozone. Because of the temperature minimum at the tropopause, almost all water vapor condenses and the upper stratosphere is very dry. In the **mesosphere** the temperature decreases up to the mesopause in 80-90 km altitude, where the coldest temperatures of the atmosphere are found (on average -90°C). At the Mesopause the air density is five orders of magnitude smaller than on the Earth's surface. Within the **thermosphere** the atmospheric temperature strongly increases to more than 1000°C . Molecules and atoms are dissociated and ionised by shortwave solar radiation generating a plasma. At approximately 500 km altitude the thermosphere transitions into the **exosphere**, the outermost layer of the atmosphere.

2.1.2 Atmospheric composition

The dry air in Earth's atmosphere consists of 78.08% nitrogen N_2 , 20.95% oxygen O_2 and 0.93% argon. Water vapor H_2O is highly variable and can reach some percents. The rest of atmospheric molecules, 0.04%, are trace gases, which comprise short-lived species such as the radical OH (lifetime only some seconds), moderately long-lived species such as nitrogen oxides NO_x (lifetime of some hours to some days) and long-lived species (lifetime more than 1 year) such as the greenhouse gases carbon dioxide CO_2 , methane CH_4 , nitrous oxide N_2O , ozone O_3 and halocarbons. H_2O is the main natural greenhouse gas.

Since concentrations in mol m^{-3} are pressure and temperature dependent (ideal gas law), the atmospheric abundance c_i of a species i is given as mole fractions:

$$c_i = \frac{n_i}{n_{total}} \quad (2.1)$$

n_i is the number of atoms or molecules of the species i , while n_{total} denotes the total number of air molecules. Because the highly variable water vapor can lead to variations of several percent for c_i , mole fractions are defined with respect to dry-air (Seinfeld and Pandis (2016)). The common units to express mole fractions are parts per trillion (ppt) (10^{-12}), parts per billion (ppb) (10^{-9}), parts per million (ppm) (10^{-6}) or % (10^{-2}). As an example, the current atmospheric CH_4 abundance is 1930 ppb (globally-averaged, monthly mean determined from marine surface sites of the NOAA GML for March 2024, Lan et al. (2023)).

2.1.3 Earth's energy budget and greenhouse effect

CH_4 and all other greenhouse gases are important constituents of the atmosphere, since they strongly influence the Earth's energy budget due to the greenhouse effect.

The approximately spherical Earth receives a solar irradiance of 340 watts per square metre (W m^{-2}) on average over the entire surface. When arriving at the top of the Earth's atmosphere, it gets scattered at atmospheric molecules, aerosols and cloud particles. Furthermore, it gets absorbed by atmospheric molecules (80 W m^{-2} or 24%) and reflected at clouds and aerosols (29%). When reaching the Earth's surface, solar irradiance is partly reflected (7%), but the largest part is absorbed (47%) inducing a warming, which in turn leads to the emission of thermal infrared (IR) radiation of the Earth (Forster et al. (2021)).

The thermal emission spectra of the Sun and the Earth can be approximated by the Planck emission curves for an ideal blackbody (a perfect emitter/absorber of light) according to their respective temperatures. Figure 2.2(a) displays both the Planck emission spectra for the Sun at an approximate temperature of 6000 K and the Earth at a temperature of 288 K. The incoming solar radiation extends from the ultraviolet (UV) ($\sim 0.1\text{-}0.38 \mu\text{m}$) to the visible ($\sim 0.38\text{-}0.78 \mu\text{m}$), near IR (~ 0.78 to $3 \mu\text{m}$) and mid IR ($> 3 \mu\text{m}$) wavelength region. Due to its lower temperature, the Earth emits thermal radiation at longer wavelengths in the IR extending from approximately 3 to $100 \mu\text{m}$.

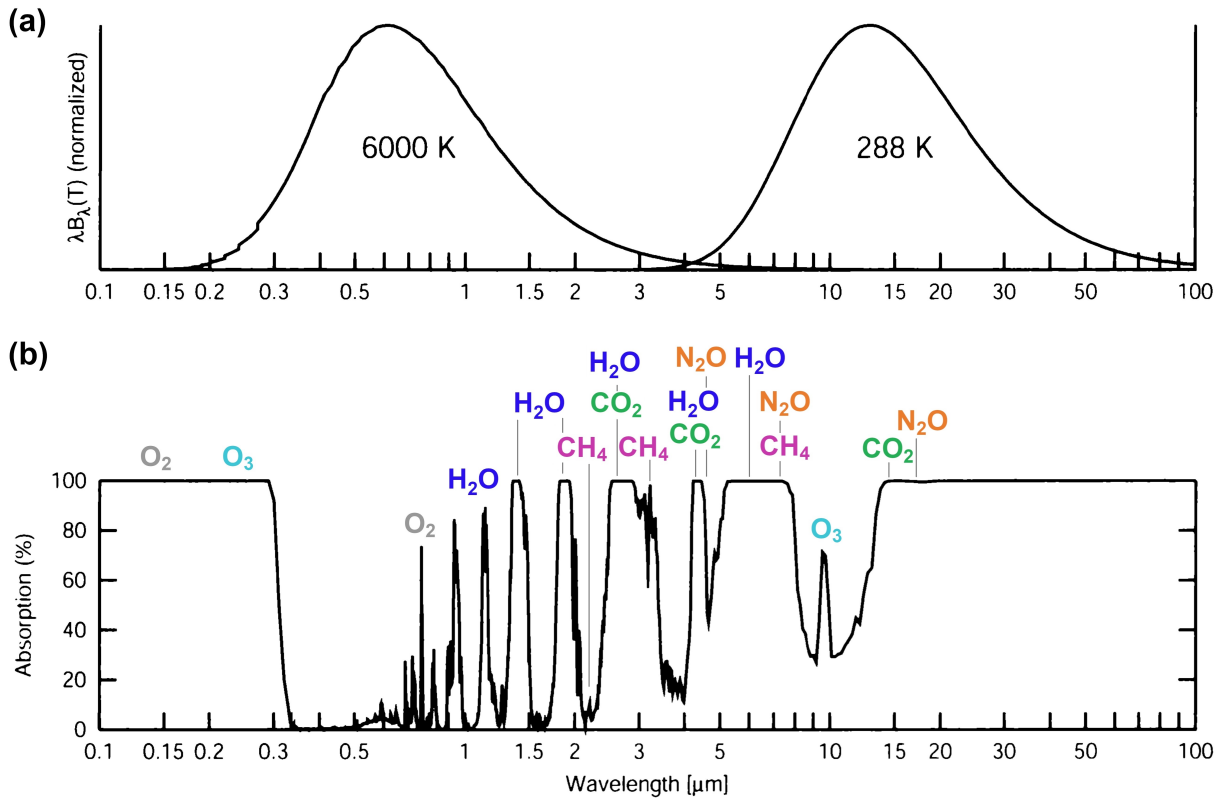


Figure 2.2: (a) Planck's blackbody emission spectra (normalized by the respective maximum) for a temperature of 6000 K (Sun) and 288 K (Earth). (b) Absorption of the entire atmosphere along the wavelength region from 0.1 to $100 \mu\text{m}$. Atmospheric molecules are highlighted at their respective characteristic absorption wavelengths (O_2 in gray; O_3 in light blue; H_2O in dark blue; CH_4 in magenta; CO_2 in green; N_2O in orange). (adapted from Petty (2006))

Figure 2.2(b) shows the absorption of the entire atmosphere from 0.1 to 100 μm . The strong absorption of solar UV radiation is due to O_2 and O_3 in the middle and upper atmosphere. O_2 gets photodissociated at wavelengths smaller than 0.24 μm and O_3 absorbs between 0.2 and 0.31 μm due to electronic excitation. In the visible wavelength region solar irradiation is highest, but the atmospheric absorption is relatively low. The absorption bands in the IR wavelength region up to 8 μm are mainly caused by absorption of IR-active molecules, i. e. the greenhouse gases H_2O , CO_2 , CH_4 , N_2O and others. The absorption of IR light at specific energies/wavelengths induces rotational-vibrational oscillations changing the dipole moment of the molecule. Each line in the absorption spectrum is unique to the molecule and to its specific transition, which is the basis for direct absorption spectroscopy (explained in Section 2.4.3). For example, CH_4 exhibits strong absorption bands at 1.7, 2.3, 3.3 and 7.6 μm (Byrom and Shine (2022)). From 8 to 12 μm the absorption of H_2O is reduced, which is why the atmosphere is more transparent in this region. The strong absorption at longer IR wavelengths ($> 25 \mu\text{m}$) is due to rotational transitions of H_2O .

Because a large part of thermal IR light emitted from the Earth's surface is absorbed by greenhouse gases (86% of 398 W m^{-2} total emitted thermal radiation, Forster et al. (2021)), which reemit the radiation to all directions, less thermal radiation (60%) escapes the atmosphere leading to a net warming. This effect is called the greenhouse effect, which leads to a global average temperature of around +15 $^\circ\text{C}$ instead of -18 $^\circ\text{C}$. A perturbation, e. g. increased absorption of thermal radiation due to an increase in greenhouse gases, would lead to an imbalance, i. e. an accumulation or decrease of energy in the Earth's system. The induced change in the net energy flux is described by the commonly used effective radiative forcing (ERF). The ERF not only describes the change at the top of the atmosphere due to the perturbation (radiative forcing), but also includes adjustments of the atmosphere to the perturbation, e. g. changes in tropospheric temperature and in cloud cover, which in turn have an impact on the radiative balance (Thornhill et al. (2021)).

CH_4 contributes with 0.54 W m^{-2} or 16 (13-20)% to the abundance-based ERF of all well-mixed greenhouse gases (CO_2 , CH_4 , N_2O and halocarbons) for the period 1750-2019 (Forster et al. (2021)). Besides the direct effects, also indirect effects exist like CH_4 increasing its own lifetime and CH_4 oxidation leading to the production of stratospheric H_2O and tropospheric O_3 (Thornhill et al. (2021), Stecher (2024)). Considering these indirect effects, the so-called emission-based ERF is 1.2 W m^{-2} and contributes with 32 (22-43)% to the emission-based ERF of all well-mixed greenhouse gases (Szopa et al. (2021), based on Thornhill et al. (2021)).

2.2 The greenhouse gas methane and tracers isotopic ratio $\delta^{13}\text{C}(\text{CH}_4)$ and ethane C_2H_6

CH_4 is the second most important anthropogenic greenhouse gas after CO_2 and far less abundant (approximately 1.93 ppm globally averaged atmospheric background mole fractions CH_4 compared to 420 ppm CO_2 in 2024). With a factor 80-83 times stronger global warming potential (GWP) per unit mass and over a 20-year time horizon compared to CO_2 (GWP=1), it contributes 16% to the abundance-based and 32% to the emission-based ERF of well-mixed greenhouse gases and causes 0.6 $^\circ\text{C}$ of the temperature rise over 1750-2019 (Szopa et al. (2021)). Moreover, it has a strong influence on the oxidising capacity of the atmosphere by reacting with the tropospheric

hydroxyl radical OH, which acts as a "cleaning agent" removing many tropospheric trace gases, such as nitrogen oxides NO_x or carbon monoxide CO. As a consequence, CH₄ indirectly influences the tropospheric O₃ production and, thus, air quality and crop productivity.

Atmospheric background measurements prove a strong increase in CH₄ since the beginning of the industrial revolution. Starting from approximately 700 ppb in the year 1750 (see Figure 2.6 and Prather et al. (2012)) the atmospheric CH₄ abundance reached 1930 ppb in March 2024 at the NOAA GML (Lan et al. (2023)). Figure 2.3 shows the globally-averaged atmospheric CH₄ mole fractions measured at remote marine sites from the NOAA GML. The increase before 2000 is attributed to increased anthropogenic emissions, especially from fossil fuel emissions, and from other anthropogenic emissions, e.g. livestock and rice cultivation (Kirschke et al. (2013)). In the years 2000-2006 the curve flattens and an equilibrium between sources and sinks was reached (Nisbet et al. (2023)), which is not yet understood. There is also no scientific consensus about the cause of the renewed increase in atmospheric CH₄ mole fractions since late 2006. The increase even accelerated from 2014 and 2020 onwards with average annual growth rates of +9.2 ppb between 2014 and 2019 and +15.6 ppb for 2020-2022. The CH₄ growth rate has reached its maximum in 2021 with an increase of (17.89 ± 0.45) ppb compared to 2020 (NOAA, Lan et al. (2023)). Hypotheses for the renewed CH₄ growth are presented at the end of this section.

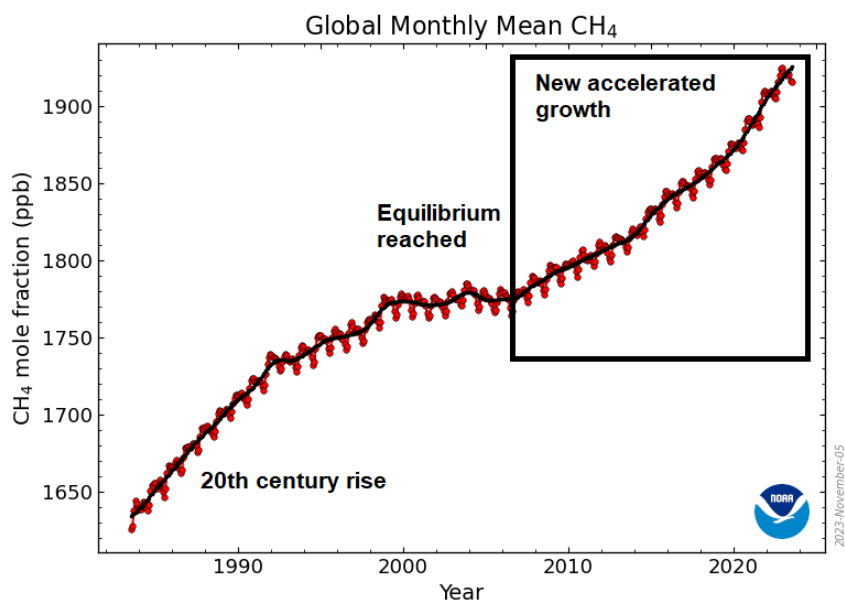


Figure 2.3: Trend of globally-averaged atmospheric CH₄ shown as monthly means (red markers). Data is taken from marine surface sites from the NOAA global observational network (modified from Nisbet et al. (2023) using recent NOAA GML data Lan et al. (2023)).

Sources and sinks

There are various sources emitting CH₄ into the atmosphere. Anthropogenic sources include the agricultural sector, waste, fossil fuels and biomass/biofuel burning. Natural sources comprise

2.2 The greenhouse gas methane and tracers isotopic ratio $\delta^{13}\text{C}(\text{CH}_4)$ and ethane C_2H_6

13

wetlands, inland waters, natural wild fires, termites, geological sources and thawing permafrost. Most of global CH_4 is emitted in the tropics (64%), followed by the mid-latitudes (32%) and the Northern high-latitudes (4%) (Saunois et al. (2020)). Figure 2.4 shows the contributions of each source sector to the total global emissions estimated from inventories (bottom-up view) and derived from measurements (top-down view) as an yearly average over 2008 to 2017.

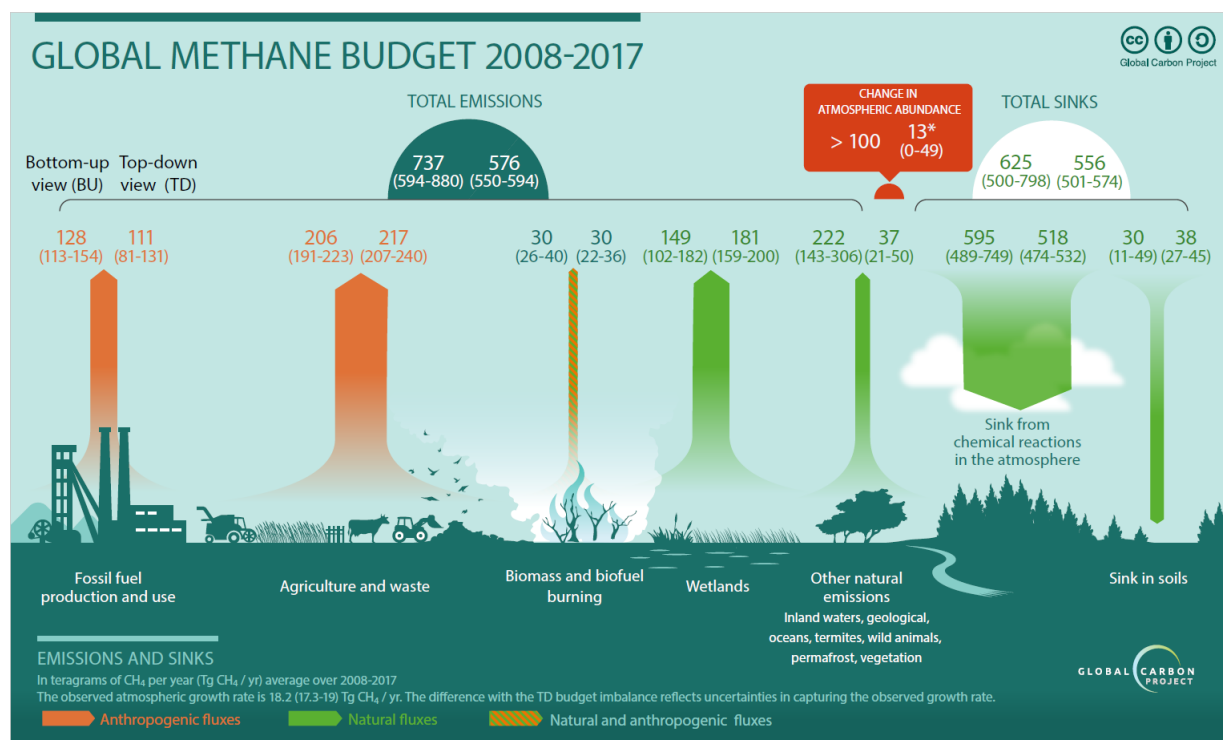


Figure 2.4: Top-down and bottom-up estimates for CH_4 sources and sinks (from Global Carbon Project, data taken from Saunois et al. (2020)).

The biggest anthropogenic source is emissions from agriculture and waste with a contribution of 38 (35-44)%. The fossil fuel sector comprises fossil fuel (oil, gas, coal) exploitation, production and use. It accounts for 19 (14-24)% of global CH_4 emissions. Emissions from wetlands are the main natural source with 31 (27-36)% contribution.

CH_4 is predominantly removed from the atmosphere by the reaction with the hydroxyl radical OH (90%), which is most abundant in the troposphere (Saunois et al. (2020), Zhao et al. (2020)):



The methyl peroxy radical CH_3O_2 then further reacts with NO_x , HO_2 radicals or other organic peroxy radicals RO_2 . CH_4 oxidation finally leads to the formation of nitric acid HNO_3 or hydrogen peroxide H_2O_2 . Additionally, CH_4 can be oxidized to CO_2 or CH_3OOH as an end product, whereby the latter is wet or dry deposited. Thereby, O_3 is produced with a maximum yield of 5 O_3 molecules per oxidized CH_4 molecule, which is usually not achieved in the atmosphere.

Other minor sinks include the uptake in soils by methanotrophs (bacteria or archaea) (7%), the oxidation with Cl atoms in marine boundary layers, stratospheric loss by reaction with excited

atomic oxygen radicals $O(^1D)$ and photochemical dissociation above the stratosphere (Saunois et al. (2020), Rigby et al. (2017), Kirschke et al. (2013)).

CH_4 mole fractions show a seasonality, since sources such as wetlands and fires and all sinks display innerannual variability (Saunois et al. (2020), Qu et al. (2022)). As an example, the availability of OH depends on the season and the latitude, i.e. it is more abundant in humid tropical regions than in higher latitudes and more abundant in summer months than in winter months (Holmes (2018)). Due to more CH_4 sources, the average background mole fractions in the Northern Hemisphere are larger than in the Southern Hemisphere.

Bottom-up versus top-down view

As indicated at the top of Figure 2.4, the emission from sources is higher than the removal of CH_4 by its sinks, which leads to a net increase in atmospheric CH_4 . At the same time, the global CH_4 budget and the exact contributions of individual sources are still uncertain. In general, total CH_4 emissions derived with the bottom-up approach (737 (594-880) Tg yr⁻¹) are higher than those based on the top-down approach (576 (550-594) Tg yr⁻¹). Top-down estimates show a higher contribution of anthropogenic sources (62%) compared to bottom-up estimates (50%). The uncertainties in the amount of natural CH_4 emissions might arise from different reasons, such as the difficulty in the definition of wetland area extents. For example, bottom-up estimates might overestimate freshwater areas by double-counting them to both wetlands and other natural freshwater systems (Saunois et al. (2020)). Also the contribution of geological fossil fuel sources might be over-estimated in bottom-up inventories, implying that anthropogenic fossil fuel sources might be underestimated (Etiopé and Schwietzke (2019)). Many top-down measurements of anthropogenic fossil fuel CH_4 sources reveal large discrepancies with bottom-up estimates indicating an underestimation of emissions in inventories (e.g. MacKay et al. (2021), Gorchoy Negron et al. (2020), Barkley et al. (2019a), Peischl et al. (2018), Johnson et al. (2017), Schwietzke et al. (2016), Pétron et al. (2014)). As an example, Gorchoy Negron et al. (2020), showed that offshore fossil fuel emissions in the U.S. Gulf of Mexico are more than a factor of two higher than estimated by inventories. Using a global inverse analysis of GOSAT-satellite observations from 2010-2018, Zhang et al. (2021) found an underestimation of fossil fuel emissions by the UNFCCC national reporting from Venezuela, Iran, Turkmenistan and the U.S.

Bottom-up estimates are calculated by multiplication of activity data (e.g. the number of cows) with emission factors (e.g. amount of released CH_4 from one cow per year). The emission factors are typically based on data taken from literature or from sparse measurements, but may vary e.g. for different regions. In the top-down view, emission fluxes are derived from measurements for specific sources. Measurements can be continuous (e.g. at ground-based measurement stations) or campaign-based (e.g. airborne measurements). For example, airborne measurements can resolve a greater area and more sources at the same time period, but, as a disadvantage, cannot resolve varying emission fluxes with time. Deviations between bottom-up and top-down estimates are not surprising, thus an intercomparison of bottom-up and top-down estimates for specific sources or regions are necessary to verify bottom-up estimates and minimize deviations in order to improve the total CH_4 budget estimate.

Lifetime of CH_4

The lifetime of CH_4 is controlled by its sinks. However, both the lifetime of CH_4 and the short-lived OH can not be measured directly. Instead, the lifetime is derived from the measurement of methyl chloroform CH_3CCl_3 , a synthetic hydrochlorocarbon. Its atmospheric abundance has decayed exponentially since 2006, when its emissions ceased, predominantly due to oxidation with OH. Using the lifetime of CH_3CCl_3 against its OH sink and the reaction rate of CH_4 with OH, a lifetime of 9.1 ± 0.9 years is deduced (for the year 2010 according to Prather et al. (2012)). Following Equation 2.2, water vapor is generated by the reaction of CH_4 with OH. Since water vapor is a precursor of OH, the reaction further accelerates the loss of CH_4 . After CH_4 , CO is the secondmost important sink for OH. Therefore, the lifetime of CH_4 can be prolonged by enhanced CO emitted from e. g. fires as observed during hot El Nino years (Zhao et al. (2020)). Its lifetime is also influenced by CH_4 itself, as enhanced CH_4 mole fractions lead to a reduction of OH (Winterstein et al. (2019)). This effect is, however, weakened by a warming feedback, since warming causes higher water vapor producing more OH (Stecher et al. (2021)).

The lifetime of CH_4 of around a decade is relatively short compared to other greenhouse gases (CO_2 approx. 5-200 years, N_2O approx. 116 ± 9 years) (Prather et al. (2015)). Therefore, a reduction of emissions would yield a relatively fast slowing-down of climate warming. To better understand the current and future impact of CH_4 on the radiative budget, and to efficiently reduce emissions, it is important to know the CH_4 sources and sinks and better understand their contributions to the total CH_4 budget. Isotopic measurements can help to better constrain these contributions, but more measurements are needed globally, especially in the tropics (Brownlow et al. (2017), Rigby et al. (2012)).

Source attribution using the tracers $\delta^{13}\text{C}(\text{CH}_4)$ and C_2H_6

Most of atmospheric CH_4 exists as methane isotopologue $^{12}\text{CH}_4$ (98.8274%). The less abundant and heavier CH_4 isotopologue $^{13}\text{CH}_4$ makes up only 1.11031% of total CH_4 in the atmosphere (Gordon et al. (2022)).

Isotopic abundances are commonly given in delta notation $\delta^{13}\text{C}(\text{CH}_4)$, which is defined as the deviation of the ratio $R = \frac{^{13}\text{CH}_4}{^{12}\text{CH}_4}$ in a sample to that in a standard:

$$\delta^{13}\text{C}(\text{CH}_4) = \frac{R_{\text{sample}}}{R_{\text{reference}}} - 1 \quad (2.3)$$

The widely used reference is the Vienna Pee Dee Belemnite (VPDB) standard, a carbonate fossil from the Peedee Formation, South Carolina (U.S.), with $R_{VPDB} = 0.0111802$ (WMO (2020), Werner and Brand (2001)). Because $\delta^{13}\text{C}(\text{CH}_4)$ values are small, they are expressed in permil (‰).

The extra neutron in the carbon atom within $^{13}\text{CH}_4$ leads to a very small difference in weight, which affects the absorption properties of the molecule (see Section 2.4.3 and Chapter 4), and formation and sink processes, as well. More specifically, the heavier ^{13}C atom at the center of the molecule generates a stronger covalent bonding (described by the an-harmonic morse Potential or Lennard-Jones potential) of the surrounding H atoms compared to the lighter ^{12}C atoms. As a consequence, higher dissociation energies are needed to break up the molecular bonds. For this reason, isotopic fractionation in sources and sinks takes place, meaning that $^{12}\text{CH}_4$ is preferred over $^{13}\text{CH}_4$. For example, when CH_4 is biogenically formed by microbes, organic

material containing ^{12}C is preferably digested. Concerning the sink reactions, the reaction with $^{12}\text{CH}_4$ happens faster than the reaction with $^{13}\text{CH}_4$, because reaction rates k are higher for lower dissociation energies according to the Arrhenius Equation (kinetic isotope effect). The fractionation factor $\alpha = \frac{k(^{12}\text{CH}_4)}{k(^{13}\text{CH}_4)}$ defines the ratio of the respective reaction rates. For example, α is 1.0039 for the sink reaction with OH leading to a shift to higher isotopic ratios by 4 to 6‰ (Saueressig et al. (2017), Cantrell et al. (1990)).

The amount of $^{13}\text{CH}_4$ released from a specific source depends decisively on its formation process. CH_4 sources can be split into three main source types: Pyrogenic, biogenic and thermogenic.

Pyrogenic CH_4 originates from the incomplete combustion of organic material under anaerobic conditions, i. e. from the burning of biofuel or biomass (e.g. grassland burning, forest fires, wildfires, use of fuel wood, shifting cultivation), and is typically rich in $^{13}\text{CH}_4$ (Brownlow et al. (2017)). In the tropics predominantly C4-type plants grow (e.g. papyrus, mais, savanna grass), which are adapted to the hot climate and have a more effective photosynthesis than C3-type plants (trees and bushes). C4-type plants make use of more $^{13}\text{CH}_4$ compared to C3-type plants, which is why pyrogenic CH_4 emissions from biomass burning have two distinct maxima with pyrogenic CH_4 of burnt C4-plants enriched in $^{13}\text{CH}_4$ (Saunois et al. (2020)).

Biogenic CH_4 , e.g. from wetlands (including wet soils, swamps, bogs and peatlands), rice paddies, eructations of ruminants, manure decomposition or organic waste disposal, is released by methanogens (archaea), which prefer warm anaerobic conditions for their metabolism to produce CH_4 from organic material. Methanogens use either CO_2 with H_2 (hydrogenotrophic methanogenesis) or acetate CH_3COOH (acetotrophic methanogenesis) to generate CH_4 (Brownlow et al. (2017), Whiticar et al. (1986)). Ambient temperature, moisture/water level and the energy content of the organic material influence the amount of CH_4 produced, since microbial productivity increases with temperature and the availability of substrate. In the case of manure decomposition, the amount of CH_4 produced depends on the type of storage. When stored in anaerobic liquid ponds, a higher amount of CH_4 is produced, but only little CH_4 is produced if deposited at aerobic conditions e.g. on pasture. The latter, however, favors the production of the greenhouse gas N_2O (Saunois et al. (2020)). Biogenic CH_4 is relatively poor in $^{13}\text{CH}_4$, since methanogens preferably digest $^{12}\text{CH}_4$, but vary depending on available C3 or C4 plants. Global source signatures from ruminants vary according to their diet (C3 or C4-plant based) and range from -45 to -77‰ (Oh et al. (2019)). Similarly, wetland source signatures vary globally from -70 to -45‰ with tropical wetlands being more enriched in $^{13}\text{CH}_4$ compared to boreal wetlands (Oh et al. (2022)).

CH_4 released from fossil fuel exploitation or geological sources, such as gas-oil seeps and mud-volcanoes, is of thermogenic origin. The formation of CH_4 results from the breakdown of organic matter under conditions of high pressure and high temperatures in great depths. More specifically, kerogen (compressed and heated organic material from plancton, bacteria, algae or plants in sediments) is subjected to a thermal maturation process, i. e. under growing pressures and temperatures ($> 50^\circ\text{C}$) oil is generated. For natural gas, which forms either directly from kerogen or from oil, formation temperatures are as high as $157\text{-}221^\circ\text{C}$ (Stolper et al. (2014)). The chemical and isotopic composition of a reservoir depends on the type of kerogen and its individual formation process. Additionally, the reservoir may consist of a mixture of thermogenic gases from different source rocks, each of which might be at different thermal maturation stages. Further, part of the gas can migrate to upper layers and be chemically or bacterially oxidised (Prinzhofer and Huc (1995)). Thus, source signatures vary globally depending on the type of source, e.g.

conventional gas, associated gas (byproduct of oil production), gas from coal mines, shale gas, volcanic gas or onshore and offshore seeps. Global thermogenic $\delta^{13}\text{C}(\text{CH}_4)$ values range widely from high values of -24‰ to low values of -68‰ (Saunio et al. (2020), Etiope et al. (2019)). Fossil-fuel sources are typically richer in $^{13}\text{CH}_4$ than biogenic sources, but poorer compared to pyrogenic sources.

Figure 2.5 displays global $\delta^{13}\text{C}(\text{CH}_4)$ source signatures from all kinds of CH_4 sources with a zoom into microbial (biogenic), fossil fuel (thermogenic) and biomass burning (pyrogenic) sources (from Sherwood et al. (2017)). The distribution is derived from a database comprising 10706 measurement samples, of which 82% stem from fossil fuel sources. As an example, $\delta^{13}\text{C}(\text{CH}_4)$ source signatures from conventional gas, which denotes reservoir gases from producing gas and oil wells, has a global maximum at approximately -42‰ . The observed $\delta^{13}\text{C}(\text{CH}_4)$ source signatures overlap within the three categories of CH_4 sources, while also the categories overlap with each other. The bulk source of global CH_4 emissions has a signature of -53.6‰ . Due to the fractionation effect of the main sink reaction with OH, whereby the reaction of OH with $^{12}\text{CH}_4$ is preferred over the reaction with $^{13}\text{CH}_4$, the measured atmospheric background $\delta^{13}\text{C}(\text{CH}_4)$ is few permils higher, around -47.3‰ at the time of the study.

Figure 1.2(b) in Chapter 1 displays the atmospheric growth of CH_4 with a simultaneous decrease in $\delta^{13}\text{C}(\text{CH}_4)$ from 2007 onwards for the global background measurement station at the Mauna Loa of the NOAA GML network (Michel et al. (2023), Lan et al. (2023)). The annual mean of 2022 has reached -47.6‰ and is further decreasing. The same trend is observed globally at other remote sites, for example at the NOAA GML sites at the South Pole and in Alaska, whereby the absolute $\delta^{13}\text{C}(\text{CH}_4)$ varies with latitude (-47.9‰ in Alaska and -47.4‰ at the South Pole).

The observed decline is in contrast to the long-term record of $\delta^{13}\text{C}(\text{CH}_4)$ from 1150 onwards (see Figure 2.6), which shows an increase at 0.01‰ per year from 1800 concurrent with CH_4 due to increased emissions dominated from fossil fuel sources (coal combustion). There was a medieval depletion of approximately 2‰ , but at much lower rates (0.0025‰ per year) than today's trend. The medieval depletion has been attributed to a decrease in biomass burning emissions, which is supported by CO records from ice cores (Ferretti et al. (2005)). However, the recent global decrease in $\delta^{13}\text{C}(\text{CH}_4)$ by approximately 0.6‰ , i. e. -0.04‰ per year from 2008 to 2023 to more isotopically lighter CH_4 is four times stronger than the past increase from 1800 and more than ten times faster than the medieval decrease (Nisbet et al. (2023), Michel et al. (2023)). It is a strong indicator for a shift in the contributions of sources and/or sinks in the global CH_4 budget. Yet, the reason for this strong shift has not been uniquely identified.

Another typical tracer for fossil fuel sources is C_2H_6 . Like CH_4 , it is a hydrocarbon molecule but consisting of two carbon atoms with each surrounded by three hydrogen atoms. C_2H_6 is emitted from natural sources, e. g. from volcanoes or fires. Regarding anthropogenic sources, C_2H_6 emissions arise from biofuel combustion (20%), biomass burning (18%) and from fossil fuel production, processing and distribution (62%) (Xiao et al. (2008)). Atmospheric background mole fractions are around 1.5-1.6 ppb (at ground station GEOSummit, Greenland, Angot et al. (2021)), which has been increasing since 2010 due to increased fossil fuel emissions (Tzompasosa et al. (2017)). A temporary pause in C_2H_6 growth is observed between 2015 and 2018 in the Northern Hemisphere and tentatively attributed to a change in fossil fuel emissions by Angot et al. (2021). C_2H_6 is removed from the atmosphere mainly by the reaction with OH. Due to the higher abundance of OH in summer, atmospheric C_2H_6 mole fractions show a seasonal cycle ranging

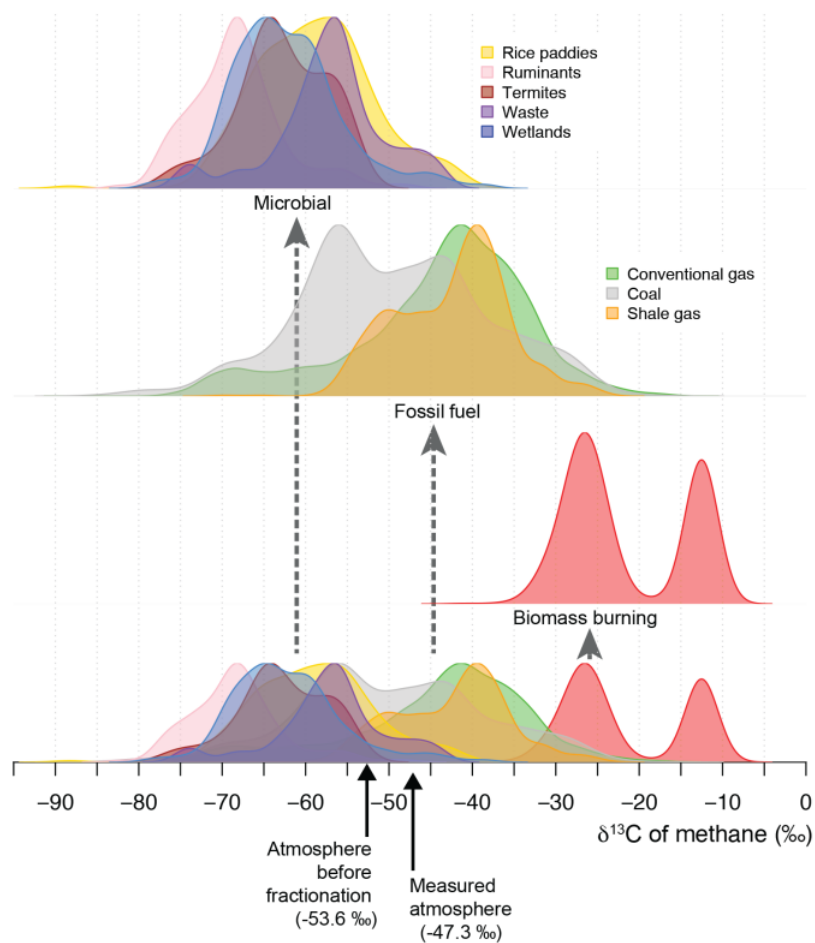


Figure 2.5: Distribution of $\delta^{13}\text{C}(\text{CH}_4)$ source signatures for CH_4 sources. The three main source categories microbial (biogenic), fossil fuel (thermogenic) and biomass burning (pyrogenic) are shown in more detail. (from Sherwood et al. (2017))

from 0.75 ppb in summer months to 2.2 ppb in winter months. Its lifetime is approximately 2 months (Angot et al. (2021)).

C_2H_6 emissions often come along with CH_4 emissions and, as it is the second largest component of natural gas after CH_4 , C_2H_6 is especially used as a tracer for fossil fuel sources (Lowry et al. (2020), Yacovitch et al. (2020), Hausmann et al. (2016)). There are numerous in situ airborne measurements of atmospheric C_2H_6 , which use C_2H_6 as a tracer for fossil fuel CH_4 emissions (e.g. Peischl et al. (2018), Barkley et al. (2019b), Peischl et al. (2016), Johnson et al. (2017), Pétron et al. (2014)). The C_2H_6 to CH_4 (C2:C1) ratio varies between CH_4 emission sources of biogenic and thermogenic origin, and, thus, allows for differentiating between sources.

Hypotheses for the CH_4 growth

According to Nisbet et al. (2023), the current global CH_4 budget is in disequilibrium. The drivers behind the renewed and accelerated increase in atmospheric CH_4 with the concurrent decrease in $\delta^{13}\text{C}(\text{CH}_4)$ since 2006 are still not fully understood and subject to debate in the literature.

Hausmann et al. (2016), and Franco et al. (2016), attributed the 2007-2014 CH_4 growth to an increase in fossil fuel emissions due to the concurrent increase in atmospheric C_2H_6 . Thereby, North American growing exploitation of shale gas and oil reservoirs was suspected to contribute to the rise in C_2H_6 and CH_4 . Basu et al. (2022) infer that the CH_4 rise with the simultaneous negative shift in atmospheric $\delta^{13}\text{C}(\text{CH}_4)$ between 2008 and 2014 can be balanced by a 15% contribution of fossil fuel emissions, if they have more positive source signatures than ambient $\delta^{13}\text{C}(\text{CH}_4)$. Worden et al. (2017) also suggested that the observed trend is caused by increased fossil fuel emissions, but with a stronger decrease in biomass burning emissions, which are isotopically heavy.

Turner et al. (2017) and Rigby et al. (2017) suggested a decrease in the OH sink as the reason for higher atmospheric CH_4 mole fractions based on methyl chloroform observations. However, according to Fujita et al. (2020), Lan et al. (2021), and Drinkwater et al. (2023), variations in the OH sink alone can not explain the observed trend in $\delta^{13}\text{C}(\text{CH}_4)$. Ni and Groffman (2018) suggested a significant decrease in the soil sink in tropical/subtropical and temperate forests.

Some other studies attributed the increase in CH_4 accompanied by a decrease in $\delta^{13}\text{C}(\text{CH}_4)$ primarily to an increase in emissions from biogenic sources. Schaefer et al. (2016) deduced that anthropogenic emissions from waste and agriculture dominated the CH_4 increase between 2007 and 2014, while Nisbet et al. (2016) and Nisbet et al. (2019) identified natural sources from wetlands in the tropics as the dominant drivers. Zhang et al. (2021) concluded from an inverse analysis of global 2010–2018 CH_4 observations from the Greenhouse Gases Observing Satellite (GOSAT) that growing anthropogenic biogenic CH_4 emissions from the agricultural sector over South Asia, tropical Africa and Brasil contributed to the overall CH_4 increase from 2010-2018. The increase from 2016-2018 was attributed to a combination of increased anthropogenic emissions and large emissions from natural biogenic sources from tropical and boreal wetlands. As an exception, they claimed that the CH_4 growth in 2014 was predominantly driven by low OH, while in 2015 the increase was dominated by high emissions from fires.

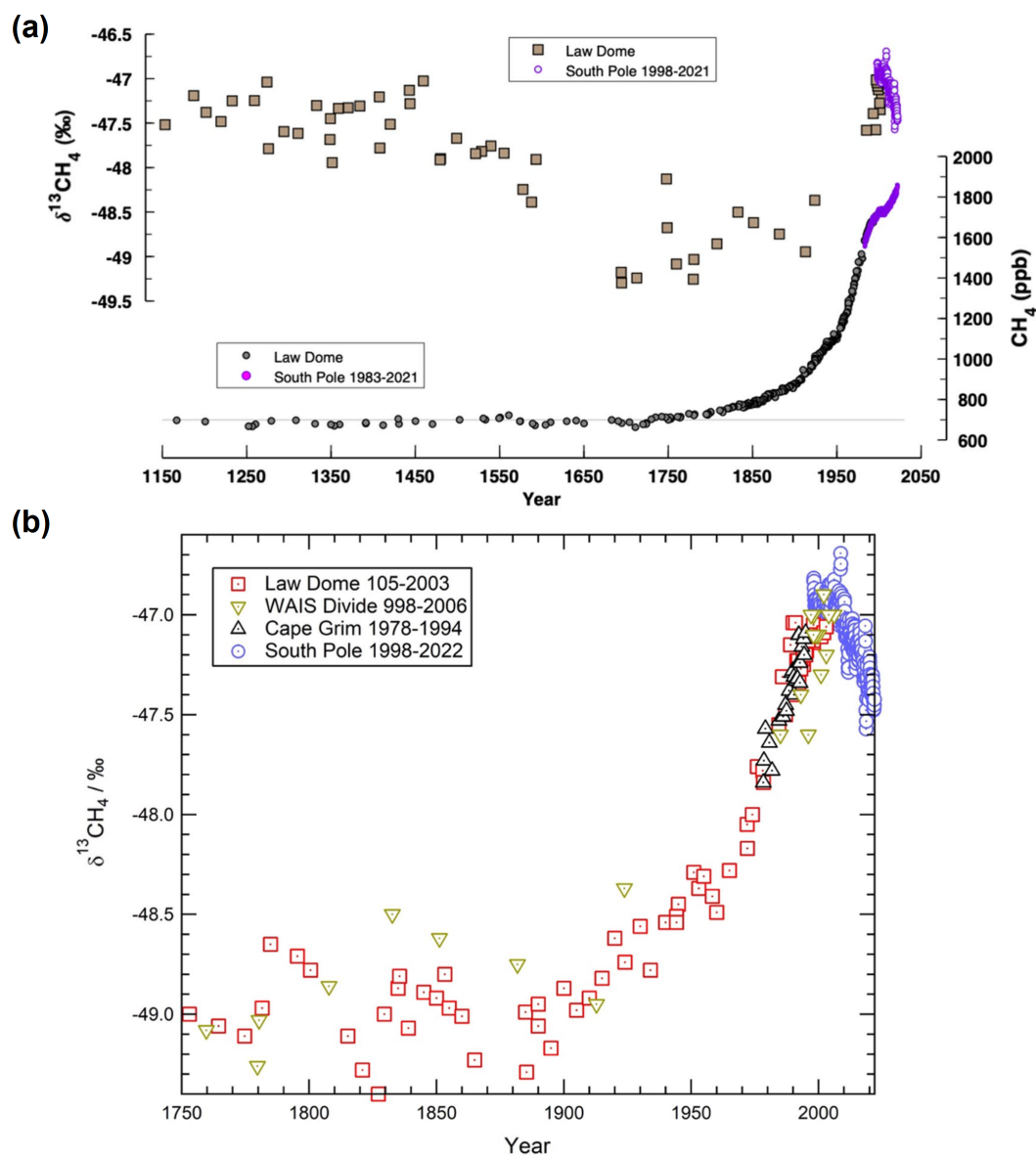


Figure 2.6: Record of global atmospheric CH_4 and $\delta^{13}\text{C}(\text{CH}_4)$ from South Pole and ice-core measurements (a) since 1150 and (b) since 1750 in more detail for $\delta^{13}\text{C}(\text{CH}_4)$ (from Nisbet et al. (2023)).

Lan et al. (2021) applied a 3D model to agree with the observed long-term trends in both CH₄ and $\delta^{13}\text{C}(\text{CH}_4)$ since 2006. They found that a small increase in fossil fuel emissions might have been surpassed by other sources, such as a strong increase in biogenic CH₄, a decrease in pyrogenic CH₄ and/or decreasing soil sinks. However, in their study they did not find a best emission partitioning and point to uncertainties arising from OH fractionation factors (-3.9‰ (Saueressig et al. (2017)) or -5.4‰ (Cantrell et al. (1990))), which in turn lead to uncertainties in the contribution of fossil fuel and biogenic sources. They concluded that long-term spatially distributed measurements of atmospheric $\delta^{13}\text{C}(\text{CH}_4)$ and source signatures would improve the understanding of the CH₄ budget.

The most recent remarkable growth in CH₄ from 2020 to 2022 is widely attributed to growing natural biogenic emissions, particularly from wetlands in the tropics (e.g. Zhang et al. (2023), Feng et al. (2023), Peng et al. (2022), Basu et al. (2022), Oh et al. (2022)). Qu et al. (2022) derived from an inverse analysis of GOSAT data that between 2019-2020, emission growth mainly took place in tropical and boreal wetlands in Africa and Canada with an additional small contribution from a reduction in the OH sink. Peng et al. (2022) equally found that the observed CH₄ growth in 2020 was due to higher natural emissions predominantly from wetlands. Additionally, due to lower NO_x emissions during the coronavirus disease 2019 (COVID-19) lockdowns, the OH abundance decreased contributing to the observed CH₄ growth. Notably, the growth from 2020-2022 is accompanied by an unusual 3-year La Niña event, which caused exceptionally strong rainfalls in the tropical regions (Hasan et al. (2022)).

Nisbet et al. (2023), suspect that rising temperatures have already led to a climate feedback in wetland emissions, since biogenic CH₄ productivity increases with temperature and precipitation (linked to anoxia level and availability of organic material). According to the study, enhanced natural emissions, especially due to this feedback mechanism, were higher than anthropogenic emissions from waste and agriculture between 2006-2022. Using model simulations and CH₄ records from ice-cores, they compared the observed trends to past interglacial termination events, when CH₄ had increased simultaneously with a decrease in $\delta^{13}\text{C}(\text{CH}_4)$ but at the same or lower rates than today's growth rates. The fast CH₄ rises in the paleoclimatological records had been driven by tropical wetland emissions responding to warming in a feedback process. Thus, they suggest that the observed trend in CH₄ and $\delta^{13}\text{C}(\text{CH}_4)$ since 2006 may be within the range of Holocene variability, or otherwise, even indicate a planetary-scale reorganization of the climate system.

2.3 Mass balance method for top-down CH₄ flux estimation

Within this work, the mass balance method is applied to quantify CH₄ emissions from airborne in situ observations of gas installations in the southern North Sea (see Chapter 3).

The mass balance method to derive emission fluxes from sources is well-established and has been used by e.g. Pitt et al. (2019), Klausner et al. (2020), Cambaliza et al. (2015) and O'Shea et al. (2014). Sources can be both point sources, e.g. an offshore gas installation or a landfill, and area sources of greater extent such as a city or a larger set of oil and gas installations.

The mass balance method makes use of Gauss' theorem, i. e. the flux through a surface around a source is the same as the constant emission flux arising from the source. Emissions arising from

a source are transported downwind and mix within the planetary boundary layer (PBL). The species of interest should not react during the time of study, i. e. the method applies to long-lived species such as CH_4 . Under ideal meteorological conditions, the wind flow and wind direction in the sampling area are steady with moderate wind speeds. The PBL should be fully-developed, as usually in afternoon-hours, and well-mixed such that emissions are dispersed with the PBL up to the boundary layer height (BLH) in a Gaussian plume shape. Uptake on the ground and flux into the free troposphere above the BLH are assumed to be negligible. For the calculation of the emission flux, the BLH is used as upper plume height and inferred from meteorological measurements (pressure, temperature) during vertical profiles.

Airborne sampling can be conducted in circles around the source describing a cylindrical surface (e. g. Yu et al. (2020), Conley et al. (2016)) or in a box-pattern (e. g. France et al. (2021), Klausner et al. (2020)). For the latter a downwind 2D-plane is covered by flying vertically stacked horizontal transects at several altitudes. Both the horizontal and vertical extension of the plume should be resolved. Upwind, at least one transect is necessary to check for possible inflow from other upwind sources. The basic flight box-pattern is depicted in Figure 2.7.

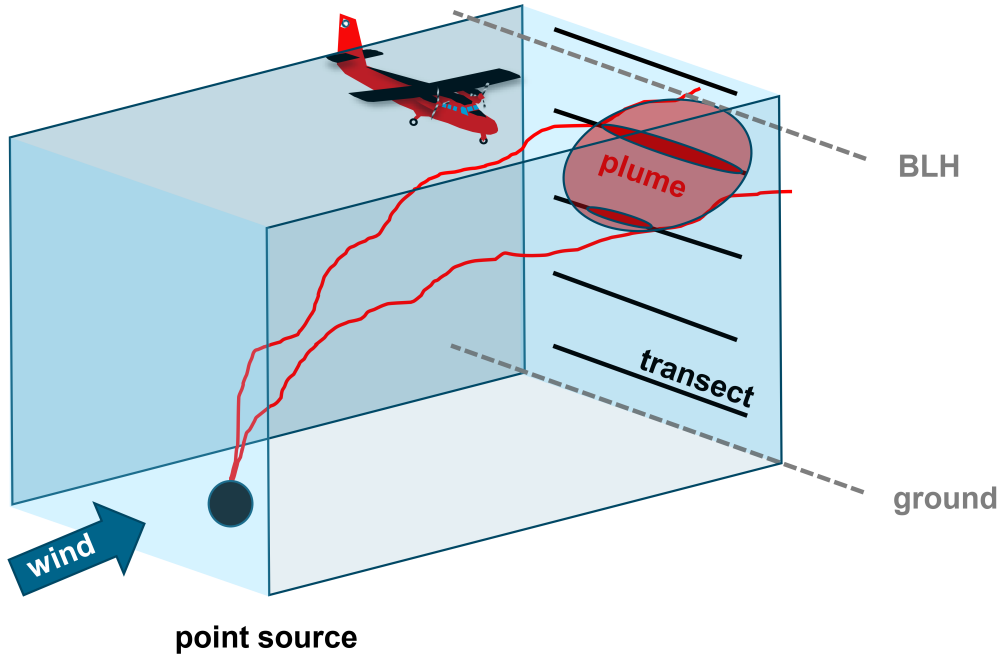


Figure 2.7: Schematic for the airborne mass balance approach: Emissions transported downwind of a point source form a plume, which disperses within the planetary boundary layer extending up to the boundary layer height (BLH). The plume extension is captured by flying vertically stacked horizontal transects at several altitudes downwind of the source and at least one transect upwind (box-pattern). This way, the flux through the downwind 2D-plane can be calculated.

The emission flux through the vertical 2D-plane is calculated by integration of the mass flow over the vertical (ground to BLH) and horizontal extent (from $-a$ to a) of the plume:

$$Flux = \int_0^{BLH} \int_{-a}^a (c_{ij} - c_{bgr,ij}) \frac{p_{ij} \cdot M}{T_{ij} \cdot R} u_{ij} dx dz \quad (2.4)$$

The indices i and j denote the location of the measurement point within the 2D-plane in horizontal (x) and vertical (z) direction. The mass flow is the difference of measured mole fractions in the plume c_{ij} and background mole fractions $c_{bgr,ij}$ multiplied with the horizontal wind speed u_{ij} (perpendicular to the 2D-plane) and converted using the ideal gas law, i. e. multiplication with pressure p_{ij} and T_{ij} and division by the ideal gas constant R and molar mass M of the emitted species.

2.4 In situ measurement techniques for CH₄, C₂H₆ and δ¹³C(CH₄)

There are different methods for the in situ measurement of CH₄, C₂H₆ and δ¹³C(CH₄): Measurements using the flask (Gas Chromatography - Isotope Ratio Mass Spectrometry (GC-IRMS)) method, cavity ring-down spectroscopy or tunable laser absorption spectroscopy. In this work, the DLR-QCLS, a tunable laser absorption spectrometer, is adapted for the first continuous airborne δ¹³C(CH₄) measurements and compared with flasks and a cavity ring-down spectrometer both in the laboratory and during in-flight measurements (see Chapter 4 and Chapter 5).

The flask (GC-IRMS) method is a widely common measurement technique for both ground-based and airborne platforms (e. g. Varga et al. (2021), Brownlow et al. (2017)). The NOAA GML network for global background measurements of atmospheric species consists of ground measurement stations, where flasks are taken at 91 sites for the measurement of CH₄ and at 25 sites for the measurement of δ¹³C(CH₄) (Lan et al. (2023), Michel et al. (2023)). For the airborne δ¹³C(CH₄) measurement, flasks are widely used. Airborne studies for the measurement of δ¹³C(CH₄) source signatures have been conducted e. g. over the South American and African wetland areas (Nisbet et al. (2021)), the European Arctic wetlands (Fisher et al. (2017)) and over the Upper Silesian Coal Basin (Fiehn et al. (2023), Gałkowski et al. (2021)). The flask (GC-IRMS) method is described in Subsection 2.4.1.

Cavity-ring down instruments have been deployed for ground-based measurements of CH₄, C₂H₆ and δ¹³C(CH₄), e. g. mobile ground-measurements around different CH₄ sources by Hoheisel et al. (2019). The technique is also widely used for the airborne measurement of CH₄ (e. g. Klausner et al. (2020)). For the airborne δ¹³C(CH₄) measurement, a combination of the cavity ring-down method with flasks has been recently applied for the Comet 2.0 campaign over Northern American wetlands (Waldmann (2022)). The cavity-ring down measurement principle is explained in Subsection 2.4.2.

Tunable laser absorption spectroscopy has been used for ground-based and airborne CH₄ and C₂H₆ measurements (e. g. Kostinek et al. (2021), Gvakharia et al. (2018), Catoire et al. (2017), Tadic et al. (2017), Pitt et al. (2016), Santoni et al. (2014)). For the measurement of δ¹³C(CH₄), a modified tunable laser absorption spectrometer has been deployed in a tower measurement campaign (Röckmann et al. (2016), Eyer et al. (2016)). The DLR-QCLS is a tunable laser absorption spectrometer and used for the continuous airborne CH₄, C₂H₆ and δ¹³C(CH₄) measurement. The principle of tunable absorption laser spectroscopy is explained in Subsection 2.4.3).

The following sections especially focus on δ¹³C(CH₄) measurements, since the DLR-QCLS has been adapted for the measurement of δ¹³C(CH₄) as part of this work.

2.4.1 Flasks (GC-IRMS)

Flasks are essentially air samples taken in glass cylinders, aluminium containers or sample bags made from special non-reactive material. The sampling time depends on the volume of the cylinder, the filling pump and the flight altitude. As an example, the sampling time for one flask of the Jena Air Sampler (JAS) is between 25 s at low altitudes and 100 s at high altitudes (Gałkowski et al. (2021)).

After the in situ sampling, the flasks are analysed in the laboratory using the GC-IRMS technique. Thereby, first, CH₄ from the sample air is trapped cryogenically at low temperatures (approx. -130 °C) using an absorption polymer material. Then it is oxidised to CO₂ when passing through a gas chromatography column in a combustion furnace (temperatures at approx. 1000 °C). Finally, the ¹²C and ¹³C content is measured by separation due to the differences in molecular masses in an isotope ratio mass spectrometer. The technique has been applied since the end of the 1980s, when the first successful measurements were made by Lowe et al. (1991), and was further improved in the mid 1990s (Brand et al. (2016), Sperlich et al. (2016)).

The precision of the laboratory $\delta^{13}\text{C}(\text{CH}_4)$ measurement is very high with typical precisions of 0.12‰ (Gałkowski et al. (2021)). As a disadvantage for airborne measurements, the amount of samples is rather small for flight times of several hours (e.g. JAS equipped with 12 flasks). To derive source signatures, at least two samples of a plume have to be taken. Unfortunately, for discrete short plumes of point sources during airborne measurements, the chances to miss a plume is high.

2.4.2 Cavity ring-down spectroscopy

Cavity ring-down spectroscopy (CRD) relies on the measurement of the ring-down time, which is a measure for the absorption of light, when passing through a medium inside a stable optical cavity.

A short pulse of a light source (e.g. a laser diode) is guided into a cavity (length L), which contains an absorbing medium with an absorption coefficient α_λ specific for the medium absorbing at wavelength λ . Since at both ends of the cavity two highly reflective mirrors with reflectivity R and transmissivity T are mounted, photons are reflected several times before leaking out of the cavity and reaching a detector. At each pass through the medium the incident light intensity I_{in} is attenuated according to the Beer-Lambert law:

$$I_{out} = I_{in} \cdot e^{-\alpha_\lambda \cdot d} \quad (2.5)$$

with d being the extension of the medium along the light path. After n complete round-trips the intensity is

$$I_{out,n}(t) = I_0 \cdot e^{\frac{-t \cdot c}{L} \cdot (1-R+\alpha_\lambda d)} = I_0 \cdot e^{\frac{-t}{\tau}} \quad (2.6)$$

The ring-down time τ is measured with and without (τ_0) the absorbing medium. It is related to the absorption coefficient α_λ at the wavelength of the incident light:

$$\alpha_\lambda = \frac{1}{c} \cdot \left(\frac{1}{\tau_0} + \frac{1}{\tau} \right) = k_\lambda \cdot N \quad (2.7)$$

Because α_λ is the known absorption cross section k_λ of the medium times its number density N , mole fractions of the medium are inferred by dividing by the number density of air. The

higher the mole fractions of the absorbing medium, the higher is the exponential decay inside the cavity and the shorter is τ (Berden and Engeln (2009)).

Cavity-ring-down analysers are commercially available from Picarro Inc. and display precisions of approx. 3‰ for the measurement of $\delta^{13}\text{C}(\text{CH}_4)$ at 0.8 Hz time resolution as for the Picarro 2210i Analyser. The latter measures $^{13}\text{CH}_4$ and $^{12}\text{CH}_4$ at wavelengths of 1658.6 nm and 1650.9 nm, respectively.

2.4.3 Tunable laser absorption spectroscopy

Laser absorption spectroscopy makes also use of the absorption of light by an absorbing species described by the Beer-Lambert law (see Eq. 2.5). For tunable laser absorption spectroscopy, the laser voltage is tuned such that light is emitted in a wavelength band as narrow as some nm width. In contrast to the cavity-ring-down instruments, the absorption spectrum of the absorbing species is directly resolved displaying single absorption lines within the wavelength band.

In the mid 1990s, first attempts of direct laser absorption spectroscopy were carried-out using cryogenic-cooled laser sources and detectors for the measurement of isotopic CH₄ (Bergamaschi et al. (1998), Bergamaschi et al. (1994)), which were not yet practical for in situ measurements. As Quantum Cascade Laser (QCL) and Interband-cascade laser (ICL) for operation at near room temperatures were invented, mid-IR laser absorption spectroscopy has been developed as a high-precision and high-temporal resolution measurement technique (McManus et al. (2015), Eyer et al. (2016)). Both QCL and ICL lasers are composed of multiple quantum well semiconductor heterostructures creating staircase shaped band potentials. Single electrons stream down along the potentials, whereby photons are emitted from each transition. QCL utilize intersubband and ICL interband (from conduction to valence band) transitions to assess continuous-wave light emission in the mid-IR spectral region.

When absorbing IR light at a specific wavelength, discrete transitions between the ground-state and excited rotational-vibrational states are induced that are represented as single absorption lines in the absorption spectrum. The state of a molecule is defined by its vibrational state (denoted by the quantum number ν), which again is subdivided into rotational states (quantum number J). Typically at room temperature, only the ground vibrational state ($\nu=0$) is populated, whereby several rotational levels might be populated. According to the selection rules for rotational-vibrational transitions ($\Delta\nu = \pm 1$; $\Delta J = \pm 1$; $\Delta J = 0$ (only for polyatomic molecules)), for example a transition from the ground vibrational state ($\nu=0$) to the first excited vibrational state ($\nu=1$) is possible. Depending on the respective rotational levels of both states, the transition belongs either to the Q-Branch ($\Delta J = 0$), the higher energetic R-branch ($\Delta J = +1$) or the P-branch ($\Delta J = -1$) at lower energies. A line in the spectrum is unique to the molecule and to its specific transition. Thus, the molecule can be identified from its absorption line like using a fingerprint.

As an example, the CH₄ molecule has a symmetric tetrahedral structure consisting of four hydrogen atoms (H) and one carbon atom (C) in its centre. It can oscillate in nine different vibration modes, which comprise three symmetric stretching and bending modes, when only the H-atoms move, and six asymmetric stretching and bending modes, when both the H-atoms and the C-atom move. Only the asymmetric modes induce a change in the dipole moment and thus, interact with IR light. As explained in Section 2.2, the stable isotopologues $^{12}\text{CH}_4$ and $^{13}\text{CH}_4$ make up approximately 99.9% of atmospheric CH₄ (Gordon et al. (2022)). The heavier ^{13}C atom

at the center of the $^{13}\text{CH}_4$ molecule generates a stronger covalent bonding (described by the an-harmonic Morse Potential or Lennard-Jones potential) of the surrounding H atoms compared to the lighter ^{12}C atoms. As a consequence, the ro-vibrational energy levels shift to lower values. This results in distinct $^{13}\text{CH}_4$ and $^{12}\text{CH}_4$ absorption lines and hence, allows for the separate detection of these CH_4 isotopologues.

Figure 2.8 shows the basic principle of direct laser absorption spectroscopy using a tunable IR-laser to excite CH_4 molecules in a sample cell. Stretching and bending motions of a CH_4 molecule are depicted in the sample cell. The laser is chosen at a suitable center wavelength and sweeps over a wavelength range of few nanometers width such that one or more absorption lines of the desired measured species are resolved.

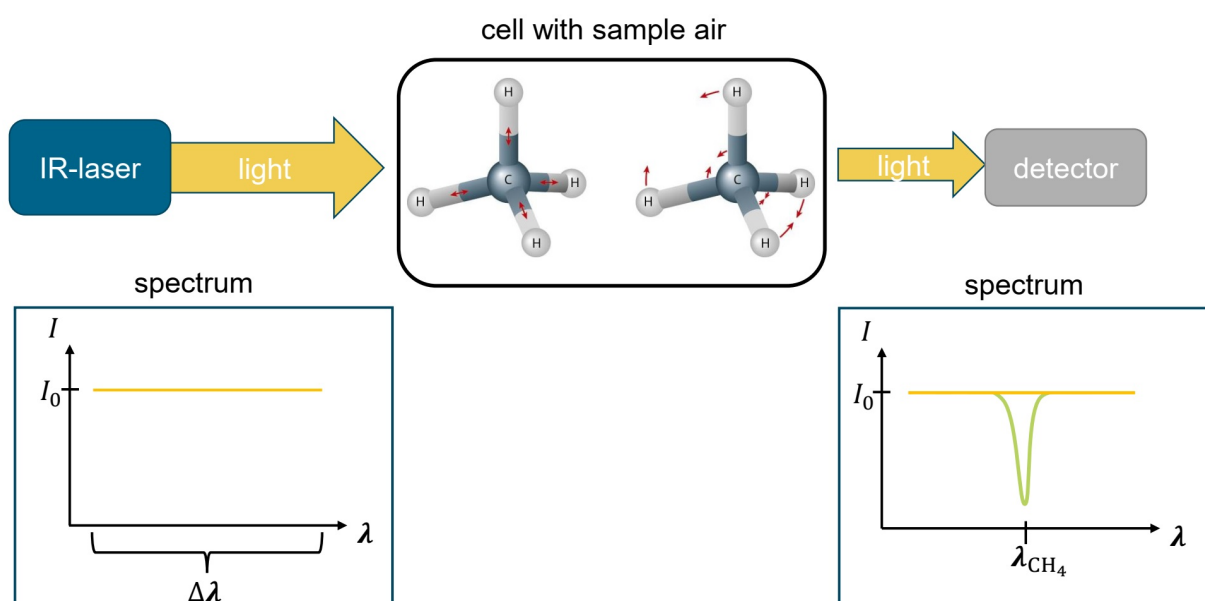


Figure 2.8: Schematic for tunable laser absorption spectroscopy: Light emitted from an infrared (IR) laser, which is tuned in the wavelength band $\Delta\lambda$, is guided into the cell. The cell contains the absorbing molecule CH_4 that is excited for a specific rotational-vibrational transition (e.g. stretching or bending mode) when it absorbs IR light at the specific wavelength λ_{CH_4} . The spectrum detected at the detector shows that the incident light intensity I_0 is attenuated at λ_{CH_4} . The absorption spectrum with the specific CH_4 absorption line is shown in green. The spectral baseline (zero absorbing molecules) is shown in orange.

The higher the abundances of the absorbing molecule in the sample cell, the stronger is the absorption (i.e. deeper absorption lines in the spectrum) and, thus, the weaker is the light intensity at the detector. The abundance of the species can be inferred from the area between the absorption line and the baseline. Therefore, the spectrum with its absorption lines is modelled using molecular spectral information from databases such as the High Resolution TRansmission molecular AbsorptioN database (HITRAN) (Gordon et al. (2022)).

To retrieve mole fractions, the absorption coefficient α_λ has to be computed. According to the right-hand side of Equation 2.7, α_λ is the absorption cross section multiplied by the number density of the molecule. The absorption coefficient/absorption cross section is pressure- and

temperature-dependent. Thus, both pressure and temperature are held constant inside the sample cell to maintain a constant pressure line broadening (induced by elastic collisions of molecules) and defined thermal line broadening from the Doppler-effect (molecules see Doppler-broadened incident light due to their own motion away or towards the incident photon). When modelling an absorption line, a Voigt profile is used, which is the convolution of a Gaussian profile (thermal broadening) and a Lorentzian profile (pressure broadening). Figure 2.9 shows a molecular absorption line with HITRAN spectral parameters. The absorption cross section $k_{ij}(\lambda)$ in units $\text{cm}^2 \text{molecule}^{-1}$ of the transition between two rotational-vibrational states i and j can be computed by multiplying the spectral line intensity S_{ij} ($\text{cm}^{-1}/(\text{molecule cm}^{-2})$) with the normalized line shape function f ($1/\text{cm}^{-1}$):

$$k_{ij}(\lambda, p, T) = S_{ij} \cdot f(\lambda, \lambda_{ij}, p, T) \quad (2.8)$$

S_{ij} depends on parameters such as the lower state energy, the statistical weight of the upper state energy and the temperature. Furthermore, it is weighted according to the natural terrestrial isotopic abundances. f contains the HITRAN parameters for Voigt-line shape, such as pressure broadening coefficients for self-broadening and air-broadening, and the thermal broadening coefficient.

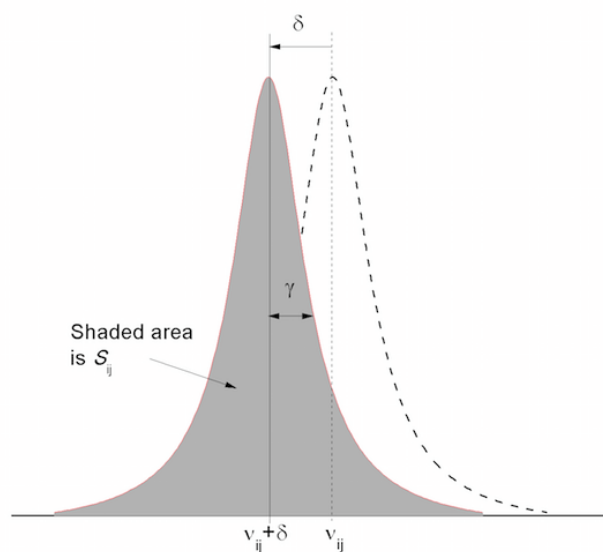


Figure 2.9: Voigt-profile of a molecular absorption line with HITRAN spectral line parameters S (spectral line intensity), ν (wavenumber), δ (pressure shift), γ (line half width at half maximum). The dotted line is the vacuum transition. (from HITRAN, <https://hitran.org/docs/definitions-and-units/>, Gordon et al. (2022)).

The DLR-QCLS sample cell pressure is set to constant 45 mbar, such that individual lines can be resolved, which would overlap with each other at ambient pressure.

Chapter 3

Quantification of CH₄ emissions from fossil fuel production in the southern North Sea

As described in the previous Chapter 2 in Section 2.2, discrepancies between bottom-up CH₄ estimates from inventories and top-down CH₄ estimates derived from measurements exist. Several studies indicate that bottom-up inventories underestimate emissions from the oil and gas industry (e. g. MacKay et al. (2021), Saunio et al. (2020), Schwietzke et al. (2016), Pétron et al. (2014)). Top-down emission estimates from direct measurements close to sources can help to independently validate bottom-up estimates in inventory data. Better understanding, monitoring, and verification of CH₄ emissions associated with oil and gas operations are crucial parts of the European Methane Strategy (EU (2020)).

Studies on measurements of CH₄ emissions from offshore installations are still rare. Satellite detection is hampered due to the location next to water (International Energy Agency (IEA) (2023)). Ship-based measurements were conducted in the US Gulf of Mexico (Yacovitch et al. (2020)), in South-East Asia (Nara et al. (2014)), and in the North Sea (Riddick et al. (2019), Hensen et al. (2019)). However, ship-based measurements rely on an additional plume model for the estimation of the vertical plume extent, which is necessary for the quantification of emissions. In contrast, the mobility of aircraft allows for sampling of emission plumes both horizontally and vertically, and thus airborne measurements provide more detailed information on marine boundary layer conditions, which are known to be complex. Furthermore, the range of aircrafts enables the coverage of larger regions within short time frames. So far, airborne measurements around offshore facilities took place in the Sureste Basin, Mexico (Zavala-Araiza et al. (2021)), in the US Gulf of Mexico (Gorchov Negron et al. (2020)), in the Norwegian Sea (Foulds et al. (2022), Roiger et al. (2015)) and in the North Sea (Lee et al. (2018), Cain et al. (2017)).

In Europe the United Kingdom (UK) is the second largest and the Netherlands the third largest natural gas producer after Norway (Eurostat (2020)). Most of the UK offshore dry gas production takes place in the southern North Sea region, which comprises 81 dry gas fields with 181 installations. In 2019, $11.1 \cdot 10^9$ Nm³ (norm cubic meter) of dry gas was produced (OGA (2019)). In comparison, the Dutch offshore gas production was $9.8 \cdot 10^9$ Nm³ from 180 offshore gas fields located in the southern North Sea (NLOG (2019)). Thus, the southern North Sea region

is an important target region to study offshore emissions.

In this chapter, first, an overview of emissions that typically occur on offshore installations is given (Section 3.1). The aircraft instrumentation and sampling strategy for the airborne field campaign conducted in the southern North Sea in 2019 is introduced in Section 3.2. In Section 3.3 the mass balance method as applied herein to derive CH₄ flux estimates is explained. The resultant top-down CH₄ flux estimates for UK and Dutch installations are presented in Section 3.4 and compared with regional and global bottom-up inventories in Section 3.4.1. Further, correlations with C₂H₆ and CO₂ and determined loss rates are analyzed (Section 3.4.2 and Section 3.4.3, respectively). Finally, the findings are placed in a wider context by comparing them with results from airborne observations in two other offshore regions (Section 3.4.4).

Parts of this chapter are published in Pühl et al. (2024) and excerpts are taken literally.

3.1 Types of emissions on offshore installations

On board offshore oil and gas platforms, CH₄ is emitted during routine operations for safety and operational reasons (e.g. shutdown or start-up of equipment during production) by either controlled venting or flaring, i.e. the release of gas or burning of gas. In the latter case, CO₂ is released simultaneously, with the CH₄/CO₂ emission ratio dependent on the flaring efficiency. Unintended leaks can significantly contribute to CH₄ emissions (Varon et al. (2019), Pandey et al. (2019), Lee et al. (2018), Zavala-Araiza et al. (2017), Conley et al. (2016), Lyon et al. (2015)). Lee et al. (2018) determined CH₄ fluxes higher than 4500 kg h⁻¹ arising from an uncontrolled CH₄ blow-out around one installation in the central North Sea.

According to the United Kingdom Continental Shelf (UKCS) Flaring and Venting Report (OGA (2020)), in 2019 a total of 2600 metric tonnes (t) of CH₄ was emitted in the southern North Sea and the minor Irish Sea region, of which 74% came from venting, 13% came from turbines and engines, 10% came from fugitive emissions (e.g. from leaky valves or compressors), and 3% came from flaring. CO₂ emission was 0.8 Mt in the same year, arising mainly from turbines and engines (95%), with minor contributions of flaring (4%) and venting (0.01%). Flaring accounts for 87% and venting for 13% of the total CO₂ and CH₄ emissions from venting and flaring. Flaring emissions consist of 99% CO₂ and 1% CH₄, while venting emissions consist of 98% CH₄ and 2% CO₂.

Dutch CH₄ emissions from the extraction of crude oil and natural gas on the Netherlands Continental Shelf (PRTR (2019)) amounted to 6500 t in 2019, of which 98% came from venting, 1.6% from the usage of natural gas (e.g. as fuel for combustion), and 0.2% from flaring. CO₂ emission was 1.1 Mt with a share of 99% from usage of natural gas, 0.8% from flaring, and 0.2% from venting. Flaring accounts for 33% and venting for 67% of the total CO₂ and CH₄ emissions from venting and flaring. Flaring emissions consisted of 99.7% CO₂ and 0.3% CH₄, while venting emissions were 89% CH₄ and 11% CO₂.

3.2 Airborne field campaign in the southern North Sea

In April and May 2019 airborne measurements of emissions from offshore installations in the southern North Sea were conducted by the British Antarctic Service (BAS) and the University

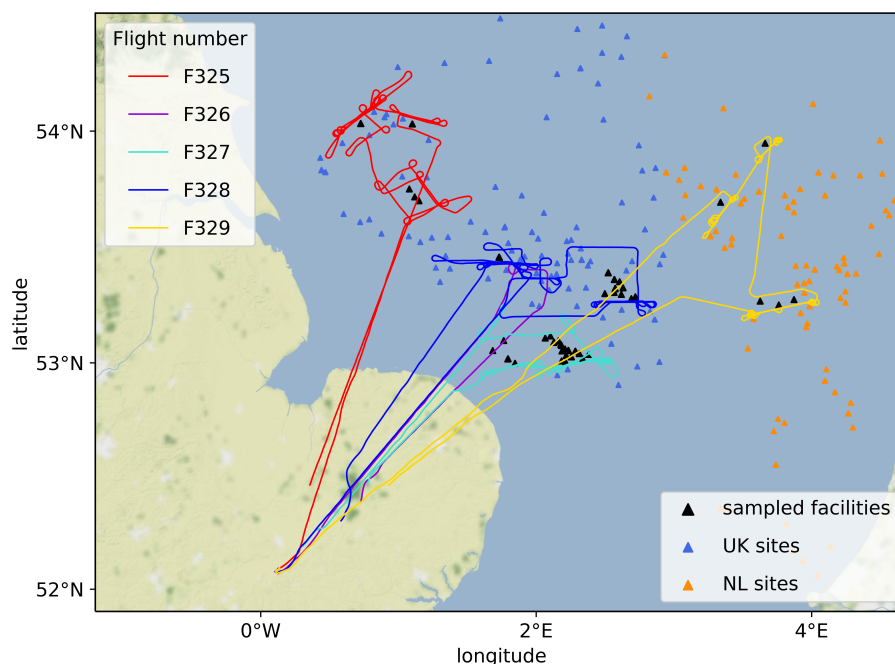


Figure 3.1: Aircraft tracks for the 2019 campaign in the southern North Sea (lines). Location of all offshore facilities in the UK (blue markers) and Dutch (orange markers) region and the sampled facilities (black markers).

of Manchester within the framework of the United Nations Climate & Clean Air Coalition (UN CCAC) objective to help characterize global CH_4 emissions arising from the oil and gas industry. In a previously conducted campaign in 2018, regional survey flights were performed for method development purposes. In 2019, the flight strategy was adapted to sample emissions from dedicated installations, which were chosen because of available inventory emission estimates (UK National Atmospheric Emissions Inventory (NAEI)) and a previously conducted shipborne study in Dutch waters (Hensen et al. (2019)). France et al. (2021)) describe the instrument payload and the sampling strategy for both campaigns. Here, this study is extended with a quantification of CH_4 emissions for the studied offshore platforms in 2019.

Figure 3.1 depicts the flight patterns for 2019. A total of five flights were conducted in the southern North Sea region. The flight conditions during the flights were generally good with moderate wind speeds (3-8 m/s). However, one flight (F326) was aborted due to poor weather conditions. Both UK and Dutch sites of offshore gas facilities were surveyed. Platform positions were taken from the Oil and Gas Authority (OGA) for UK sites and the Dutch Oil and gas portal (NLOG) for Dutch sites. Multiple vertically stacked transects (4-9 transects) in a 2D-plane were flown downwind of targeted platforms to fully capture the vertical extent of a plume. This measurement strategy allows for calculation of emission fluxes using the mass balance approach, i. e. calculating the flux of emissions through a vertical plane downwind of a emission source (see Section 2.3). Measurements were made at distances varying from 2 to 7 km from the facilities at altitudes between 45 m and 1300 m above sea level. The flights took place in the afternoon hours, when the planetary boundary layer (PBL) was expected to be well-mixed.

The DHC6 Twin Otter research aircraft, operated by the BAS, was equipped with several instruments to collect in situ data of atmospheric trace gases. A Picarro G2311-f 10 Hz Analyser measured dry-air CH₄ and CO₂ mole fractions at a response time of 0.4 s and at a precision of 1.2 ppb (1 σ at 1 Hz) for CH₄. A tunable infrared laser direct absorption spectrometer (TILDAS) (Aerodyne Research Inc.) was deployed to detect C₂H₆ (response time < 2 s; precision 50 ppt over 10 s) (Yacovitch et al. (2014)). To assess PBL physics, sensors for temperature, pressure, humidity and 3D-wind were mounted at the front nose of the aircraft. A NOAA “Best Air Turbulence” probe was installed at the boom of the aircraft and provided wind measurements at a resolution of 50 Hz (Weiss et al. (2011), Garman et al. (2006)).

3.3 Method for top-down CH₄ flux estimation of off-shore installations

The mass balance method is applied to determine the amount of CH₄ emitted by the platforms/multi-platform complexes and passing through a 2D vertical plane downwind (see Section 2.3). For the flux calculation, measured wind speeds in the target region are required to be relatively steady. In general, the mass balance method is applied with the approximation that the plume is vertically well-mixed within the PBL. However, to reduce the uncertainty of this approximation under the given meteorological conditions, horizontal transects at several altitudes are conducted in order to get a higher resolution of the dispersed plume in the vertical. Thereby, the 2D vertical plane is subdivided into discrete mixing layers to account for a possible non-uniformly spread plume. Equation 3.1 is used to derive the CH₄ flux (unit mass per time) across each individual horizontal transect i within the plane, followed by an integration over the vertical plume extent:

$$Flux_i = \Delta C_i \cdot \frac{p_i \cdot M}{T_i \cdot R} \cdot V_{\perp} \cdot \Delta x_i \cdot D_i \quad (3.1)$$

ΔC_i represents the difference of CH₄ molar ratios measured in- (C_i) and outside (C_0) of the plume ($\Delta C_i = C_i - C_0$). The background mole fractions C_0 during the time of flight through the plume are individually calculated for each transect. Thereby, the average CH₄ mole fractions over a 30 s time span at either side of the plume are used and interpolated linearly in between to account for any drift in background. CH₄ mole fractions are converted to a CH₄ mass density by applying the ideal gas law, i. e. multiplication with molar mass M and measured pressure p_i and division by temperature T_i and the ideal gas constant R . The CH₄ mass density is then multiplied with the average wind speed perpendicular to the flight track V_{\perp} , which is calculated from the measured average wind speed, wind direction and aircraft heading over all transects. Finally, the CH₄ flux for each single transect is obtained by multiplying with the plume width Δx_i and the vertical depth of each mixing layer D_i . Δx_i is determined by the distance the aircraft covered while crossing the plume. Thereby, the measured velocity of the aircraft is multiplied with the time span of the plume. The enhancement measured in each transect is assumed for a layer reaching halfway to the next upper and lower transect. All horizontal transects are used for the flux calculation with the highest transect, where enhancements are found, as the upper plume boundary. In the case where CH₄ enhancements were detected up to the highest transect of the aircraft, the BLH is taken as the maximal upper plume boundary assuming that the entrainment flux is small. The BLH is inferred from inspection of the vertical gradient of the

potential temperature, which is calculated using the in situ measured meteorological parameters during the vertical profiling of the aircraft (Stull, 1988). In case of enhanced CH₄ being detected in the lowest transect, the sea surface is assumed as lower plume boundary.

As a result, the bulk net CH₄ flux through the plane $Flux_{total}$ is the sum over the fluxes $Flux_i$ calculated for each transect i where CH₄ was enhanced:

$$Flux_{total} = \sum_i^{tracescts} Flux_i \quad (3.2)$$

The flux calculation method is similar to the method applied by Foulds et al. (2022), but differs slightly in the calculation of ΔC_i . Foulds et al. (2022) calculate the background CH₄ mole fractions over a greater time period (50 s) due to a more variable CH₄ background seen in the Norwegian Continental Shelf.

The CH₄ flux calculation is illustrated by using observations of platform P1 on 30 April 2019 (see Figure 3.2). Measurements were performed downwind at a distance of around 3-4 km from the platform (wind direction $(179.5 \pm 29.8)^\circ$; perpendicular wind speed $V_i = (3.2 \pm 1.5) \text{ m s}^{-1}$). To fully capture the emitted CH₄ plume dispersed within the PBL, which extended up to $(420 \pm 20) \text{ m}$, vertically stacked transects were flown between 97 m and 305 m. Figure 3.2(a) shows the downwind horizontal transects with CH₄ mole fractions color-coded and the corresponding time series in (b). CH₄ enhancements were detected in all seven transects. The calculated CH₄ fluxes for each transect result in a total flux of $(86.5 \pm 41.2) \text{ kg h}^{-1}$. The uncertainty is given for confidence intervals of 1σ and arises mainly due to wind measurements. Detailed information on the uncertainty calculation method is provided in the Appendix A.

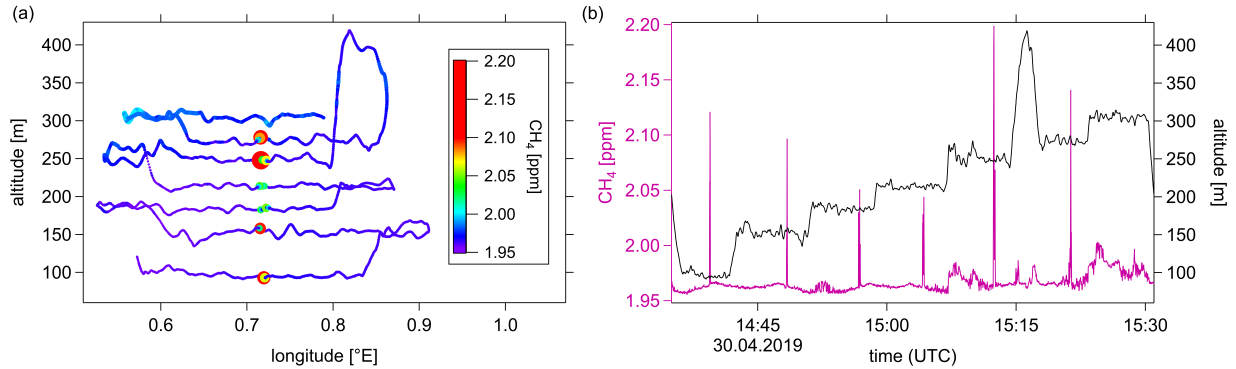


Figure 3.2: Example for measurements downwind of platform P1 during the offshore flight on 30 April 2019: (a) horizontal transects at altitudes between 94 m and 304 m above sea level. CH₄ enhancements are elucidated with a color-scale, whereby the size of plotted symbols is scaled to CH₄ mole fractions. (b) corresponding CH₄ time series.

3.4 Calculated Top-down CH₄ fluxes for UK and NL offshore installations

CH₄ emission fluxes have been determined for six UK and five Dutch facilities sampled during flight surveys on 30 April 2019, 2 May 2019 and 6 May 2019, using the mass balance method described above (see Figure 3.3, Table 3.1 and Table 3.2). The installations, for which the flux calculation was successful, comprise 17% of the UK southern North Sea dry gas production (OGA (2019)) and 6% of the Dutch offshore dry gas production (NLOG (2019)). Under the prevailing conditions found during the three flights, the level of detection, which is a result of the maximum uncertainty of all measured flux calculation parameters (wind speed V_{\perp} , layer depth D_i , CH₄ enhancement ΔC_i , pressure p_i , temperature T_i , plume width Δx_i), is 0.3 kg h^{-1} (2σ). No CH₄ enhancement was detected downstream of 4 out of 11 specifically targeted platforms (P3, P5, P6, P9). In addition, a number of several other platforms were passed downwind with no indication of CH₄ enhancements. These observations are listed in the Appendix A.

Typically, one installation denotes a platform for drilling, accommodation, and production. P3 consists of three platforms, and P6 has one central platform with three satellite platforms. P4 and P5, both multi-platform complexes, have two central platforms with a compression unit and a terminal and several more producing platforms around. P4 consists of 2 central platforms, 6 platforms for production, and 3 wellhead platforms (19 platforms in total). P5 has 2 central platforms, 4 platforms for production, and 3 wellhead platforms (15 platforms in total). Emissions in both regions are the same magnitude and range from 12.1 to 86.5 kg h^{-1} . Only the multi-platform complex P4 stands out with higher emissions (1258.7 kg h^{-1}). The relative uncertainties of the determined fluxes range from 23% to 70%, with the wind measurements as the main contributors (> 90%).

3.4.1 Comparison with bottom-up inventories

In this section the top-down measured CH₄ fluxes are compared with bottom-up reported emissions and a ship-based top-down study for Dutch sites (Hensen et al. (2019)). Table 3.1 and Table 3.2 show the measured CH₄ fluxes for the UK and for the Dutch sites along with bottom-up estimates and the ship-based measurements for Dutch sites.

In the comparison with bottom-up estimates the globally gridded annual inventory GFEI (2019) based on IPCC Tier 1 methods (IPCC (2006)) is referred to, as well as to the UK national point source inventories NAEI (2018) and EEMS (2018, 2019) and daily facility-level reporting by Dutch operators.

Observational based top-down methods only provide “snap-shot” emission estimates representing emissions only for the time of the measurements. This means that a) to allow for a comparison the yearly inventory data needs to be scaled to the temporal resolution of the measurement (or vice-versa), and b) a detailed one-by-one comparison is hampered, which is especially true for cases when observations are made during times of non-typical operational conditions, as well as for intermittent emissions (Foulds et al. (2022), Chen et al. (2023)). Therefore, for the comparison with inventories a set of “snap-shot” measurements around a group of sites, which represent a distribution of emissions in a region, are preferred over a one-by-one comparison (Tullos et al. (2023)).

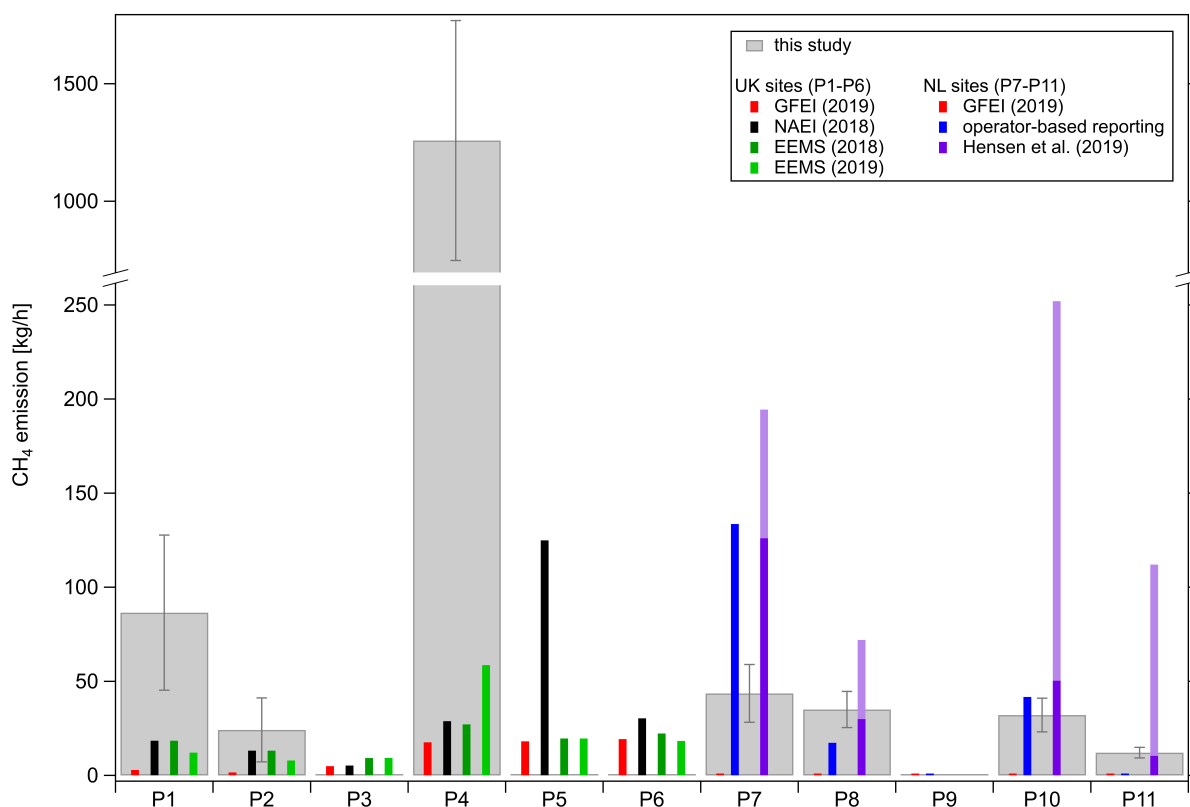


Figure 3.3: Comparison of calculated CH₄ fluxes from this study (grey) for UK sites (P1-P6) and Dutch sites (P7-P11) to the Global Fuel Exploitation Inventory (GFEI) (2019) (red), the UK National Atmospheric Emissions Inventory (NAEI) (black), UK Environmental and Emissions Monitoring System database (EEMS) (dark green for 2018; light green for 2019), reported fluxes from operators (blue) and a ship-based top-down study (range in light purple; minimal flux in dark purple) for Dutch sites (Hensen et al. (2019)). The inventory annual emission data is converted to hourly emissions. For 4 out of 11 targeted installations no downwind enhancements were detected (P3, P5, P6, P9). GFEI (2019) emission data for P7-P11 and operator-based reporting for P9 and P11 is smaller than 0.3 kg h^{-1} . Operator reported values were not available for UK sites.

3. Quantification of CH₄ emissions from fossil fuel production in the southern North Sea

Table 3.1: Observed CH₄ fluxes for UK sites from this study and emissions from annual reporting from the UK National Atmospheric Emissions Inventory (NAEI (2018)), the UK Environmental and Emissions Monitoring System database (EEMS (2018) and EEMS (2019)) and the Global Fuel Exploitation Inventory (GFEI (2019)). For 3 out of the 6 targeted installations emissions are measured to be below the level of detection (LoD, 0.3 kg h⁻¹). In GFEI emission sources are subdivided into gas processing (gas proc), gas production (gas prod) and gas exploration (gas expl). Information on emission processes is given for venting (vent), fugitives (fug) and flaring (flar).

Survey date		30 April 2019			2 May 2019			
Country		UK			UK			
Installation		P1	P2	P3	P4 complex	P5 complex	P6	
CH ₄ flux [kg h ⁻¹]	This study		86.5 ± 41.2	24.2 ± 17.0	< LoD	1258.7 ± 510.1	< LoD	< LoD
	GFEI (2019)	all	2.9	1.6	4.9	18.1	19.3	19.1
		gas proc - fug	1.3	0	0	0	0	7.5
		gas proc - flar	1.2	0	0	0	0	7.3
		gas prod - flar	0.1	0.5	1.4	5.2	5.6	1.3
		gas expl - fug, vent, flar	0.3	1.1	3.5	12.9	13.7	3.1
	NAEI (2018)		18.4	13.1	5.2	28.8	124.9	30.3
	EEMS (2018 / 2019)	all	18.4 / 12.1	13.1 / 7.9	9.2 / 9.3	27.1 / 58.6	19.6 / 19.6	22.3 / 18.3
		turbines, engines	0.4 / 0.4	0.5 / 0.4	4.7 / 4.7	3.8 / 5.5	11.4 / 8.2	0.01 / 0.7
		fug	3.9 / 0	6.1 / 0	n.a. / n.a.	0 / 0	4.5 / 4.6	0
vent		14.0 / 11.6	6.5 / 7.5	4.5 / 4.6	23.3 / 53.1	3.8 / 6.8	22.3 / 17.7	
flar		0 / 0	0 / 0	0	0 / 0	0 / 0	0	

Table 3.2: Observed CH₄ fluxes for Dutch sites from this study and emissions from annual reporting from the Global Fuel Exploitation Inventory (GFEI (2019)). For 1 out of the 5 targeted installations emissions are measured to be below the level of detection (LoD, 0.3 kg h⁻¹). In GFEI emission sources are subdivided into gas processing (gas proc), gas production (gas prod) and gas exploration (gas expl). Data from individual operator-based reporting was available for the survey date. Information on emission processes is given for venting (vent), fugitives (fug) and flaring (flar). Results from a ship-based top-down study (Hensen et al. (2019)) is listed for 4 out of 5 sampled sites.

Survey date		6 May 2019					
Country		NL					
Installation		P7	P8	P9	P10	P11	
CH ₄ flux [kg h ⁻¹]	This study		43.6 ± 15.4	35.1 ± 9.6	< LoD	32.1 ± 9.0	12.1 ± 2.8
	GFEI (2019)	all	0.21	0.21	0.003	0.006	0.01
		gas proc -fug	0	0	0	0	0
		gas proc - flar	0.2	0.2	0	0	0
		gas prod - flar	0.005	0.006	0.003	0.006	0.01
		gas expl - fug, vent, flar	0	0	0	0	0
	Reporting by operators (survey date)		133.8	17.3	0.03	41.7	0
		vent + fug	vent + fug	vent + fug	vent, no flar	no vent, no flar	
Ship observation (11/2018) (Hensen et al. (2019))		126 - 194.4	29.9 - 72	not sampled	50.4 - 252	10.4 - 18.4	

Globally gridded annual inventory of CH₄ emissions from fossil fuels exploitation (GFEI)

The Global Fuel Exploitation Inventory (GFEI) (Scarpelli and Jacob (2019), Scarpelli et al. (2020)) is a globally gridded 0.1° x 0.1° inventory containing CH₄ emissions arising from fossil fuel exploitation for the year 2019. National emission totals, which are based on country-specific emission factors, are reported to the UNFCCC and used in the inventory for a spatial downscaling to the locations of potential sources (Scarpelli et al. (2020)). Thereby, global data sets for oil and gas infrastructure are used. The UK UNFCCC reporting for emissions from the offshore oil and gas exploitation is based on the UK Environmental and Emissions Monitoring System (EEMS) database (Brown et al. (2023)) and the Dutch reporting is based on the Dutch Pollutant Release and Transfer Register (Honig et al. (2022)). In the UNFCCC reported data, fugitive emissions are already categorized into subsectors, whereas venting and flaring emissions are reported as totals. Thus, the latter are disaggregated by the inventory to the subsectors using IPCC Tier 1 methods (IPCC (2006)). As a result, the inventory resolves the different fossil fuels sectors (oil, gas, coal) and associated subsectors (distribution (fugitive), exploration (fugitive + venting + flaring), processing (fugitive, flaring), production (fugitive, flaring), storage (fugitive) and transmission (fugitive, venting)). The emission estimates determined in this work are compared with the GFEI v2 data set for total global fuel exploitation for gas from the Harvard Dataverse (Scarpelli and Jacob (2019)). Thereby, the inventory data given for each grid cell (Mt km⁻²) is used to calculate the emission from the grid cell area.

The platforms surveyed in this study are considered to be processing, production and exploration sites by the inventory. As an example, the total CH₄ emissions reported for P1 (2.9 kg h⁻¹) break down to: 44% estimated to arise from fugitives during gas processing, 43 from flaring during gas processing, 10% from exploration (fugitives + venting + flaring emissions) and 4% from flaring during production. According to the inventory, UK emissions are fugitive, venting and flaring emissions, whereas emissions on Dutch sites arise only from flaring. For all sampled installations, operations other than exploration, production and processing are claimed to emit no CH₄. Compared to the GFEI v2 data set for total CH₄ emissions from gas exploitation, the measured fluxes of (1369.4 ± 568.3) kg h⁻¹ are 21 times higher than GFEI data (65.9 kg h⁻¹) for all sampled UK facilities in aggregate. However, the highest emitting UK site (P4 complex) is identified as the highest emitter by the GFEI, as well. The factor by which measured emissions around Dutch sites are underestimated by the GFEI is an order of magnitude higher compared to UK sites: Measured fluxes ((122.9 ± 36.8) kg h⁻¹) are 279 times higher than GFEI data (0.44 kg h⁻¹) in aggregate for all sites. This high discrepancy points to the weaknesses in using global inventories for field-specific emissions characterisations especially when compared with snap-shot measurement studies. However, similar to UK sites, the two platforms (P7, P8) with highest emissions measured are correctly identified by the GFEI as the highest emitters.

For the sampled installations in this study, Dutch GFEI data is two orders of magnitude smaller compared to UK GFEI data. GFEI relies on UNFCCC reported emissions. Using the UNFCCC GHG Data Interface (UNFCCC (2022)), Dutch annual CH₄ fugitive emissions from the natural gas energy production sector and reported for the year 2019 are 14 times smaller compared to the UK equivalent. Further, in contrast to UK reporting, no data is reported for the natural gas subsectors exploration, production and processing. Thus, GFEI values for Dutch sites can only arise from UNFCCC reported total venting and flaring emissions, since those are disaggregated by the inventory to the subsectors. For the sampled Dutch sites in this study, the

inventory gives only flaring emissions from production and processing. Therefore, the UNFCCC reported Dutch emissions, which the inventory is based on, could explain the high discrepancy between GFEI Dutch and UK values.

A related study of 21 oil and gas facilities in the Norwegian Sea finds a better agreement of the GFEI v1 (2016) with the measured fluxes being only a factor 1.4 higher in aggregate for all platforms (Foulds et al. (2022)). Similar to the Dutch UNFCCC reporting, the Norwegian UNFCCC reporting does not show emissions for the natural gas subsectors exploration, production and processing. Considering that Foulds et al. (2022) sampled both oil and gas producing installations, the better agreement could possibly be attributed to UNFCCC reported emissions for the oil sector.

UK annual point source inventories (NAEI, EEMS)

The UK Environmental and Emissions Monitoring System (EEMS) database is the environmental database of the UK oil and gas industry maintained by the Offshore Petroleum Regulator for Environment and Decommissioning (OPRED) and the UK Department for Business, Energy & Industrial Strategy (BEIS). It provides annual data from measurements and calculations made for single offshore installations based on reported data from operators. According to the EEMS Atmospheric Emission Calculations (OPRED (BEIS) (2008)), monitoring systems of emitted gases are rare at offshore installations. Where no direct measurement data is available, the emission is calculated by the inventory multiplying activity data (e. g. fuel consumption or flow to flare/venting stack) with locally derived or default emission factors, which are mainly taken from literature. Inventory sources for CH₄ and CO₂ are differentiated into: engines, heaters and turbines for either diesel, fuel oil or gas consumption; total fugitive emissions; gas flaring from maintenance, routine or upsets/other; total gas venting and emissions from ship oil loading. Latest EEMS data is available for 2018 and 2019.

The UK National Atmospheric Emissions Inventory (NAEI) is an emission database listing all UK point sources and is provided by BEIS. For offshore oil and gas installations it is based on the Emissions Trading Scheme (ETS) dataset for combustion and flaring sources and on the EEMS inventory for fugitives, venting and other sources such as oil loading (with combustion and flaring data only used if not available in ETS) (Brown et al. (2023); personal communication with the technical director for the NAEI). The inventory compilation process includes quality checks against other reporting systems such as the Petroleum Production Reporting System (PPRS), which also reports venting, flaring and gas use data. In the NAEI inventory, emission data is aggregated for all platforms associated with a certain oil or gas field. Offshore emission data is available for CH₄ and for CO₂.

The fluxes observed in this study arise from installations within a certain field and are compared to the inventory data from 2018. The annual estimates of the UK national point source inventories NAEI and EEMS are smaller than the fluxes measured during this study. The measured fluxes for P1 and P4 are underestimated, while P2 agrees with both inventories within uncertainties. For 2018 the measurement-derived fluxes are a factor of 6 (NAEI; 220 kg h⁻¹) and 12 (EEMS; 109.7 kg h⁻¹) higher cumulatively for all sampled facilities. However, EEMS emission data for 2019 agree slightly better with the observations taken in 2019: Top-down estimates are a factor of 11 higher compared to the EEMS reported data (125.8 kg h⁻¹). Most CH₄ emissions of sampled installations and reported by EEMS are attributed to venting (35% - 96%) besides emissions arising from the operation of turbines and engines (0.1% - 50%). It is worth noting

that for all platforms listed in EEMS, zero flaring emissions are reported. During the flights no visible flaring was observed. Nevertheless, flaring is stated to have a share of 3% of the southern North Sea region's total CH₄ emissions in 2019 (OGA (2020)). The Global Gas Flare Catalog 2019 from the Earth Observation Group at the Payne Institute for Public Policy (Elvidge et al. (2015), Elvidge et al. (2013)), which uses Visible Infrared Imaging Radiometer Suite (VIIRS) data, shows flaring in the North Sea region. However, for the sampled installations no flaring is observed in 2019, which confirms the inventories zero flaring claim at least for the sampled installations.

Since EEMS data is fed into the NAEI inventory, NAEI (2018) reported values are expected to be the same or higher than EEMS (2018) data. A comparison between NAEI data and EEMS data from 2018 shows that NAEI numbers are consistent with EEMS for two (P1, P2) and higher than EEMS data for three (P4, P5, P6) UK platforms. However, for P3 the NAEI reported value is smaller compared to EEMS (2018). This could either indicate an error in the EEMS reporting or it might be that the emissions of P3, which consists of 3 platforms, are misallocated in the NAEI.

In EEMS emissions are listed for one specific platform, also in the case of multi-platform complexes (P4, P5). Those platforms might be interpreted as being representative platforms with the reported emissions being aggregated emissions for the complex. Regarding the multi-platform complex P4, the FLEXible PARTicle (FLEXPART) dispersion model was applied by I. Pisso (Norwegian Institute for Air Research, Pisso et al. (2019)) to attribute the measured emission plumes to individual platforms located within the complex. The platforms that the observed fluxes were attributed to do not match with the (representative) platforms listed in EEMS (2018/2019).

The discrepancy to UK national inventories detected in this study is higher than reported in previous airborne studies of other offshore regions. Zavala-Araiza et al. (2021) estimated offshore CH₄ emissions in the Sureste Basin, Mexico, to be more than an order of magnitude lower than the values given in the Mexican greenhouse gas emission inventory. Gorchoy Negron et al. (2020) generated an airborne measurement-based inventory comprising offshore facilities located in the U.S. Gulf of Mexico. They showed that for shallow-water facilities CH₄ emissions are more than a factor of two higher than the estimate of the U.S. Environmental Protection Agency Greenhouse Gas Inventory (EPA GHGI) and the Gulfwide Offshore Activity Data System (GOADS) inventory.

Facility-level reporting by Dutch platform operators for the survey date

For the sampled Dutch sites facility-level operator-based reporting on CH₄ emission was provided after the flights. The Oil & Gas Methane Partnership (OGMP) 2.0 level of the reporting corresponds to level 3, i.e. using generic emission factors for individual source types. The reporting comprises information on the status of the installation (producing or offline on an hourly basis), the total amount of gas produced and CH₄ and CO₂ emissions on the survey day including additional information on emission types and sources (venting, flaring, fugitives). Such information was unavailable for the UK facilities upon request via the trade association Oil & Gas UK.

As expected, the smallest discrepancy between top-down and bottom-up estimates exists for the comparison with emission data of individual facilities provided by platform operators for the specific survey day. Operator-based reporting was only available for the five sampled Dutch installations (P7-P11). The facility-level estimates deviate by up to a factor of 12 compared to the reporting, whereby two out of five facilities (P7, P10) are overestimated and another two

facilities underestimated (P8, P11). P9 is reported as offline on the survey day, which agrees with the measurements showing no elevated CH₄, C₂H₆ and CO₂. According to the operators, CH₄ emissions arise from venting and fugitives for 4 out of 5 installations (P7-P10). P10 is reported as offline during the time of flight, while emissions are still measured and smaller than the reported venting CH₄ emissions. For P11 no venting or flaring was recorded, although CH₄ was detected during the measurements conducted downstream. The measured emissions might be attributed to fugitives, which are not excluded by the operator in this case. Flaring emissions are explicitly excluded only for two out of five installations (P10, P11). For P7-P9 flaring emissions could contribute, though. For all sampled Dutch installations together, the estimated flux of $(122.9 \pm 36.8) \text{ kg h}^{-1}$ deviates by a factor 0.64 (ranging from 0.33-12 for individual facilities) from reported values (192.8 kg h^{-1}). A comparison with operator-reported data for offshore installations in the Norwegian Sea by Foulds et al. (2022) shows that although there are deviations for individual facilities, reported data agree similarly well in aggregate for a larger sample size (18 facilities) with the measured fluxes being smaller than reported emissions by a factor 0.8 (ranging from 0.1-22 for individual facilities).

Shipborne measurements for Dutch sites

The planning for the flight on 06 May 2019 around Dutch installations relied on a ship-based top-down study conducted by the Dutch Organisation for Applied Scientific Research (TNO) in 2018 (Hensen et al. (2019)). With the aim to derive CH₄ emission fluxes, measurements were taken at distances up to 3 km downwind of 33 platforms in November 2018. CH₄ was measured with a TILDAS spectrometer (Aerodyne Research, Inc.) and a Picarro instrument, whereby the inlet was installed at 35 m above sea level. The results shown in Table 3.2 were obtained by combining the measurements with a Gaussian plume model and a tracer-release experiment. The derived fluxes range from 10 kg h^{-1} to 252 kg h^{-1} .

For P8 and P11 the herein determined flux estimates are within the range of the fluxes from the ship-based study, whereas in case of P7 and P10 the determined flux estimates are smaller. For the studied 4 Dutch facilities in aggregate, the estimated flux of $(122.9 \pm 36.8) \text{ kg h}^{-1}$ is smaller with respect to the ship-based measurements (216.7 kg h^{-1} - 536.8 kg h^{-1}) and deviates by factor 0.23-0.57.

3.4.2 Correlations of CH₄ with C₂H₆ and CO₂

For all sampled installations for which enhanced CH₄ was detected, C₂H₆ was enhanced, which is an indicator for fossil fuel emissions (Lowry et al. (2020); Peischl et al. (2018); Hausmann et al. (2016); Smith et al. (2015)). Co-emitted CO₂ was measured only for some of the sampled installations indicating a combustion source from either flared CH₄ or other combustion sources such as turbines or engines.

Figure 3.4 shows the time series for a transect flown downwind of P1 with simultaneous enhancements in CH₄, CO₂ and C₂H₆ mole fractions as an example of the observed plumes.

Measured C₂H₆ and CH₄ (C₂:C₁) ratios are used to characterize fossil fuel emissions, because they depend on the type of field/reservoir (gas, gas condensate, oil). Panel (a) in Figure 3.5 shows the time series of measured C₂H₆ and CH₄ for the transect at 250 m altitude downwind of P1 to illustrate the calculation of the C₂:C₁ ratio. The peak areas for C₂H₆ and CH₄ enhancements over the background are shown in yellow. The C₂:C₁ ratio is calculated by dividing the integrated

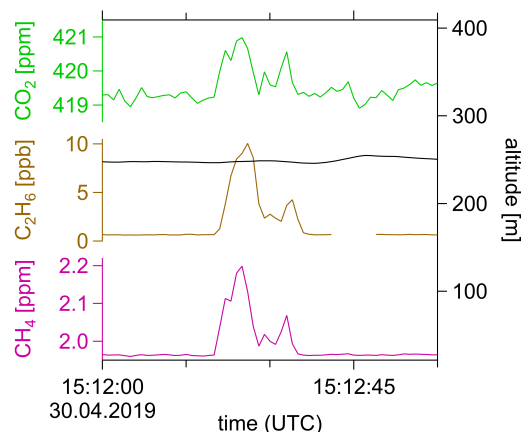


Figure 3.4: Time series (1 Hz) of a transect at 250 m altitude downwind of P1 (peak #5): Coinciding elevations in CO₂ (green), C₂H₆ (brown) and CH₄ (magenta) mole fractions. C₂H₆ is a tracer for fossil fuel emission and CO₂ indicates a combustion source.

peak area of C₂H₆ by the integrated peak area of CH₄, which results in a C2:C1 ratio of 4.3% in this case. The C2:C1 ratio for a sampled installation is the average of the determined ratios over all transects.

Since the southern North Sea region contains predominantly dry gas fields with relatively low gas condensate (wet gas) production, low C2:C1 ratios are expected, ranging from 1-5% (dry gas) and 5-10% (gas condensate) (Xiao et al. (2008), Jones et al. (2000)) or 1-6% (dry gas) and >6% (wet gas) (Yacovitch et al. (2014)). Measured values range from 2.5% to 7.8% for all installations. Comparing the measured ratios to reported values from the OGA Shell/ExxonMobil Geochemistry Database for Central North Sea (OGA (2017)) for UK sites and the NLOG (NLOG (2019)) for Dutch sites, the reporting underestimates the measurements for P7 and P10 and overestimates the measured value for P11, but is consistent for P4 and P8 (see Table 3.3). In general, the dry gas and gas condensate binary categorization matches for the observed and reported ratios.

Enhanced CO₂ mole fractions accompanied the CH₄ enhancements at five installations (P1, P2, P4, P7, P10). For P8 and P11 C₂H₆ was enhanced while no CO₂ enhancement was observed (< LoD). For three of the platforms (P1, P4, P10), CH₄ and CO₂ were well-correlated and CO₂ fluxes have been determined. The CO₂ flux is determined from the gradient of a linear regression between the CO₂ and CH₄ enhancements since both species are detected by the same instrument (Picarro Analyser). Figure 3.5(b) shows the CH₄ to CO₂ scatter plot for P1, where enhanced CO₂ was found for two peaks at altitudes above 240 m. The observation of co-emitted CO₂ points to a buoyant plume adding up to the CH₄ plume at altitudes above 240 m.

Table 3.3 shows the measured CO₂ fluxes along with inventory emission data from the UK point source inventories NAEI and EEMS and Dutch operator data. For P1 EEMS (2018) and EEMS (2019) overestimate emissions, while the NAEI inventory states lower emissions, but matches within the uncertainties. Likewise, EEMS (2019) agrees within the uncertainties with measured CO₂ fluxes from P4, while both NAEI (2018) and EEMS (2018) underestimate emissions. According to EEMS, which categorizes emissions into turbines/engines, fugitives, venting and flaring, CO₂ emissions arise mainly from the combustion of diesel and gas in turbines and

3. Quantification of CH₄ emissions from fossil fuel production in the southern North Sea

42

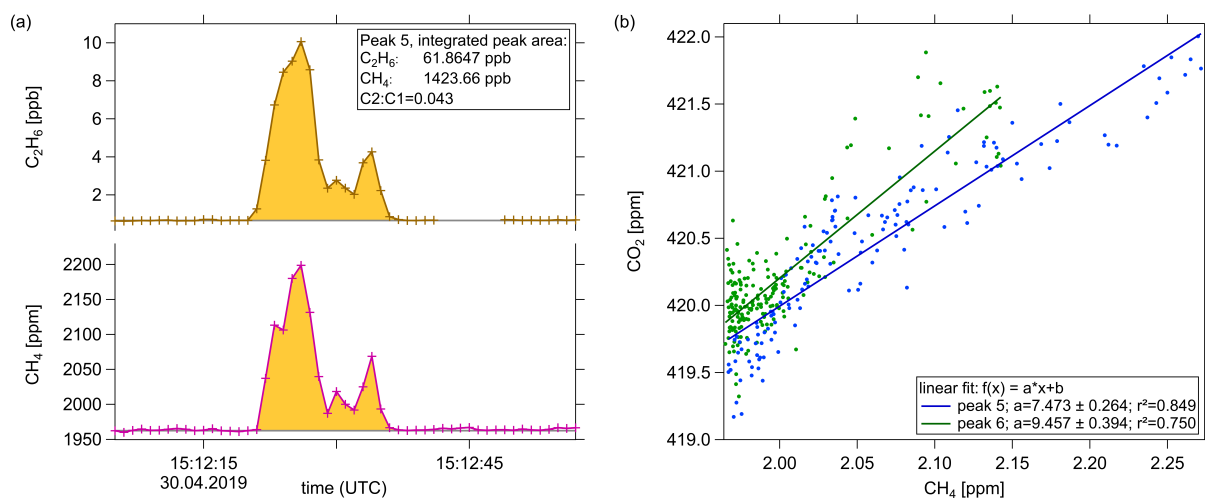


Figure 3.5: (a) Time series (1 Hz) of the transect at 250 m altitude downwind of P1 (peak #5): Coinciding elevations in C₂H₆ (brown) and CH₄ (magenta) mole fractions. The C₂H₆ to CH₄ (C2:C1) ratio is calculated from the fraction of the integrated peak areas (yellow) over the background mole fractions (gray) and over the time span of the peak (18 s). (b) Scatter plot for co-emitted CO₂ downwind of platform P1. Enhanced CO₂ was found for two peaks at altitudes above 240 m.

engines. Only for the platform complex P5 minor emissions from fugitives and venting are listed. In EEMS (2018/2019) flaring emissions are zero for all UK platforms. This is inconsistent with data from the UK OGA, which reports that 4% of CO₂ emissions in the SNS region are supposed to arise from flaring in 2019 (OGA (2020)). From the amount of CO₂ and CH₄ flaring emissions in 2019 in the southern North Sea and Irish Sea region given in the OGA Flaring and Venting Report (OGA (2020)), the unburnt fraction, i. e. the ratio of unburnt CH₄ to CO₂ from flaring emissions, is 6.4%. Calculating this ratio for the sampled CH₄ and CO₂ plumes at the UK platforms, higher ratios are obtained: 12.4% (P1) and 14.7% (P4). This means that either there is no flaring on the platform, or if some flaring occurred, there were additional CH₄ fugitive or venting sources.

Comparing to Dutch operator data, no simultaneously emitted CO₂ was detected around two Dutch platforms (P8, P11), although Dutch operator data states CO₂ emission on the survey date. For P10 a CO₂ flux half the size of the emissions reported for the survey date is derived. Dutch operator data explicitly excludes flaring sources for P10 and P11 (see Table 3.2) and lists only combustion sources such as turbines and engines.

To sum up, for five out of the seven installations very likely a flaring or combustion source contributed to the total emissions. However, from the measured total emissions flaring can not be clearly differentiated from other combustion sources. But if there were any flaring sources, there must have been additional fugitive/venting CH₄ sources according to the measured CH₄ to CO₂ ratios.

3.4 Calculated Top-down CH₄ fluxes for UK and NL offshore installations 43

Table 3.3: Measured and reported (OGA, NLOG) C₂H₆ to CH₄ (C2:C1) ratios for all sampled platforms at 2σ. All installations for which CH₄ was enhanced were accompanied by co-emitted C₂H₆. No detected C₂H₆ and CO₂ enhancements are indicated with < LoD. Measured CO₂ emissions are compared to UK inventory data (NAEI, EEMS) and Dutch operator data. Information on emission processes is given for venting (vent), fugitives (fug) and flaring (flar). CO₂ emissions are rounded to two significant digits.

Survey date		30 April 2019			2 May 2019			6 May 2019					
Country		UK			UK			NL					
Installation		P1	P2	P3	P4 complex	P5 complex	P6	P7	P8	P9	P10	P11	
C2:C1 [%]	This study	4.3 ± 0.2	2.5 ± 1.1	<LoD	2.8 ± 0.4	<LoD	<LoD	5.6 ± 0.5	4.3 ± 0.9	<LoD	7.8 ± 1.0	5.3 ± 0.7	
	OGA/NLOG	n.a.	n.a.	3.3	3.2	4.9	4.3	3.3	3.6	4.3	6.0	6.1	
CO ₂ flux [kg/h]	This study	640 ± 300	weak correlation	<LoD	21850 ± 8870	<LoD	<LoD	<LoD	weak correlation	<LoD	5290 ± 1580	<LoD	
	NAEI (2018)	410	390	200	3110	4160	1070	n.a.					
	EEMS (2018/2019)	all	1490 / 1490	1430 / 1210	740 / 740	11400 / 17110	15260 / 11880	3930 / 2180	n.a.				
		turbines, engines	1490 / 1490	1430 / 1210	740 / 740	11400 / 17110	15260 / 11880	3930 / 2180					
		fug	0 / 0	0 / 0	n.a. / n.a.	0 / 0	0.07 / 0.05	0 / 0					
		vent	0 / 0	0 / 0	0 / 0	0 / 0	0.07 / 0.08	0.02 / 0.02					
		flar	0 / 0	0 / 0	0 / 0	0 / 0	0 / 0	0 / 0					
	Reporting by operators	n.a.						16520	330	0	10690	570	
								turbines	turbines		turbines power generators	turbines engines furnaces diesel	

3.4.3 CH₄ loss rates

Figure 3.6 shows gas lost to the atmosphere, which is calculated from CH₄ emission rates and the CH₄ mol % (UK sites: Shell/ExxonMobil Geochemistry Database for Central North Sea (OGA (2017)); Dutch sites: operator data) for the respective gas installation. The determined loss rates are the ratio of gas loss and dry gas production, i.e. normalized CH₄ emissions against natural gas production rates. UK production rates are given as monthly values by OGA (2019). Thereby, production from upstream fields with only subsea wells and no platform infrastructure is included. Dutch production data was provided by Dutch operators for the specific survey day. Determined loss rates for Dutch and UK sites are smaller than 1.0%, except for P4, which shows an higher loss rate of 3.1% (see Table A.1 in Appendix A for individual platform production rates along with calculated loss rates). Besides the fact, that P4 is a multi-platform complex and relatively old, i.e. producing since 50 years, there is no indication of abnormal activities on the survey date. For three UK facilities (P3, P5, P6) no emissions were detected, although they were producing during the month of survey. According to the Dutch operator, P9 did not produce on the survey day, and neither a plume was detected by the measurements.

3.4.4 Comparison with CH₄ emissions from other offshore regions

Figure 3.7 depicts the determined CH₄ emission rates and production rates compared with the results obtained in two other airborne studies conducted by Foulds et al. (2022) in the Norwegian Sea and Gorchov Negron et al. (2020) in the Northern Gulf of Mexico.

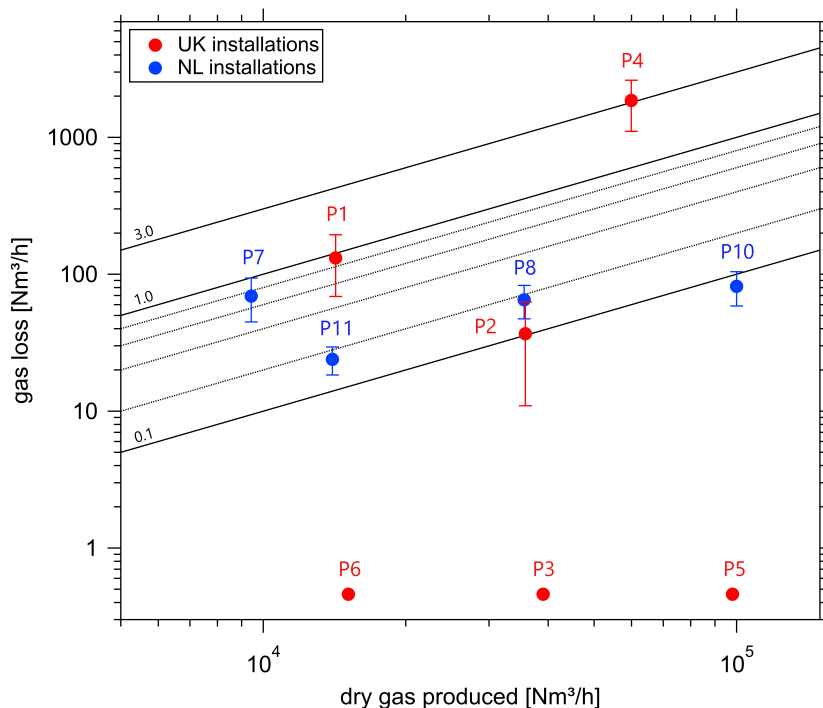


Figure 3.6: Gas lost to the atmosphere against the amount of dry gas produced in norm cubic meters (Nm³) per hour (production data from OGA (UK installations) and operator data (Dutch installations)). Dutch installations are shown in blue, UK installations in red. Note that no downwind enhancements were detected for 4 installations (P3, P5, P6, P9) with only P9 not producing (excluded). Lines of constant loss rates (%) are shown in black (see Table A.1 in Appendix A for all production and loss rates).

Comparing the CH₄ emission fluxes for individual facilities (left side of Figure 3.7), the emission rate of P4 is as high as the emissions measured around similar infrastructure types in the Northern Gulf of Mexico. Those are multi-platform complexes in shallow waters showing both in the southern North Sea and in the Northern Gulf of Mexico emissions higher than 500 kg h⁻¹. In the Gulf inconstant temporal variability of those infrastructure types was seen, what might correspond to the non-detectable emissions of the multi-platform complex P5. Comparing average absolute emission rates per facility (red vertical lines), the lowest average emission rates were determined around 18 installations in the Norwegian Sea (24 kg h⁻¹) and highest emission rates around 9 installations in the Gulf (457 kg h⁻¹) with a factor of 20 difference. The average emission estimate in the southern North Sea is 136 kg h⁻¹ and compares well with the average absolute emission rate in a regional mass balance in the Gulf with a larger sample size in the Gulf (117 kg h⁻¹). When excluding the multi-platform complex P4, the southern North Sea average emission estimate amounts to 23 kg h⁻¹, which compares well with the average emission rate in the Norwegian Sea, where no multi-platform complex was sampled.

In contrast to the southern North Sea, where gas (with little gas condensate) production dominates, in the Northern Gulf of Mexico natural gas is produced as a side product from oil exploitation (associated gas) and in the Norwegian Sea both oil and gas production takes place.

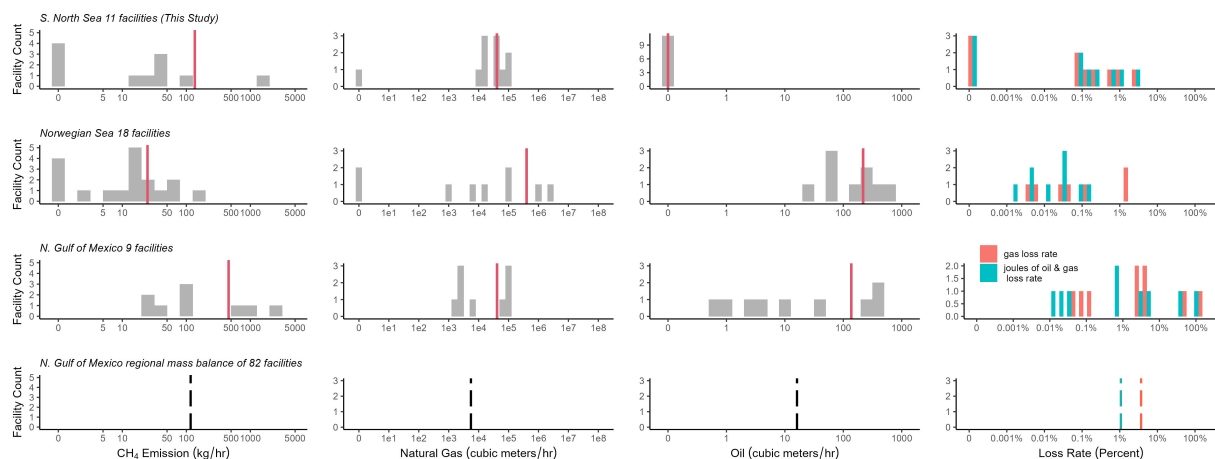


Figure 3.7: Comparison of measured CH₄ emission rates (first column), corresponding natural gas (second column) and oil (third column) production rates and loss rates (fourth column) in the southern North Sea with two other airborne studies conducted in the Norwegian Sea (Foulds et al. (2022)) and in the Northern Gulf of Mexico (Gorchov Negron et al. (2020)). Red lines denote the respective average values. The dotted lines show the average value obtained in a regional mass balance in the Northern Gulf of Mexico. The facility count does not include satellite structures.

The natural gas production rates for the facilities in the southern North Sea shown in the centre column in Figure 3.7, are on average one order of magnitude smaller than in the Norwegian Sea and one order of magnitude higher than in the Gulf regional estimate, but almost the same value as the Gulf facility-wise estimate. Average oil production rates in the Norwegian Sea and in the Northern Gulf of Mexico are comparable.

Total loss rates, i. e. all gas lost to the atmosphere divided by total production rates in the respective region, can be determined either from gas production only or from the sum of oil and gas production. Thereby, oil and gas production rates units are converted according to the energy content. Considering only gas production, the total loss rate in the southern North Sea (0.54% (0%-3.1%)) is one order of magnitude higher than in the Norwegian Sea (0.02% (0.003%-1.6%)) and one order of magnitude smaller than in the Gulf. The latter amounts to 1.9% for the facility-level measurements and 3.7% for the regional measurements. Including oil production, total loss rates in the Norwegian Sea (0.01% (0.001%-0.2%)) and in the Gulf (0.51% (0.01%-112%)) for the facility study; 1.1% for the regional study) are reduced. Overall, differences in loss rates are rather driven by different production rates than absolute gas loss or emission rates.

In Chapter 5 the western Central African offshore region at the Gabonese and Angolan Coast is described. In this region measurements took place in September 2022 with the DLR-QCLS instrument deployed. Within this work the DLR-QCLS was prepared for CH₄ isotope measurements for the campaign (see Chapter 4).

3.5 Summary Chapter 3

CH₄ flux estimates are reported for six UK and five Dutch offshore gas production installations in the southern North Sea derived from airborne measurements conducted in spring 2019. The

observed CH₄ enhancements are identified as emissions arising from natural gas based on co-emitted C₂H₆. For each offshore installation C₂H₆ to CH₄ (C₂:C₁) ratios are calculated, which are in the expected range for gas fields. For part of the installations also enhanced CO₂ was measured indicating that a flaring or combustion source contributed to the total emissions.

Comparison with a ship-based top-down study conducted around Dutch facilities in 2018 (Hensen et al. (2019)) shows that the derived CH₄ fluxes deviate by a factor 0.23-0.57 and hence are smaller than the fluxes derived by Hensen et al.

The CH₄ flux estimates were compared with different bottom-up inventories available for the southern North Sea region, including the Global Fuel Exploitation Inventory (GFEI) (Scarpelli and Jacob (2019)), the UK Environmental and Emissions Monitoring System database (EEMS), the UK National Atmospheric Emissions Inventory (NAEI), and direct facility-level reporting by Dutch operators. In general, the comparison for individual facilities shows a large discrepancy between the top-down derived emissions and all bottom-up inventory estimates, which may be expected because of the nature of single snap-shot measurements per facility and potential temporal variability per facility demonstrated via repeated measurements by Foulds et al. (2022). The largest discrepancy exists with the annual emission data from the globally gridded GFEI inventory for the year 2019, showing that measured aggregated emissions from UK and Dutch sites are higher by a factor of 21 and 279, respectively. On the one hand, these high discrepancy factors reflect the weaknesses in using global inventories based on Tier 1 methods for field-specific emissions characterizations, especially when comparing with snap-shot measurements. On the other hand, Dutch UNFCCC reported emissions, which the inventory is based on, are much smaller compared with UK UNFCCC reporting and could give rise to the exceptionally large factor for Dutch sites. The top-down emission fluxes for all sampled UK installations in aggregate deviate from UK national annualized emission data from NAEI and EEMS for the year 2018 by factors of 6 and 12, respectively. NAEI inventory data, which is based on EEMS operator-based reporting, is equal to or higher than EEMS, except for one out of six installations. Latest UK national inventory data available for 2019 from EEMS deviate slightly less from the measurements with the latter being a factor 11 higher for all sampled UK facilities in aggregate. According to the EEMS inventory, CO₂ emissions measured around UK facilities and correlating with CH₄ emissions are solely attributable to combustion sources (turbines, engines) while flaring emissions are reported as zero for both CO₂ and CH₄. The measurements cannot differentiate flaring from other combustive sources. Still, the measured ratios of emitted CH₄ to CO₂ point at existing venting/fugitive CH₄ sources, whereby flaring sources could be contributing.

As expected, the best agreement with the flux estimates exists with facility-level reporting from Dutch operators for the specific survey date. The measurements deviate by a factor of 0.64 (0.33-12) and are smaller with respect to Dutch reported emissions for all sampled facilities in aggregate. The results for operator-based facility-level reporting compare very well to a study conducted in the Norwegian Sea by Foulds et al. (2022), which find their measurements deviating by a factor 0.8 and being smaller compared to the reporting by operators. Thus, for sites with operator-based facility-level reporting in Dutch waters, – as suggested in the reporting framework Oil and Gas Methane Partnership (OGMP) 2.0 (www.ogmpartnership.com) – the highest accuracy is demonstrated compared to measurements. The adoption of facility-level estimation in national inventories would be expected to increase the accuracy of national CH₄ emissions accounting for the offshore oil and gas sector. To improve comparisons of top-down and bottom-up observation and resolve discrepancies, generating bottom-up inventories at facility-scale and

accounting for temporal variability when including top-down measurements would be extremely valuable.

A regional comparison with airborne studies in the Norwegian Sea (Foulds et al. (2022)) and in the Northern Gulf of Mexico (Gorchov Negrón et al. (2020)) shows that the absolute facility-level emission rates agree with the general distribution found in other offshore basins. This is despite differing gas production rates, which span two orders of magnitudes across geographies. Total loss rates (emissions normalized against production rates) of the southern North Sea compare to total loss rates in the Gulf, whereas loss rates in the Norwegian Sea are one order of magnitude smaller. As a consequence of the similar absolute emission rates, mitigation is needed equally across geographies. Furthermore, average absolute emission rates are substantially larger in the UK compared to the Netherlands, which is largely driven by one super-emitter in the UK (installation P4). The emission of the super-emitter is as high as the emissions measured around similar infrastructure types (multi-platform complexes in shallow water) in the study in the Northern Gulf of Mexico, but additional sampling in future studies is needed to investigate representativeness.

Chapter 4

Modifying the DLR-QCLS for the measurement of $\delta^{13}\text{C}(\text{CH}_4)$

As described in the Chapters 2 and 3, measurements of the isotopic ratio $\delta^{13}\text{C}(\text{CH}_4)$, i. e. of the CH_4 isotopologues $^{13}\text{CH}_4$ and $^{12}\text{CH}_4$, are a useful tool to assess the contribution from different emission sources to the observed growth of atmospheric CH_4 . More specifically, the quantification of fossil fuel emission sources and their characterisation by measuring the isotopic source signatures helps to clarify the contribution of fossil fuel sources to this trend. Due to the remote location, airborne measurements are especially suitable for the characterisation of offshore emissions. However, fast measurement techniques are necessary to allow for continuous observations during plume encounters from point source emissions, which typically only last for a few seconds. This is underpinned by the problems observed during the southern North Sea flights (see Chapter 3). The procedure to sample flasks for the measurement of $\delta^{13}\text{C}(\text{CH}_4)$ to derive source signatures was not successful since it was not possible to take samples within the spatially narrow plumes. Therefore, the DLR-QCLS, a fast (2 Hz time resolution) tunable laser absorption spectrometer (based on the commercial available Dual Laser Trace Gas Monitor from Aerodyne Research Inc. (Billerica, USA; McManus et al. (2015), McManus et al. (2010))), was modified in-house and adapted for the continuous measurement of $^{13}\text{CH}_4$ and $^{12}\text{CH}_4$ as part of this thesis. To this end, one of the two original lasers was replaced by a new specifically selected laser. The instrument performance was examined in the laboratory and followed by the deployment of the instrument during two airborne measurement campaigns (see Chapters 4 and 5). It has to be noted that during the time span of this thesis, the manufacturer Aerodyne Research Inc., Billerica, USA, brought a QCLS to measure $\delta^{13}\text{C}(\text{CH}_4)$ on the market. However, the in-house adaptation is still attractive. It allows the measurement of various species as needed by the science objective of a specific measurement campaign, just by changing the laser configuration.

In this chapter, first, the expected variability in the isotopic composition of air masses of interest is calculated. This serves as a basis to derive the precision requirements needed for the successful determination of isotopic source signatures (Section 4.1). The instrument setup of the core DLR-QCLS is presented in Section 4.2, followed by the description of the adaptation for the isotopic measurement in Section 4.3. This involves the selection of the new laser, the adaptation of the data retrieval as well as the calibration strategy. Section 4.4 shows the experiments conducted in the laboratory for the characterisation of the new instrument modification including

a comparison measurement with a commercial Picarro Isotope Analyser. Finally, the laboratory results are evaluated and compared with the requirements (Section 4.5).

4.1 Precision requirements for the study of CH_4 isotopic source signatures

CH_4 emitted from a source is typically transported downwind and mixed with the ambient air, which itself contains a specific CH_4 background mole fraction c_{bcg} . Hence, the measured CH_4 mole fraction c_{meas} equals the c_{bcg} with an additional source contribution c_{sc} . The mass balance equation for atmospheric CH_4 mole fractions is:

$$c_{meas} = c_{sc} + c_{bcg} \quad (4.1)$$

Considering that c_{sc} and c_{bcg} exhibit a certain isotopic signature respectively, and using the approximation that $(\delta^{13}\text{C}(\text{CH}_4) \cdot c)$ is conserved, the isotopic signature measured downwind of the source $\delta^{13}\text{C}(\text{CH}_4)_{meas}$ is given by the isotopic mass balance equation (Miller and Tans (2003)):

$$\delta^{13}\text{C}(\text{CH}_4)_{meas} \cdot c_{meas} = \delta^{13}\text{C}(\text{CH}_4)_{sc} \cdot c_{sc} + \delta^{13}\text{C}(\text{CH}_4)_{bcg} \cdot c_{bcg} \quad (4.2)$$

As described in Section 2.2, the ambient isotopic signature $\delta^{13}\text{C}(\text{CH}_4)_{bcg}$ is globally around -47.6‰ , while isotopic source signatures $\delta^{13}\text{C}(\text{CH}_4)_{sc}$ typically range from -70‰ to -20‰ depending on the type of source. The higher the measured CH_4 enhancement Δc_{meas} and the larger the difference between $\delta^{13}\text{C}(\text{CH}_4)_{sc}$ and $\delta^{13}\text{C}(\text{CH}_4)_{bcg}$, the larger will be the measured signal $\Delta\delta^{13}\text{C}(\text{CH}_4)_{meas} = \delta^{13}\text{C}(\text{CH}_4)_{meas} - \delta^{13}\text{C}(\text{CH}_4)_{bcg}$.

Figure 4.1 illustrates the expected $\delta^{13}\text{C}(\text{CH}_4)_{meas}$ for CH_4 enhancements Δc_{meas} up to 300 ppb within plumes. The ambient $\delta^{13}\text{C}(\text{CH}_4)_{bcg}$ is set to -47.6‰ . Different colors define different isotopic source signatures ranging from -20‰ to -70‰ . For example, for a source with $\delta^{13}\text{C}(\text{CH}_4)_{sc} = -40\text{‰}$ and $\Delta c_{meas} = 300$ ppb, $\Delta\delta^{13}\text{C}(\text{CH}_4)_{meas}$ is 1‰ , since $\delta^{13}\text{C}(\text{CH}_4)_{meas}$ is 1.0‰ higher compared to the ambient $\delta^{13}\text{C}(\text{CH}_4)_{bcg}$. For a source with $\delta^{13}\text{C}(\text{CH}_4)_{sc} = -60\text{‰}$, which deviates more from the ambient $\delta^{13}\text{C}(\text{CH}_4)_{bcg}$, $\Delta\delta^{13}\text{C}(\text{CH}_4)_{meas}$ is -1.7‰ , because $\delta^{13}\text{C}(\text{CH}_4)_{meas}$ is 1.7‰ lower compared to the ambient $\delta^{13}\text{C}(\text{CH}_4)_{bcg}$. Variations in c_{bcg} only have a small impact, with the signal $\Delta\delta^{13}\text{C}(\text{CH}_4)_{meas}$ (absolute value) getting larger for lower c_{bcg} . For example, for a source with $\delta^{13}\text{C}(\text{CH}_4)_{sc} = -60\text{‰}$ at $\Delta c_{meas} = 300$ ppb, $\delta^{13}\text{C}(\text{CH}_4)_{bcg}$ is 0.04‰ smaller for a 50 ppb lower c_{bcg} .

The isotopic source signature $\delta^{13}\text{C}(\text{CH}_4)_{sc}$ of a sampled plume can be derived using the Keeling plot method (Fisher et al. (2017); Keeling (1958)). The Keeling plot equation follows from the combination of Equation 4.1 with Equation 4.2:

$$\delta^{13}\text{C}(\text{CH}_4)_{meas} = \frac{c_{bcg} \cdot (\delta^{13}\text{C}(\text{CH}_4)_{bcg} - \delta^{13}\text{C}(\text{CH}_4)_{sc})}{c_{meas}} + \delta^{13}\text{C}(\text{CH}_4)_{sc} \quad (4.3)$$

To generate a Keeling plot, $\delta^{13}\text{C}(\text{CH}_4)_{meas}$ is plotted against $(1/c_{meas})$. Figure 4.2 shows an example for a Keeling plot from two data points of a CH_4 plume of pyrogenic ($\delta^{13}\text{C}(\text{CH}_4)_{sc} = -30\text{‰}$) and thermogenic origin ($\delta^{13}\text{C}(\text{CH}_4)_{sc} = -50\text{‰}$). Because of the linear relationship between $\delta^{13}\text{C}(\text{CH}_4)_{meas}$ and $(1/c_{meas})$, the y-intercept of the linear regression corresponds to the isotopic

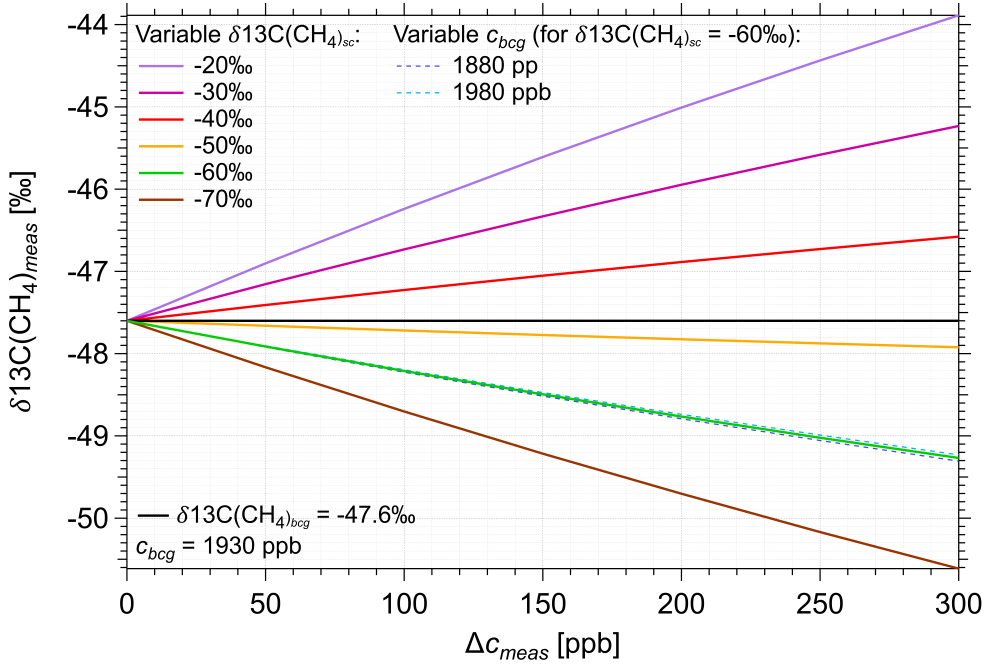


Figure 4.1: Calculation of expected measured atmospheric $\delta^{13}\text{C}(\text{CH}_4)_{meas}$ for CH₄ enhancements ΔC_{meas} up to 300 ppb within a plume and for isotopic source signatures from -20‰ to -70‰. Ambient background $\delta^{13}\text{C}(\text{CH}_4)_{bcg}$ is set to -47.6‰ (black line) at ambient background mole fractions of $C_{bcg}=1930$ ppb CH₄. For the example of $\delta^{13}\text{C}(\text{CH}_4)_{sc}=-60\text{‰}$, the resulting $\delta^{13}\text{C}(\text{CH}_4)_{meas}$ is additionally shown for a 50 ppb higher (light blue dotted line) and 50 ppb lower (dark blue dotted line) C_{bcg} .

source signature $\delta^{13}\text{C}(\text{CH}_4)_{sc}$. For the Keeling plot method, the ambient background mole fractions and ambient $\delta^{13}\text{C}(\text{CH}_4)_{bcg}$ can remain unknown, but are required to stay constant for the time of the measurement.

In general, three factors are important for the accurate determination of a source signature: It improves with higher instrument precision, higher CH₄ plume enhancements and for a higher number of sampled data points within the plume (Hoheisel et al. (2019)).

The instrument precision required for the successful determination of $\delta^{13}\text{C}(\text{CH}_4)_{sc}$ of a specific source, has to be high enough (i. e. the lower the values of the precision the better) to detect an isotopic signal ($\Delta\delta^{13}\text{C}(\text{CH}_4)_{meas}$) over the background measurement. The required precision depends on the type of the source or rather its isotopic source signature, and especially on the CH₄ enhancement ΔC_{meas} within the plume. This favors in principle a sampling close to a source, where the plume is not yet too diluted into the background atmosphere. However, in this case the emission plumes downwind of point sources are spatially narrow (up to hundreds of meters), which means that at typical aircraft velocities of 50 to 200 m s^{-1} , the plume encounters usually only last a few seconds. At the same time, at least two sample points are necessary to produce a Keeling plot and hence, to derive $\delta^{13}\text{C}(\text{CH}_4)_{sc}$. Thereby, the accuracy of the derived source signature typically increases with the number of data points within a plume and with the number of plume encounters. This means, that there is a trade-off between a high temporal resolution in

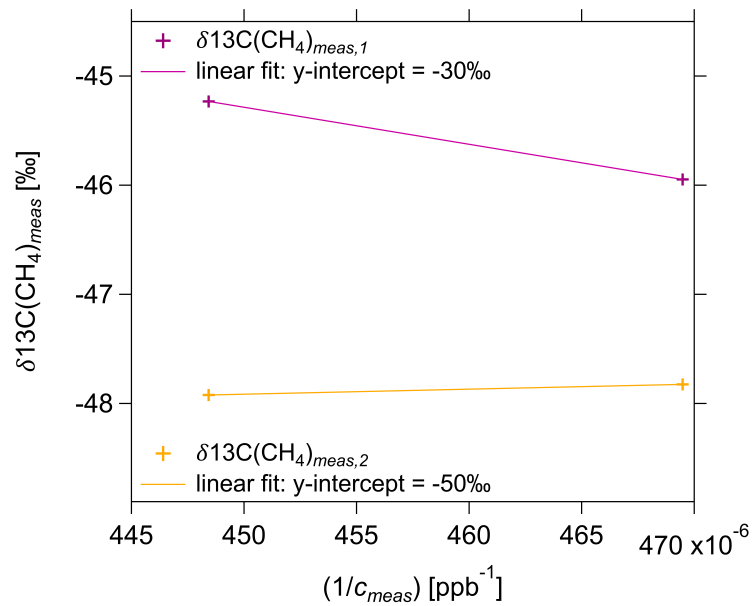


Figure 4.2: Example for the Keeling plot of two theoretically measured CH_4 plumes of pyrogenic (orange markers) and thermogenic (magenta markers) origin. Thereby, $\delta^{13}\text{C}(\text{CH}_4)_{meas}$ is plotted against $(1/c_{meas})$ and correspond to the calculated values for 200 ppb and 300 ppb CH_4 enhancement shown in Figure 4.1. The y-intercept of the linear fit gives the respective isotopic source signatures $\delta^{13}\text{C}(\text{CH}_4)_{sc}$ (see Equation 4.3).

combination with a high precision required to determine a source signature.

4.2 Instrument description: The DLR-Quantum Cascade Laser Spectrometer (DLR-QCLS)

In general, the adaptation of measurement instruments for the deployment onboard research aircraft poses several challenges. Because of limitations regarding space and weight, light-weight instrument components shall be selected. This includes also the amount of calibration gas needed for in-flight measurements. Further, changing atmospheric parameters such as temperature, pressure and water vapor are especially challenging for (IR-)laser-based measurement methods, which need precise optical alignment and cell pressure regulations. Airborne instruments shall measure at high temporal resolution to obtain good spatial resolution of the measurement, especially in case of point source measurements. The instrument shall be robust and have little warm-up times to be ready in short times. Last but not least, the instrument setup should fulfill safety requirements for the airborne deployment.

In the following, the setup of the DLR-QCLS instrument and its modifications for the airborne deployment is described.

The DLR-Quantum Cascade Laser Spectrometer (DLR-QCLS) is based on the commercial available Dual Laser Trace Gas Monitor from Aerodyne Research Inc. (Billerica, USA; McManus et al. (2015), McManus et al. (2010)) and has been adapted and optimized for airborne deployment (Kostinek et al. (2021); Kostinek (2019)). The measurement principle is direct absorption spectroscopy using tunable lasers as described in Section 2.4.3.

Figure 4.3 depicts the main components of the DLR-QCLS instrument. The analyser itself consists of an optics and an electronics compartment. The operation of the instrument additionally requires a cooling/heating unit (SOLID STATE COOLING SYSTEMS, New York, USA), a power supply unit and a scroll pump. Further, a calibration unit is part of the DLR-QCLS rack when installed inside a research aircraft enabling in-flight calibrations.

The electronics compartment of the instrument contains an embedded computing system for the data acquisition and two thermoelectric cooling controllers (TEC), which ensure a temperature-stabilized operation of the two lasers.

Figure 4.4 shows a top-down photograph of the inside of the optics compartment. It comprises two lasers, an aluminium sample cell, a pressure controller (BRONKHORST High-Tech B.V., Ruurlo, Netherlands), a TEC-cooled detector and guiding optics (mirrors, lenses).

Sample flow

The scroll pump pulls air through the inlet (3/8" perfluoroalkoxy (PFA) tubing) and the sample cell, passing a 2 μm particle filter to avoid cell contamination. The pressure controller regulates the sample cell pressure to 50 mbar such that it is ensured to obtain a sufficient amount of molecules inside the sample cell, but at the same time reduce the spectral pressure broadening effect and thus avoid overlapping of the discrete absorption lines. The scroll pump maintains a constant flow rate of 23 slmin^{-1} to provide a continuous exchange of sample air through the sample cell (length 50 cm; volume 2.1 l). At the given sample cell volume, flow rate and sample cell pressure, the gas inside the sample cell is exchanged every 0.27 s, which defines the maximum achievable time resolution of the measurement. Herein, the DLR-QCLS data output is set at a time resolution of 0.5 s or 2 Hz.

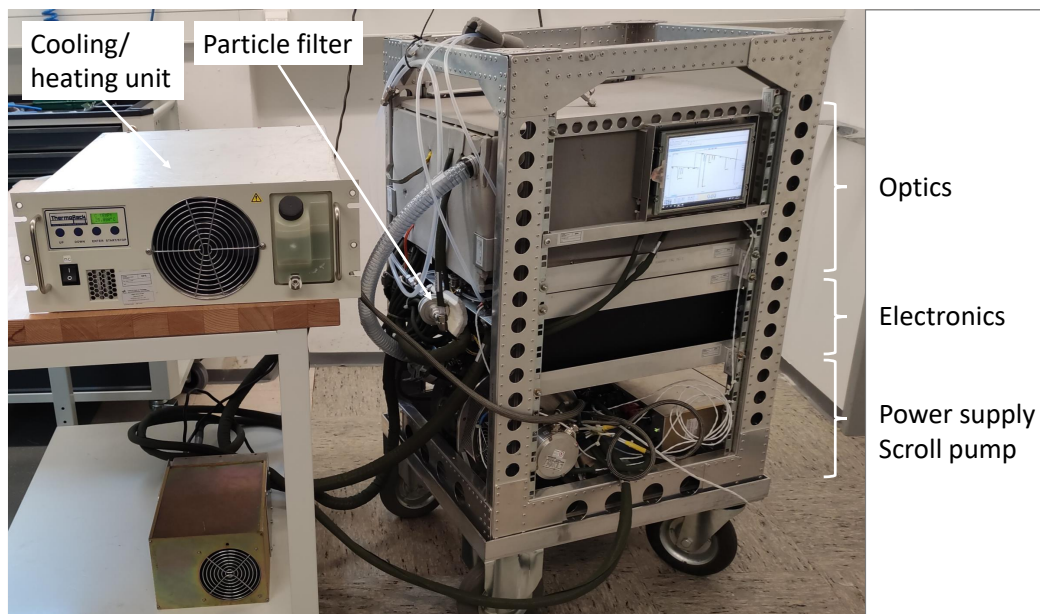


Figure 4.3: Photograph of the DLR-QCLS instrument integrated in a 19" rack consisting of the optics compartment, the electronics compartment, the power supply unit, the scroll pump and the cooling/heating unit. A particle filter is added upstream to avoid sample cell contamination.

Laser beam path

The laser beams of both lasers travel approximately 1.6 m via the guiding optics from the lasers to the sample cell (highlighted in red). After the sample cell, the laser beams are guided to the detector (orange line).

The cell contains two highly reflective astigmatic Herriott mirrors (reflectivity $R > 0.9999$) at both ends and exhibits an effective absorption path length of 204 m to minimize the signal-to-noise ratio. The two lasers are operated in the mid-infrared region at a specific center wavelength, which is defined by the operating temperatures of the lasers. The laser temperature is adjusted using Peltier elements within the laser housings. The lasers are sequentially tuned/modulated at a fixed frequency of 1.5 kHz using a linear current ramp. Retrieved spectra are then co-added to 2 Hz delivering measurements with a high temporal resolution but relatively low noise (adjustable from 1 to 10 Hz; see Kostinek (2019)). Further, an etalon can be added to the beam path to examine the laser tuning rate, which relates the emitted wavelength to the laser supply current.

The first laser (hereafter denoted as laser #1) is a continuous wave Interband Cascade laser (ICL) (see Section 2.4.3) (nanoplus GmbH, Gerbrunn, Germany) and scans over absorption lines of CH_4 , C_2H_6 and H_2O . It is operated at 4.7°C and modulated from 3344.009 nm to 3346.205 nm. Within this work, the second laser (hereafter denoted as laser #2) was exchanged to measure isotopic $^{13}\text{C}(\text{CH}_4)$. This is further described in the following Section 4.3.1.

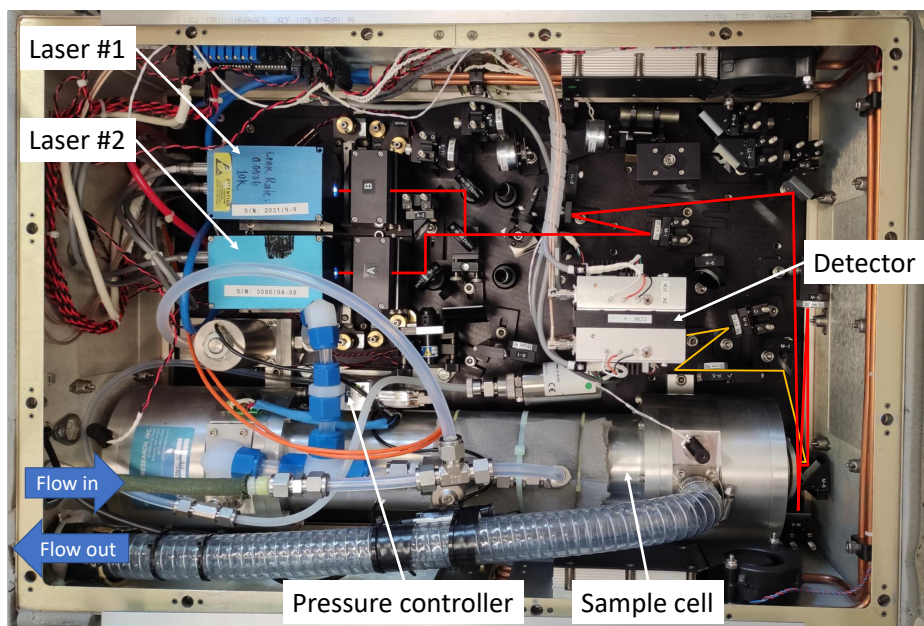


Figure 4.4: Top view of the DLR-QCLS optics compartment: The blue arrows indicate the in- and outflow of the sample air, the red lines are the laser beams travelling to the sample cell and the orange lines show the laser path from the sample cell to the detector.

4.3 Adaptations for the measurement of $\delta^{13}\text{C}(\text{CH}_4)$

4.3.1 Selection of a new laser for the measurement of $^{13}\text{CH}_4$

Measuring $^{13}\text{CH}_4$ with the DLR-QCLS first required to select the optimal wavelength range for the new laser #2, which originally aimed for the measurement of N_2O , CO_2 and CO . Three aspects have to be considered when selecting the most appropriate spectral features and hence, wavelength range to measure a specific gas of interest:

- To avoid interference, the absorption line(s) should be isolated and not overlap with absorption lines from other gases typically abundant in the atmosphere.
- The chosen absorption line(s) should be strong, since a higher signal to noise ratio results in more precise measurements.
- Even though the absorption line needs to be strong, the line must not be saturated for atmospheric mole fractions of the species to be measured.

Within this work, a calculation tool was set up to investigate absorption/transmission lines of $^{13}\text{CH}_4$ and other trace gases (e. g. $^{12}\text{CH}_4$, CO , CO_2). This tool plots synthetic spectra as it would be seen by the DLR-QCLS instrument. Lines are modelled as Voigt profiles using spectral parameters taken from the High Resolution TRansmission molecular AbsorptioN database (HITRAN) (Gordon et al. (2022)) and using the DLR-QCLS specifications (absorption path length 204 m, cell pressure 50 mbar). Along the absorption path, thermal equilibrium at ambient temperature

is assumed. Additionally, the absorption lines can be adjusted to reflect higher and lower $^{13}\text{CH}_4$ and $^{12}\text{CH}_4$ mole fractions and hence, changing the $\delta^{13}\text{C}(\text{CH}_4)$.

Figure 4.5 shows, as an example, how the different absorption/transmission lines are investigated. Figure 4.5(a) depicts the modelled synthetic transmission spectrum of $^{13}\text{CH}_4$ in the near- and mid-IR spectral region from $1000\text{--}3300\text{ cm}^{-1}$ wave numbers. $^{13}\text{CH}_4$ exhibits two bands of transitions at approximately 1370 cm^{-1} and 3160 cm^{-1} . These two bands correspond to the vibrational asymmetric bending modes and the vibrational asymmetric stretching modes, respectively (see Section 2.4). In Figure 4.5(a) a green dotted line is shown, which serves as an indication for the smallest line intensity detectable by the DLR-QCLS. It corresponds to the small CO (50 ppb) line at approximately 2250 cm^{-1} , which could have been resolved by the DLR-QCLS with the previously operated and replaced laser.

Figure 4.5(b) and (c) depict subsections of the two spectral bands in more detail. CH_4 mole fractions were set to 1800 ppb, with the atmospheric abundance of 1.11031 % for $^{13}\text{CH}_4$ given in HITRAN. $\delta^{13}\text{C}(\text{CH}_4)$ was set to the typical value present in atmospheric background, which was -47.3‰ (Sherwood et al. (2017)). Besides the modelled synthetic transmission lines of $^{13}\text{CH}_4$ and $^{12}\text{CH}_4$, transmission lines of other relevant atmospheric gases are shown at typical atmospheric mole fractions in the planetary boundary layer (H_2O (10000 ppm), C_2H_6 (3 ppb), CO_2 (400 ppm), N_2O (330 ppb)). While both bands contain distinct $^{13}\text{CH}_4$ lines, the $^{13}\text{CH}_4$ lines in (c) are stronger than in (b).

Considering the three above mentioned prerequisites, the spectral window shown in (c) at around 3058 cm^{-1} was found to be the optimal spectral window to measure $^{13}\text{CH}_4$ mole fractions with the DLR-QCLS. The $^{13}\text{CH}_4$ absorption lines overlap slightly with the $^{12}\text{CH}_4$ line, but give a clear signal allowing for precise mole fraction retrievals. Since the currently deployed detector has its lower cut-off at 2000 cm^{-1} , it is possible to further use it for both laser #1 and laser #2. The commercial QCLS system which became recently available on the market by Aerodyne Research Inc. (Billerica, USA), is based on these spectral features, as well.

A continuous wave ICL from nanoplus (nanoplus GmbH, Gerbrunn, German) has been selected as the new laser #2 for the isotopic $^{13}\text{CH}_4$ measurement. It emits light in the mid-IR at the center wavelength 3270 nm or 3058.1 cm^{-1} wave numbers. Operating the laser at a narrow spectral window increases the spectral resolution of the measurement enabling a more accurate retrieval (see Section 4.3.2). Here, the chosen spectral window for laser #2 is 3 times smaller compared to laser #1 (see Table 4.1). The laser is operated at 35.7 °C covering the spectral window from 3346.205 cm^{-1} to 3344.009 cm^{-1} ($\Delta k=0.676\text{ cm}^{-1}$). It scans over three $^{12}\text{CH}_4$ absorption lines (ro-vibrational transition in the R-branch $J = 3 \rightarrow J = 4$) and four $^{13}\text{CH}_4$ absorption lines (ro-vibrational transition in the R-branch $J = 4 \rightarrow J = 5$). The spectral line intensity of the strongest $^{13}\text{CH}_4$ absorption line is of the same magnitude as the strongest absorption line of the adjacent $^{12}\text{CH}_4$ lines. The reason for the difference in measured line strength is the low $^{13}\text{CH}_4$ atmospheric abundance of only 1.11031%.

4.3.2 Adaptation of the data retrieval

To obtain dry-air mole fractions from the raw spectral data, a retrieval software is required. There is a commercial software available by the manufacturer, but the in-house retrieval software Jfit, which was build up by Kostinek (2019), is applied herein as it allows for implementing new adaptations to the retrieval. Jfit uses spectral line parameters from the HITRAN database (Gordon et al.

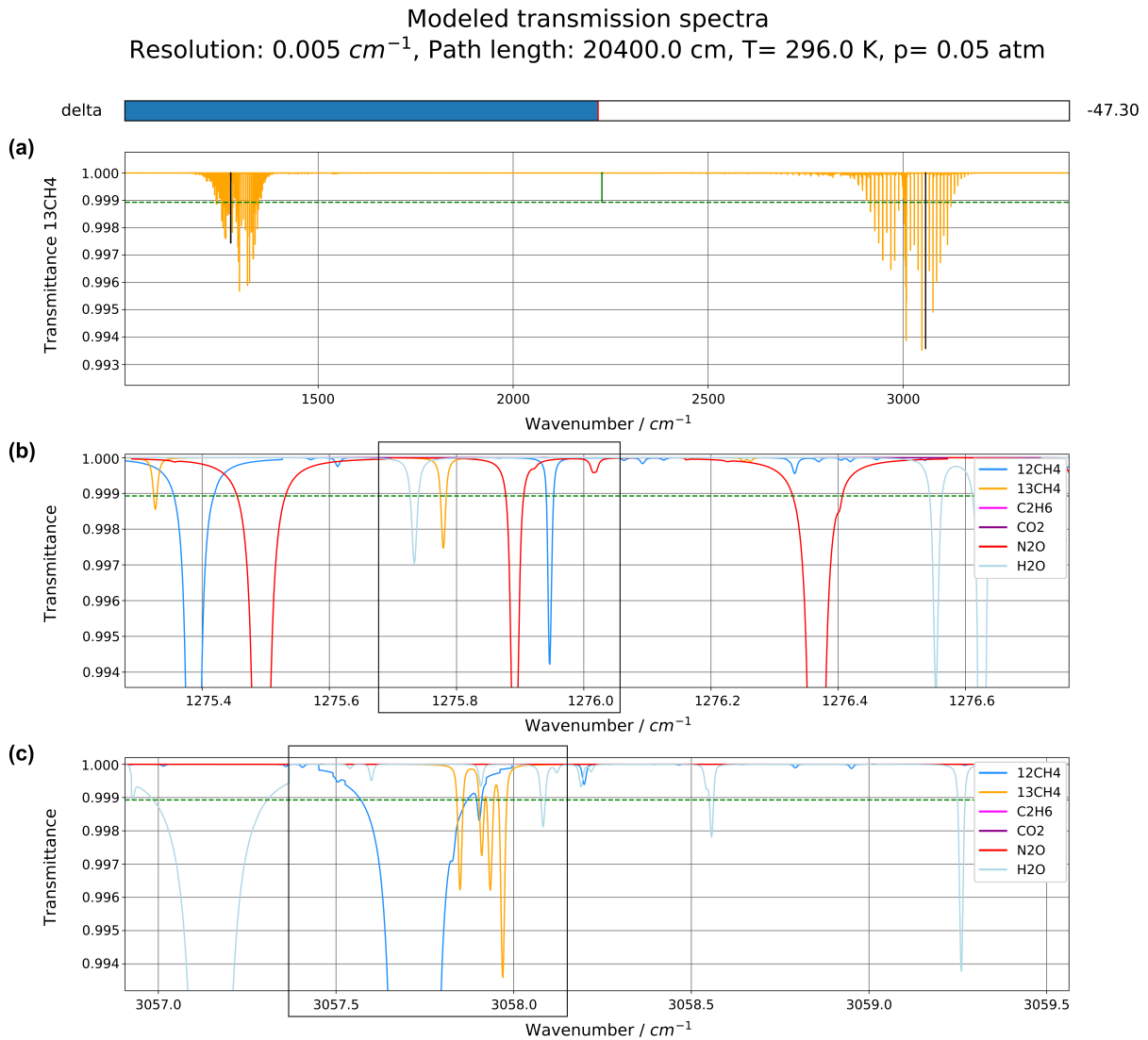


Figure 4.5: Modelled synthetic transmission spectra (a) for the $^{13}\text{CH}_4$ absorption/transmission spectrum (orange) in the near- and mid-infrared wavelength region with a threshold for the smallest line intensity detectable by the DLR-QCLS (green dotted line; corresponds to the CO line used in the previous laser). (b-c) Black $^{13}\text{CH}_4$ lines of (a) in more detail. $^{13}\text{CH}_4$ is shown in orange together with $^{12}\text{CH}_4$ (dark blue) and other relevant atmospheric gases (H_2O (light blue), C_2H_6 (pink), CO_2 (magenta), N_2O (red)).

Table 4.1: Spectral windows in wavenumbers k (Δk) and measured species of the two lasers in the new configuration of the DLR-QCLS.

Laser	spectral region	k (Δk) [cm^{-1}]	measured species
Laser #1	mid-IR	3346.205 - 3344.009 (2.196)	CH_4 ($^{12}\text{CH}_4$), C_2H_6 , H_2O
Laser #2	mid-IR	3057.530 - 3058.206 (0.676)	CH_4 ($^{12}\text{CH}_4$), $^{13}\text{CH}_4$

(2022)) to generate a synthetic spectrum. The fitting routine uses a Voigt profile to fit absorption lines and a polynomial fit for the spectral baseline. The shape of the spectral baseline, which corresponds to no molecular absorption, is determined by the laser characteristics, the detector response function and the optical properties of the guiding optics. The difference of synthetic and measured spectra is minimized with a nonlinear least-squares algorithm (Levenberg-Marquardt). As a result, mole fractions are calculated from the area under the synthetic absorption lines, i. e. between absorption line fit and baseline fit. For the retrieval process, the spectrum is subdivided into micro windows for each measured species. Additionally, shift parameters are included to allow for freely movement of individual absorption features on the spectral axis due to drifts from e. g. changing temperature. Jfit is described in detail by Kostinek (2019).

The detector exhibits 960 channels/data points in total. In Channel 1-900 the spectra of both laser #2 (Channel 1-400) and laser #1 (Channel 401-900), generated by sweeping over the respective spectral windows, are acquired. There is no incident laser light during data acquisition of Channels 901-960 for the reason to determine the offset arising from the dark current of the detector.

Within this work, for the application of the new laser #2 the spectral data from HITRAN was fed into Jfit, the micro windows were adjusted to the CH_4 ($^{12}\text{CH}_4$) and $^{13}\text{CH}_4$ absorption lines. Thereby, the size of the $^{13}\text{CH}_4$ micro window was varied to test the retrieval for all four $^{13}\text{CH}_4$ absorption lines in comparison to only using a subset of lines. Thereby, the fit was best when using all four lines within the $^{13}\text{CH}_4$ micro window. Further, the H_2O correction factors for spectral line broadening were derived empirically (see Section 4.4.3). The channel numbers for each laser were varied and chosen such to achieve a high spectral resolution for laser #2 to accurately fit the small $^{13}\text{CH}_4$ absorption lines and most suitable in combination with laser #1. Despite the fact that for laser #1 more Channels are used (Channel 401-900 versus Channel 1-400 for laser #2), the spectral resolution for laser #2 is higher, since the chosen spectral window is three times narrower compared to laser #1.

Figure 4.6 illustrates a typical raw spectrum measured in the laboratory under typical atmospheric conditions with the Voigt line fit and the baselines determined by Jfit for each micro window. On the left side in (a), laser #2 is shown, which sweeps over CH_4 ($^{12}\text{CH}_4$) and $^{13}\text{CH}_4$ absorption lines. On the right side in (a), the spectra of laser #1 is depicted with absorption lines of H_2O , CH_4 and C_2H_6 . In (b), a detailed view of the chosen micro window (channel #200-320) for the fit of the four $^{13}\text{CH}_4$ absorption lines is shown. The residual, which is the difference between fit and spectrum and indicates the goodness of the fit, is shown in black. The channel numbers can be converted to spectral units using the known laser tuning rate.

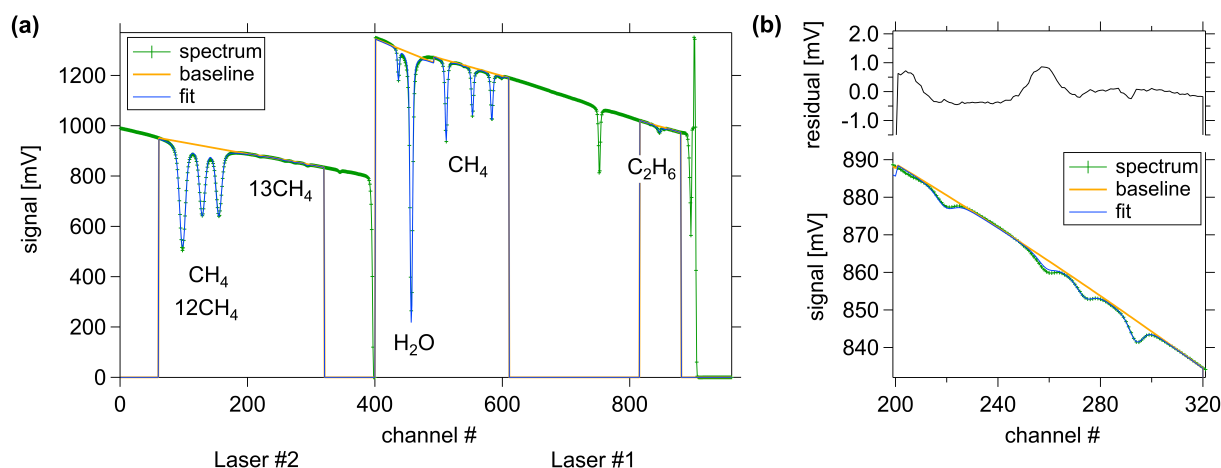


Figure 4.6: DLR-QCLS raw spectrum (green) with Voigt line fit (blue) and polynomial baseline (orange) generated by the retrieval software Jfit. (a) The spectrum of the new laser #2 is obtained in channels #1-400. It sweeps over CH_4 ($^{12}\text{CH}_4$) and $^{13}\text{CH}_4$ absorption lines. The spectrum of laser #1 is obtained in channels #401-900, where it scans over absorption lines of H_2O , CH_4 and C_2H_6 . (b) The spectrum of the new laser #2 in more detail: Micro window (channel #200-320) for the fit of the four $^{13}\text{CH}_4$ absorption lines. The residual, which is the difference between fit and spectrum, is shown in black.

4.3.3 Calibration strategy

The calibration of the instrument is essential to eliminate influences from drift effects (see Section 4.4.1) and to make the measurement traceable, meaning that they are comparable to other measurements referring to the same reference. In this section, first the origin and determination of reference values of the primary used calibration gas standards and the approach for the isotopic calibration is described. Then the laboratory setup for a calibration and its evaluation to obtain the calibration values (slope, y-intercept) is explained exemplary for the isotopic calibration.

Two calibration gas cylinders from the National Oceanic and Atmospheric Administration (NOAA) are used as primary high- and low-standards (in the following referred to as DLR-NOAA standards). The reference values of the DLR-NOAA standards for CH_4 and C_2H_6 have been measured at the World Meteorological Organization (WMO)/Global Atmosphere Watch Programme (GAW) Central Calibration Laboratories located at the NOAA Global Monitoring Division. Those values are expressed on a WMO/GAW mole fraction calibration scale to provide comparability across laboratories (WMO (2020), Hall et al. (2007), Dlugokencky et al. (2005)).

For the isotopic calibration, the DLR-NOAA standards were calibrated at the Stable Isotope Service Group (BGC-IsoLab, Jena) using the GC-IRMS technique (see Section 2.4.1). Thereby, the measured $\delta^{13}\text{C}(\text{CH}_4)$ of both cylinders were related to a primary standard (reference material NBS19/LSVEC), which is used to define the VPDB reference scale for $\delta^{13}\text{C}(\text{CH}_4)$ (Sperlich et al. (2016)). Both the total CH_4 content and the $\delta^{13}\text{C}(\text{CH}_4)$ were determined. The resulting CH_4 mole fractions compared very well with the CH_4 mole fractions stated in the NOAA certificate of the cylinders.

For the calibration of the DLR-QCLS isotopic measurement, the $^{13}\text{CH}_4$ and $^{12}\text{CH}_4$ mole fractions are directly calibrated against the DLR-NOAA reference values and then used to calculate

$\delta^{13}\text{C}(\text{CH}_4)$ following Equation 2.3. This approach of direct calibration rather than the calibration of $\delta^{13}\text{C}(\text{CH}_4)$ is recommended for direct absorption laser spectroscopy, where individual absorption lines are measured (Griffith (2018)). To this end, the $^{13}\text{CH}_4$ and $^{12}\text{CH}_4$ mole fractions of the NOAA-DLR standards are calculated from the reference values for CH_4 and $\delta^{13}\text{C}(\text{CH}_4)$. Thereby, $R_{\text{sample}} = \frac{^{13}\text{CH}_4}{^{12}\text{CH}_4}$ is derived using Equation 2.3. Assuming that CH_4 consists of $^{13}\text{CH}_4$ and $^{12}\text{CH}_4$ and neglecting other isotopologues, which make up less than 0.01% (Gordon et al. (2022)), it follows:

$$^{13}\text{CH}_4 = \frac{\text{CH}_4}{\frac{1}{R_{\text{sample}}} + 1}; \quad ^{12}\text{CH}_4 = \frac{\text{CH}_4}{R_{\text{sample}} + 1} \quad (4.4)$$

Table 4.2 summarizes all reference values of the DLR-NOAA standards.

Table 4.2: Reference values for DLR-NOAA calibration standards: CH_4 and C_2H_6 mole fractions are taken from the certificate as measured at the WMO/GAW Central Calibration Laboratories (CCL) located at the NOAA Global Monitoring Division. $^{12}\text{CH}_4$ and $^{13}\text{CH}_4$ mole fractions are calculated from $\delta^{13}\text{C}(\text{CH}_4)$ and CH_4 measured at the Stable Isotope Service Group (BGC-IsoLab, Jena).

NOAA cylinder	CH_4 [ppb]	C_2H_6 [ppb]	$\delta^{13}\text{C}(\text{CH}_4)$ [‰]	$^{12}\text{CH}_4$ [ppb] $^{13}\text{CH}_4$ [ppb]
CC720371 - high	2053.52 ± 3.9	26.56 ± 0.13	-47.153 ± 0.176	2031.9239 ± 0.1386 21.6461 ± 0.0042
CC726922 - low	1783.46 ± 3.4	1.44 ± 0.01	-47.664 ± 0.201	1764.7106 ± 0.1089 18.7894 ± 0.0041

In the following, the procedure for the calibration of the DLR-QCLS in the laboratory is explained in detail. The laboratory setup is depicted in Figure 4.7. The DLR-QCLS measures calibration gas at a flow rate of 23 sl min^{-1} , while calibration gas flows at a higher flow rate ($> 25 \text{ sl min}^{-1}$) through the PFA tubing and exits at an overflow tubing. Using an overflow prevents the inflow of and hence, mixing with ambient air. Assuming a linear behavior of the DLR-QCLS with increasing mole fractions (see Section 4.4.2), a high- and a low-standard are needed to obtain the linear calibration curve, i. e. the linear regression (slope, y-intercept) between measured mole fractions and reference mole fractions. As an example, on the right side of Figure 4.7 measured $^{13}\text{CH}_4$ and $^{12}\text{CH}_4$ mole fractions obtained from the calibration against the DLR-NOAA standards are depicted. Each cylinder was measured for 3 min. In this case, the slope of the linear regression for $^{12}\text{CH}_4$ and $^{13}\text{CH}_4$ is 0.9796 and 1.0218, respectively.

The following equation relates measured c_{meas} and true c_{true} mole fractions of species i assuming linearity:

$$c_{\text{true}} = \frac{c_{\text{meas}} - a_i}{b_i} \quad (4.5)$$

where a_i and b_i are the y-intercept and the slope of the calibration curve, respectively.

For economic reasons, so-called secondary-standards from Air Liquide (Air Liquide Deutschland GmbH, Düsseldorf) are used for laboratory tests and in-flight calibrations. Those secondary-standards are less accurate (2% compared to 0.2% for NOAA CH_4). Therefore, they are cross-

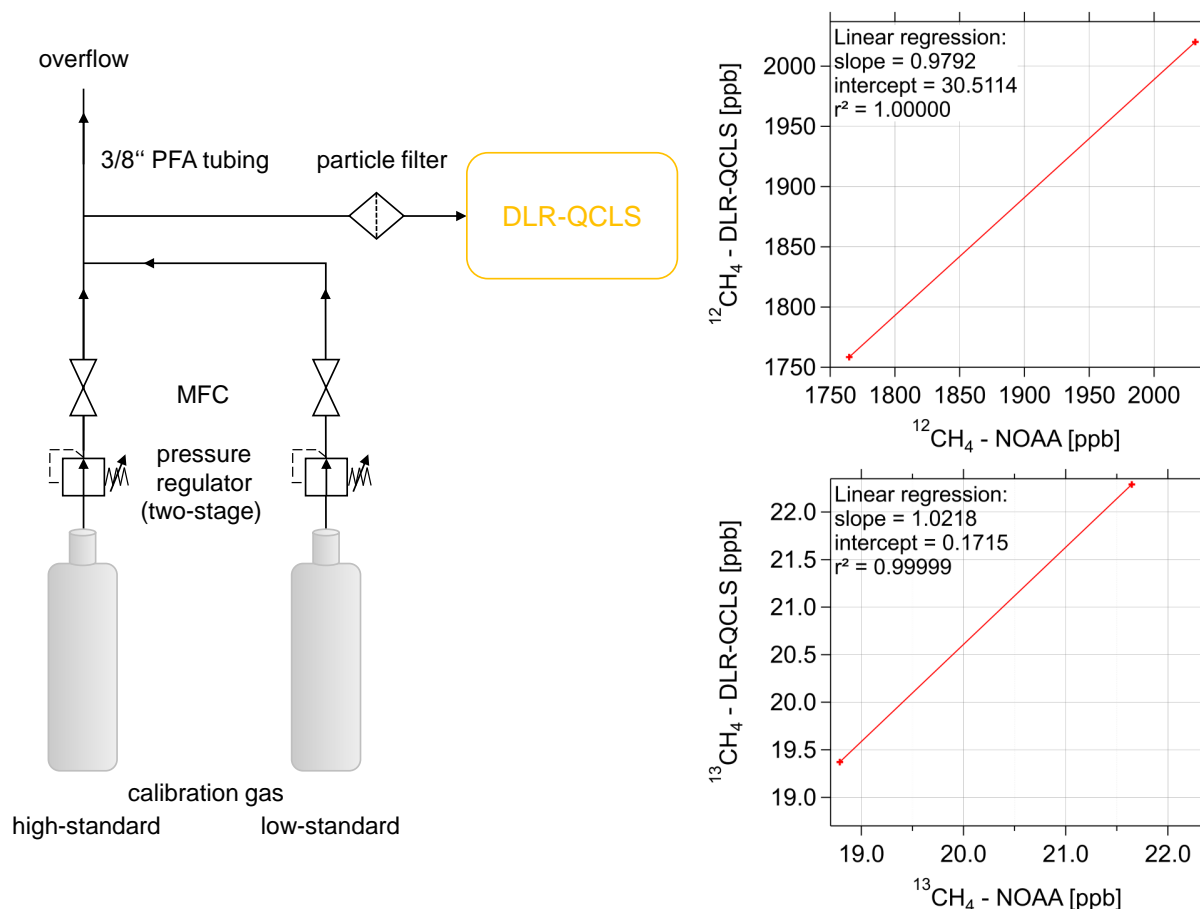


Figure 4.7: Schematic of calibration setup for the DLR-QCLS to relate measured mole fractions to known mole fractions: Calibration gas from two reference gas cylinders (high- and low-standard) is guided through 3/8" PFA tubing passing a particle filter to the DLR-QCLS. The pressure at the high pressure gas cylinders (20-150 bar) is reduced with a pressure reducer and the flow is controlled by mass flow controller (MFC). The overflow prevents the inflow of ambient air. On the right side an example for the calibration of measured $^{12}\text{CH}_4$ and $^{13}\text{CH}_4$ mole fractions by the DLR-QCLS against known mole fraction of two DLR-NOAA standards is shown. The linear regression gives the calibration values slope and intercept, which are used to relate measured and true mole fractions.

calibrated against the primary DLR-NOAA standards in the laboratory using the DLR-QCLS enabling measurements traceable to the WMO scale. To narrow down uncertainties arising from a possible drift of the DLR-QCLS, a cross-calibration starts with the measurement of the primary DLR-NOAA standards, followed by the measurement of the secondary-standards and ends with the measurement of the DLR-NOAA standards. The calibration values obtained from both calibrations against the DLR-NOAA standards are interpolated. Using the interpolated calibration values, the correction formular according to Equation 4.5 is then applied to the measured mole fractions of the secondary-standards to obtain their cross-calibrated reference values.

4.4 Laboratory characterization of the new DLR-QCLS laser configuration

The DLR-QCLS, equipped with the new $^{13}\text{CH}_4$ laser, was intensively characterised in the laboratory. This included the investigation of the stability inferred from precision and drift (Section 4.4.1), the instrument linearity (Section 4.4.2), and the water correction (Section 4.4.3). Finally, the performance of the DLR-QCLS is compared to the commercial cavity-ring-down spectrometer Picarro G-2210i by side-by-side measurements on the ground (Section 4.4.4).

4.4.1 Stability

Laser based absorption spectrometers exhibit Gaussian distributed white noise and drifts due to changing environmental conditions like temperature (Werle et al. (1993)). The noise determines the precision of the measurement and, thus, the detectability of a plume above the background (signal-to-noise ratio). Typically, the precision is given as one standard deviation σ of a time series measuring constant mole fractions. Reducing the temporal resolution by averaging the measurement improves the precision until drift effects dominate.

The stability of the instrument can be described using the Allan variance σ_A^2 (Werle et al. (1993)). It depends on the averaging time τ :

$$\sigma_A^2(\tau) = \frac{1}{M-1} \sum_{i=1}^M (A(\tau)_{i+1} - A(\tau)_i)^2 \quad (4.6)$$

$A(\tau)$ is the average mole fraction within a time interval, i. e. within the averaging time τ . M denotes the number of time intervals.

Precision, Allan variance and drift of the DLR-QCLS were determined at most stable conditions, which is the measurement of calibration gas under controlled laboratory conditions. The laboratory setup is shown in Figure 4.7, but only one gas cylinder was used. The calibration gas contains synthetic air (nitrogen + 20% oxygen) with known $\delta^{13}\text{C}(\text{CH}_4)$ and mole fractions of CH_4 (1870 ppb) and C_2H_6 (440 ppb) and for this test, was measured for 30 min.

Figure 4.8 shows the Allan variance σ_A^2 for averaging times τ up to 900 s (15 min). The Allan variance decreases with τ as long as white noise dominates. In this case the Allan variance equals the standard variance. The Allan variance however increases proportional to τ^2 , when the influence of linear drift begins to deteriorate the precision. For $\delta^{13}\text{C}(\text{CH}_4)$ the Allan variance decreases for τ up to 300 s, while for longer τ the variance deteriorates. Comparing the Allan variance for the CH_4 measurement of the two lasers shows that the measurement of laser #2 is more stable, since drift effects begin to dominate at averaging times longer than 180 s for laser #2 and at 30 s for laser #1.

Table 4.3 summarizes the precision ($1\sigma(\tau)$) for the raw 2 Hz data and for several averaging times τ . The precision of the raw 2 Hz CH_4 data, i. e. for 0.5 s time resolution, is better for laser #2 than for laser #1. For longer averaging times up to 30 s, the precision of all measured species improves. The precision of $\delta^{13}\text{C}(\text{CH}_4)$ at 0.5 s is 0.86 ‰ and for $\tau=5$ s it is 0.30 ‰. However, longer averaging times than 10 s are not favorable when measuring sharp enhancements during plume encounters from point sources, which usually last only few seconds depending on the aircraft velocity and distance to the source.

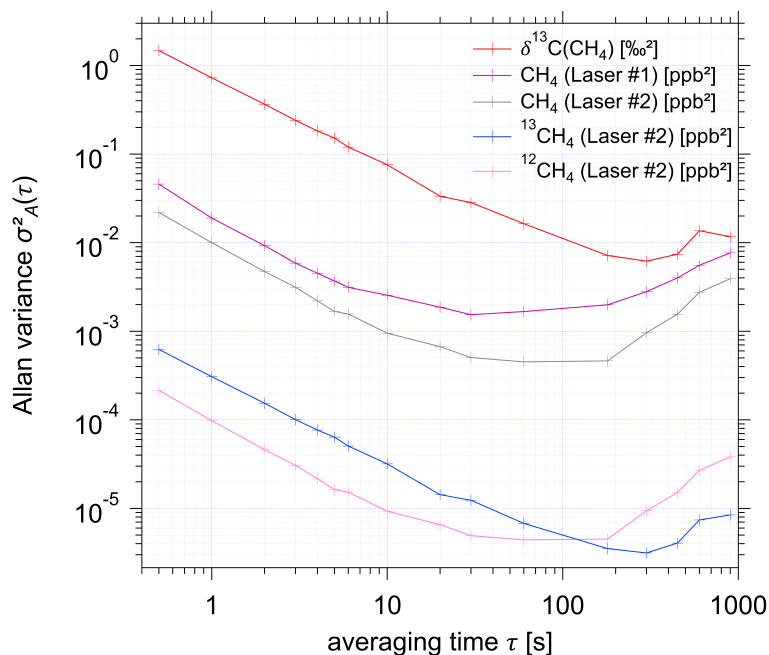


Figure 4.8: Allan variance for CH_4 (both original laser #1 and new laser #2), $^{12}\text{CH}_4$, $^{13}\text{CH}_4$ and $\delta^{13}\text{C}(\text{CH}_4)$ from a laboratory experiment measuring calibration gas, containing known mole fractions in dry synthetic air, for 30 min.

The drift over the 30 min measurement of calibration gas is also given in Table 4.3. It is determined as the difference of 30 s-average mole fractions at the beginning and at the end of the measurement. Because of drift effects, the measured mole fractions decrease for all species, in this case.

These results give a first hint that the intervals of in-flight calibrations should be selected to allow for correcting drift effects, e. g. calibration intervals of 180 s or 3 min for CH_4 of laser #2. However, it is important to note that the in-flight behaviour of instruments often is worse than under controlled laboratory conditions due to e. g. vibrations. Other aspects such as the limited amount of available calibration gas need to be considered, as well. For airborne measurements usually calibrations every 5 to 10 minutes are chosen (see Sections 5.1.2 and 5.2.3).

4.4.2 Linearity

Two-point calibrations, as described in the previous Section 4.3.3, are justified in case of linear response of the instrument to changes of the mole fractions (at least within the range of expected ambient mole fractions). To this end, the DLR-QCLS is tested upon linearity for all its measured species in the range of 0-2435 ppb for CH_4 and 0-514 ppb for C_2H_6 . Figure 4.9 displays the setup of the linearity experiment. Calibration gas of known $\delta^{13}\text{C}(\text{CH}_4)$ (-36 ‰), CH_4 (2435 ppb) and C_2H_6 (514 ppb) is diluted with synthetic air (nitrogen + 20 % oxygen) using two mass flow controllers (MFCs, Bronkhorst). The setpoints of both MFCs were adjusted to decrease and increase calibration gas and synthetic air in 7-9 steps to obtain dilution ratios ranging from 4.1-100%. As an example, the MFC for the calibration gas is adjusted to a flow of 10.7 sl min^{-1}

Table 4.3: Ground-based measured precision given as the standard deviation σ for the raw 2 Hz data ($\tau=0.5$ s) and at averaging times of $\tau=1$ s, $\tau=5$ s and $\tau=30$ s. The drift over 30 min measurement of calibration gas is determined as the difference of 30 s-average mole fractions at the beginning and at the end of the measurement.

species	CH_4 (L1) [ppb]	CH_4 (L2) [ppb]	$^{13}\text{CH}_4$ [ppb]	$^{12}\text{CH}_4$ [ppb]	$\delta^{13}\text{CH}_4$ [‰]	C_2H_6 [ppb]
precision ($1\sigma(0.5$ s))	0.17	0.12	0.018	0.114	0.86	0.21
precision ($1\sigma(1$ s))	0.13	0.09	0.013	0.089	0.60	0.20
precision ($1\sigma(5$ s))	0.10	0.06	0.006	0.061	0.30	0.17
precision ($1\sigma(30$ s))	0.09	0.06	0.003	0.055	0.16	0.14
drift (30 min)	-0.18	-0.15	-0.007	-0.15	-0.24	-0.13

and the MFC for synthetic air to 15 sl min^{-1} (total flow 25.7 sl min^{-1}). The resulting dilution of the calibration gas is 41.7%. Via PFA tubing the mixed and diluted calibration gas is guided to the DLR-QCLS, which measures at a flow rate of 23 sl min^{-1} . The excess flow (2.7 sl min^{-1}) is released using an overflow tubing to prevent the inflow of ambient air.

Figure 4.10(a-c) shows measured mole fractions of CH_4 , C_2H_6 and $^{13}\text{CH}_4$ against the mole fractions of the diluted calibration gas with linear regression lines (slope a and correlation coefficient r^2). Error bars of the diluted calibration gas mole fractions are due to the uncertainty of the MFCs, while error bars of measured species are due to instrumental noise. Measured CH_4 , C_2H_6 and $^{13}\text{CH}_4$ are linear within error bounds over the range of measured mole fractions. In Figure 4.10(d), the ratio of both absorption lines $r_{meas} = ^{13}\text{CH}_{4,meas} / ^{12}\text{CH}_{4,meas}$ is depicted against CH_4 mole fractions. r_{meas} is a measure for $\delta^{13}\text{C}(\text{CH}_4)$ of the calibration gas cylinder and should be constant, since both $^{12}\text{CH}_{4,meas}$ and $^{13}\text{CH}_{4,meas}$ are diluted equally. For ambient mole fractions, i. e. from 1400 ppb to 2500 ppb CH_4 , r_{meas} is constant. However, interestingly, below 1400 ppb, r_{meas} is not longer stable and increases. This observation can likely be attributed to fractionation effects on the MFCs and on the pressure reducers mounted at the calibration cylinders (personal communication S. Bauguitte, Cranfield University). Nevertheless, this observation does not affect ambient measurements and hence, instrument linearity is demonstrated for all measured species for ambient mole fractions.

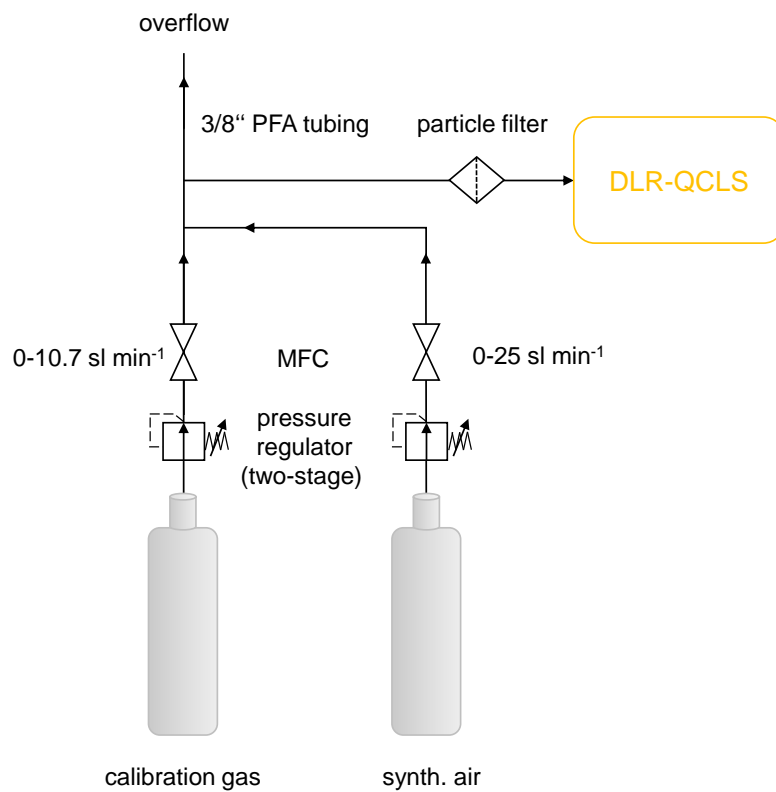


Figure 4.9: Laboratory setup for the linearity experiment: Calibration gas and synthetic air are mixed using mass flow controllers (MFCs) to generate mole fractions in the range of 0-2435 ppb for CH_4 and 0-514 ppb for C_2H_6 .

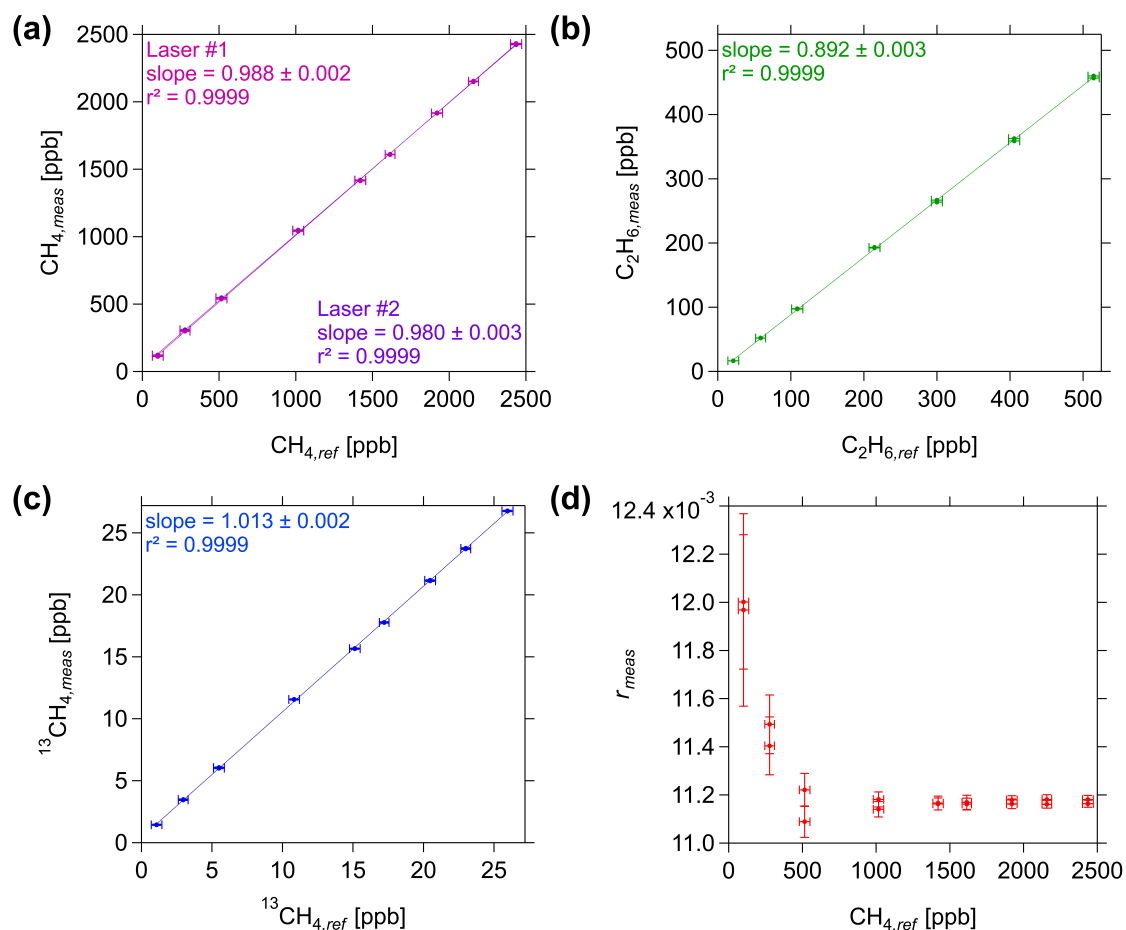


Figure 4.10: Linearity experiment for species measured by the DLR-QCLS in the range of 0-2435 ppb for CH_4 and 0-514 ppb for C_2H_6 . (a) CH_4, meas for Laser #1 (magenta) and Laser #2 (violet), (b) for $\text{C}_2\text{H}_6, \text{meas}$ (green) and (c) for $^{13}\text{CH}_4, \text{meas}$ (blue) against reference mole fractions of diluted calibration gas. (d) $r_{\text{meas}} = ^{13}\text{CH}_4, \text{meas} / ^{12}\text{CH}_4, \text{meas}$ as measure for $\delta^{13}\text{C}(\text{CH}_4)$ (red).

4.4.3 Water correction

Since the water vapor content of the atmosphere is highly variable, ranging from ppm to a few percent, and has a non-negligible influence on measured mole fractions, it is common to report mole fractions relative to dry air. Therefore, measured mole fractions are corrected according to ambient water vapor measured with the same instrument. Two effects are important for the correction: Dilution and water broadening. Due to the dilution effect, measured mole fractions in wet air appear lower compared to dry air. The dilution effect is accounted for by applying the following equation (Harazono et al. (2015)):

$$c_{dry} = \frac{c_{moist}}{1 - c_{H_2O}} \quad (4.7)$$

where c_{moist} is the measured mole fraction of a specific trace gas in wet air, c_{dry} the dry-air mole fraction and c_{H_2O} the water vapor mole fraction. For the new laser #2, the water correction due to the dilution is included in the Jfit retrieval software using Equation 4.7.

The effect of the water broadening on the mole fractions of trace gases is typically one order of magnitude smaller than the dilution effect, but still important. Elastic collisions of molecules of a certain trace gas with other molecules cause spectral pressure broadening influencing the retrieved mole fraction of the trace gas. The spectral data from the HITRAN database and used in Jfit contains pressure broadening coefficients for the mutual collision of molecules of a specific gas (self-broadening γ_{self}) and for the collision with other molecules in air (air-broadening γ_{air}). An additional pressure broadening coefficient for the collisions with H_2O molecules (water-broadening γ_{H_2O}) is included in the HITRAN equation used in Jfit to calculate the pressure-broadened half width at half maximum γ for a gas at ambient pressure p and temperature T (Gordon et al. (2022), Kostinek (2019), Kooijmans et al. (2016)):

$$\gamma(p, T) = \left(\frac{T_{ref}}{T}\right)^{n_{air}} \cdot (\gamma_{air}(p - p_{self} - p_{H_2O}) + \gamma_{self}p_{self} + \gamma_{H_2O}p_{H_2O}) \quad (4.8)$$

p_{self} and p_{H_2O} are the partial pressures of the specific gas itself and H_2O , respectively. $T_{ref}=296$ K is the reference temperature and n_{air} the coefficient of the temperature dependence of the air-broadened half width, which is available in the HITRAN database, as well.

For the new laser #2, water broadening correction factors were determined experimentally using the laboratory setup shown in Figure 4.11. Synthetic air is used as a carrier gas and streams through a water reservoir before mixing with calibration gas of known mole fractions. Both the calibration gas flow and the moist synthetic air flow are controlled by MFCs to generate typical atmospheric H_2O mole fractions in the range of 0-2.5%. The humidified mixed gas is evaporated in an evaporator mixer to prevent liquid H_2O from reaching the DLR-QCLS sample cell. This way, CH_4 mole fractions remain constant at varying absolute H_2O vapor content.

The water broadening correction factors were adjusted empirically in the in-house fitting software Jfit such that the dependency of retrieved dry-air mole fractions on H_2O mole fractions is as small as possible. Figure 4.12 shows the time series of varied H_2O vapor with retrieved CH_4 , C_2H_6 and $^{13}CH_4$ mole fractions. As an illustration, the time series of $^{13}CH_4$ is shown for different water broadening correction factors $\gamma_{H_2O} = 0, 1, 2$. For $\gamma_{H_2O} = 0$ the retrieved $^{13}CH_4$ is least variable. Table 4.4 summarizes the resultant water broadening correction factors γ_{H_2O} as multiple of γ_{air} for all retrieved species.

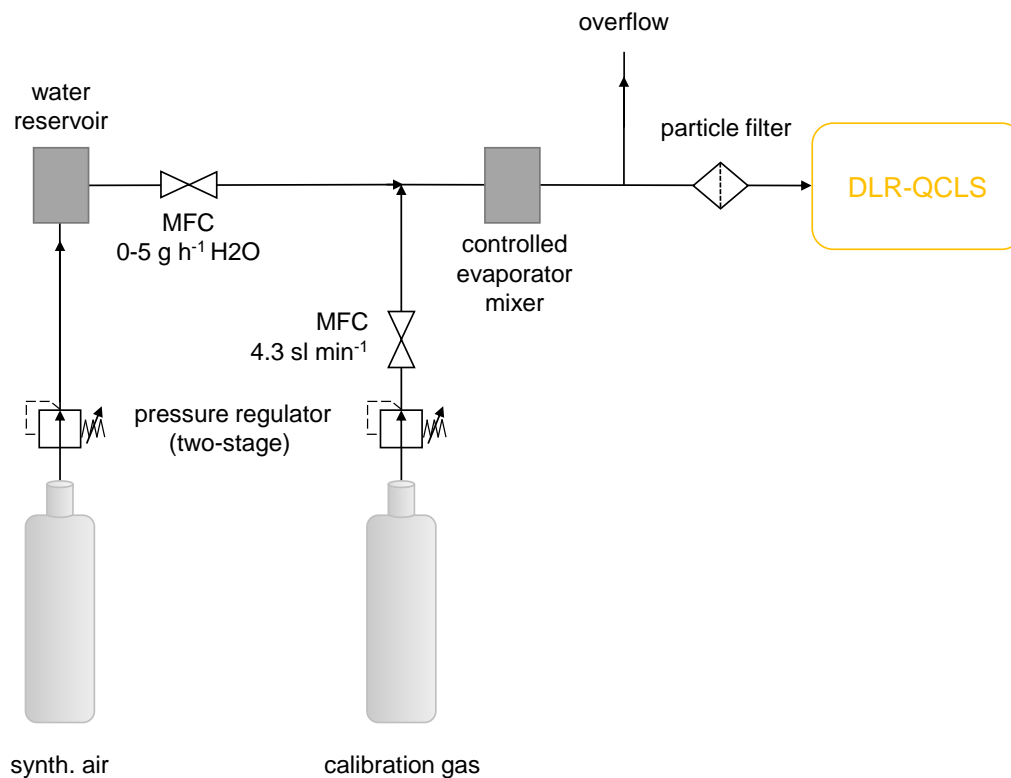


Figure 4.11: Schematic of the laboratory setup to test the water vapor dependency: Calibration gas is mixed with humidified synthetic air using a water reservoir and an evaporator mixer. The water vapor abundance is varied in typical atmospheric mole fractions in the range of 0-2.5 mole fraction-% using mass flow controllers (MFCs).

Figure 4.13 displays the correlation plots of the retrieved CH_4 (Laser #1 and Laser #2), $^{13}\text{CH}_4$ and C_2H_6 mole fractions with measured H_2O vapor when the correction for water dilution and water broadening are applied. The retrieved mole fractions still exhibit a small dependency on H_2O . For CH_4 measurements of both lasers the variation of CH_4 is 4 ppb for H_2O up to 2.5%. The $^{13}\text{CH}_4$ measured mole fractions vary by approximately 0.1 ppb (accounting for the atmospheric abundance) and the C_2H_6 measured mole fractions by 3 ppb. The observed dependency is a characteristic for the individual setup of the retrieval software Jfit and its set water broadening corrections factors and here, for the new adapted software, corrected for by applying additional polynomial fits to the retrieved mole fractions. These polynomial fits are shown in black in Figure 4.13 for all species (see Appendix for individual fit parameters). In Figure 4.12 the applied polynomial correction for $^{13}\text{CH}_4$ (with $\gamma_{\text{H}_2\text{O}} = 0$) is also shown in black.

As an example for all the water corrections applied to report dry mole fractions, Figure 4.14 depicts a time series of measured $^{12}\text{CH}_4$ and $^{13}\text{CH}_4$ (accounted for the atmospheric abundance)

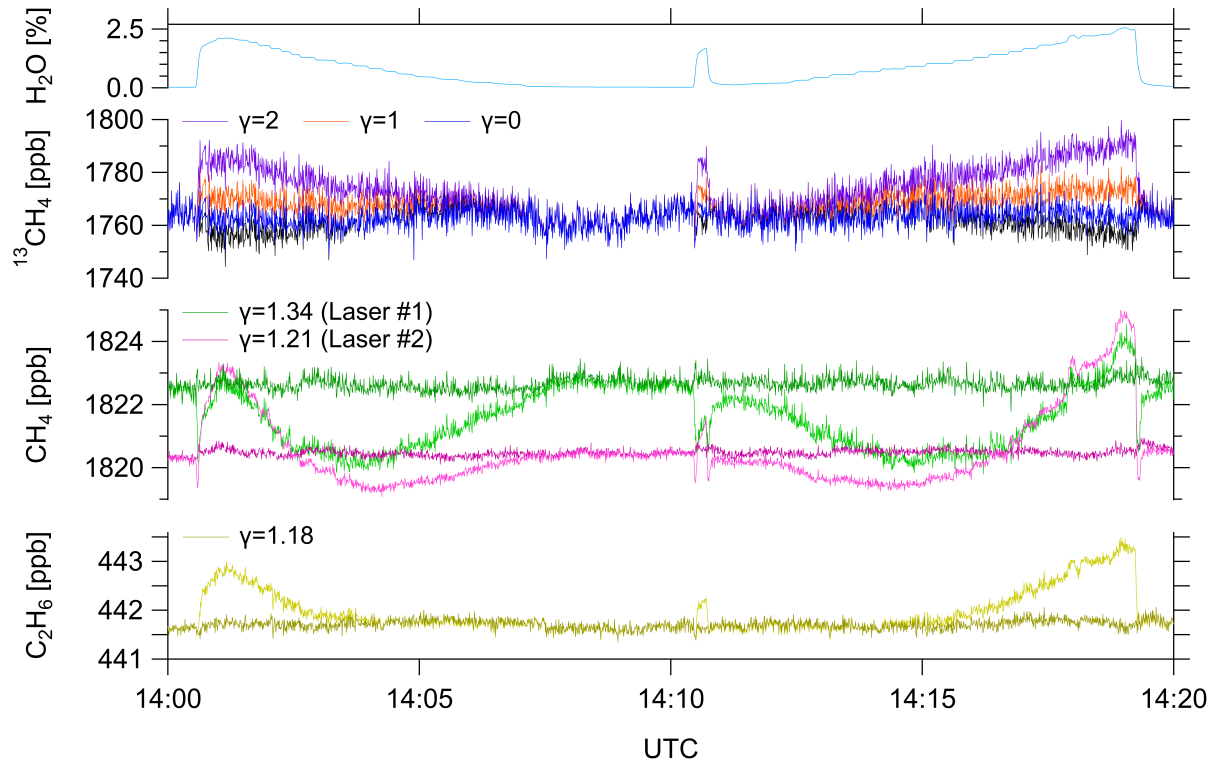


Figure 4.12: Time series of the laboratory experiment to evaluate water vapor dependency: Retrieved mole fractions of CH_4 (laser #1 (green), laser #2 (magenta)) and C_2H_6 (yellow). The time series is shown in lighter colors for when the water broadening correction is applied using the respective correction factors γ . Retrieved mole fractions of $^{13}\text{CH}_4$ are shown in black and for different water broadening correction factors $\gamma_{\text{H}_2\text{O}} = 0, 1, 2$ (blue, orange, violet).

with variable H_2O . The raw mole fractions measured in wet air, i.e. without the correction for water dilution, is shown in red. Applying the correction for water dilution and pressure broadening, higher dry mole fractions are obtained. For $c_{\text{H}_2\text{O}} = 1.5\%$, $^{12}\text{CH}_4$ and $^{13}\text{CH}_4$ are corrected by +30 ppb and +0.3 ppb, respectively. The additional polynomial correction for $^{12}\text{CH}_4$ and $^{13}\text{CH}_4$ is -0.3 ppb and +0.04 ppb, respectively (see Figure 4.13(b) and (d)).

Table 4.4: Water broadening correction factors $\gamma_{\text{H}_2\text{O}}$ as multiple of γ_{air} used in the retrieval software Jfit.

species	CH_4 (Laser #1)	CH_4 (Laser #2)	$^{13}\text{CH}_4$ (Laser #2)	C_2H_6 (Laser #1)
$\gamma_{\text{H}_2\text{O}}$	1.34	1.21	0	1.18

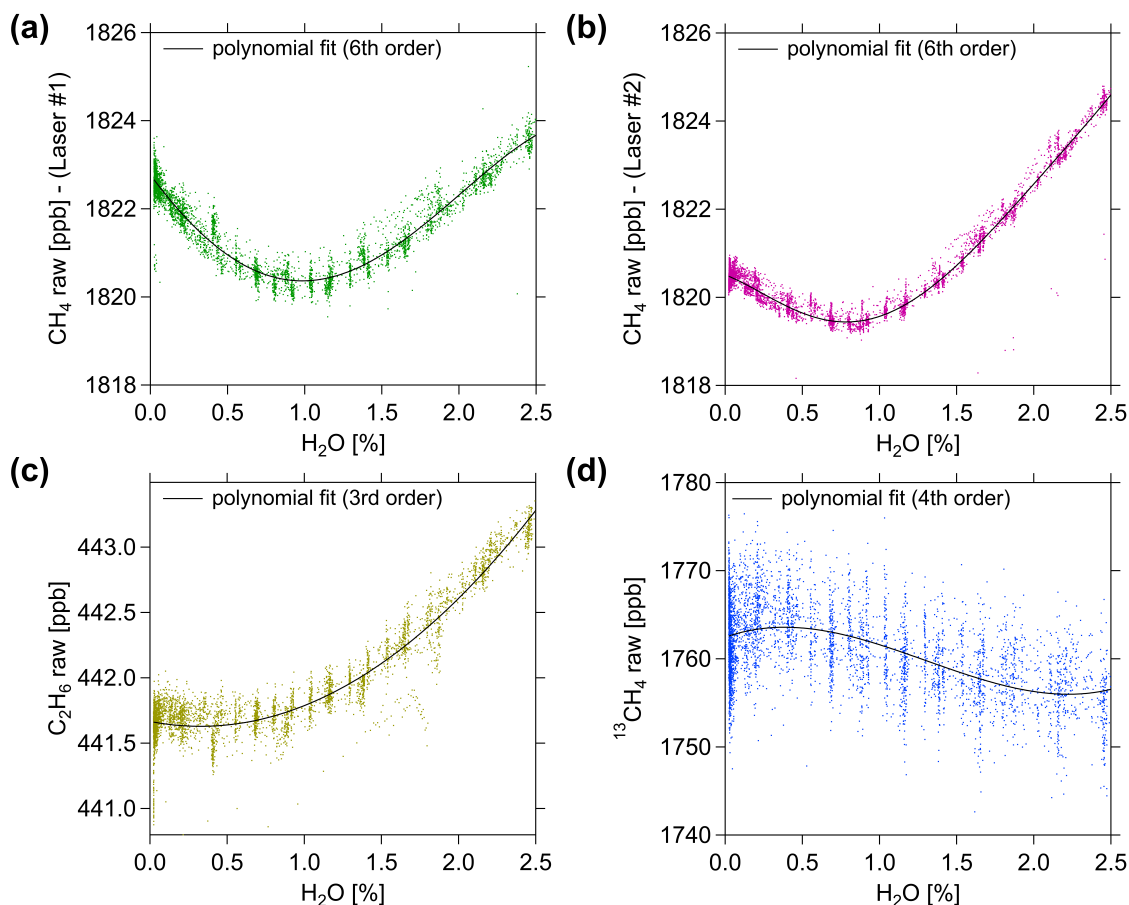


Figure 4.13: Water vapor dependency of retrieved mole fractions (corrected for water dilution and water broadening) of (a) CH₄ (laser #1), (b) CH₄ (new laser #2), (c) C₂H₆ (laser #1) and (d) ¹³CH₄ (laser #2; not accounted for atmospheric abundance) for varying H₂O vapor content in the range of 0-2.5%. For each species polynomial fits (black lines) are shown, which are used for an additional water correction of the retrieved mole fractions.

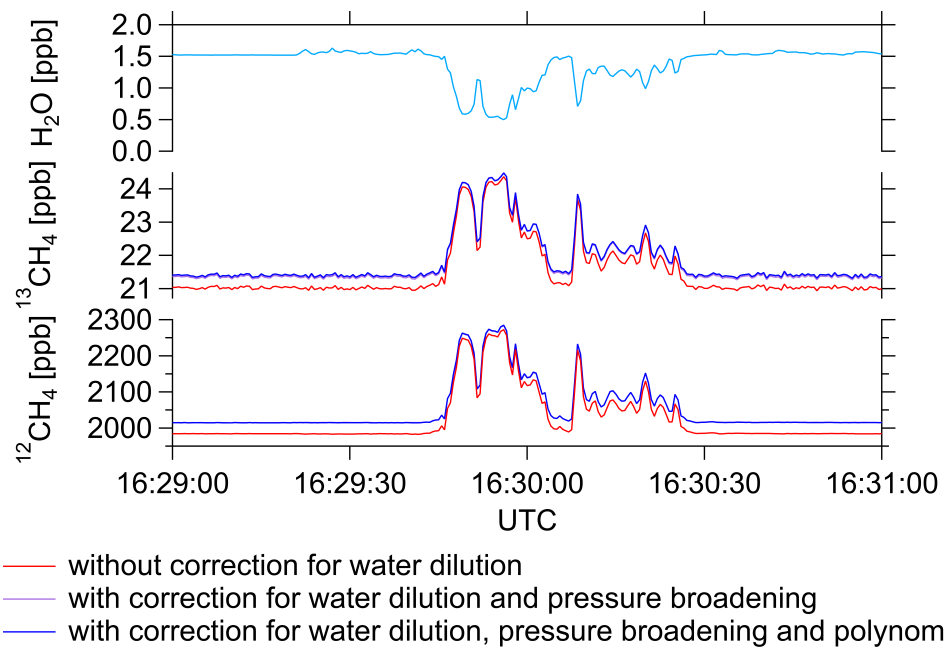


Figure 4.14: Example for applied water corrections for a time series of measured ¹²CH₄ and ¹³CH₄ (accounted for the atmospheric abundance): Retrieved mole fractions without the correction for water dilution (red), with correction for water dilution and water broadening (violet) and with the additional polynomial correction (blue).

4.4.4 Comparison with the Picarro Isotope Analyser (G2210i)

The DLR-QCLS is compared with the Picarro Isotope Analyser (G2210i) during simultaneous measurements of both calibration gas of different gas cylinders and the measurement of ambient air on the ground. The Picarro relies on the cavity ring-down measurement principle explained in Section 2.4.2. Picarro instruments are usually well designed and provide stable measurements. However, adaptations, as for example needed for airborne applications, are difficult because of limited available information, e.g. on the exact data algorithm. Also, in this specific case aiming for airborne sampling of point sources, the instrument has a too low sampling flow rate ($0.025 \text{ sl min}^{-1}$) at a slower sampling rate (1 Hz) compared to the DLR-QCLS (23 sl min^{-1} at 2 Hz).

Simultaneous measurement of gas cylinders

For the comparison, first, both instruments simultaneously measured calibration gas from the primary DLR-NOAA standards. This way, both instruments were calibrated against the same standards referring to the CH_4 reference values given in Table 4.2. For the $\delta^{13}\text{C}(\text{CH}_4)$ calibration, the DLR-QCLS uses the DLR-NOAA reference values of $^{13}\text{CH}_4$ and $^{12}\text{CH}_4$ for a direct calibration, whereas the Picarro's $\delta^{13}\text{C}(\text{CH}_4)$ measurement is calibrated against the $\delta^{13}\text{C}(\text{CH}_4)$ reference of the DLR-NOAA standards (see Section 4.3.3).

Next, both instruments simultaneously measured gas from 5 different cylinders for 2-5 min each. The mole fractions of the cylinders are determined applying Equation 4.5, i.e. calculating the true mole fractions from measured mole fractions using the calibration values obtained from the calibration against the DLR-NOAA standards (see Section 4.3.3). Figure 4.15 shows retrieved $\delta^{13}\text{C}(\text{CH}_4)$ for the 5 cylinders. The deviations of determined $\delta^{13}\text{C}(\text{CH}_4)$ between Picarro and DLR-QCLS range from 0.2‰ to 1.7‰, but agree within the precisions of both instruments (DLR-QCLS 1.89‰ (1σ , 2 Hz); Picarro Isotope Analyser: 2.43‰ (1σ , 1 Hz)).

Simultaneous measurement of ambient air

Figure 4.16 illustrates the laboratory setup of the comparison measurement of ambient air. The sampling lines of both instruments ($3/8$ " diameter for the DLR-QCLS and $1/4$ " for the Picarro Analyser) are attached to each other, similar to the airborne inlet installation, to measure ambient air at the same inlet position. Compared to the Picarro Analyser, which measures at a flow rate of $0.025 \text{ sl min}^{-1}$, the flow rate of the DLR-QCLS is three orders of magnitude higher (23 sl min^{-1}).

During the measurement, the DLR-QCLS is calibrated every 10 min for 60 s applying a two-point calibration with a secondary high- and low-standard of known mole fractions to minimize the impact of drift effects (see Section 4.3.3 and Section 4.4.1). The measured mole fractions are corrected for the measured water vapor content to obtain dry-air mole fractions (see Section 4.4.3) and calibrated applying an interpolation of calibration values between the calibration intervals. The Picarro Analyser was calibrated before the ambient measurement against the DLR-NOAA standards by using the obtained calibration values and water-corrected for CH_4 and C_2H_6 . According to Picarro, also the output of $^{13}\text{CH}_4$ and $\delta^{13}\text{C}(\text{CH}_4)$ is automatically internally corrected for water vapor.

Figure 4.17(a) shows $\delta^{13}\text{C}(\text{CH}_4)$, CH_4 and C_2H_6 of both instruments measuring the same ambient air for 40 min. Comparing the measured ambient CH_4 dry-air mole fractions, high

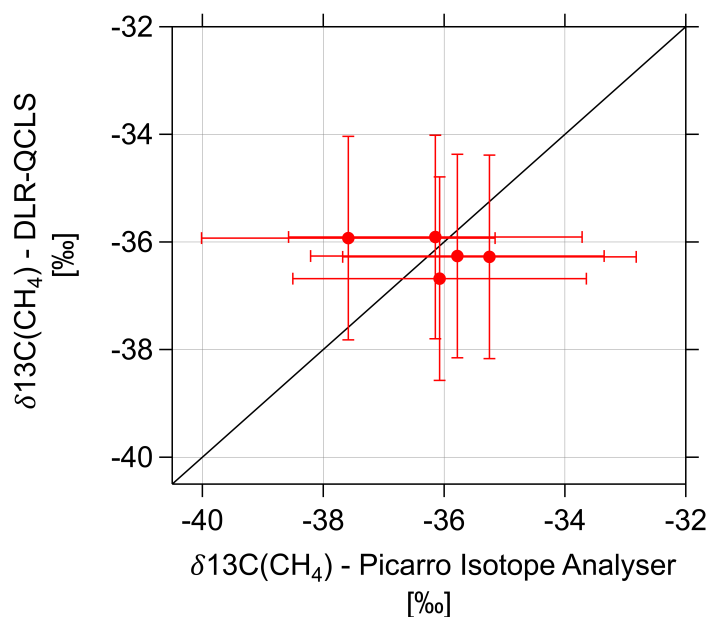


Figure 4.15: Comparison of the DLR-QCLS with the Picarro Isotope Analyser (G2210i): $\delta^{13}\text{C}(\text{CH}_4)$ of five measured gas cylinders. Uncertainty bars are the precisions of both instruments (DLR-QCLS: 1.89‰ (1σ , 2 Hz); Picarro Isotope Analyser: 2.43‰ (1σ , 1 Hz)). Both instruments were calibrated against the same primary calibration standards (DLR-NOAA high- and low-standard).

consistency is found for both DLR-QCLS lasers with the Picarro Isotope Analyser. The precision, determined as the standard deviation for the 10 min time interval, is 0.18 ppb (2 Hz, 1σ) for the DLR-QCLS CH_4 measurement (see Section 4.4.1) and, hence, better than the Picarro with a precision of 0.43 ppb (1 Hz, 1σ). The precision of DLR-QCLS measured ambient $\delta^{13}\text{C}(\text{CH}_4)$ is 1.89‰ and smaller, i. e. better than the precision of the Picarro measurement (2.43‰). Ambient $\delta^{13}\text{C}(\text{CH}_4)_{amb}$ measured by the DLR-QCLS follows the same trend as the Picarro measurement. The average DLR-QCLS $\delta^{13}\text{C}(\text{CH}_4)_{amb}$ is slightly lower ($\sim 2\text{‰}$) than for the Picarro Analyser, but within combined precisions of both instruments. The C_2H_6 mole fractions measured with the DLR-QCLS are more reasonable than the Picarro measurement, which shows negative values. The precision for the DLR-QCLS measured C_2H_6 (0.07 ppb) is smaller compared to the Picarro (2.60 ppb).

In addition to the ambient air measurement, CH_4 plumes were simulated by the release of calibration gas of known CH_4 , C_2H_6 and $\delta^{13}\text{C}(\text{CH}_4)$ in the vicinity of both instrument inlets. At 16:22:50 UTC gas from cylinder #D5AWYW0 (Figure 4.17(b)) and at 16:30 UTC gas from cylinder #D2CA44L (Figure 4.17(c)) was released. Since the sample flow rates of both instruments are very different with the DLR-QCLS having a 1000 times higher flow rate compared to the Picarro, the plume is detected virtually immediately by the DLR-QCLS, while the delay time for the Picarro is about 125 s. For better illustration of the measured peaks, this was accounted for in Figure 4.17. Due to its lower sample flow rate, the Picarro detects smaller absolute peak heights with the structure of the plume getting smeared out. Thus, fast measurements at high flow rates as for the DLR-QCLS are beneficial for the detection of narrow-width peaks, which is especially

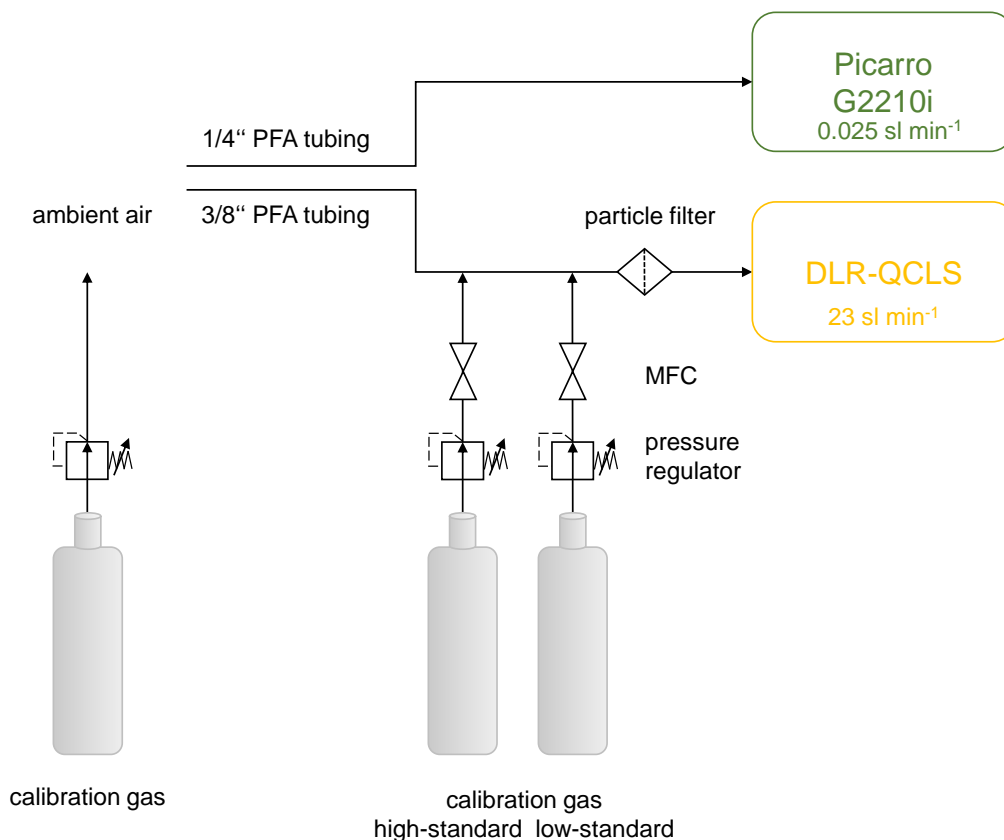


Figure 4.16: Comparison of the DLR-QCLS (yellow) with the Picarro Analyser G2210i (green) by contemporaneous measurement of ambient air. The DLR-QCLS is continuously calibrated with two calibration gases (high- and low-secondary standards).

the case for airborne measurements downwind of point sources. However, the integrated mole fractions along the plume, which are required to derive e. g. emission fluxes, should be equal.

For the plume in (b) a negative CH_4 and $\delta^{13}\text{C}(\text{CH}_4)$ signal is expected, because CH_4 and $\delta^{13}\text{C}(\text{CH}_4)_{sc}$ of the used cylinder ($\text{CH}_4 \sim 1880$ ppb; $\delta^{13}\text{C}(\text{CH}_4)_{sc} \sim -58\text{‰}$) are lower than the ambient background (see Section 4.1). Indeed, both instruments detect CH_4 signals lower than the ambient background CH_4 mole fractions (DLR-QCLS: -36 ppb; Picarro Isotope Analyser: -12 ppb). However, in contrast to the Picarro Isotope Analyser, only the DLR-QCLS measures $\delta^{13}\text{C}(\text{CH}_4)$ being decreased by -2.4‰. The precision of the Picarro $\delta^{13}\text{C}(\text{CH}_4)$ measurement is not sufficient to detect a signal.

Since the CH_4 content and the source signature of the cylinder used in (c) ($\text{CH}_4 \sim 2508$ ppb; $\delta^{13}\text{C}(\text{CH}_4)_{sc} \sim -36\text{‰}$) are higher than the ambient background, a positive CH_4 and $\delta^{13}\text{C}(\text{CH}_4)$ signal is expected. Indeed, both instruments detect a CH_4 enhancement higher than the ambient background CH_4 mole fractions (DLR-QCLS: +240 ppb; Picarro Isotope Analyser: +56 ppb). For $\delta^{13}\text{C}(\text{CH}_4)$, only the DLR-QCLS measures an enhancement of +7.4‰. Again, the precision

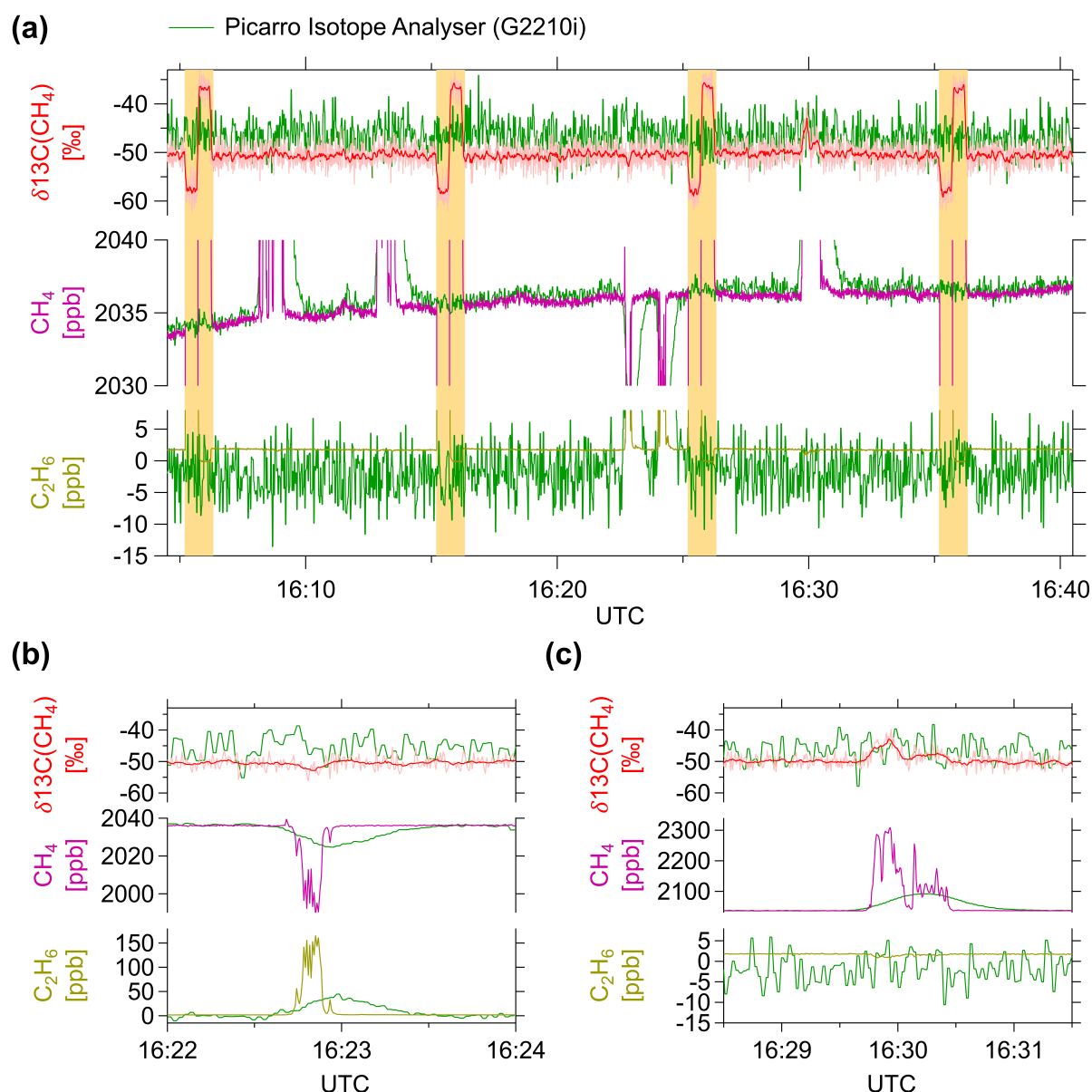


Figure 4.17: Laboratory comparison of the DLR-QCLS with the Picarro Analyser G2210i: (a) Ambient air is measured by both instruments for 40 min. Calibrated dry-air CH_4 (laser #2) is shown in magenta, $\delta^{13}\text{C}(\text{CH}_4)$ in light red with a 6 s-average in dark red, and C_2H_6 in dark yellow. Calibration intervals of the DLR-QCLS every 10 min for 60 s (30 s low- and high-secondary standard, respectively) are highlighted in orange. Picarro data for $\delta^{13}\text{C}(\text{CH}_4)$, CH_4 and C_2H_6 is shown in green. Detailed view of laboratory plumes measured at (b) 16:22:50 UTC (cylinder #D5AWYW0) and (c) 16:30 UTC (cylinder #D2CA44L).

of the Picarro $\delta^{13}\text{C}(\text{CH}_4)$ measurement is probably not sufficient to detect the $\delta^{13}\text{C}(\text{CH}_4)$ signal.

Thus, the detected signals in $\delta^{13}\text{C}(\text{CH}_4)$ are, as expected, negative in (b) and positive in (c) due to the different cylinder source signatures. However, comparing the DLR-QCLS measured

$\delta^{13}\text{C}(\text{CH}_4)$ signals with expected signals, which can be calculated from the measured CH_4 enhancement and the background ($c_{\text{amb}} \sim 2036$ ppb and $\delta^{13}\text{C}(\text{CH}_4)_{\text{bcg}} \sim -50.3\text{‰}$) (see Section 4.1), the measured signals are too high: For the plume in (b) a signal of only -0.14‰ and in (c) of $+1.5\text{‰}$ is expected.

To derive the cylinder source signature from the measured $\delta^{13}\text{C}(\text{CH}_4)$, the plumes are analysed using the Keeling plot method (see Section 4.1). Figure 4.18(a) displays the plume from 4.17(c) in more detail for both $\delta^{13}\text{C}(\text{CH}_4)_{\text{meas}}$ and $^{13}\text{CH}_{4\text{meas}}$. Figure 4.18(b) shows the corresponding Keeling plot with the linear regression in red. The derived source signature from the y-intercept ($+8.15\text{‰}$) is larger than the signature of the cylinder (-35.9‰), which is a consequence from the overestimation in the $\delta^{13}\text{C}(\text{CH}_4)_{\text{meas}}$ signal. The mismatch might be due to a linearity problem of the $^{13}\text{CH}_4$ measurement, albeit linearity was successfully verified in the range of atmospheric mole fractions (see Section 4.4.2). Another reason might be the composition of the used calibration gas, which is a mixture of CH_4 with synthetic air (nitrogen + 20 % oxygen) instead of ambient air. The impact of the gas matrix was found to influence measured $\delta^{13}\text{C}(\text{CH}_4)$, predominantly depending on the O_2 content and especially for high CH_4 mole fractions (Harris et al. (2020)).

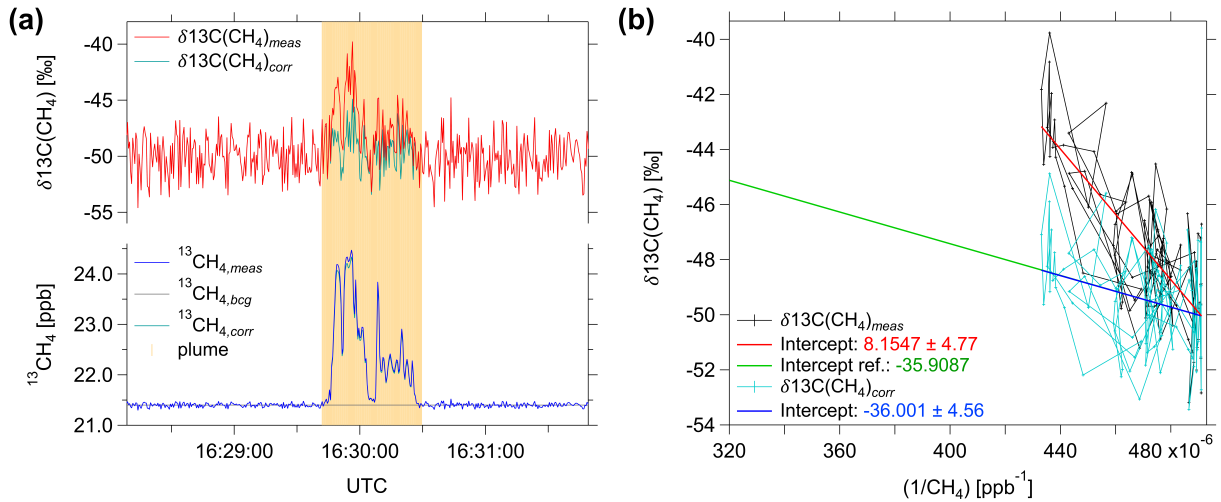


Figure 4.18: Correction of $^{13}\text{CH}_{4\text{meas}}$ and $\delta^{13}\text{C}(\text{CH}_4)_{\text{meas}}$ for the expected source signature: (a) time series as in Figure 4.17(c) showing the plume (highlighted in orange) in $^{13}\text{CH}_4$ (blue) and $\delta^{13}\text{C}(\text{CH}_4)$ (red) at 16:30 UTC. Within the plume, $^{13}\text{CH}_4$ is corrected by downscaling with the factor 0.9562 resulting in a lower $\delta^{13}\text{C}(\text{CH}_4)$ signal (light blue) in order to match the cylinder source signature -36‰ . (b) Keeling-plot, i. e. $\delta^{13}\text{C}(\text{CH}_4)$ against $(1/\text{CH}_4)$, for uncorrected $\delta^{13}\text{C}(\text{CH}_4)_{\text{meas}}$ (black) and corrected $\delta^{13}\text{C}(\text{CH}_4)_{\text{corr}}$ (light blue). The respective linear regressions are shown in red (uncorrected) and dark blue (corrected).

To match the linear regression of the Keeling plot (red line) with the expected linear regression (green line), $^{13}\text{C}(\text{CH}_4)_{\text{meas}}$ is downscaled within the plume by the factor 0.9562 resulting in a lower $\delta^{13}\text{C}(\text{CH}_4)$ signal (light blue in (a) and (b)). The downscaling factor was chosen such that the intercept of the corrected linear regression (blue line in (b)) is closest to the expected intercept corresponding to the $\delta^{13}\text{C}(\text{CH}_4)_{\text{sc}}$ of the cylinder. However, due to logistic and time constraints, this correction factor is the result of only one specific laboratory experiment, and therefore may be not representative. More measurements are needed to study the representativity of this correction

factor and the correction approach in general. Its application is tested for airborne conditions in the following Chapter 5.

4.5 Summary Chapter 4

This section summarizes the laboratory performance of the DLR-QCLS with respect to the requirements defined in Section 4.1.

As a result from the laboratory measurements, the achievable precision of the $\delta^{13}\text{C}(\text{CH}_4)$ is smaller and thus better than for other commercially available instruments (Picarro Isotope Analyser (G2210i); see Section 4.4.4). Figure 4.19 is similar to Figure 4.1 (from Section 4.1), but extended by the best achievable laboratory precision of the DLR-QCLS ($\delta^{13}\text{C}(\text{CH}_4)_{prec}=0.86\text{‰}$) as gray shaded area. Plumes can be measured, when $\delta^{13}\text{C}(\text{CH}_4)_{meas}$ signals exceed the ambient background by at least $\delta^{13}\text{C}(\text{CH}_4)_{prec}$. In principle, signals in $\delta^{13}\text{C}(\text{CH}_4)_{meas}$ are detectable for all source types, provided that CH_4 enhancements Δc_{meas} are high enough. For example, a plume of thermogenic origin, e. g. a natural gas leak, with a source signature of -40‰ can be isotopically detected, if Δc_{meas} is larger than 250 ppb. In contrast, a biogenic CH_4 plume with a source signature of -60‰ and $\Delta c_{meas}=50$ ppb can not be resolved by the DLR-QCLS $\delta^{13}\text{C}(\text{CH}_4)$ measurement.

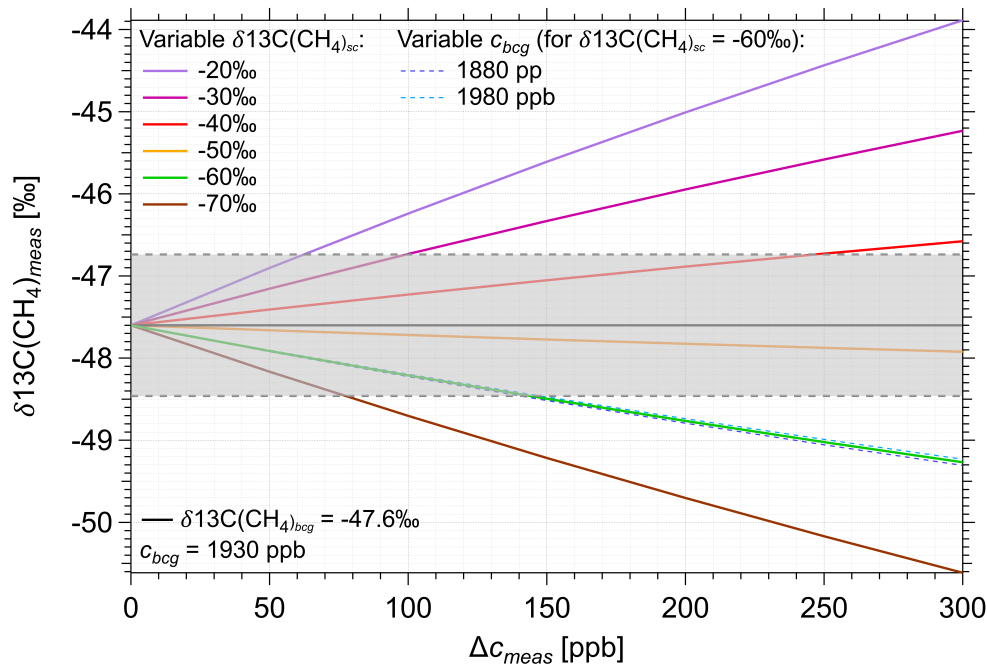


Figure 4.19: As Figure 4.1, but with the DLR-QCLS laboratory precision shown in gray. Measured $\delta^{13}\text{C}(\text{CH}_4)_{meas}$ signals of plumes can be resolved, when deviating from the atmospheric background $\delta^{13}\text{C}(\text{CH}_4)_{amb} = -47.6\text{‰}$ (black line) by at least the precision 0.86‰ .

The precision can be further improved by averaging up to 300 s (see Section 4.4.1). However, averaging is not desirable for the case studies presented herein, since high-resolution measurements

are needed for the detection of small-scale, sharp enhancements from point source emissions, which usually only last a few seconds during airborne sampling. A high time resolution is also beneficial for accurately determining source signatures with the Keeling-plot method (see Section 4.1).

An ambient air measurement in comparison with the Picarro Isotope Analyser (G2210i) on the ground, shows that CH_4 measurements agree very well within the combined laboratory precisions of both instruments (DLR-QCLS: 1.89‰; Picarro Isotope Analyser: 2.43‰). In contrast to the Picarro, CH_4 plumes of gas cylinders with different source signatures ($\sim -36\text{‰}$ and $\sim -58\text{‰}$) could be detected by the DLR-QCLS due to its better precision. The signs of the $\delta^{13}\text{C}(\text{CH}_4)$ signals corresponded with the expected signals of the cylinders due to their respective source signatures. However, calculating the cylinders source signatures from the DLR-QCLS measurements with the Keeling-plot method (see Section 4.1), did not yield the correct source signatures, but were overestimated. To resolve the mismatch, an empirical correction factor was derived to downscale the $^{13}\text{CH}_4$ mole fractions, and such the $\delta^{13}\text{C}(\text{CH}_4)$ within the plume. Its application is tested for airborne conditions in the following Chapter 5.

Chapter 5

Instrument deployment during MAGIC and MTGA

The DLR-QCLS with its new laser configuration was originally planned to be deployed for the first time during the "METHANE-To-Go Africa" (MTGA) campaign onboard the DLR Falcon. The objective of the Methane-To-Go campaign series is to study thermogenic fossil fuel emissions, hence, strong point source emitters. MTGA was envisaged to study emissions off the coast of Gabon and Angola, and originally was planned for summer 2020. A delay of this logistically very complex campaign until summer 2022 led to the opportunity to test the new setup first on another DLR aircraft, the DLR Cessna Grand Caravan. The "Monitoring of Atmospheric composition and Greenhouse gases through multi-Instruments Campaign" (MAGIC) was conducted out of Kiruna, Sweden, in August 2021 with the objective to study biogenic wetland emissions. It was expected that the airborne measurement of spatially extensive emission sources such as wetlands is much more challenging due to smaller signals from these kind of diffuse sources. However, MAGIC provided the opportunity to investigate the airborne performance of the DLR-QCLS and to derive lessons learned for improvements to be implemented for the later MTGA deployment.

The extensive CH₄ measurement data set gained with the DLR-QCLS during MTGA has been used to derive emission estimates of 30 individual oil and gas installations and 12 groups of installations off the coasts of Angola and Gabon, using similar mass balance methods as described in Chapter 3. The emission rates are in the same range as for the southern North Sea, with 5 installations showing exceptionally large emission rates between 1 and 10 t h⁻¹ similar to the one super-emitter found in the southern North Sea. The analysis confirms the findings discussed in Chapter 3 for the southern North Sea data set, which is the non-linear behavior between CH₄ emissions and production rates. As a consequence, the use of facility age or maintenance state rather than production volume as a proxy is suggested, in order to improve bottom-up reporting of emissions and to incent better maintenance by operators. These results will be published by Fiehn and Pühl et al. by end of 2024 ("Angolan offshore oil and gas methane emissions below inventory estimates", to be submitted to Atmos. Chem. Phys., see Appendix C).

This thesis focuses on the DLR-QCLS instrument performance during MAGIC and MTGA and especially investigates its suitability for high-resolution measurements of the tracers $\delta^{13}\text{C}(\text{CH}_4)$ and C₂H₆. As described in Chapter 4, the airborne deployment of measurement instruments poses several challenges due to limitations in space and weight and changes in ambient water vapor, pressure and temperature. In this chapter, first, the general information about the MAGIC

campaign, the campaign objectives, airborne payload and flight tracks are given (Section 5.1). Furthermore, an instrument comparison with flasks (GC-IRMS) is shown for one flight. Section 5.2 presents the MTGA objectives, airborne payload and flight patterns and shows first analysis of isotopic source signatures. The overall instrument performance including the in-flight calibration strategy is evaluated for both campaigns in the respective sections.

5.1 MAGIC campaign

5.1.1 MAGIC objectives, airborne payload and flight pattern

The MAGIC campaign took place in Kiruna, Sweden, in August 2021. Twelve flights with the DLR Cessna research aircraft were conducted within two weeks from 14th to 27th August. The objective of the multi-instruments campaign was to study biogenic CH₄ emissions from wetlands, lakes and peatlands in Northern Sweden and Finland using a combination of aircraft-borne, balloon-borne and ground-based measurement approaches (MAGIC Initiative). Wetlands are the largest natural CH₄ source (Saunois et al. (2020)) and their contribution to the recent growth in global CH₄ and the simultaneous decline in $\delta^{13}\text{C}(\text{CH}_4)$ is subject of investigation. The measurement of natural biogenic CH₄ sources from northern latitudes is especially important to reveal potentially growing emissions due to global warming as a climate feedback-process.

Figure 5.1(a) depicts a map showing the flight tracks of the 12 research flights along with a photograph of one of the target regions taken during a research flight. Flight pattern were planned based on the meteorology and the gridded CH₄ emission estimates from the biogeochemical model JSBACH-HIMMELI for August 2020 (color-coded underlying grid in Figure 5.1(a) left-hand side) (cooperation with T. Markkanen and M. Raivonen from Finish Meteorological Institute). A photograph of the DLR Cessna and the DLR-QCLS inside the cabin is depicted in Figure 5.1(b). The rear-facing inlet (PFA tubing) was installed in the dummy pod under the right wing of the DLR Cessna going through the wing into the cabin where the instruments are mounted in aluminium racks. The rear-facing inlet prevents the entrainment of large particles, liquid water droplets and ice, which would affect the instruments performances. Table 5.1 lists all instruments deployed. Besides the DLR-QCLS for the measurement of CH₄, C₂H₆ and $\delta^{13}\text{C}(\text{CH}_4)$, the DLR-Cessna was equipped with a Picarro cavity ring-down instrument (see Section 2.4.2) to measure CH₄ and CO₂. Additionally, the Jena Air Sampler (JAS) was deployed for the precise measurement of $\delta^{13}\text{C}(\text{CH}_4)$ by collecting a limited amount of air samples (flasks), which were analysed in the laboratory with the GC-IRMS technique afterwards (see Section 2.4.1). The MetPod, installed under the left wing of the aircraft, measured meteorological parameters such as 3D-wind, temperature and pressure. The DLR Cessna research aircraft is an agile, unpressurized single-engine turboprop Cessna C-208B Grand Caravan allowing for low-speed (approximately 70 ms⁻¹) measurements and hence detailed scanning of regional emissions. With the payload, flights of 2-3 h duration were feasible. Flights predominantly took place in the afternoon when the boundary layer is well mixed, and at altitudes up to 3 km.

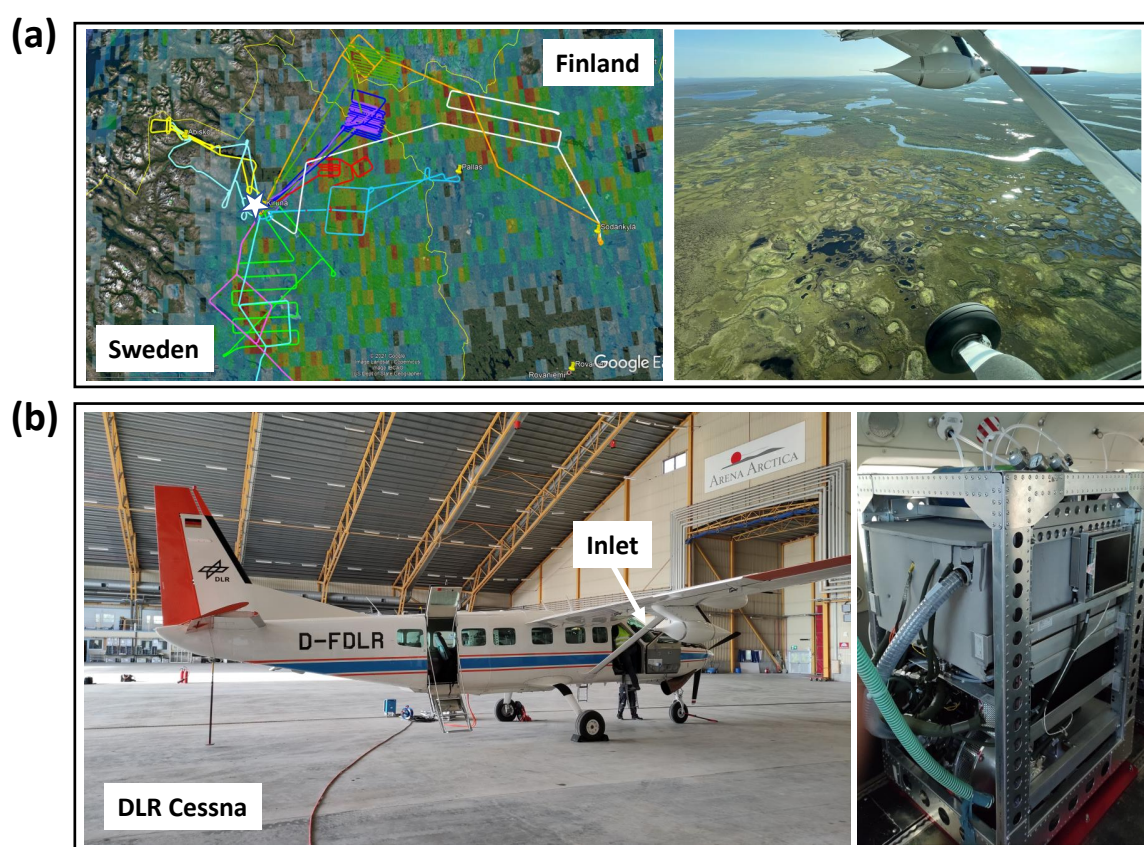


Figure 5.1: (a) Flight pattern of the 12 MAGIC flights in Northern Sweden and Finland. Flight patterns were planned based on gridded CH₄ emission estimates from the biogeochemical model JSBACH-HIMMELI for August 2020 (color-coded underlying grid). A photograph on the right shows the wetland area as seen from the DLR research aircraft Cessna. (b) Photograph of the DLR Cessna research aircraft on the left side and the DLR-QCLS installed in a rack inside the cabin on the right side. The rear-facing inlet was installed under the right wing of the DLR Cessna.

5.1.2 DLR-QCLS performance during MAGIC

The measurement period was governed by rainy weather, which mainly impacted the remote sensing measurements and hence, the overall campaign measurement strategy. Since in situ measurements are generally not affected by clouds and less affected by rain, in total twelve research flights were conducted whenever possible in coordination with other measurements during the campaign period. The DLR-QCLS successfully measured during all 12 flights of MAGIC.

Table 5.1: Payload of the DLR Cessna during the MAGIC field campaign.

MAGIC		
instrument	species	technique
DLR-QCLS	CH ₄ , C ₂ H ₆ , $\delta^{13}\text{C}(\text{CH}_4)$, H ₂ O	direct laser absorption spectroscopy
Picarro G1301m	CH ₄ , CO ₂ , H ₂ O	cavity ring-down spectroscopy
Jena Air Sampler	$\delta^{13}\text{C}(\text{CH}_4)$	flasks and GC-IRMS (laboratory)
MetPod	3D-wind, T, p, H ₂ O	different commercial and in-house built sensors (Mallaun et al. (2015))

In-flight calibration strategy

To account for drift due to pressure, temperature and humidity changes in the aircraft cabin, calibrations during a measurement flight were performed more frequently than during ground measurements (see Section 4.4.4), every 5-10 minutes (see also previous work by Kostinek (2019)). Two calibration gas bottles (high- and low-secondary standards) were installed on top of the instrument's rack, from where the calibration gas is guided through 1/4" and 3/8" PFA tubing to the instrument (see Figure 5.2). During calibrations, the inlet tubing was used as an overflow to prevent the inflow of ambient air. The duration of one calibration was set to 20 s (10 s per calibration standard) to keep the loss of measurement data in reasonable bounds. As low-standard, dry synthetic air was used. For the MAGIC campaign, where biogenic CH₄ source emissions were probed, the high-standard consisted of dry synthetic air (nitrogen + 20% oxygen) mixed with CH₄ and C₂H₆ (approx. 1850 ppb CH₄ and 500 ppb C₂H₆). After each flight, the 21 high-standard in-flight bottle was refilled on the ground using gas from a 50 l secondary calibration standard. Table B.1 in the Appendix B lists the reference values for the used secondary standards, which have been determined from laboratory cross-calibrations against the DLR-NOAA primary standards to be traceable to the WMO calibration scales (see Section 4.3.3).

DLR-QCLS measurement during MAGIC

Usually, a flight starts with the transfer to the measurement region. In order to determine the boundary layer height, profiles from the lowest feasible flying altitude up to higher altitudes crossing the boundary layer are performed close to or in the measurement area. The planned flight pattern is conducted in the measurement area to sample CH₄ emissions from the targeted emission source.

Measured $\delta^{13}\text{C}(\text{CH}_4)$ is, as expected, around ambient background values at constant flight levels. For all flights, the observed variations of $\delta^{13}\text{C}(\text{CH}_4)$ range typically from -40 to -55‰, while the variability during ascents/descents (-60 to -30‰) was observed to be much higher.

Figure 5.3(a) shows the time series of CH₄, ¹³CH₄ and $\delta^{13}\text{C}(\text{CH}_4)$ during a profile measurement between 600 m and 1100 m altitude during the flight on 22 August 2021. Absolute CH₄ mole fractions, ¹³CH₄ and hence $\delta^{13}\text{C}(\text{CH}_4)$ are less stable increasing up to -30‰. When measuring ambient air during ascents/descents, both decreases and increases in ¹³CH₄ and $\delta^{13}\text{C}(\text{CH}_4)$ are observed (see Figure 5.3(a) and Figure 5.5 descent/ascent at 12:25 and 13:55 UTC). Since the DLR Cessna is unpressurized, ambient parameters change inside the aircraft cabin during ascents/descents. The effect that cabin pressure changes (and also sharp turns of the aircraft) have

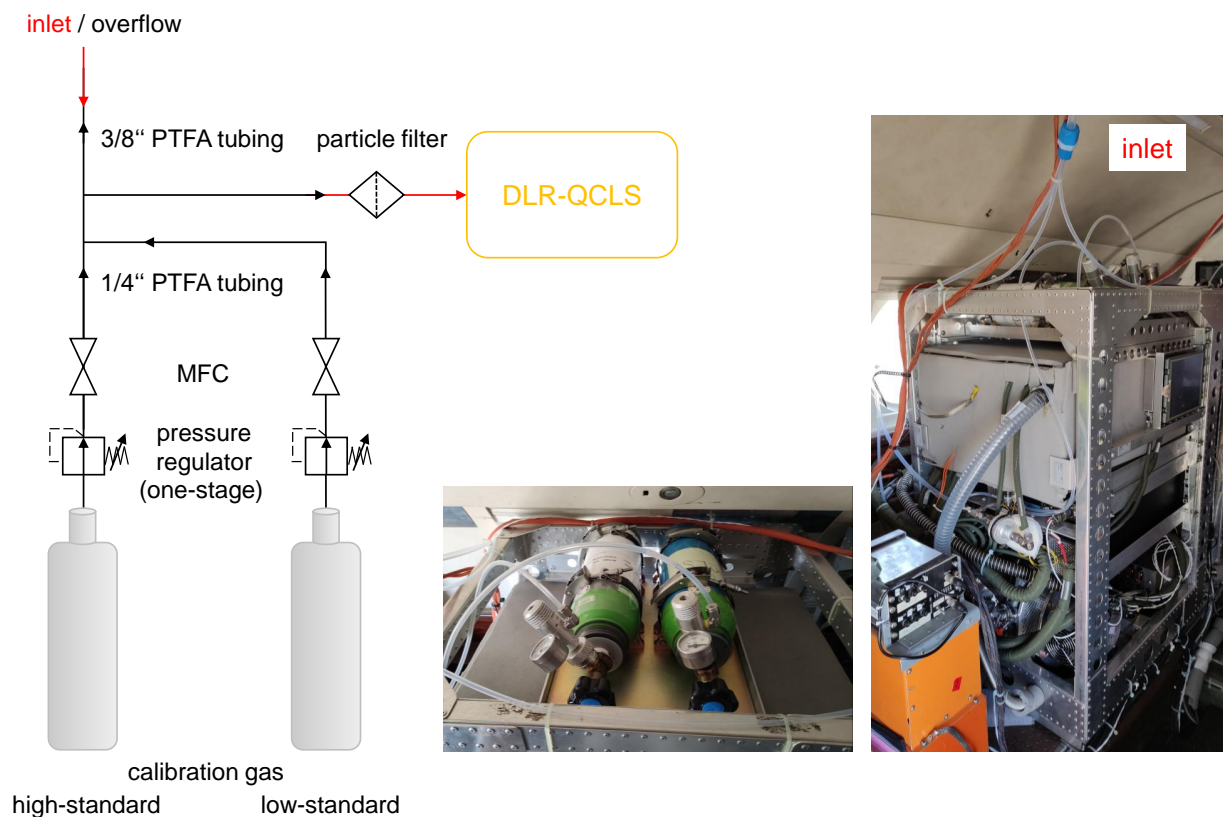


Figure 5.2: Schematic for DLR-QCLS in-flight calibration similar to ground calibrations (see Figure 4.7). On the right side, two photographs of the DLR-QCLS rack are shown (top view with calibration unit and side view). The calibration unit consists of two calibration gas cylinders (high- and low-secondary standards) mounted on top of the instrument's rack.

an influence on the optical alignment inside the Aerodyne DLR-QCLS and hence, on retrieved mole fractions, was reported before (e. g. Pitt et al. (2016)). Pitt et al. (2016) also reported from decreasing mole fractions of CH_4 and N_2O with increasing cabin pressure. Inside the DLR-QCLS, the optical path from the lasers to the measurement cell and further to the detector (1.6 m length) are open and susceptible to changes in temperature, pressure and humidity. To investigate the potential influence on retrieved mole fractions, an in-flight experiment was performed. Thereby, the DLR-QCLS measured calibration gas during one full ascent and two full descents during three flights. Figure 5.3 depicts retrieved $^{13}\text{CH}_4$ against the pressure (panel (b)) and against the relative humidity (panel (c)) measured inside the optical compartment. During the descents of flights 26a and 26b, $^{13}\text{CH}_4$ decreases by 0.28 ppb (accounting for the atmospheric abundance) with increasing compartment pressure. During the ascent of flight 23a, $^{13}\text{CH}_4$ seems to be more stable. $^{13}\text{CH}_4$ also varies with relative humidity, which changes by 0.9%. There is no obvious dependency on optical compartment temperature, which only varies by 0.05 °C. No clear and re-

producibility dependency on pressure and relative humidity changes can be derived. As mentioned above, this behaviour is similar to observations from other QCLS measurement groups. One solution might be better sealing off the DLR-QCLS optical compartment from ambient air (Pitt et al. (2016)), which however is difficult to realize.

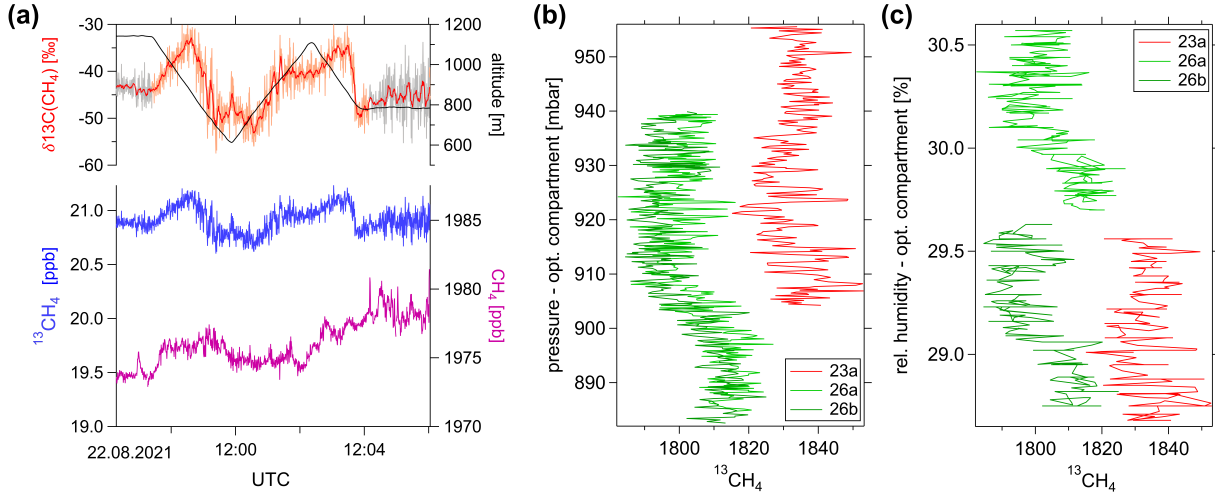


Figure 5.3: MAGIC field campaign: DLR-QCLS measurement during ascents/descents (profiles). (a) time series of $\delta^{13}\text{C}(\text{CH}_4)$ (gray; 6 s-average in red), $^{13}\text{CH}_4$ (blue) and CH_4 (magenta) with altitude (black). $\delta^{13}\text{C}(\text{CH}_4)$ during the profile measurement is highlighted in orange. Pressure (b) and relative humidity (c) inside the DLR-QCLS optical compartment against $^{13}\text{CH}_4$ for in-flight experimental tests during one ascent (flight 23a in red) and two descents (flight 26a and 26b in green) with the DLR-QCLS measuring calibration gas.

The further analysis of the $\delta^{13}\text{C}(\text{CH}_4)$ measurement focuses on straight-level observations, which typically show values close to expected ambient $\delta^{13}\text{C}(\text{CH}_4)$ of around -47‰ . During MAGIC, CH_4 enhancements up to 40 ppb were observed with no correlating signals from C_2H_6 and $\delta^{13}\text{C}(\text{CH}_4)$. Given the expected biogenic source signatures of around -60‰ and in combination with the instrument precision derived in the laboratory (see Section 4.4.1), these CH_4 enhancements are too small to detect $\delta^{13}\text{C}(\text{CH}_4)$ signatures.

In-flight uncertainty

Table 5.2 shows the total uncertainty of the species measured with the DLR-QCLS for MAGIC. The total uncertainty is calculated as the root of the quadrature sum of the uncertainties arising from the measurement precision, the reproducibility of calibration standards, the measurement calibration and the H_2O correction. The measurement calibration denotes the uncertainty in determining calibration values during the in-flight calibrations and contributes most, followed by the precision. Uncertainties due to the linear temperature drifts are assumed to be negligible because of the regular in-flight calibrations. Typical in-flight precision is determined for measurements at stable ambient conditions. It is enhanced compared to the laboratory precision due to aircraft vibrations, which affect the instrument optics and induce slight changes in optical alignment. The reproducibility of calibration standards is calculated from all cross-calibrations of the

used secondary-standards. The uncertainty of measurement calibration is assumed as two times the measurement precision. The uncertainty of the H₂O correction comprises the correction for water dilution and water broadening. The uncertainty of the water dilution correction is derived from the precision combined with Equation 4.7 with an uncertainty of 0.03% of typical H₂O mole fractions. The uncertainty of the water broadening correction is derived from the deviation of average mole fractions close to zero H₂O with the polynomial fit at zero H₂O mole fractions (see Figure 4.13).

Table 5.2: Total uncertainty of DLR-QCLS measurement for MAGIC. It is calculated as quadrature sum of the individual contributors precision, reproducibility of calibration standards, measurement calibration and H₂O correction.

MAGIC					
species	H ₂ O [ppm]	CH ₄ [ppb]	¹³ CH ₄ [ppb]	$\delta^{13}\text{C}(\text{CH}_4)$ (0.5 s; 6 s- avg)[‰]	C ₂ H ₆ [ppb]
precision (1 σ ; 2 Hz)	16.15	0.715	0.049	2.19; 0.44	0.082
reproducibility of calibration standards (1 σ)	-	0.43	0.012	0.76	0.131
measurement calibration	-	1.43	0.098	4.38; 0.88	0.164
H ₂ O correc- tion	-	0.66	0.007	1.28	0.048
total uncer- tainty	-	1.78	0.11	5.12; 1.8	0.23

Comparison of the CH₄ measurement with the Picarro Analyser

Figure 5.4 shows the DLR-QCLS CH₄ against the Picarro CH₄ measurement for all observations during MAGIC flights. For the comparison, the DLR-QCLS (2 Hz; 23 slpm flow rate) and the Picarro (1, Hz; 0.4 slpm flow rate) measurements are linearly interpolated to 1 s time resolution. Both instruments correlate well within their uncertainties (2 σ) for most of the flights. In contrast to the DLR-QCLS, the Picarro is not calibrated in-flight. It was calibrated on the ground several times during the campaign against four secondary standards, which were calibrated against DLR-NOAA primary standards in the laboratory before and after the campaign. The total uncertainty of the Picarro CH₄ measurement is 1.18 ppb. Deviations arise from the higher time resolution of the DLR-QCLS, which measures plumes at higher resolution, while the Picarro smears out (similar to the Picarro used in Section 4.4.4). For flight 24b and 26a the offset (3 and 6 ppb respectively) is higher than the combined uncertainty of both instruments, with the DLR-QCLS measurement showing lower CH₄ mole fractions than the Picarro. In this case, the 501 high-standard used to refill the in-flight 21 calibration bottle was changed (see Table B.1). The larger

deviation compared to other flights indicates that the 2l bottle was not properly flushed during the refilling process. The experience shows that during the refilling process, the 2l-bottles must be flushed for 3 times (filling and releasing the gas), especially when changing to a new high-standard with different mole fractions, to avoid a mixture of two different calibration gas standards.

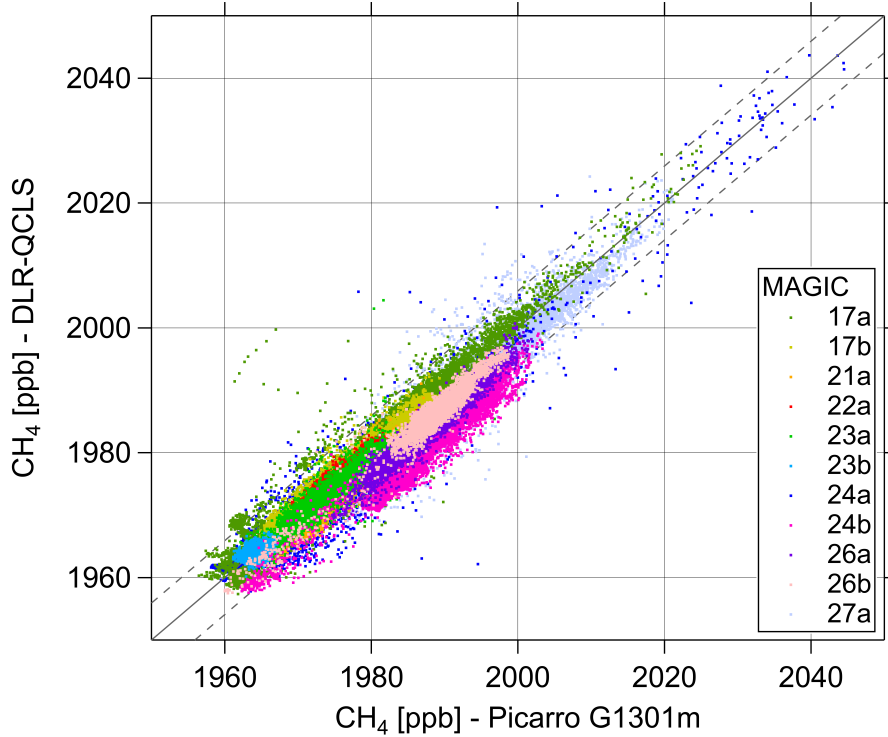


Figure 5.4: Comparison of the DLR-QCLS and Picarro CH_4 measurement for MAGIC flights. The sum of the uncertainties of the DLR-QCLS and the Picarro (2σ) is depicted as gray dashed lines.

5.1.3 Comparison with flask samples

The comparison with accurate, $\delta^{13}\text{C}(\text{CH}_4)$ measurements obtained with other state-of-the-art measurement techniques allows for determining the accuracy of the DLR-QCLS $\delta^{13}\text{C}(\text{CH}_4)$ in situ measurement.

The Jena Air Sampler (JAS) (Galkowski et al. (2021)) was installed onboard the Cessna and usually collects up to 12 flasks during a flight. A flask, which is a 1l-volume glass cylinder, is continuously flushed with ambient air at a flow rate of 6.84sl min^{-1} and manually closed at any time of interest during the flight. Unfortunately, due to an instrumental problem, only 8 flasks could be filled properly during one flight. These flasks were analysed in the laboratory after the MAGIC campaign. At the BGC-IsoLab (Max Planck Institute for Biogeochemistry, Jena), the $\delta^{13}\text{C}(\text{CH}_4)$ of the flasks were measured using GC-IRMS (see Section 2.4.1). The analytical precision of the $\delta^{13}\text{C}(\text{CH}_4)$ measurement is 0.14‰ (personal communication with M. Galkowski, BGC-IsoLab).

Figure 5.5 displays the time series of the flight on 22 August 2021 over a wetland area in northern Sweden with CH_4 , H_2O , $^{13}\text{CH}_4$ and $\delta^{13}\text{C}(\text{CH}_4)$ as measured by the DLR-QCLS. Violet markers show the $\delta^{13}\text{C}(\text{CH}_4)$ measurement obtained from the flask measurement at the time, when the flasks were closed. Additionally, the Picarro CH_4 measurement is shown in green.

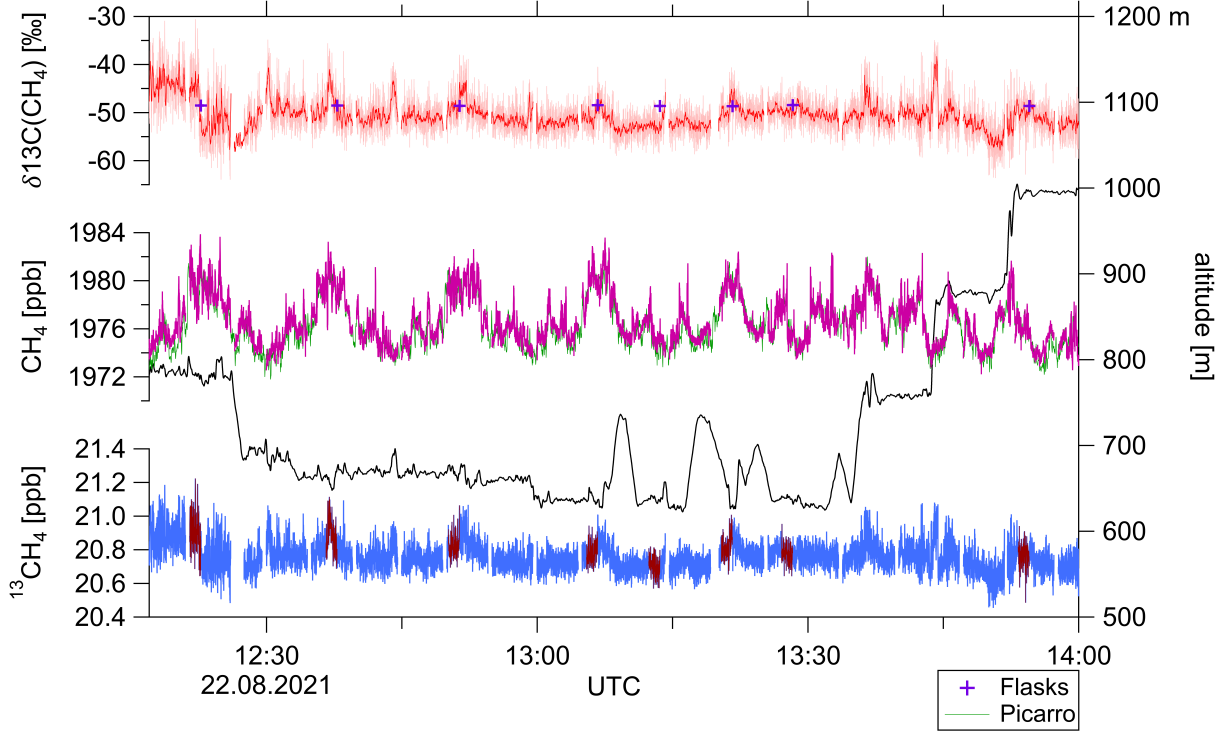


Figure 5.5: MAGIC flight on 22/08/2019: time series of DLR-QCLS measured $\delta^{13}\text{C}(\text{CH}_4)$ (light red; 6 s-average in dark red), CH_4 (magenta) and $^{13}\text{CH}_4$ (dark blue). $\delta^{13}\text{C}(\text{CH}_4)$ from flask samples are shown as violet markers at the closing time of the flask. The DLR-QCLS measured $^{13}\text{CH}_4$ during the time of the flask measurement and taken for the comparison is highlighted in dark brown (75 s duration). The Picarro CH_4 measurement is shown in dark green.

During the sampling process, the air entering a flask continuously mixes with the air inside the flask. Therefore, the in situ measurements are not directly compared with the flask analysis results at a certain time. Instead, an integration of in situ measured mole fractions is applied using a weighting function $W(t)$, which describes the mixing inside the flask prior the closing time t_W (Chen et al. (2012)):

$$W(t) = a \cdot \frac{e^{-(t_W-t) \cdot a}}{e^{-t_W \cdot a}} \quad (5.1)$$

where a is the flow rate through the flask divided by the volume of the flask. Subsequently, the in situ measured mole fractions c_i of a specific gas i are weighted within the time interval $(t_W - t_0)$:

$$c_i = \int_{t_0}^{t_W} c_i(t) \cdot W(t) \quad (5.2)$$

$W(t)$ is calculated for a time interval of 75 s, which is the smallest flushing time of the 8 flasks, and applied for the calculation of weighted DLR-QCLS measured $^{13}\text{CH}_4$ and $^{12}\text{CH}_4$ mole fractions. The respective $\delta^{13}\text{C}(\text{CH}_4)$ is calculated from the $^{13}\text{CH}_4$ and $^{12}\text{CH}_4$ weighted mole fractions following Equation 2.3. Because of the weighting function, the mole fractions measured at times closer to t_W have a stronger influence on the result. Here, the measurement of the last 10 s accounts for 70% of the weighted mole fractions.

As a result, Figure 5.6 displays the in situ measured and weighted $\delta^{13}\text{C}(\text{CH}_4)_{QCLS}$ against the flask analysis results $\delta^{13}\text{C}(\text{CH}_4)_{flask}$ for the 8 flasks. The DLR-QCLS underestimates 6 flasks out of 8 with two flasks (flask #3 and flask #6) being overestimated. The deviations between the DLR-QCLS measurement and the flask analysis results range between 0.7‰ and 1.5‰ for all flasks except for flask #5, which shows the largest discrepancy (4.4‰). The variability of $\delta^{13}\text{C}(\text{CH}_4)_{DLR-QCLS}$ is much larger than the variability of $\delta^{13}\text{C}(\text{CH}_4)_{flask}$. This reflects the larger measurement uncertainty of the DLR-QCLS compared to the flask measurement. Considering the total uncertainty of $\delta^{13}\text{C}(\text{CH}_4)_{QCLS}$ (1.8‰, see Table 5.2), the measurements agree within uncertainties except for flask #5, whereby the DLR-QCLS could not resolve the small differences in $\delta^{13}\text{C}(\text{CH}_4)$ seen by the flask measurements. This in turn means, that as expected from the instrument precision, it is only possible to detect changes $\delta^{13}\text{C}(\text{CH}_4)$ higher than the measurement uncertainty.

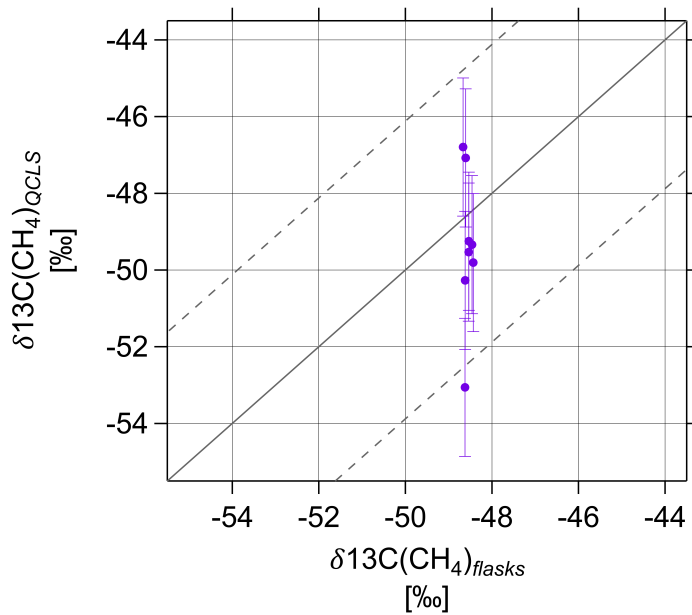


Figure 5.6: $\delta^{13}\text{C}(\text{CH}_4)_{QCLS}$ against $\delta^{13}\text{C}(\text{CH}_4)_{flask}$ resulting from the analysis of the flask samples for 8 flasks sampled during the MAGIC flight on 22 August 2021. The sum of the uncertainties of the DLR-QCLS and the flask measurement (2σ) is depicted as gray dashed lines.

5.2 MTGA campaign

5.2.1 MTGA objectives, airborne payload and flight strategy

The objectives of the MTGA campaign was to study the thermogenic CH_4 emissions from offshore oil exploration off the coasts of Gabon and Angola. African oil production makes up 8% of the World's oil production with Angola and Gabon contributing 16% and 2.5%, respectively, to the total African oil production (International Energy Agency (IEA), bp (2022)). Although oil and gas production is large in western Central Africa, emissions are highly uncertain, also because measurements are extremely sparse in this region.

From 10th to 22th September 2022, 15 flights were conducted using the DLR Falcon research aircraft (Dassault Falcon 20 E-5). The aircraft is a highly modified, pressurized twin engine jet able to fly at low altitudes down to 30 m above water. With an endurance of 4-5 h for the payload of MTGA it allowed to cover a wide measurement area. The flight strategy was a mass-balance approach optimized for regional top-down estimates of CH_4 emissions, similar to the southern North Sea study described in Chapter 3. The MTGA flights were the first airborne measurements to estimate fossil fuel emissions from Central African offshore installations. The CH_4 measurements shall contribute to a better understanding of the regional emissions of Central Africa and provide guidance to develop CH_4 emission mitigation strategies. In addition, the observations of C_2H_6 and $\delta^{13}\text{C}(\text{CH}_4)$ source signatures shall contribute to global data sets like the one described in Sherwood et al. (2017), which in turn are an important input for studies aiming at investigating the global CH_4 trend using tracers.

Figure 5.7(a) depicts a map showing the tracks of the flights conducted during MTGA along with a photograph of an offshore oil installation as seen from the research aircraft DLR Falcon. In Figure 5.7(b) a photograph of the DLR Falcon is shown with the DLR-QCLS mounted in a rack inside the aircraft cabin (right side). The inlet was installed on top of the aircraft facing backwards. The instrumental payload for the measurement of several trace gases and species is listed in Table 5.3. Besides the DLR-QCLS, the Picarro Analyser G2401m is deployed for the measurement of CH_4 and CO_2 , with the latter being an additional tracer for flared CH_4 emissions or combustion sources (e.g. gas or diesel turbines) located on the platforms (see Section 3.1). The DLR Falcon is further equipped with a nose boom to measure meteorological parameters such as 3D-wind, temperature and humidity. Flights were performed at approximately 120 m^{-1} speed at altitudes up to 6 km, and predominantly took place in the afternoon for a well mixed boundary layer, as required for the mass balance method (see Section 2.3).

5.2.2 Changes applied to the DLR-QCLS after MAGIC

During laboratory testing after the MAGIC campaign, it was observed that the mirrors in the sample cell of the DLR-QCLS got contaminated and scratched, thereby reducing the signal strength reaching the detector. Hence, to allow for high-quality measurements during MTGA, the mirrors were replaced by the manufacturer in the USA. The first laboratory tests showed that this lead higher signals and in turn, higher precision.

For the MTGA campaign, the calibration strategy was changed, because compared to MAGIC higher CH_4 enhancements were expected. Instead of using synthetic air as low-standard, both the low- and the high-standard were composed of synthetic air mixed with CH_4 and C_2H_6 at mole fractions close to ambient or higher than ambient mole fractions.



Figure 5.7: (a) Flight tracks of the 15 MTGA flights off the coasts of Gabon and Angola. A photograph of an oil platform as seen from the research aircraft is shown on the right. (b) Photograph of the DLR Falcon (Dassault Falcon 20 E-5) research aircraft on the left and the DLR-QCLS mounted inside the cabin on the right side.

Table 5.3: Payload of the DLR Falcon for the MTGA field campaign.

MTGA		
instrument	species	technique
DLR-QCLS	CH ₄ , C ₂ H ₆ , $\delta^{13}\text{C}(\text{CH}_4)$, H ₂ O	direct laser absorption spectroscopy
Picarro G2401m	CH ₄ , CO ₂ , CO, H ₂ O	cavity ring-down spectroscopy
MetPod	3D-wind, T, p, H ₂ O	5-hole pressure deducer
CIMS	SO ₂	Ion-trap chemical ionization mass spectrometer
ECO Physics TR	NO, NO _y	chemiluminescence technique
Aerosol	volatile and non-volatile particles	condensation particle counters and thermodenuder

5.2.3 DLR-QCLS performance during MTGA

Compared to MAGIC, the conditions during MTGA were much more challenging due to very high cabin temperatures of around 40 °C, both on the ground and during the measurement flights at low altitudes. This caused problems to many instruments due to overheating. As a result, during the first three scientific flights the DLR-QCLS measurements suffered because of overheating and breakdown of the pump. Hence, the cabin cooling system was improved as far as possible by using external ventilators and cool packs. In addition, it was decided to operate the DLR-QCLS only when flying over the measurement region but not during transfers driven by the impact of the powerful DLR-QCLS pump on the heat budget of the second CH₄ instrument onboard, the Picarro G2401m. The hot air flowing from the DLR-QCLS thermorack to the Picarro rack installed next to the DLR-QCLS rack caused an overheating of the Picarro cavity temperature and hence, degraded the measurements. Therefore, both instruments were operated in a way to guarantee that at least one of the two instruments provided high-quality CH₄ measurements. Nevertheless, the DLR-QCLS provided measurements during large parts of 12 out of 15 flights.

In-flight calibration strategy

For the in-flight calibration bottles filled with a mix of synthetic air with expected mole fractions of CH₄ and C₂H₆ were used. The high-standard contained approximately 2500 ppb CH₄ and 0 ppb C₂H₆ and the low-standard contained approximately 1850 ppb CH₄ and 500 ppb C₂H₆. Table B.2 in the Appendix B lists all used calibration standards with reference values for measured species. The latter were determined from the laboratory cross-calibration against NOAA primary standards to be traceable to the WMO calibration scales (see Section 4.3.3). Two 50l calibration gas bottles were used as low-standards, from which the low-standard 2l-bottle for the in-flight calibration was refilled after each flight. Five high-standard 2l-bottles were sufficient for all flights due to the shorter operating times only in the measurement area.

The calibration cycles were kept at 20 s duration with 5-10 min periods between calibrations, because both the time span and the periods were observed to be sufficient after the analysis of the MAGIC data.

DLR-QCLS measurement during MTGA

During the measurements downstream of the sampled offshore installations, CH_4 enhancements reached peak values up to 6330 ppb accompanied with clear signals in $\delta^{13}\text{C}(\text{CH}_4)$. Additionally, significant C_2H_6 enhancements up to 635 ppb were detected within these strong CH_4 plumes. The fact that plumes are detected simultaneously in CH_4 and C_2H_6 indicate a fossil fuel origin of the plume, since C_2H_6 is a tracer for fossil fuel emissions. Hence, the signals are used to calculate C2:C1 ratios to characterize the type of offshore field (oil or natural gas, see Section 5.2.4).

As an example, Figure 5.8 depicts the time series of part of the MTGA flight on 14 September 2022 around a set of Angolan installations. Enhancements are very high both in CH_4 and in C_2H_6 . For CH_4 absolute peak heights range from 2100 ppb to 5400 ppb over a stable background (~ 1880 ppb) and for C_2H_6 , peak mole fractions range from 24 ppb to 630 ppb over background mole fractions of approximately 1.5 ppb. Picarro and DLR-QCLS CH_4 measurements agree well (detailed comparison for all flights at the end of this section).

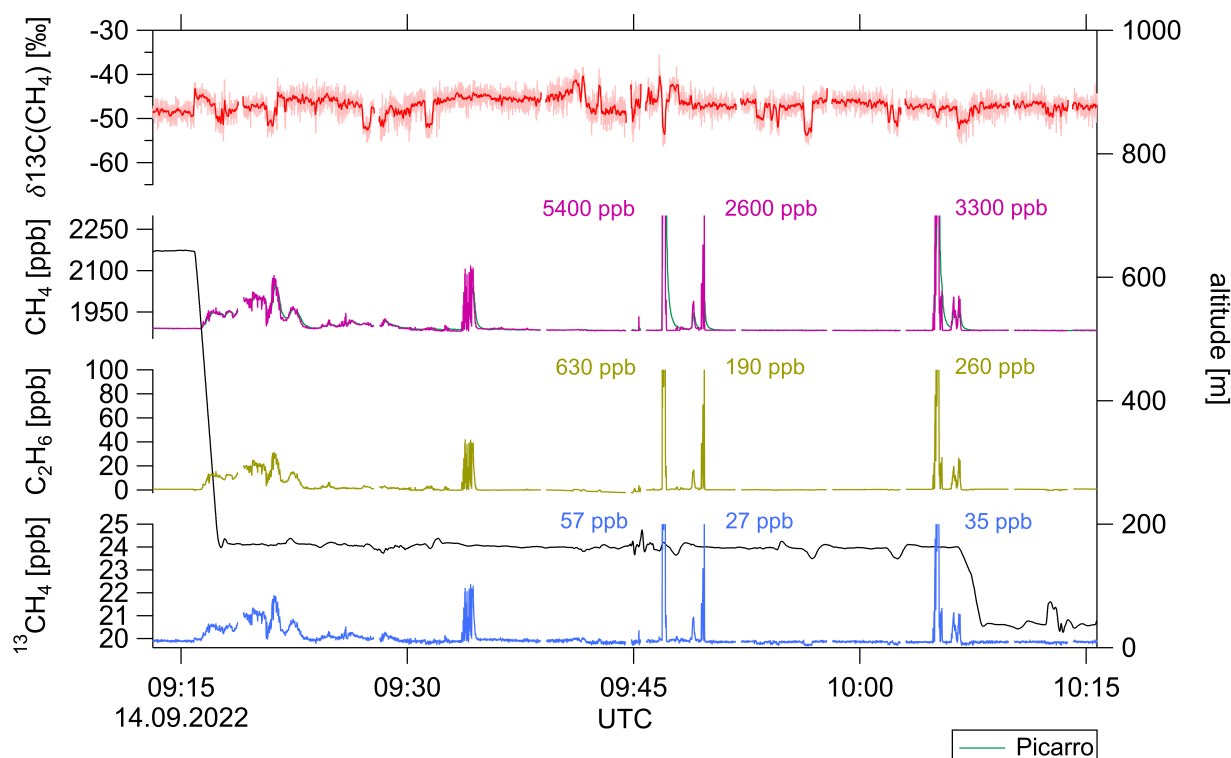


Figure 5.8: MTGA flight on 14 September 2022: DLR-QCLS measured $\delta^{13}\text{C}(\text{CH}_4)$ (light red; 6s-average in dark red), CH_4 (magenta), $^{13}\text{CH}_4$ (blue) and C_2H_6 (yellow). The Picarro CH_4 measurement is shown in green.

In comparison to the observations during MAGIC, variations of $\delta^{13}\text{C}(\text{CH}_4)$ are slightly higher and range from -60‰ to -30‰ , with $\delta^{13}\text{C}(\text{CH}_4)$ showing expected values during measuring ambient background air and at flight levels at constant altitude. However, in contrast to MAGIC, sudden decreases in measured mole fractions are observed for all species measured with both lasers, showing a duration of up to 40 s (see Figure 5.8 09:54-09:57 and 10:07-10:11). By way of

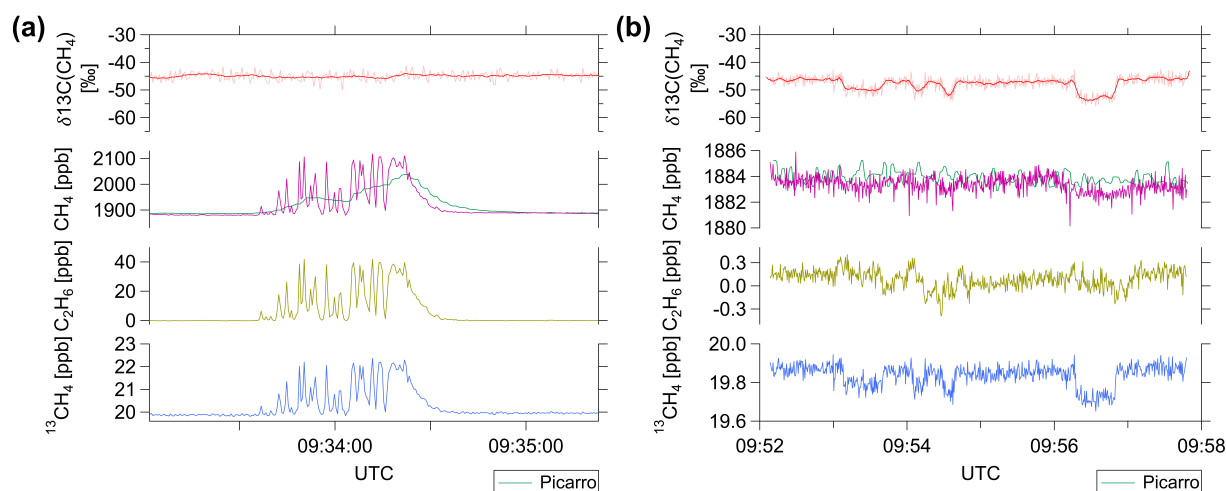


Figure 5.9: Time series of a subset of the MTGA flight on 14 September 2022: DLR-QCLS measured $\delta^{13}\text{C}(\text{CH}_4)$ (light red; 6 s-average in dark red), CH_4 (magenta), $^{13}\text{CH}_4$ (blue) and C_2H_6 (yellow). The Picarro CH_4 measurement is shown in green. (a) time series from 09:33:00-09:35:30 UTC showing a measured plume (b) time series from 09:53:10-09:56:50 UTC showing artefacts.

illustration, Figure 5.9(b) shows a subset of the time series in more detail. $^{13}\text{CH}_4$ decreases by 0.15 ppb and CH_4 by 1 ppb, leading to a decreased $\delta^{13}\text{C}(\text{CH}_4)$ by 6‰. Measured C_2H_6 decreases by 0.3 ppb. Since these structures are also visible in CH_6 and CH_4 measured by the original laser #1, but not in the Picarro measurements, they are most likely an instrument artefact. To investigate the possible reason, the laser parameters laser current and laser voltage were checked upon irregularities, but no anomalies could be found. However, the signals of both lasers simultaneously decrease during the artefacts. As a next step, the residuals of the measured and fitted spectra were examined by applying the statistical χ^2 -test as measure for the goodness of the fit for each micro window of the fit (residuals normalized to the spectra and summed up over a micro window). Irregularities of the calculated χ^2 indicate a change in the fit. Although the actual reason for the observed artefacts could not be found, both a check of the laser signal and the fit quality allow to identify measurements of bad quality and hence, to disregard the corresponding data.

In-flight uncertainty

Table 5.4 shows the total uncertainty of the DLR-QCLS measured species for MTGA. The total uncertainty is calculated similar as for MAGIC. Compared to MAGIC, the uncertainties have improved for all species, which is attributed to the higher precision due to the replacement of the sample cell mirrors.

Comparison of the CH_4 measurement with the Picarro Analyser

Figure 5.10 shows the DLR-QCLS CH_4 against the Picarro CH_4 measurement for all flights of MTGA. Figure 5.11 depicts a zoom of Figure 5.10 closer to background mole fractions. For the comparison of both instruments, measured CH_4 is linearly interpolated to 1 s time resolution,

Table 5.4: Total uncertainty of DLR-QCLS measurement for MTGA. It is calculated as quadrature sum of the individual contributors precision, reproducibility of calibration standards, measurement calibration and H₂O correction.

MTGA					
species	H ₂ O [ppm]	CH ₄ [ppb]	¹³ C(CH ₄)[ppb]	$\delta^{13}\text{C}(\text{CH}_4)$ (0.5 s; 6 s- avg)[‰]	C ₂ H ₆ [ppb]
precision (1 σ ; 2 Hz)	17.93	0.602	0.037	1.810; 0.231	0.089
reproducibility of calibration standards (1 σ)	-	0.43	0.012	0.76	0.131
measurement calibration	-	1.204	0.074	3.620 ; 0.462	0.178
H ₂ O correc- tion	-	0.645	0.0067	1.29	0.048
total uncer- tainty	-	1.55	0.08	4.32; 1.59	0.24

since the DLR-QCLS measures at higher time resolution than the Picarro (0.5 s versus 1.1 s of the Picarro G2401m). A one-by-one comparison is hampered by the different response times and time resolutions of the two instruments. The faster DLR-QCLS measurement allows for a better temporal and hence, spatial resolution of spatially narrow plumes, as illustrated in Figure 5.9(a). The overall uncertainty of the Picarro CH₄ measurement is 21 ppb and higher compared to MAGIC due to distorted measurement when the Picarro was overheated. Deviations between both instruments arise from the higher time resolution of the DLR-QCLS, which, as a consequence, measures higher peak enhancements than the Picarro. In contrast, the peaks measured with the Picarro are smeared out and hence, broader. This in turn results in higher measured mole fractions of the Picarro towards the end of peaks, when the DLR-QCLS already measures background mole fractions (see Section 4.4.4). As a result, the slopes of the linear regression are on average for all flights 1.2 and measurements deviate surpassing the sum of the uncertainties of both instruments.

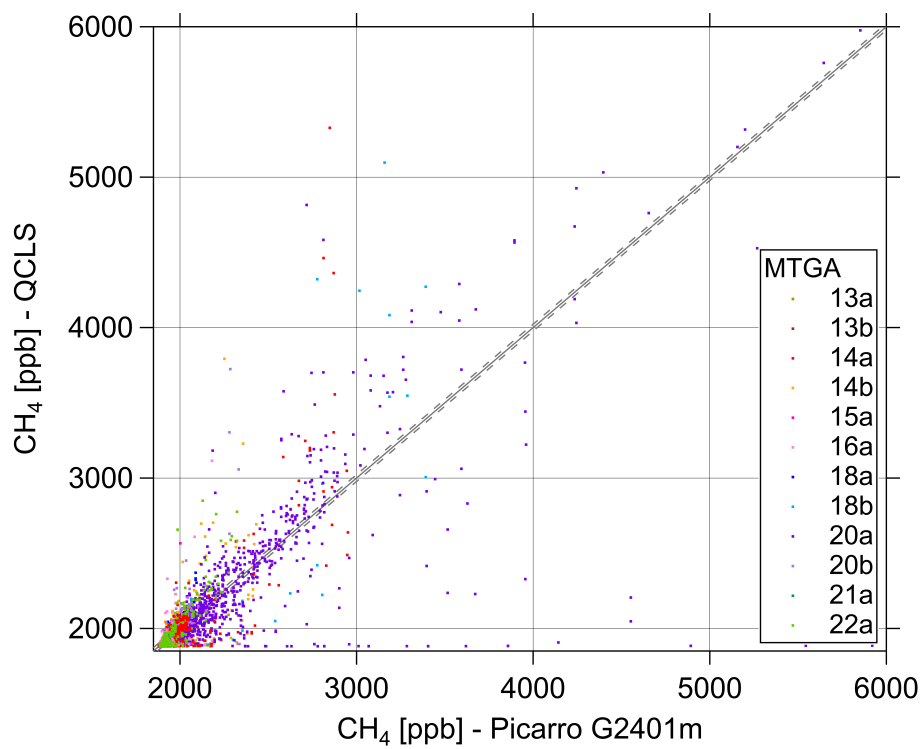


Figure 5.10: Comparison of DLR-QCLS and Picarro CH₄ measurement for MTGA flights. The sum of the uncertainties of both instruments is depicted as gray dashed line.

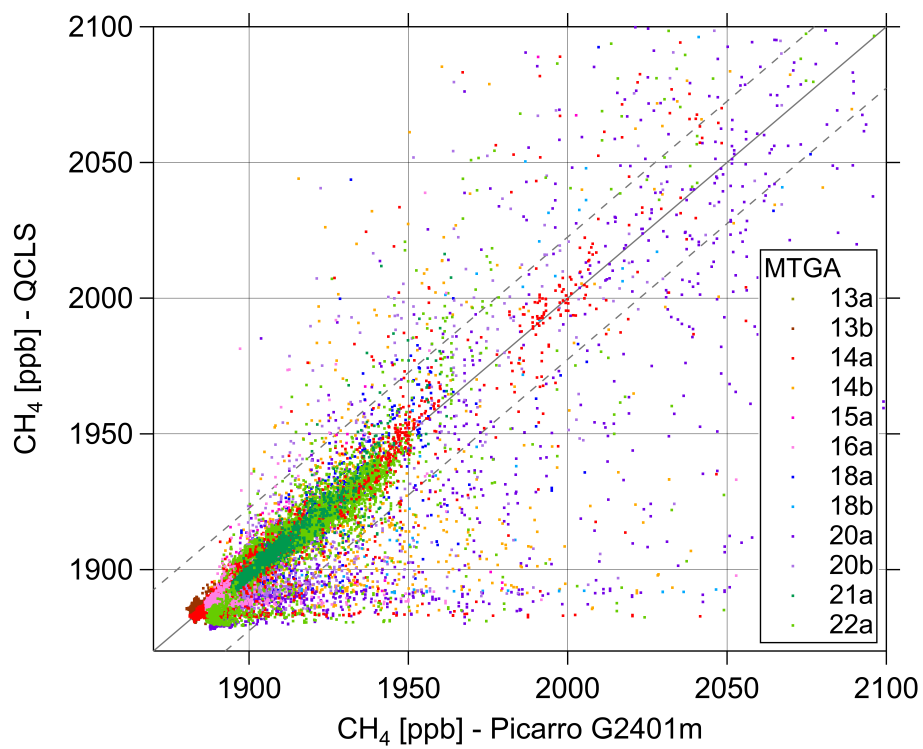


Figure 5.11: Zoom in of the comparison of DLR-QCLS and Picarro CH_4 measurement for MTGA flights. The sum of the uncertainties of both instruments is depicted as gray dashed line.

5.2.4 Source signatures and C₂:C₁ ratios for selected plumes

In this section, the DLR-QCLS tracer measurements of $\delta^{13}\text{C}(\text{CH}_4)$ and C_2H_6 are applied to derive source signatures and C_2H_6 to CH_4 (C₂:C₁) ratios characteristic for the individual fossil fuel source.

Angolan installations

During two flights (14a and 18b), mass-balance flights were conducted around a selected group of Angolan offshore oil installations. Since the meteorological conditions and particularly the wind direction and speed were stable during these flights, measured plumes downstream can be attributed most likely to the same group of installations. Figure 5.12 shows the flight paths of both flights with enhanced CH_4 north-west downwind of the sampled installations.

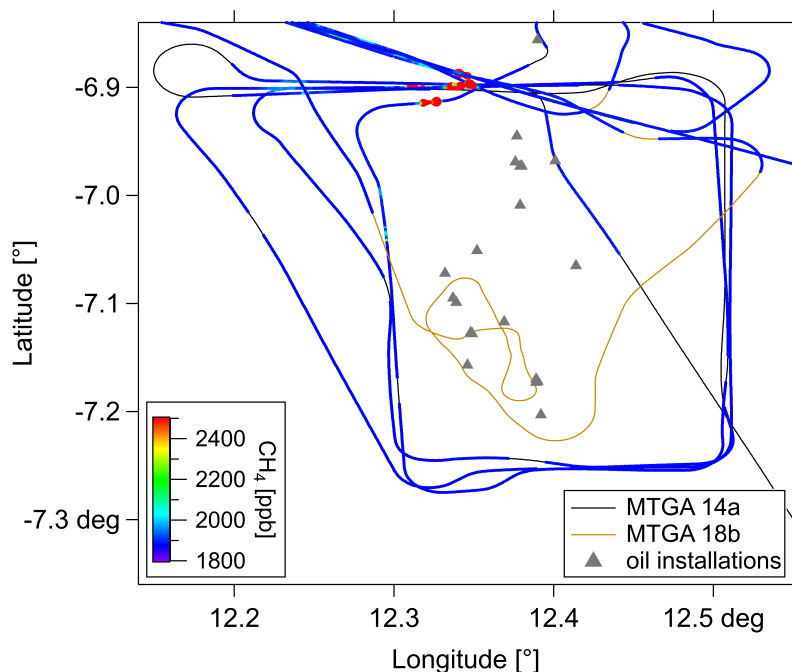


Figure 5.12: Flight path of MTGA flights 14a (black line) and 18b (brown line) around a set of Angolan oil installations (gray markers). Size and color of CH_4 markers is according to measured mole fractions.

To derive the isotopic source signature, Keeling plots are generated for pronounced CH_4 enhancements for both flights, respectively. As an example for the source signature analysis, Figure 5.13(a) gives a detailed view of plume #1 of flight 14a with measured CH_4 , $^{13}\text{CH}_4$, $\delta^{13}\text{C}(\text{CH}_4)$ and C_2H_6 dry air mole fractions. The plume was detected during a time span of 19s, which at the average aircraft speed of 114 m s^{-1} corresponds to a width of approximately 2.1 km. The corresponding Keeling plot of plume #1, i.e. measured $\delta^{13}\text{C}(\text{CH}_4)$ against the inverse CH_4 mole fractions, is shown in Figure 5.13(b) in black. The source signature obtained from the intercept of the linear regression is $(-62.22 \pm 1.01)\text{‰}$. The uncertainty of $\delta^{13}\text{C}(\text{CH}_4)_{sc}$ is the sum of the measurement uncertainty, which is calculated from the maximum and minimum

$\delta^{13}\text{C}(\text{CH}_4)_{sc}$ using the total uncertainties of CH_4 and $\delta^{13}\text{C}(\text{CH}_4)$, and the uncertainty of the linear regression.

A summary of the determined source signatures of three measured plume during both flights, respectively, is shown in Table 5.5. All measured $\delta^{13}\text{C}(\text{CH}_4)$ within the plumes are more negative with respect to the background, whereby only one plume (#2 of flight 18b) stands out with increased $\delta^{13}\text{C}(\text{CH}_4)$ within the plume. The determined $\delta^{13}\text{C}(\text{CH}_4)_{sc}$ range between -62.2% and -33.3% . The average source signature is -52.7% , which lies at the lower end of globally measured $\delta^{13}\text{C}(\text{CH}_4)_{sc}$ according to the global database for conventional gas (Sherwood et al. (2017)). The latter has a maximum at approximately -42% but spreads from -15 to -80% (see Figure 2.5). The database contains 8 samples specifically from Angolan basins ranging from -34 to -42% (Prinzhofer and Huc (1995)). However, these are not directly comparable with the herein measurements, since they were not necessarily determined from the same basin.

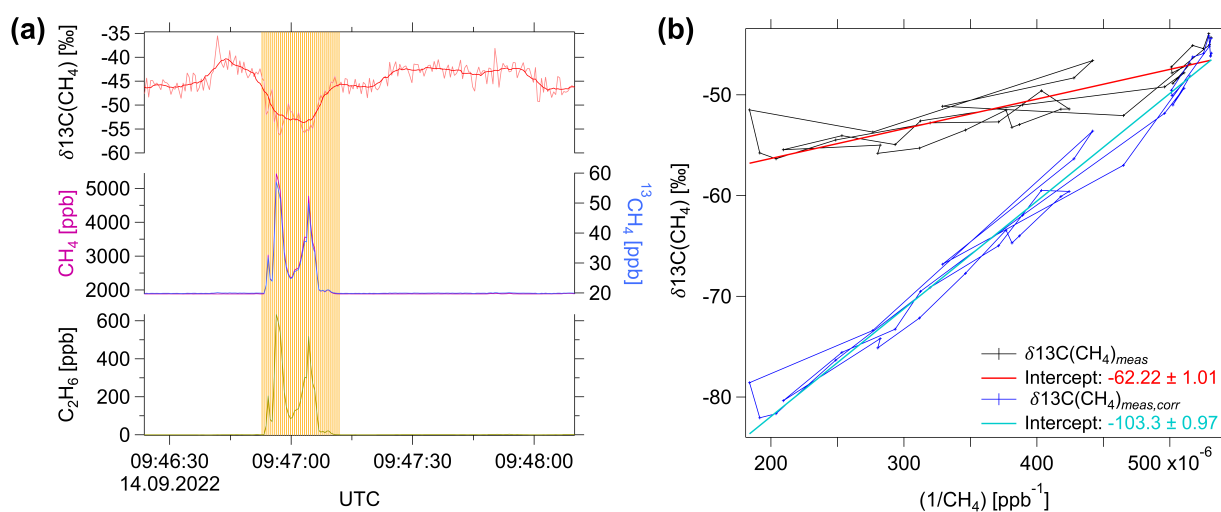


Figure 5.13: Detailed view of peak #1 at 09:47 from MTGA flight on 14/09/2022: (a) time series of DLR-QCLS measured $\delta^{13}\text{C}(\text{CH}_4)$ (light red; 6s-average in dark red), CH_4 (magenta), $^{13}\text{CH}_4$ (dark blue) and C_2H_6 (gold). The time of the peak is highlighted in orange (peak width 19s or approximately 2.1 km). (b) $\delta^{13}\text{C}(\text{CH}_4)$ against $(1/\text{CH}_4)$ (Keeling-Plot) for the data within the plume (black). The intercept of the linear regression (red) gives the source signature ($(-62.22 \pm 1.01)\%$). The correction from laboratory measurements (see Section 4.4.4) applied to the plume data (blue) is shown with its linear regression (cyan) and obtained source signature ($(-103.3 \pm 0.97)\%$).

Applying the correction factor from laboratory measurements to scale down $^{13}\text{CH}_4$ (see Section 4.4.4) yields a lower source signature, $(-103.3 \pm 0.97)\%$, out of the expected range. In contrast to laboratory conditions, where a calibration gas in dry synthetic air (nitrogen + 20% oxygen) was measured, here, the $\delta^{13}\text{C}(\text{CH}_4)$ signals are detected in ambient air, which has a different composition. Cross-sensitivities between different species might explain why the correction is not applicable for ambient air and hence in-flight conditions. According to Harris et al. (2020) QCLS laser spectrometer performance (for isotopic N_2O) is mainly driven by instrument drift, precision, spectral interferences and matrix effects. Regarding the latter, differences between sample and reference gas compositions, i. e. different mole fractions of atmospheric background gases (N_2 , Ar

Table 5.5: Methane enhancements ΔCH_4 downwind of the same Angolan set of installations studied during two MTGA flights (14a and 18b). For each plume, C2:C1 ratios and source signatures $\delta^{13}\text{C}(\text{CH}_4)_{sc}$ are determined. Uncertainties are given at 1σ .

flight time	plume #	ΔCH_4 [ppb]	C2:C1 [%]	$\delta^{13}\text{C}(\text{CH}_4)_{sc}$ [‰]
14 Sept 2022 (07:49-11:27 UTC)	1	3555	17.8 ± 0.3	-62.2 ± 5.3
	2	1450	18.1 ± 1.4	-54.0 ± 5.3
	3	1995	19.7 ± 1.2	-57.9 ± 5.6
18 Sept 2022 (13:27-17:20 UTC)	1	3350	17.6 ± 0.3	-50.6 ± 5.3
	2	3290	18.2 ± 0.4	-33.3 ± 5.6
	3	1605	18.0 ± 0.5	-58.0 ± 5.5

and especially O_2) can affect the accuracy of measurements due to different pressure-broadening coefficients. Further, here the enhancements in $^{13}\text{CH}_4$ are a factor 10 higher compared to the laboratory studies and also higher than the mole fractions used to conduct the linearity experiment (see Section 4.4.2). This gives rise to the supposition that the DLR-QCLS might not behave linearly for such high mole fractions. Harris et al. (2020) found a linear instrument-specific dependency between the isotopic measurement and inverse (N_2O) mole fractions, which in combination with matrix effects varies especially for high mole fractions of the target gas.

Compared to the water vapor measurement of the MetPod, the water vapor measured by the DLR-QCLS is lower by 0.05% during the conducted flights. To estimate the possible impact of the DLR-QCLS water vapor measurement on the determined source signatures, the $\delta^{13}\text{C}(\text{CH}_4)_{sc}$ of plume #1 is calculated using the water vapor measurement of the MetPod. The influence on the source signature of plume #1 is rather small with a 0.74‰ higher source signature (-61.48‰).

Additionally to the source signature analysis, C_2H_6 to CH_4 (C2:C1) ratios are calculated as the ratio of the integrated peaks over background mole fractions analogously to the method described in Section 3.4.2. As an example, the C2:C1 ratio for plume #1 of flight 14a depicted in Figure 5.13(a) was determined for the duration of the plume (19 s) and yields $(17.9 \pm 0.3)\%$. Uncertainties of the C2:C1 ratios are calculated from the total uncertainties of CH_4 and C_2H_6 applying the Gaussian error propagation. In Table 5.5 all C2:C1 ratios are summarized for the Angolan group of oil installations. C2:C1 ratios are on average 18.3% (17.8-19.7%), which is within the range of C2:C1 ratios for emissions from oil fields (10-25%) (Xiao et al. (2008)). Compared to the 8 Angolan samples from the global database for conventional gas (Sherwood et al. (2017), Prinzhofer and Huc (1995)), which reach from 7 to 15%, the measured ratios are higher. However, those measurements might not originate from the same oil and gas reservoir studied herein and thus might not be comparable. In general, the C2:C1 ratios depend on the individual stage and history of fossil fuel formation within a reservoir (see Section 2.2). For the block of wells, which the sampled Angolan installations are part of, operator data for the gas composition showed an average C2:C1 ratio of 14% (measurements in December 2019; personal communication with the operator). However, the greater extent of the block of wells might also include other reservoirs, which might contribute to the C2:C1 ratio provided by the operator.

Gabonese installations

Source signatures and C2:C1 ratios were also derived from fly-bys of single Gabonese installations for the flight on 22 September 2022 (see Table 5.6). Source signatures $\delta^{13}\text{C}(\text{CH}_4)_{sc}$ are the same magnitude as for the Angolan set of installations. The average C2:C1 ratio is 12.0% (11.8-12.3) and are within the expected range for oil fields (10-25%, Xiao et al. (2008)). Compared to the sampled Angolan installations, the C2:C1 ratios are smaller, which indicates that the basins are different in their chemical compositions due to their individual formation processes (see Section 2.2).

Table 5.6: Methane enhancements ΔCH_4 downwind of single Gabonese installations during the flight on 22 Sept 2022 of MTGA. C2:C1 ratios and source signatures $\delta^{13}\text{C}(\text{CH}_4)_{sc}$ are determined. Uncertainties are given at 1σ .

flight time	plume #	ΔCH_4 [ppb]	C2:C1 [%]	$\delta^{13}\text{C}(\text{CH}_4)_{sc}$ [‰]
22 Sept 2022 (11:31-15:13 UTC)	1	1281	11.8 ± 1.7	-55.8 ± 6.8
	2	442	11.9 ± 2.7	-69.7 ± 7.7
	3	908	12.3 ± 1.9	-60.7 ± 7.2
	4	416	12.0 ± 2.5	-62.6 ± 8.8

5.3 Summary Chapter 5

The DLR-QCLS with a new laser configuration to measure $\delta^{13}\text{C}(\text{CH}_4)$ was tested during two field campaigns to investigate its ability to derive in-flight source signatures of biogenic sources from wetlands (MAGIC) and fossil fuel sources from offshore oil and gas installations (MTGA).

The calibration strategy for in-flight calibrations was changed for MTGA using calibration gases with mole fractions for CH_4 and C_2H_6 close to ambient and expected mole fractions instead of synthetic air as low-standard (MAGIC). Further, the measurement precision could be improved for MTGA after a renewal of the sample cell mirrors.

A comparison with the well-established Picarro measurement (cavity-ring-down spectroscopy), shows that CH_4 measurements agree well within combined uncertainties for MAGIC, but deviated for MTGA. The latter can be explained by the faster instrument response and higher time resolution of the DLR-QCLS, leading to higher peak enhancements and faster decrease to ambient background concentrations after a plume interception.

Detected variations of $\delta^{13}\text{C}(\text{CH}_4)$ range from -60 to -30‰ in both campaigns. It was found that especially during ascents/descents during MAGIC (unpressurized aircraft), $\delta^{13}\text{C}(\text{CH}_4)$ shows variabilities, similar to earlier measurements of other species measured with DLR-QCLS methods. Reasons for the observed instrument artefacts were investigated, indicating an impact of pressure and humidity changes on derived mole fractions, but could not be finally clarified within the framework of this thesis. Within this study, the focus is on the measurement at constant altitude levels, where $\delta^{13}\text{C}(\text{CH}_4)$ is more stable and close to expected ambient levels.

Total in-flight uncertainties of $\delta^{13}\text{C}(\text{CH}_4)$ are 5.12‰ for MAGIC and 4.32‰ for MTGA. Since, as expected, CH_4 enhancements during MAGIC were rather low (<40 ppb), no $\delta^{13}\text{C}(\text{CH}_4)$ signals of the investigated sources of biogenic origin were detected. However, a comparison with

flask measurements during one flight, shows agreement with measured (ambient) $\delta^{13}\text{C}(\text{CH}_4)$ within uncertainties. For MTGA strong signals in $\delta^{13}\text{C}(\text{CH}_4)$ were detected, mainly due to much larger CH_4 enhancements up to several ppm during dedicated plume interceptions. Source signatures derived from Keeling plots for repeated measurements of the same set of Angolan installations, indicate an average source signature $\delta^{13}\text{C}(\text{CH}_4)_{sc}$ of approximately -52% . Compared to the global $\delta^{13}\text{C}(\text{CH}_4)_{sc}$ database with a maximum at -42% and spreading from -15 to -80% for conventional gas (see Figure 2.5, Sherwood et al. (2017)), the derived source signature is more depleted in $^{13}\text{CH}_4$ than other measurements, but still within the range. To underpin the airborne observations, laboratory tests have been conducted, suggesting a correction to lower source signatures. However, the laboratory measurements might not be applicable to ambient air measurements, due to its different composition (matrix effect). As an example, Harris et al. (2020) suggest to use the same composition of sample and calibration gas, since especially variations in the background O_2 introduces a matrix effect on retrieved mole fractions because of different spectral pressure broadening. Another difference between the laboratory studies and the airborne measurements is the different concentration range. It was not possible to reproduce the very high enhancements measured during MTGA, for which the DLR-QCLS $\delta^{13}\text{C}(\text{CH}_4)$ might not behave linearly anymore. According to Harris et al. (2020) matrix effects in combination with high mole fractions of the target species are variable and instrument-specific, thus requiring extensive testing for the determination of the individual dependency.

The second DLR-QCLS tracer measurement is C_2H_6 , a tracer for fossil fuel emissions and its C_2H_6 to CH_4 (C2:C1) ratios characteristic for the type of field. During the MTGA campaign simultaneous enhancements in C_2H_6 were measured as an indicator for fossil fuel emissions. From the beforementioned repeated measurement around Angolan installations, the C2:C1 ratios are calculated and on average 18.3% (17.8 - 19.7%). For a set of Gabonese installations, the C2:C1 ratios are lower and 12.0% (11.8 - 12.3). Compared to the study conducted in the southern North Sea around gas installations (see Chapter 3), the herein measured ratios are higher and lie well within the expected range for emissions from oil fields (10 - 25% ; Xiao et al. (2008)).

In summary, the results of this thesis indicate that the DLR-QCLS is able to detect qualitative changes in $\delta^{13}\text{C}(\text{CH}_4)$ signals, which is also shown in laboratory experiments (Section 4.4.4). However, the first airborne deployments reveal significant challenges to reliably quantify source signatures $\delta^{13}\text{C}(\text{CH}_4)_{sc}$. Challenges include instrument artefacts and suspected dependencies of the $\delta^{13}\text{C}(\text{CH}_4)$ measurement on the sampled gas matrix and/or high CH_4 mole fractions. Therefore, the following studies are suggested for improvements and to further test the availability of the DLR-QCLS to study in-flight source signatures of different methane sources: To examine the linearity of the DLR-QCLS and to quantitatively derive $\delta^{13}\text{C}(\text{CH}_4)_{sc}$, laboratory experiments need to be conducted within a higher range of CH_4 and $^{13}\text{CH}_4$ mole fractions, including for different gas matrix compositions (e. g. varying O_2 and Ar). The instrument could be calibrated against known source signatures from ambient air samples collected from different sources. Additional in-flight calibration against one or more target cylinders with known source signatures could help to improve the in-flight source detection.

Chapter 6

Summary and Outlook

The increase in global mean surface temperature since industrialization is alarming, reaching a 1.48 °C higher level in 2023 (ECMWF (09 January 2024)). Mankind has the responsibility to abate climate change by reducing emissions of greenhouse gases. CH₄ is the second most important anthropogenic greenhouse gas after CO₂ in terms of emissions and contributes with 16% to the abundance-based or 32% to the emission-based effective radiative forcing of long-lived greenhouse gases causing 0.6 °C of the temperature rise over 1750-2019. Atmospheric CH₄ mole fractions have almost tripled compared to pre-industrial levels in 1750. It is an attractive target for mitigation strategies due to its relatively short lifetime compared to CO₂ of roughly a decade. Mitigating CH₄ emissions holds great promise and would have rapid impact on the global CH₄ burden (Nisbet et al. (2023), Nisbet et al. (2019)). To effectively prioritize actions to mitigate emissions, a detailed knowledge of CH₄ sources is required. However, the decline of the ratio of the isotopologues ¹³CH₄/¹²CH₄ in atmospheric CH₄ (expressed as δ¹³C(CH₄)) simultaneous to the renewed accelerated CH₄ increase indicates a profound change in sources and/or sinks since 2007, which is not well understood. Therefore, measurements of CH₄ source emissions are required. Fossil fuel sources account for 19% of global CH₄ emissions (Saunio et al. (2020)), but many top-down measurements suggest an underestimation of fossil fuel emissions by bottom-up inventories (e.g. Gorchoy Negrón et al. (2020), Johnson et al. (2017), Schwietzke et al. (2016)). Political initiatives, like the Global Methane Pledge, have already been set into motion aiming to reduce global CH₄ emissions by at least 30% from 2020 levels by 2030 (UNEP (2023)).

This study aims to quantify CH₄ emissions from offshore fossil fuel sources and to study whether fast tracer measurements (δ¹³C(CH₄) and C₂H₆) are a useful tool to better characterize the composition of those emissions. So far, offshore fossil fuel sources are poorly studied. Due to their remote locations next to water, they are a difficult target for satellite detection, but a very suitable target for airborne point source emission quantification. It is hypothesized that generic emission reporting methods used in global inventories and for UNFCCC reporting do not correctly reflect offshore emissions (see Chapter 1). Aircraft-based top-down CH₄ emission estimates help to evaluate discrepancies between different reported bottom-up emission estimates. To this end, an existing data set of airborne measurements conducted in the southern North Sea by the British Antarctic Survey around offshore gas installations was analysed and compared with bottom-up inventories and top-down studies in other offshore oil and gas regions. The analysis of the southern North Sea flights revealed that the low time resolution of the well-established flask sampling technique to measure δ¹³C(CH₄) limits its ability to use it for the study of source

signatures from point source emitters. Hence, the second part of this thesis is dedicated to test the hypothesis that recent developments and improvements of laser absorption spectroscopy allow for the continuous airborne measurement of the two tracers $\delta^{13}\text{C}(\text{CH}_4)$ and C_2H_6 in order to support the characterization of offshore fossil fuel emissions. It investigates the feasibility of conducting continuous $\delta^{13}\text{C}(\text{CH}_4)$ measurements using infrared laser absorption. This involves the adaptation and characterization of the tunable infrared absorption spectrometer DLR-QCLS for the measurement of $\delta^{13}\text{C}(\text{CH}_4)$, and its successful deployment on two different research aircraft during the MAGIC and MTGA campaigns to investigate CH_4 sources of biogenic (wetlands) and thermogenic (fossil fuel) origin, respectively. MAGIC served as initial test-campaign to evaluate the airborne performance of the DLR-QCLS, enabling improvements for the subsequent MTGA deployment.

Driven by the hypothesis of this work, answers to the research questions are given in the following:

RQ 1: How high and variable are top-down derived CH_4 emission estimates and C_2H_6 to CH_4 (C2:C1) ratios for offshore fossil fuel installations in the southern North Sea?

CH_4 emission fluxes were calculated for six UK and five Dutch offshore gas production installations located in the southern North Sea from airborne top-down measurements conducted in spring 2019. Emission fluxes range from 12.1 kg h^{-1} to 1258.7 kg h^{-1} .

To identify the fossil fuel CH_4 emissions, co-emitted C_2H_6 was used as a tracer. Emissions originated either from venting and/or fugitives. Additional flaring or combustion from other sources such as diesel or gas turbines was identified using CO_2 as a tracer. For five out of the seven installations, that showed CH_4 and C_2H_6 emissions, also enhanced CO_2 was measured. Thus, for these installations very likely a flaring or combustion source contributed to the total emissions.

For each offshore installation the C_2H_6 to CH_4 (C2:C1) ratio was calculated. The C2:C1 ratios determined from repeated measurements around each respective facility are consistent. For all facilities together the C2:C1 ratios range between 2.5% and 7.8%, which is in the range of expected ratios for gas fields (0-10%, Xiao et al. (2008)). The derivation of isotopic source signatures using the flask measurements failed, because the short enhancements during the flights were missed.

RQ 2: How do the top-down CH_4 emission estimates in the southern North Sea compare with bottom-up inventory estimates?

For the comparison of CH_4 emission fluxes, the annual bottom-up inventories were scaled down to match the timescale of the measurement. The comparison reveals a large discrepancy between bottom-up and top-down emissions, which is somewhat expected because of the nature of single snap-shot measurements per facility in combination with potential temporal variability in emissions for each respective facility. The regional point source inventories UK Environmental and Emissions Monitoring System database (EEMS, 2019) and the UK National Atmospheric Emissions Inventory (NAEI, 2018 and 2019) underestimate emissions by factors ranging from 6 to 13. The most significant disparity is observed with the globally gridded ($1^\circ \times 1^\circ$) Global Fuel Exploitation Inventory (GFEI, 2019), which underestimates aggregated emissions from UK and Dutch sites by a factor of 21 and 279, respectively. One

reason for the exceptionally large discrepancy concerning Dutch sites might be that Dutch emissions reported to UNFCCC, which GFEI uses for downscaling to infrastructure data, are unexpectedly small compared with UK reporting. Additionally, discrepancies among inventories are identified. NAEI inventory data, which is based on EEMS and, thus, should be consistent with EEMS, equals or exceeds EEMS inventory data, except for one of the six installations. The best agreement is found for facility-level reporting provided by Dutch operators for the specific survey date. The measurements deviate by a factor of 0.64 (0.33-12) and compare well to a study conducted in the Norwegian Sea by Foulds et al. (2022).

RQ 3: How do the top-down CH₄ emission estimates in the southern North Sea compare with top-down studies in other offshore regions?

Interestingly, despite differing production types (oil, gas), CH₄ emission rates (kg h⁻¹) in the southern North Sea are in the same order of magnitude compared to those from other airborne studies conducted in the Norwegian Sea (Foulds et al. (2022)) and in the northern Gulf of Mexico (Gorchov Negron et al. (2020)). Total loss rates (emission rates divided by production rates) compare well to total loss rates in the northern Gulf of Mexico, whereas total loss rates in the Norwegian Sea are one order of magnitude smaller due to higher production rates.

RQ 4: How well can we measure important tracers for CH₄ source attribution ($\delta^{13}\text{C}(\text{CH}_4)$, C₂H₆) using airborne laser-based absorption spectroscopy?

The successful detection of $\delta^{13}\text{C}(\text{CH}_4)$ signals decisively depends on the measurement frequency and the precision of the laser absorption spectrometer, but also on the source type or rather its source signature. The greater the deviation of source signatures from ambient $\delta^{13}\text{C}(\text{CH}_4)$ (around -47.6‰), the easier it is to detect a signal.

Depending on the instrument precision, signals in $\delta^{13}\text{C}(\text{CH}_4)$ are detectable for all source types, provided that CH₄ enhancements are sufficiently high. At the best achievable laboratory precision of 0.86‰, fossil fuel sources with CH₄ enhancements of at least approximately 250 ppb (source signature -40‰) are detectable. Within this work, airborne $\delta^{13}\text{C}(\text{CH}_4)$ measurements at a precision of 2.19‰ (1 σ , 2 Hz) for the MAGIC campaign and 1.81‰ (1 σ , 2 Hz) for the MTGA campaign were obtained. Total in-flight uncertainties including precision, calibration uncertainties and H₂O correction were 5.12‰ for MAGIC and 4.32‰ for MTGA. An improvement of the precision for MTGA compared to MAGIC was achieved by the replacement of the sample cell mirrors leading to higher signal to noise ratios.

A laboratory comparison between the DLR-QCLS and the commercial Picarro Isotope Analyser reveals good agreement between both instruments during simultaneous measurements of ambient air. The laboratory measurement of CH₄ plumes with different source signatures demonstrates that the DLR-QCLS is capable to qualitatively detect source signatures, meaning that source signatures higher and lower than the ambient background could be differentiated. Due to its higher precision compared to the Picarro Isotope Analyser, the DLR-QCLS is able to detect sources with smaller

enhancements. A higher frequent measurement, such as from the DLR-QCLS, increases the accuracy of source signature determination with the Keeling-plot method, especially with the aim to detect plumes from point sources, which typically only last for a few seconds during airborne sampling.

A comparison with flask measurements, feasible for one flight during MAGIC, shows agreement with measured (ambient) $\delta^{13}\text{C}(\text{CH}_4)$ within uncertainties.

RQ 5: How well do the observational-based C_2H_6 to CH_4 (C2:C1) ratios and $\delta^{13}\text{C}(\text{CH}_4)$ source signatures of Angolan and Gabonese offshore oil installations agree with data from the literature?

As expected, CH_4 enhancements detected during MAGIC were too small to derive source signatures from wetland sources. In contrast, very high CH_4 enhancements up to several ppm with correlating signals in $\delta^{13}\text{C}(\text{CH}_4)$ and C_2H_6 were measured during MTGA.

C_2H_6 to CH_4 (C2:C1) ratios were calculated for a set of Angolan and Gabonese offshore oil and gas installations. C2:C1 ratios are on average 18.3% (Angolan installations) and 12.0% (Gabonese installations) and, thus, in the expected range for oil fields (10-25%, Xiao et al. (2008)).

Determined source signatures for both Angolan and Gabonese installations are around -52‰ and -62‰ and, thus, more depleted in $^{13}\text{C}(\text{CH}_4)$ than expected if compared with the global $\delta^{13}\text{C}(\text{CH}_4)_{sc}$ database (see Figure 2.5, Sherwood et al. (2017)), which has a maximum at -42‰ but spreads from -15 to -80‰ for conventional gas. Uncertainties of derived source signatures range between 5.3‰ and 8.8‰ and arise from the total measurement uncertainty (precision, calibration, H_2O correction) and the uncertainty of the linear regression to derive source signatures (Keeling-plot method). However, the derived source signatures from repeated measurements around the same group of installations were not consistent, which points to the necessity for further improvement of the quantitative detection of source signatures.

RQ 6: What are the challenges of airborne $\delta^{13}\text{C}(\text{CH}_4)$ measurements and what are necessary improvements?

The variability of measured $\delta^{13}\text{C}(\text{CH}_4)$ during both campaigns is high (ranging from -30‰ to -60‰), which is rather due to the measurement uncertainty instead of natural variability. Instrument artefacts exist, which occasionally lead to instabilities of the spectral fit causing declines of $\delta^{13}\text{C}(\text{CH}_4)$ of several ‰. The DLR-QCLS was capable to detect the high CH_4 enhancements of MTGA. However, for these high CH_4 enhancements, linearity of the DLR-QCLS might be compromised, as laboratory experiments and other studies suggest (Harris et al. (2020)). A dependency of the $\delta^{13}\text{C}(\text{CH}_4)$ measurement on the gas matrix could explain the difference in laboratory compared to in-flight plume measurements (Harris et al. (2020)) and needs to be further investigated.

To answer the hypothesis of this work, generic emission reporting methods, which are commonly used in global inventories and for UNFCCC reporting do not correctly reflect offshore emissions in the southern North Sea. Recent developments and improvements of laser absorption spectroscopy

allow for continuous airborne measurements of the two tracers $\delta^{13}\text{C}(\text{CH}_4)$ and C_2H_6 . In this work, the $\delta^{13}\text{C}(\text{CH}_4)$ measurement is still of limited value in supporting the characterization of offshore fossil fuel emissions in western Central Africa.

The following studies are suggested for improvements and to further test the ability of the DLR-QCLS to study in-flight source signatures of different CH_4 sources: To quantitatively derive source signatures, extended laboratory tests need to be conducted across a wider range of CH_4 and $^{13}\text{CH}_4$ mole fractions to examine the linearity of the $\delta^{13}\text{C}(\text{CH}_4)$ measurement. Further, tests for varying compositions of the gas matrix (e. g. varying O_2 and Ar) might be conducted. To minimize dependencies on different gas matrix compositions, gas mixtures in ambient air instead of synthetic air need to be used for in-flight calibrations, which is envisaged for future measurements. Additionally, regular ground calibration of the instrument against known source signatures from various ambient sources, alongside the Picarro Isotope Analyser, should be implemented. Furthermore, in-flight measurements of one or more target cylinders with known source signatures might aid in improving in-flight source detection by relating measured enhancements and source signatures to those from the target cylinders.

To facilitate comparisons of top-down and bottom-up observations and hence, better resolve discrepancies, generating bottom-up inventories at facility-scale and accounting for temporal variability would be extremely valuable. Given the similar absolute emission rates of offshore emissions across different geographical regions, mitigation efforts are equally imperative across fossil fuel production sites. Generally, more measurements are needed world-wide to reveal mitigation potentials in order to successfully reduce CH_4 emissions and such global warming.

Appendix A

Additional information on Chapter 3

Calculation of uncertainties for CH₄ flux estimates

The uncertainty of the flux calculation (see Eq. 3.1 and Eq. 3.2 in Section 3.3), represented as confidence intervals of one standard deviation (1σ), is determined using the Gaussian error propagation. The uncertainties of the calculated CH₄ fluxes $Flux_i$ for each layer i result from the uncertainties of each measured parameter q (Eq. A.1). These parameters are the elevated CH₄ mole fractions C_i , wind speed V_{\perp} , pressure p_i , temperature T_i , plume width x_i , and plume height D_i . The total uncertainty is the sum of the uncertainties of the fluxes calculated for each transect (Eq. A.2).

$$u(Flux_i) = Flux_i \cdot \sqrt{\sum_q^{parameters} \left(\frac{u(q)}{q}\right)^2} \quad (\text{A.1})$$

$$u(Flux_{total}) = \sum_i^{transects} u(Flux_i) \quad (\text{A.2})$$

The beginning of the plume is defined as a measured concentration enhancement that is higher than 2σ of the background mole fractions. For ΔC_i the CH₄ mole fractions measured inside (C_i) and outside (C_0) the plume are used. Both C_i and C_0 have a systematic uncertainty resulting from the Picarro instrument uncertainty of 1.2 ppb (France et al. (2021)) (Eq. A.3). The background mole fraction at each point j within the plume is determined from an interpolation between $C_{0,a}$ and $C_{0,b}$, which are the mean CH₄ mole fractions within 30s before and after the plume. The uncertainty of the interpolated background at each point $u(C_{0,j})$ is calculated from the standard deviations $\sigma_{0,a}$ and $\sigma_{0,b}$ of $C_{0,a}$ and $C_{0,b}$ (Eq. A.4). The parameter n denotes the number of points within the plume.

$$u(\Delta C_i) = \sqrt{\sum_a^b (u(C_{i,j})^2 + u(C_{0,j})^2)} \quad (\text{A.3})$$

$$u(\Delta C_{0,j}) = \sqrt{(\sigma_{0,a} \cdot \frac{n_i - j}{n_i})^2 + (\sigma_{0,b} \cdot \frac{j}{n_i})^2} \quad (\text{A.4})$$

The perpendicular wind speed V_{\perp} is determined from the average aircraft heading, measured average horizontal wind speed and average wind angle over all the transects. The uncertainty of

the perpendicular wind speed $u(V_{\perp})$ is a result of the standard deviations and is valid for all the transects.

$$u(V_{\perp}) = \sqrt{\left(\frac{\partial V_{\perp}}{\partial heading} \cdot \sigma_{heading}\right)^2 + \left(\frac{\partial V_{\perp}}{\partial windspeed} \cdot \sigma_{windspeed}\right)^2 + \left(\frac{\partial V_{\perp}}{\partial windangle} \cdot \sigma_{windangle}\right)^2} \quad (\text{A.5})$$

For the uncertainties of pressure $u(p_i)$ and temperature $u(T_i)$, the standard deviations of the mean values across the plume and the 30 s background are taken.

The plume width Δx_i is calculated from the measured aircraft speed and the time span of the plume encounter. The uncertainty of the plume width $u(x_i)$ is derived from the uncertainty (standard deviation) of the measured velocity of the aircraft.

Since a well-mixed plume within the boundary layer is assumed, the uncertainty of plume height $u(D_i)$ is characterized by the uncertainty arising from the estimation of the boundary layer height. Therefore, $u(D_i)$ is only relevant for the uncertainty of the flux calculated for the uppermost layer. The uncertainty of the wind measurement is the biggest contributor to the total uncertainty of the flux calculation (typically 90%). Uncertainties of wind speed and wind direction measurements range from 1 to 3 m s⁻¹ (23%–70% relative uncertainty at 1 σ) and from 8 to 39° (2%–19% relative uncertainty at 1 σ), respectively. The uncertainty of plume height ranges from 20 to 32 m and accounts for less than 10% of the total uncertainty of the flux calculated for the uppermost layer.

Production and loss rates for sampled installations in the southern North Sea

Table A.1 shows platform production rates along with calculated loss rates. No loss rates were determined for installations, where emissions were below detection limit (0.3 kg h⁻¹ (2 σ)) and thus, no enhancements measured (abbreviation “no enh.”). Z1-Z8 are non-emitting installations from fly-bys. Individual platform production data for 2019 were taken from the UK Oil and Gas Authority (OGA), the Dutch Oil and gas portal (NLOG) and operator reported data. UK production rates are given as monthly values by OGA. Thereby, production from upstream fields with only subsea wells and no platform infrastructure is included. Operator reported production data as available for Dutch sites was provided by Dutch operators for the specific survey day.

Table A.1: Reported production rates and calculated loss rates for sampled UK (P1-P6) and Dutch (P7-P11) installations (see Figure 3.6 in Section 3.4.3). Z1-Z8 are (non-emitting) installations from fly-bys.

facility	Dry gas production (OGA (UK), NLOG (Dutch)) [Nm ³ month ⁻¹]	Operator reported gas production [Nm ³ day ⁻¹]	loss rate [%]	Start of production [yr]
P1 ^a	10238885 (+ 98 Nm ³ gas condensate)	n.a.	0.92 ± 0.42	1988
P2 ^b	25765475	n.a.	0.10 ± 0.07	1990
P3	28090814 (+ 44 Nm ³ gas condensate)	n.a.	no enh.	1967
P4 ^b	44571997 (+ 194 Nm ³ gas condensate)	n.a.	3.10 ± 1.19	1968
P5	72934875 (+ 72 Nm ³ gas condensate)	n.a.	no enh.	1968
P6 ^b	11259835 (+ 150 Nm ³ gas condensate)	n.a.	no enh.	1969
P7	855993	226383	0.73 ± 0.27	1977
P8	11049455	854000	0.18 ± 0.05	1983
P9	0	0	no enh.	1991
P10	28340954	2400000 ^c	0.08 ± 0.02	1994
P11	13314491	335996	0.17 ± 0.04	2005
Z1 ^d	3145322 (+ 3 Nm ³ gas condensate)	n.a.	no enh.	1993
Z2 ^d	14321737 (+ 198 Nm ³ gas condensate)	n.a.	no enh.	2003
Z3	0	n.a.	no enh.	1987
Z4	3794100	n.a.	no enh.	1985
Z5	0	n.a.	no enh.	2007
Z6	0	n.a.	no enh.	2004
Z7	13542079	n.a.	no enh.	2002
Z8	3251685	n.a.	no enh.	1990

^a no gas production for the month of survey. Production only of delivering subsea wells.

^b including one delivering subsea well

^c gas production with little gas condensate (gas condensate is injected back into export gas)

^d unmanned installation

Appendix B

Additional information on Chapter 5

Calibration standards used for in-flight calibrations during MAGIC

Table B.1: MAGIC calibration gas cylinders used for in-flight calibrations with reference values for CH_4 , $^{12}\text{C}(\text{CH}_4)$, $^{13}\text{C}(\text{CH}_4)$ and C_2H_6 . The cylinders are secondary-standards, which were cross-calibrated against primary DLR-NOAA standards (see Section 4.3.3).

MAGIC				
cylinder #	CH_4 [ppb]	$^{12}\text{C}(\text{CH}_4)$ [ppb]	$^{13}\text{C}(\text{CH}_4)$ [ppb]	C_2H_6 [ppb]
#1 - high	1889.11	1869.2425	19.6901	517.96
#2 - high	1877.58	1857.8335	19.5792	493.40
#3 - high	1836.80	1817.4820	19.1313	522.73

Calibration standards used for in-flight calibrations during MTGA

Table B.2: MTGA calibration gas cylinders used for in-flight calibrations with reference values for CH_4 , $^{12}\text{C}(\text{CH}_4)$, $^{13}\text{C}(\text{CH}_4)$ and C_2H_6 . The cylinders are secondary-standards, which were cross-calibrated against primary DLR-NOAA standards (see Section 4.3.3).

MTGA				
cylinder #	CH_4 [ppb]	$^{12}\text{C}(\text{CH}_4)$ [ppb]	$^{13}\text{C}(\text{CH}_4)$ [ppb]	C_2H_6 [ppb]
#1 - low	1866.67	1846.7231	19.4664	510.17
#2 - low	1798.48	1779.2699	18.6863	555.6
#3 - high	2407.47	2385.3212	25.7566	0
#4 - high	2405.61	2382.0272	25.7313	0
#5 - high	2434.14	2380.2262	25.7364	0
#6 - high	2408.59	2408.4750	26.0237	0
#7 - high	2511.77	2383.2082	25.7262	0

Appendix C

Publications

Pühl, M., Roiger, A., Fiehn, A., Gorchov Negron, A. M., Kort, E. A., Schwietzke, S., Pisso, I., Foulds, A., Lee, J., France, J. L., Jones, A. E., Lowry, D., Fisher, R. E., Huang, L., Shaw, J., Bateson, P., Andrews, S., Young, S., Dominutti, P., Lachlan-Cope, T., Weiss, A. and Allen, G.: Aircraft-based mass balance estimate of methane emissions from offshore gas facilities in the southern North Sea, *Atmos. Chem. Phys.*, 24, 1005-1024, <https://doi.org/10.5194/acp-24-1005-2024>, 2024.

Publications as co-author, sorted chronologically:

Klausner, T., Mertens, M., Huntrieser, H., Galkowski, M., Kuhlmann, G., Baumann, R., Fiehn, A., Jöckel, P., **Pühl, M.** and Roiger, A.: Urban greenhouse gas emissions from the Berlin area: A case study using airborne CO₂ and CH₄ in situ observations in summer 2018, *Elem. Sci. Anth.*, 8(15), <https://doi.org/10.1525/elementa.411>, 2020.

Foulds, A., Allen, G., Shaw, J. T., Bateson, P., Barker, P. A., Huang, L., Pitt, J. R., Lee, J. D., Wilde, S. E., Dominutti, P., Purvis, R. M., Lowry, D., France, J. L., Fisher, R. E., Fiehn, A., **Pühl, M.**, Bauguitte, S. J. B., Conley, S. A., Smith, M. L., Lachlan-Cope, T., Pisso, I. and Schwietzke, S.: Quantification and assessment of methane emissions from offshore oil and gas facilities on the Norwegian continental shelf, *Atmos. Chem. Phys.*, 22, 4303-4322, <https://doi.org/10.5194/acp-22-4303-2022>, 2022.

Reum, F., Roiger, A., Pätzold, F., Bretschneider, L., Gottschaldt, K.-D., Huntrieser, H., Lichtenstern, M., Marshall, J., **Pühl, M.** and Lampert, A.: Atmospheric methane, carbon dioxide and meteorological observations with the helicopter-borne probe HELiPOD after the Nord Stream leaks from 2022, *Nature Communications*, accepted.

Fiehn, A., Eckl, M., **Pühl, M.**, Bräuer, T., Gottschaldt, K.-D., Aufmhoff, H., Eirenschmalz, L., Neumann, G., Sakellariou, F., Sauer, D., De Aguiar Ventura, G., Nayole Cadete, W., Luciano Zua, D., Xavier, M., Correia, P., Roiger, A.: Angolan offshore oil and gas methane emissions below inventory estimates, to be submitted to *Atmos. Chem. Phys.* by end of 2024.

List of Figures

1.1	Global surface temperature change since 1850	2
1.2	Growth of atmospheric CH ₄ and change in $\delta^{13}\text{C}(\text{CH}_4)$ since 1998	4
2.1	Mean temperature profile of the atmosphere with its layers	8
2.2	Solar and Earth's emission spectra and atmospheric absorption	10
2.3	Trend of global atmospheric CH ₄	12
2.4	Top-down and bottom-up estimates for CH ₄ sources and sinks	13
2.5	Distribution of $\delta^{13}\text{C}(\text{CH}_4)$ for CH ₄ sources	18
2.6	Record of global atmospheric CH ₄ and $\delta^{13}\text{C}(\text{CH}_4)$ since 1150 and 1750	20
2.7	Schematic for the airborne mass balance approach	22
2.8	Schematic for tunable laser absorption spectroscopy	26
2.9	Voigt profile of molecular absorption line	27
3.1	Southern North Sea study: Flight paths	31
3.2	CH ₄ measurements downwind of P1	33
3.3	Comparison of calculated CH ₄ fluxes to bottom-up and top-down estimates	35
3.4	Transect downwind of P1 with time series of CH ₄ , CO ₂ and C ₂ H ₆	41
3.5	Correlation of CH ₄ with CO ₂ and C ₂ H ₆	42
3.6	Loss rates of sampled installations	44
3.7	Comparison of calculated CH ₄ fluxes, production rates and loss rates to other offshore regions	45
4.1	Isotopic plume detection: Estimation of the measured atmospheric $\delta^{13}\text{C}(\text{CH}_4)_{meas}$	51
4.2	Isotopic source signature: Example for Keeling plot	52
4.3	DLR-QCLS instrument components.	54
4.4	DLR-QCLS optics compartment top view.	55
4.5	Selection of a suitable isotope laser: Modelled synthetic transmission spectra	57
4.6	DLR-QCLS raw spectrum with fit and baseline generated by Jfit	59
4.7	Schematic of calibration setup with calibrations curves for ¹² CH ₄ and ¹³ CH ₄	61
4.8	Allan variance for species measured by DLR-QCLS	63
4.9	Laboratory setup for the linearity experiment	65
4.10	Linearity experiment of DLR-QCLS measured species	66
4.11	Laboratory setup for water vapor experiment	68
4.12	Time series of laboratory water vapour dependency experiment	69
4.13	Water vapor dependency of retrieved mole fractions	70
4.14	Applied water corrections to retrieved mole fractions	71

4.15	Comparison of DLR-QCLS with the Picarro Analyser G2210i: Simultaneous measurement of gas cylinders	73
4.16	Schematic for laboratory comparison of the DLR-QCLS with the Picarro Analyser G2210i.	74
4.17	Laboratory comparison of the DLR-QCLS with the Picarro Analyser G2210i	75
4.18	Correction of $\delta^{13}\text{C}(\text{CH}_4)$ signal for the right source signature.	76
4.19	Isotopic plume detection: Estimation of the measured atmospheric $\delta^{13}\text{CH}_{4\text{meas}}$ at the DLR-QCLS laboratory precision	77
5.1	MAGIC field campaign: Flight paths, target area and research aircraft	81
5.2	MAGIC and MTGA field campaigns: Calibration setup for DLR-QCLS	83
5.3	MAGIC field campaign: DLR-QCLS measurement during ascents/descents	84
5.4	Comparison of DLR-QCLS and Picarro CH_4 measurement for all flights during MAGIC	86
5.5	MAGIC flight on 22/08/2019: Flight pattern and time series	87
5.6	MAGIC flight on 22/08/2019: Comparison of DLR-QCLS to flask measurement	88
5.7	MTGA field campaign: Flight paths, target area and research aircraft	90
5.8	MTGA flight 14a: Time series	92
5.9	MTGA flight 14a: Zoom in time series and artefacts	93
5.10	Comparison of DLR-QCLS and Picarro CH_4 measurement for all flights during MTGA	95
5.11	Comparison of DLR-QCLS and Picarro CH_4 measurement for all flights during MTGA (zoom)	96
5.12	MTGA flight 14a and 18b: Flight path with color-coded CH_4	97
5.13	MTGA flight on 14/09/20: time series and Keeling plot for peak #1	98

List of Tables

3.1	Comparison of calculated CH ₄ fluxes to bottom-up and top-down estimates for UK sites	36
3.2	Comparison of calculated CH ₄ fluxes to bottom-up and top-down estimates for Dutch sites	36
3.3	Measured and reported CO ₂ fluxes and C2:C1 ratios	43
4.1	DLR-QCLS: Deployed lasers	58
4.2	Reference values for DLR-NOAA calibration standards	60
4.3	Laboratory precision and drift of the DLR-QCLS measured species	64
4.4	Water broadening correction factors in retrieval software Jfit.	69
5.1	Payload of the DLR Cessna for the MAGIC campaign	82
5.2	Total uncertainty of DLR-QCLS measurement for MAGIC	85
5.3	Payload of the DLR Falcon for the MTGA campaign	91
5.4	Total uncertainty of DLR-QCLS measurement for MTGA	94
5.5	MTGA: Results for C2:C1 ratios and source signatures of a set of Angolan installations.	99
5.6	MTGA: Results for C2:C1 ratios and source signatures of a set of Gabonese installations.	100
A.1	Southern North Sea: reported production rates and calculated loss rates	111
B.1	Calibration gas cylinders used for in-flight calibrations during MAGIC	113
B.2	Calibration standards used for in-flight calibrations during MTGA	114

Acronyms

BAS	British Antarctic Service
BEIS	Business, Energy & Industrial Strategy
BLH	boundary layer height
COVID-19	coronavirus disease 2019
DLR	Deutsches Zentrum für Luft- und Raumfahrt
DLR-QCLS	DLR-Quantum Cascade Laser Spectrometer
EEMS	Environmental and Emissions Monitoring System database
EPA GHGI	Environmental Protection Agency Greenhouse Gas Inventory
ERF	effective radiative forcing
ETS	Emissions Trading Scheme
FLEXPART	FLEXible PARTicle
GAW	Global Atmosphere Watch Programme
GC-IRMS	Gas Chromatography - Isotope Ratio Mass Spectrometry
GFEI	Global Fuel Exploitation Inventory
GML	Global Monitoring Laboratory
GOADS	Gulfwide Offshore Activity Data System
GOSAT	Greenhouse Gases Observing Satellite
GWP	global warming potential
HITRAN	High Resolution TRansmission molecular AbsorptioN database
ICL	Interband-cascade laser
IPCC	Intergovernmental Panel on Climate Change
IR	infrared
JAS	Jena Air Sampler
MAGIC	Monitoring of Atmospheric composition and Greenhouse gases through multi-Instruments Campaign
MFC	mass flow controller
MLO	Mauna Loa
MTGA	METHANE-To-Go Africa

NAEI	National Atmospheric Emissions Inventory
NLOG	Dutch Oil and gas portal
NOAA	National Oceanic and Atmospheric Administration
OGA	Oil and Gas Authority
OGMP	Oil & Gas Methane Partnership
OPRED	Offshore Petroleum Regulator for Environment and Decommissioning
PBL	planetary boundary layer
PFA	perfluoroalkoxy
ppb	parts per billion
ppm	parts per million
PPRS	Petroleum Production Reporting System
ppt	parts per trillion
QCL	Quantum Cascade Laser
SSP	Shared Socioeconomic Pathway
TEC	thermoelectric cooling controllers
TILDAS	tunable infrared laser direct absorption spectrometer
UK	United Kingdom
UKCS	United Kingdom Continental Shelf
UN CCAC	United Nations Climate & Clean Air Coalition
UNFCCC	United Nations Framework Convention on Climate Change
UV	ultraviolet
VIIRS	Visible Infrared Imaging Radiometer Suite
VPDB	Vienna Pee Dee Belemnite
WMO	World Meteorological Organization

Bibliography

- Angot, H., Davel, C., Wiedinmyer, C., et al.: Temporary pause in the growth of atmospheric ethane and propane in 2015-2018, *Atmos. Chem. Phys.*, 21, 15 153–15 170, <https://doi.org/10.5194/acp-21-15153-2021>, 2021.
- Barkley, Z. R., Davis, K. J., Feng, S., et al.: Forward Modeling and Optimization of Methane Emissions in the South Central United States Using Aircraft Transects Across Frontal Boundaries, *Geophysical Research Letters*, 46, 13 564–13 573, <https://doi.org/10.1029/2019GL084495>, 2019a.
- Barkley, Z. R., Lauvaux, T., Davis, K. J., et al.: Estimating Methane Emissions From Underground Coal and Natural Gas Production in Southwestern Pennsylvania, *Geophysical Research Letters*, 46, 4531–4540, <https://doi.org/10.1029/2019GL082131>, 2019b.
- Basu, S., Lan, X., Dlugokencky, E., et al.: Estimating emissions of methane consistent with atmospheric measurements of methane and $\delta^{13}\text{C}$ of methane, *Atmos. Chem. Phys.*, 22, 15 351–15 377, <https://doi.org/10.5194/acp-22-15351-2022>, 2022.
- Berden, G. and Engeln, R.: *Cavity ring-down spectroscopy: techniques and applications*, Blackwell Publishing Ltd., <https://doi.org/10.1002/9781444308259>, 2009.
- Bergamaschi, P., Schupp, M., and Harris, G. W.: High-precision direct measurements of $^{13}\text{CH}_4/^{12}\text{CH}_4$ and $\text{CH}_3\text{D}/^{12}\text{CH}_4$ ratios in atmospheric methane sources by means of a long-path tunable diode laser absorption spectrometer, *Appl. Optics*, 33, 7704–7716, <https://doi.org/10.1364/AO.33.007704>, 1994.
- Bergamaschi, P., Lubina, C., Konigstedt, R., et al.: Stable isotopic signatures ($\delta^{13}\text{C}$, δD) of methane from European landfill site, *J. Geophys. Res.*, 103, 8251–8265, <https://doi.org/10.1029/98jd00105>, 1998.
- bp: Statistical Review of World Energy, <http://www.bp.com/statisticalreview>, 2022.
- Brand, W. A., Rothe, M., Sperlich, P., Strube, M., and Wendeberg, M.: Automated simultaneous measurement of the $\delta^{13}\text{C}$ and $\delta^2\text{H}$ values of methane and the $\delta^{13}\text{C}$ and $\delta^{18}\text{O}$ values of carbon dioxide in flask air samples using a new multi cryo-trap/gas chromatography/isotope ratio mass spectrometry system, *Rapid Commun. Mass Spectrom.*, 30, 1523–1539, <https://doi.org/10.1002/rcm.7587>, 2016.

- Brown, P., Cardenas, L., Del Vento, S., et al.: UK Greenhouse Gas Inventory 1990 to 2021: Annual Report for submission under the Framework Convention on Climate Change, Ricardo Energy & Environment for the Department for Business, Energy & Industrial Strategy (BEIS), ISBN 978-0-9933975-9-2, 2023.
- Brownlow, R., Lowry, D., Fisher, R. E., et al.: Isotopic Ratios of Tropical Methane Emissions by Atmospheric Measurement, *Global Biogeochemical Cycles*, 31, 1408–1419, <https://doi.org/10.1002/2017GB005689>, 2017.
- Byrom, R. E. and Shine, K. P.: Methane’s solar radiative forcing, *Geophysical Research Letters*, 49, <https://doi.org/10.1029/2022GL098270>, 2022.
- Cain, M., J., W. N., Fisher, R. E., et al.: A study of a methane enhancement over the North Sea, *J. Geophys. Res.-Atmos.*, 122, 7630–7645, <https://doi.org/10.1002/2017JD026626>, 2017.
- Cambaliza, M. O. L., Shepson, P. B., Bogner, J., Caulton, D. R., Stirm, B., et al.: Quantification and source apportionment of the methane emission flux from the city of Indianapolis, *Elem. Sci. Anth.*, 14, 13 159–13 174, <https://doi.org/10.12952/journal.elementa.000037>, 2015.
- Cantrell, C. A., Shetter, R. E., McDaniel, A. H., et al.: Carbon kinetic isotope effect in the oxidation of methane by the hydroxyl radical, *J. Geophys. Res. Atmos.*, 95, 22 455–22 462, <https://doi.org/10.1029/JD095iD13p22455>, 1990.
- Catoire, V., Robert, C., Chartier, M., et al.: The SPIRIT airborne instrument: a three-channel infrared absorption spectrometer with quantum cascade lasers for in situ atmospheric trace-gas measurements, *Appl. Phys. B*, 123, <https://doi.org/10.1007/s00340-017-6820-x>, 2017.
- Chen, H., Winderlich, J., Gerbig, C., et al.: Validation of routine continuous airborne CO₂ observations near the Bialystok Tall Tower, *Atmos. Meas. Tech.*, 5, 873–889, <https://doi.org/10.5194/amt-5-873-2012>, 2012.
- Chen, Z., Yacovitch, T. I., Daube, C., et al.: Reconciling Methane Emission Measurements for Off-shore Oil and Gas Platforms with Detailed Emission Inventories: Accounting for Emission Intermittency, *ACS Environ. Au*, 3, 87–93, <https://doi.org/10.1021/acsenvironau.2c00041>, 2023.
- Conley, S., Franco, G., Faloon, I., et al.: Methane emissions from the 2015 Aliso Canyon blowout in Los Angeles, CA, *Science*, 351, 1317–1320, <https://doi.org/10.1126/science.aaf2348>, 2016.
- Connolly, M., Dingley, O., Connolly, R., and Soon, W.: Comparing different tropopause estimates from high-resolution ozonesondes, *Earth and Space Science*, 11, <https://doi.org/10.1029/2024EA003584>, 2024.
- Dlugokencky, E. J., Myers, R. C., Lang, P. M., et al.: Conversion of NOAA atmospheric dry air CH₄ mole fractions to a gravimetrically prepared standard scale, *J. Geochphys. Res.*, 110, <https://doi.org/10.1029/2005JD006035>, 2005.

- Drinkwater, A., Palmer, P., Feng, L., et al.: Atmospheric data support a multi-decadal shift in the global methane budget towards natural tropical emissions, *Atmos. Chem. Phys.*, 23, 8429–8452, <https://doi.org/10.5194/acp-23-8429-2023>, 2023.
- ECMWF: The 2023 Annual Climate Summary: Global Climate Highlights 2023, <https://climate.copernicus.eu/global-climate-highlights-2023>, 09 January 2024.
- Elvidge, C. D., Zhizhin, M., Hsu, F.-C., and Baugh, K. E.: VIIRS Nightfire: Satellite Pyrometry at Night, *Remote Sens.*, 5, 4423–4449, <https://doi.org/10.3390/rs5094423>, 2013.
- Elvidge, C. D., Zhizhin, M., Baugh, K., Hsu, F.-C., and Ghosh, T.: Methods for Global Survey of Natural Gas Flaring from Visible Infrared Imaging Radiometer Suite Data, *Energies*, 9, <https://doi.org/10.3390/en9010014>, 2015.
- Etiopie, G. and Schwietzke, S.: Global geological methane emissions: An update of top-down and bottom-up estimates, *Elem. Sci. Anth.*, 7, <https://doi.org/10.1525/elementa.383>, 2019.
- Etiopie, G., Ciotoli, G., Schwietzke, S., and Schoell, M.: Gridded maps of geological methane emissions and their isotopic signature, *Earth Syst. Sci. Data*, 11, 1–22, <https://doi.org/10.5194/essd-11-1-2019>, 2019.
- EU: European Commission: EU strategy to reduce methane emissions, <https://eur-lex.europa.eu/legal-content/EN/TXT/?uri=CELEX:52020DC0663>, 2020.
- Eurostat: Energy, transport and environment statistics - 2020 edition: Energy Production 2018, Publications Office of the European Union, <https://doi.org/10.2785/522192>, 2020.
- Eyer, S., Tuzson, B., Popa, M. E., et al.: Real-time analysis of $\delta^{13}\text{C}$ and $\delta\text{D-CH}_4$ in ambient air with laser spectroscopy: method development and first intercomparison results, *Atmos. Meas. Tech.*, 9, 263–280, <https://doi.org/10.5194/amt-9-263-2016>, 2016.
- Eyring, V., Gillett, N., Achuta Rao, K., et al.: Human Influence on the Climate System. In *Climate Change 2021: The Physical Science Basis. Contribution of Working Group I to the Sixth Assessment Report of the Intergovernmental Panel on Climate Change* [Masson-Delmotte, V., P. Zhai, A. Pirani, S.L. Connors, C. Péan, S. Berger, N. Caud, Y. Chen, L. Goldfarb, M.I. Gomis, M. Huang, K. Leitzell, E. Lonnoy, J.B.R. Matthews, T.K. Maycock, T. Waterfield, O. Yelekçi, R. Yu, and B. Zhou (eds.)], Cambridge University Press, Cambridge, United Kingdom and New York, NY, USA, <https://doi.org/10.1017/9781009157896.005>, 2021.
- Feng, L., Palmer, P. I., Parker, R. J., Lunt, M. F., and Bösch, H.: Methane emissions are predominantly responsible for record-breaking atmospheric methane growth rates in 2020 and 2021, *Atmos. Chem. Phys.*, 23, 4863–4880, <https://doi.org/10.5194/acp-23-4863-2023>, 2023.
- Ferretti, D. F., Miller, J. B., White, J. W., et al.: Unexpected changes to the global methane budget over the past 2000 years, *Science*, 309, 1714–7–1717, <https://doi.org/10.1126/science.1115193>, 2005.

- Fiehn, A., Eckl, M., Kostinek, J., et al.: Source apportionment of methane emissions from the Upper Silesian Coal Basin using isotopic signatures, *Atmos. Chem. Phys.*, 23, 15 749–15 765, <https://doi.org/10.5194/acp-23-15749-2023>, 2023.
- Fisher, R. E., France, J. L., Lowry, D., et al.: Measurement of the ^{13}C isotopic signature of methane emissions from northern European wetlands, *Global Biogeochem. Cycles*, 31, 605–623, <https://doi.org/10.1002/2016GB005504>, 2017.
- Forster, P., Storelvmo, T., Armour, K., et al.: The Earth’s Energy Budget, Climate Feedbacks, and Climate Sensitivity. In *Climate Change 2021: The Physical Science Basis. Contribution of Working Group I to the Sixth Assessment Report of the Intergovernmental Panel on Climate Change* [Masson-Delmotte, V., P. Zhai, A. Pirani, S.L. Connors, C. Péan, S. Berger, N. Caud, Y. Chen, L. Goldfarb, M.I. Gomis, M. Huang, K. Leitzell, E. Lonnoy, J.B.R. Matthews, T.K. Maycock, T. Waterfield, O. Yelekçi, R. Yu, and B. Zhou (eds.)], Cambridge University Press, Cambridge, United Kingdom and New York, NY, USA, <https://doi.org/10.1017/9781009157896.009>, 2021.
- Foulds, A., Allen, G., Shaw, J. T., et al.: Quantification and assessment of methane emissions from offshore oil and gas facilities on the Norwegian continental shelf, *Atmos. Chem. Phys.*, 22, 4303–4322, <https://doi.org/10.5194/acp-22-4303-2022>, 2022.
- France, J. L., Bateson, P., Dominutti, P., et al.: Facility level measurement of offshore oil and gas installations from a medium-sized airborne platform: method development for quantification and source identification of methane emissions, *Atmos. Meas. Tech.*, 14, 71–88, <https://doi.org/10.5194/amt-14-71-2021>, 2021.
- Franco, B., Mahieu, E., Emmons, L. K., et al.: Evaluating ethane and methane emissions associated with the development of oil and natural gas extraction in North America, *Environ. Res. Lett.*, 11, <https://doi.org/10.1088/1748-9326/11/4/044010>, 2016.
- Fujita, R., Morimoto, S., Maksyutov, S., et al.: Global and Regional CH_4 Emissions for 1995–2013 Derived From Atmospheric CH_4 , $\delta^{13}\text{C}\text{-CH}_4$, and $\delta D\text{-CH}_4$ Observations and a Chemical Transport Model, *J. Geophys. Res. Atmos.*, 125, <https://doi.org/10.1029/2020JD032903>, 2020.
- Garman, K. E., Hill, K. A., Wyss, P., et al.: An Airborne and Wind Tunnel Evaluation of a Wind Turbulence Measurement System for Aircraft-Based Flux Measurements, *J. Atmos. Ocean. Tech.*, 23, 1696–1708, <https://doi.org/10.1175/JTECH1940.1>, 2006.
- Gałkowski, M., Jordan, A., Rothe, M., et al.: In situ observations of greenhouse gases over Europe during the CoMet 1.0 campaign aboard the HALO aircraft, *Atmos. Meas. Tech.*, 14, 1525–154, <https://doi.org/10.5194/amt-14-1525-2021>, 2021.
- Gorchov Negron, A. M., Kort, E. A., Conley, S. A., and Smith, M. L.: Airborne Assessment of Methane Emissions from Offshore Platforms in the U.S. Gulf of Mexico, *Environ. Sci. Technol.*, 54, 5112–5120, <https://doi.org/10.1021/acs.est.0c00179>, 2020.
- Gordon, I. E., Rothman, L. S., Hargreaves, R. J., et al.: The HITRAN2020 molecular spectroscopic database, *J. Quant. Spectrosc. Radiat. Transfer*, 277, <https://doi.org/10.1016/j.jqsrt.2021.107949>, 2022.

- Griffith, D. W. T.: Calibration of isotopologue-specific optical trace gas analysers: a practical guide, *Atmos. Meas. Tech.*, 11, 6189–6201, <https://doi.org/10.5194/amt-11-6189-2018>, 2018.
- Gulev, S., Thorne, P. W., Ahn, J., et al.: Changing State of the Climate System. In *Climate Change 2021: The Physical Science Basis. Contribution of Working Group I to the Sixth Assessment Report of the Intergovernmental Panel on Climate Change* [Masson-Delmotte, V., P. Zhai, A. Pirani, S.L. Connors, C. Péan, S. Berger, N. Caud, Y. Chen, L. Goldfarb, M.I. Gomis, M. Huang, K. Leitzell, E. Lonnoy, J.B.R. Matthews, T.K. Maycock, T. Waterfield, O. Yelekçi, R. Yu, and B. Zhou (eds.)], Cambridge University Press, Cambridge, United Kingdom and New York, NY, USA, <https://doi.org/10.1017/9781009157896.004>, 2021.
- Gvakharia, A., Kort, E. A., Smith, M. L., and Conley, S.: Testing and evaluation of a new airborne system for continuous N₂O, CO₂, CO, and H₂O measurements: the Frequent Calibration High-performance Airborne Observation System (FCHAOS), *Atmos. Meas. Tech.*, 6059–6074, <https://doi.org/10.5194/amt-11-6059-2018>, 2018.
- Hall, B. D., Dutton, G. S., and Elkins, J. W.: The NOAA nitrous oxide standard scale for atmospheric observations, *J. Geophys. Res.*, 112, <https://doi.org/10.1029/2006JD007954>, 2007.
- Harazono, Y., Iwata, H., Sakabe, A., et al.: Effects of water vapor dilution on trace gas flux, and practical correction methods, *Journal of Agricultural Meteorology*, 71, 65–76, <https://doi.org/10.2480/agrmet.D-14-00003>, 2015.
- Harris, S. J., Liisberg, J., Xia, L., et al.: N₂O isotopocule measurements using laser spectroscopy: analyzer characterization and intercomparison, *Atmos. Meas. Tech.*, 13, 2797–2831, <https://doi.org/10.5194/amt-13-2797-2020>, 2020.
- Hasan, N. A., Chikamoto, Y., , and McPhaden, M. J.: The influence of tropical basin interactions on the 2020–2022 double-dip La Niña, *Frontiers in Climate*, 4, <https://doi.org/10.3389/fclim.2022.1001174>, 2022.
- Hausmann, P., Sussmann, R., and Smale, D.: Contribution of oil and natural gas production to renewed increase in atmospheric methane (2007–2014): top-down estimate from ethane and methane column observations, *Atmos. Chem. Phys.*, 16, 3227–3244, <https://doi.org/10.5194/acp-16-3227-2016>, 2016.
- Hensen, A., Velzeboer, I., Frumau, K. F. A., van den Bulk, W. C. M., and van Dinther, D.: Methane emission measurements of offshore oil and gas platforms, National Institute for Public Health and the Environment, RIVM, TNO Report 2019 R1089, <http://resolver.tudelft.nl/uuid:a9c705b9-ec88-4316-827f-f9d7ffbd05c2>, 2019.
- Hoheisel, A., Yeman, C., Dinger, F., Eckhardt, H., and Schmidt, M.: An improved method for mobile characterisation of $\delta^{13}\text{CH}_4$ source signatures and its application in Germany, *Atmos. Meas. Tech.*, 12, 1123–1139, <https://doi.org/10.5194/amt-12-1123-2019>, 2019.

- Holmes, C. D.: Methane Feedback on Atmospheric Chemistry: Methods, Models, and Mechanisms, *Journal of Advances in Modeling Earth Systems*, 10, 1087–1099, <https://doi.org/10.1002/2017MS001196>, 2018.
- Honig, E., Montfoort, J. A., Dröge, R., et al.: Methodology for the calculation of emissions to air from the sectors Energy, Industry and Waste, National Institute for Public Health and the Environment, RIVM report 2022-0001, <https://doi.org/10.21945/RIVM-2022-0001>, 2022.
- International Energy Agency (IEA): Global Methane Tracker, <https://www.iea.org/reports/global-methane-tracker-2023#overview>, Licence: CC BY 4.0, February 2023.
- International Energy Agency (IEA): The Imperative of Cutting Methane from Fossil Fuels, <https://www.iea.org/reports/the-imperative-of-cutting-methane-from-fossil-fuels>, Licence: CC BY 4.0, October 2023.
- IPCC: Chapter 4: Fugitive Emissions, in: 2006 IPCC Guidelines for National Greenhouse Gas Inventories, vol. 2: Energy, The National Greenhouse Gas Inventories Program, Hayama, Kanagawa, Japan, ISBN 4-88788-032-4, 2006.
- Johnson, M. R., Tyner, D. R., Conley, S., Schwietzke, S., and Zavala-Araiza, D.: Comparisons of Airborne Measurements and Inventory Estimates of Methane Emissions in the Alberta Upstream Oil and Gas Sector, *Environ. Sci. Technol.*, 51, 13008–13017, <https://doi.org/10.1021/acs.est.7b03525>, 2017.
- Jones, V. T., Matthews, M. D., and Richers, D. M.: Light hydrocarbons for petroleum and gas prospecting, in *Geochemical Remote Sensing of the Subsurface, Handbook of Exploration Geochemistry*, vol. 7, Elsevier, New York, [https://doi.org/10.1016/S0168-6275\(00\)80029-X](https://doi.org/10.1016/S0168-6275(00)80029-X), 2000.
- Keeling, C. D.: The concentration and isotopic abundances of atmospheric carbon dioxide in rural areas, *Geochim. Cosmochim. Acta*, 13, 322–334, 1958.
- Kirschke, S., Bousquet, P., Ciais, P., et al.: Three decades of global methane sources and sinks, *Nature Geosci*, 6, 813–823, <https://doi.org/10.1038/ngeo1955>, 2013.
- Klausner, T., Mertens, M., Huntrieser, H., et al.: Urban greenhouse gas emissions from the Berlin area: A case study using airborne CO₂ and CH₄ in situ observations in summer 2018, *Elem. Sci. Anth.*, 8, <https://doi.org/10.1525/elementa.411>, 2020.
- Kooijmans, L. M. J., Uitslag, N. A. M., Zahniser, M. S., et al.: Continuous and high-precision atmospheric concentration measurements of COS, CO₂, CO and H₂O using a quantum cascade laser spectrometer (QCLS), *Atmos. Meas. Tech.*, 9, 5293–5314, <https://doi.org/10.5194/amt-9-5293-2016>, 2016.
- Kostinek, J.: Quantification of greenhouse gas fluxes by a new airborne laser absorption spectrometer, Ludwig-Maximilian-Universität, München, dissertation, 2019.

- Kostinek, J., Roiger, A., Eckl, M., et al.: Estimating Upper Silesian coal mine methane emissions from airborne in situ observations and dispersion modeling, *Atmos. Chem. Phys.*, 21, 8791–8807, <https://doi.org/10.5194/acp-21-8791-2021>, 2021.
- Lan, X., Basu, S., Schwietzke, S., et al.: Improved constraints on global methane emissions and sinks using $\delta^{13}\text{C-CH}_4$, *Global Biogeochemical Cycles*, 35, <https://doi.org/10.1029/2021GB007000>, 2021.
- Lan, X., Mund, J., Crotwell, A., et al.: Atmospheric Methane Dry Air Mole Fractions from the NOAA GML Carbon Cycle Cooperative Global Air Sampling Network, 1983-2022, Version 2023-08-28, <https://doi.org/10.15138/VNCZ-M766>, 2023.
- Lee, D. J., Mobbs, S. D., Wellpott, A., et al.: Flow rate and source reservoir identification from airborne chemical sampling of the uncontrolled Elgin platform gas release, *Atmos. Meas. Tech.*, 11, 1725–1739, <https://doi.org/10.5194/amt-11-1725-2018>, 2018.
- Lowe, D. C., Brenninkmeijer, C. A. M., Tyler, S. C., and Dlugkenky, E. J.: Determination of the isotopic composition of atmospheric methane and its application in the Antarctic, *J. Geophys. Res. Atmos.*, 96, <https://doi.org/10.1029/91JD01119>, 1991.
- Lowry, D., Fisher, R. E., France, J. L., et al.: Environmental baseline monitoring for shale gas development in the UK: Identification and geochemical characterisation of local source emissions of methane to atmosphere, *Science of the Total Environment*, 708, <https://doi.org/10.1016/j.scitotenv.2019.134600>, 2020.
- Lyon, D. R., Zavala-Araiza, D., Alvarez, R. A., et al.: Constructing a Spatially Resolved Methane Emission Inventory for the Barnett Shale Region, *Environ. Sci. Technol.*, 49, 8147–8157, <https://doi.org/10.1021/es506359c>, 2015.
- MacKay, K., Lavoie, M., Bournon, E., et al.: Methane emissions from upstream oil and gas production in Canada are underestimated, *Sci. Rep.*, 11, <https://doi.org/10.1038/s41598-021-87610-3>, 2021.
- Mallaun, C., Giez, A., and Baumann, R.: Calibration of 3-D wind measurements on a single engine research aircraft, *Atmos. Meas. Tech.*, 8, 3177–3196, <https://doi.org/10.5194/amt-8-3177-2015>, 2015.
- McManus, J. B., Zahniser, M. S., and Nelson, D. D.: Dual quantum cascade laser trace gas instrument with astigmatic Herriott cell at high pass number, *Appl. Opt.*, 50, A74–A85, <https://doi.org/10.1364/AO.50.000A74>, 2010.
- McManus, J. B., Zahniser, M. S., Nelson, D. D., et al.: Recent progress in laser-based trace gas instruments: performance and noise analysis, *Appl. Phys. B*, 119, 203–218, <https://doi.org/10.1007/s00340-015-6033-0>, 2015.
- Michel, S., Clark, J., Vaughn, B., et al.: Stable Isotopic Composition of Atmospheric Methane (^{13}C) from the NOAA GML Carbon Cycle Cooperative Global Air Sampling Network, 1998-2022, Version 2023-09-21, University of Colorado, Institute of Arctic and Alpine Research (INSTAAR), <https://doi.org/10.15138/9p89-1x02>, 2023.

- Miller, J. B. and Tans, P. P.: Calculating isotopic fractionation from atmospheric measurements at various scales, *Tellus B*, 55, 207–214, <https://doi.org/10.1034/j.1600-0889.2003.00020.x>, 2003.
- Nara, H., Tanimoto, H., Tohjima, Y., et al.: Emissions of methane from offshore oil and gas platforms in Southeast Asia, *Sci. Rep.*, 4, <https://doi.org/10.1038/srep06503>, 2014.
- Ni, X. and Groffman, P. M.: Declines in methane uptake in forest soils, *Proc. Natl. Acad. Sci. U.S.A.*, 115, 8587–8590, <https://doi.org/10.1073/pnas.1807377115>, 2018.
- Nisbet, E. G., Dlugokencky, E. J., Manning, M. R., et al.: Rising atmospheric methane: 2007–2014 growth and isotopic shift, *Global Biogeochemical Cycles*, 30, 1356–1370, <https://doi.org/10.1002/2016GB005406>, 2016.
- Nisbet, E. G., Manning, M. R., Dlugokencky, E. J., et al.: Very strong atmospheric methane growth in the 4 years 2014–2017: Implications for the Paris Agreement, *Global Biogeochemical Cycles*, 33, 318–342, <https://doi.org/10.1029/2018GB006009>, 2019.
- Nisbet, E. G., Fisher, R. E., Lowry, D., et al.: Methane mitigation: Methods to reduce emissions, on the path to the Paris agreement, *Reviews of Geophysics*, 58, <https://doi.org/10.1029/2019rg000675>, 2020.
- Nisbet, E. G., Allen, G., Fisher, R. E., et al.: Isotopic signatures of methane emissions from tropical fires, agriculture and wetlands: the MOYA and ZWAMPS flights, *Phil. Trans. R. Soc. A*, 380, <https://doi.org/10.1098/rsta.2021.0112>, 2021.
- Nisbet, E. G., Manning, M. R., Dlugokencky, E. J., et al.: Atmospheric Methane: Comparison Between Methane’s Record in 2006–2022 and During Glacial Terminations, *Global Biogeochemical Cycles*, 37, <https://doi.org/10.1029/2023GB007875>, 2023.
- NLOG: Dutch Oil and Gas Portal: Production figures for fields in 2019, <https://www.nlog.nl/datacenter/prodfigures/fields>, 2019.
- OGA: OGA Shell/Exxon Mobil Geochemistry Database for Southern North Sea, <https://opendata-nstauthority.hub.arcgis.com/documents/53769edfbc0f4938a7b07a5ee1d30204/about>, 2017.
- OGA: Oil and Gas Authority (North Sea Transition Authority): NSTA Field Production Points, PPRS (WGS84), <https://opendata-nstauthority.hub.arcgis.com/search>, 2019.
- OGA: UKCS Flaring and Venting Report, <https://ogauthorityreports.wixsite.com/ukcs-f-v-report-2020>, 2020.
- Oh, Y., Zhuang, Q., Welp, L. R., et al.: Revisiting enteric methane emissions from domestic ruminants and their $\delta^{13}\text{C}(\text{CH}_4)$ source signature, *Nat Commun*, 10, <https://doi.org/10.1038/s41467-019-11066-3>, 2019.
- Oh, Y., Zhuang, Q., Welp, L. R., et al.: Improved global wetland carbon isotopic signatures support post-2006 microbial methane emission increase, *Commun Earth Environ*, 3, <https://doi.org/10.1038/s43247-022-00488-5>, 2022.

- OPRED (BEIS): EEMS Atmospheric Emissions Calculations, https://assets.publishing.service.gov.uk/government/uploads/system/uploads/attachment_data/file/136461/atmos-calcs.pdf, 2008.
- O'Shea, S. J., Allen, G., Gallagher, M. W., et al.: Methane and carbon dioxide fluxes and their regional scalability for the European Arctic wetlands during the MAMM project in summer 2012, *Atmos. Chem. Phys.*, 14, 13 159–13 174, <https://doi.org/10.5194/acp-14-13159-2014>, 2014.
- Pandey, S., Gautam, R., Houweling, S., et al.: Satellite observations reveal extreme methane leakage from a natural gas well blowout, *P. Natl. Acad. Sci.*, 116, 26 376–26 381, <https://doi.org/10.1073/pnas.1908712116>, 2019.
- Peischl, J., Karion, A., Sweeney, C., et al.: Quantifying atmospheric methane emissions from oil and natural gas production in the Bakken shaleregion of North Dakota, *J. Geophys. Res. Atmos.*, 121, 6101–6111, <https://doi.org/10.1002/2015JD024631>, 2016.
- Peischl, J., Eilerman, S. J., Neuman, J. A., et al.: Quantifying Methane and Ethane Emissions to the Atmosphere From Central and Western U.S. Oil and Natural Gas Production Regions, *J. Geophys. Res. Atmos.*, 123, 7725–7740, <https://doi.org/10.1029/2018JD028622>, 2018.
- Peng, S., Lin, X., Thompson, R. L., et al.: Wetland emission and atmospheric sink changes explain methane growth in 2020, *Nature*, 612, 477–482, <https://doi.org/10.1038/s41586-022-05447-w>, 2022.
- Petty, G. W.: *A First Course in Atmospheric Radiation*, Sundog Publishing, 2 edn., 2006.
- Pisso, I., Sollum, E., Grythe, H., et al.: The Lagrangian particle dispersion model FLEX-PART version 10.4, *Geosci. Model Dev.*, 12, 4955–4997, <https://doi.org/10.5194/gmd-12-4955-2019>, 2019.
- Pitt, J. R., Le Breton, M., Allen, G., et al.: The development and evaluation of airborne in situ N₂O and CH₄ sampling using a quantum cascade laser absorption spectrometer (QCLAS), *Atmos. Meas. Tech.*, 9, 63–77, <https://doi.org/10.5194/amt-9-63-2016>, 2016.
- Pitt, J. R., Allen, G., Bauguitte, S. J.-B., et al.: Assessing London CO₂, CH₄ and CO emissions using aircraft measurements and dispersion modelling, *Atmos. Chem. Phys.*, 19, 8931–8945, <https://doi.org/10.5194/acp-19-8931-2019>, 2019.
- Prather, M. J., Holmes, C. D., and Hsu, J.: Reactive greenhouse gas scenarios: Systematic exploration of uncertainties and the role of atmospheric chemistry, *Geophysical Research Letters*, 39, <https://doi.org/10.1029/2012GL051440>, 2012.
- Prather, M. J., Hsu, J., DeLuca, N. M., et al.: Measuring and modeling the lifetime of nitrous oxide including its variability, *J. Geophys. Res. Atmos.*, 120, 5693–5705, <https://agupubs.onlinelibrary.wiley.com/doi/10.1002/2015JD023267>, 2015.
- Prinzhofer, A. A. and Huc, A. Y.: Genetic and post-genetic molecular and isotopic fractionations in natural gases, *Chemical Geology*, 126, 281–290, [https://doi.org/10.1016/0009-2541\(95\)00123-9](https://doi.org/10.1016/0009-2541(95)00123-9), 1995.

- PRTR: Pollutant Release and Transfer Register: Oil and Gas industry, Netherlands Continental Shelf, <https://legacy.emissieregistratie.nl/erpubliek/erpub/selectie/criteria.aspx>, 2019.
- Pétron, G., Karion, A., Sweeney, C., et al.: A new look at methane and nonmethane hydrocarbon emissions from oil and natural gas operations in the Colorado Denver-Julesburg Basin, *J. Geophys. Res. Atmos.*, 119, 6836–6852, <https://doi.org/10.1002/2013JD021272>, 2014.
- Pühl, M., Roiger, A., Fiehn, A., et al.: Aircraft-based mass balance estimate of methane emissions from offshore gas facilities in the southern North Sea, *Atmos. Chem. Phys.*, 24, 1005–1024, <https://doi.org/10.5194/acp-24-1005-2024>, 2024.
- Qu, Z., Jacob, D. J., Zhang, Y., et al.: Attribution of the 2020 surge in atmospheric methane by inverse analysis of GOSAT observations, *Environ. Res. Lett.*, 17, <https://doi.org/10.1088/1748-9326/ac8754>, 2022.
- Riddick, S. N., Mauzerall, D. L., Celia, M., et al.: Methane emissions from oil and gas platforms in the North Sea, *Atmos. Chem. Phys.*, 19, 9787–9796, <https://doi.org/10.5194/acp-19-9787-2019>, 2019.
- Rigby, M., Manning, A. J., and Prinn, R. G.: The value of high-frequency, high-precision methane isotopologue measurements for source and sink estimation, *J. Geophys. Res.*, 117, <https://doi.org/10.1029/2011JD017384>, 2012.
- Rigby, M., Montzka, S. A., Prinn, R. G., et al.: Role of atmospheric oxidation in recent methane growth, *P. Natl. Acad. Sci. USA*, 144, 5373–5377, <https://doi.org/10.1002/2015JD023267>, 2017.
- Roedel, W. and Wagner, T.: *Physik unserer Umwelt: Die Atmosphäre*, Springer, 5 edn., 2017.
- Roiger, A., Thomas, J.-L., Schlager, H., et al.: Quantifying Emerging Local Anthropogenic Emissions in the Arctic Region: The ACCESS Aircraft Campaign Experiment, *Bulletin of the American Meteorological Society*, 96, 441–460, <https://doi.org/10.1175/BAMS-D-13-00169.1>, 2015.
- Röckmann, T., Eyer, S., van der Veen, C., et al.: In situ observations of the isotopic composition of methane at the Cabauw tall tower site, *Atmos. Chem. Phys.*, 16, 10 469–10 487, <https://doi.org/10.5194/acp-16-10469-2016>, 2016.
- Santoni, G. W., Daube, B. C., Kort, E. A., et al.: Evaluation of the airborne quantum cascade laser spectrometer (QCLS) measurements of the carbon and greenhouse gas suite CO₂, CH₄, N₂O, and CO during the CalNex and HIPPO campaigns, *Appl. Meas. Tech.*, 7, 1509–1526, <https://doi.org/10.5194/amt-7-1509-2014>, 2014.
- Saueressig, G., Crowley, J. N., Bergamaschi, P., et al.: Carbon 13 and D kinetic isotope effects in the reactions of CH₄ with O(¹D) and OH: New laboratory measurements and their implications for the isotopic composition of stratospheric methane, *J. Geophys. Res.*, 106, 23,127–23,138, <https://doi.org/10.1029/2000JD000120>, 2017.

- Saunio, M., Stavert, A. R., Poulter, B., et al.: The Global Methane Budget 2000–2017, *Earth System Science Data*, 12, 1561–1623, <https://doi.org/10.5194/essd-12-1561-2020>, <https://essd.copernicus.org/articles/12/1561/2020/>, 2020.
- Scarpelli, T. R. and Jacob, D. J.: Global Fuel Exploitation Inventory (GFEI), Harvard Dataverse [data set], V2, <https://doi.org/10.7910/DVN/HH4EUM>, 2019.
- Scarpelli, T. R., Jacob, D. J., Maasakkers, J. D., et al.: A global gridded ($0.1^\circ \times 0.1^\circ$) inventory of methane emissions from oil, gas, and coal exploitation based on national reports to the United Nations Framework Convention on Climate Change, *Earth Syst. Sci. Data*, 12, 563–575, <https://doi.org/10.5194/essd-12-563-2020>, 2020.
- Schaefer, H., Mikaloff Fletcher, A. E., Veidt, C., et al.: A 21st-century shift from fossil-fuel to biogenic methane emissions indicated by $^{13}\text{CH}_4$, *Science*, 352, 80–84, <https://www.science.org/doi/10.1126/science.aad2705>, 2016.
- Schuit, B. J., Maasakkers, J. D., Bijl, P., et al.: Automated detection and monitoring of methane super-emitters using satellite data, *Atmos. Chem. Phys.*, 23, 9071–9098, <https://doi.org/10.5194/acp-23-9071-2023>, 2023.
- Schwietzke, S., Sherwood, O. A., Bruhwiler, L. M. P., et al.: Upward revision of global fossil fuel methane emissions based on isotope database, *Nature*, 538, 88–91, <https://doi.org/10.1038/nature19797>, 2016.
- Seinfeld, J. H. and Pandis, S. H.: *Atmospheric chemistry and physics: From air pollution to climate change.*, John Wiley and Sons, Inc., 2016.
- Sherwood, O. A., Schwietzke, S., Arling, V. A., and Etiope, G.: Global Inventory of Gas Geochemistry Data from Fossil Fuel, Microbial and Burning Sources, version 2017, *Earth Syst. Sci. Data*, 9, 639–656, <https://doi.org/10.5194/essd-9-639-2017>, 2017.
- Smith, M. L., Kort, E. A., Karion, A., et al.: Airborne Ethane Observations in the Barnett Shale: Quantification of Ethane Flux and Attribution of Methane Emissions, *Environ. Sci. Technol.*, 59, 8158–8166, <https://doi.org/10.1021/acs.est.5b00219>, 2015.
- Sperlich, P., Uitslag, N. A. M., Richter, J. M., et al.: Development and evaluation of a suite of isotope reference gases for methane in air, *Atmos. Meas. Tech.*, 9, 3717–3737, <https://doi.org/10.5194/amt-9-3717-2016>, 2016.
- Staniaszek, Z., Griffiths, P., Folberth, G., et al.: The role of future anthropogenic methane emissions in air quality and climate, *npj Climate and Atmospheric Science*, 5, <https://doi.org/10.1038/s41612-022-00247-5>, 2022.
- Stecher, L.: The role of methane for chemistry-climate interactions, Ludwig-Maximilian-Universität, München, dissertation, 2024.
- Stecher, L., Winterstein, F., Dameris, M., et al.: Slow feedbacks resulting from strongly enhanced atmospheric methane mixing ratios in a chemistry–climate model with mixed–layer ocean, *Atmos. Chem. Phys.*, 21, 731–754, <https://doi.org/10.5194/acp-21-731-2021>, 2021.

- Stolper, D. A., Lawson, M., Davis, C. L., et al.: Formation temperatures of thermogenic and biogenic methane, *Science*, 344, 1500–1503, <https://doi.org/10.1126/science.1254509>, 2014.
- Szopa, S., Naik, V., Adhikary, B., Artaxo, P., et al.: Short-Lived Climate Forcers. In *Climate Change 2021: The Physical Science Basis. Contribution of Working Group I to the Sixth Assessment Report of the Intergovernmental Panel on Climate Change* [Masson-Delmotte, V., P. Zhai, A. Pirani, S.L. Connors, C. Péan, S. Berger, N. Caud, Y. Chen, L. Goldfarb, M.I. Gomis, M. Huang, K. Leitzell, E. Lonnoy, J.B.R. Matthews, T.K. Maycock, T. Waterfield, O. Yelekçi, R. Yu, and B. Zhou (eds.)], Cambridge University Press, Cambridge, United Kingdom and New York, NY, USA, <https://doi.org/10.1017/9781009157896.008>, 2021.
- Tadic, I., Parchatka, U., Königstedt, R., and Fischer, H.: In-flight stability of quantum cascade laser-based infrared absorption spectroscopy measurements of atmospheric carbon monoxide, *Appl. Phys. B.*, 123, <https://doi.org/10.1007/s00340-017-6721-z>, 2017.
- Thornhill, G. D., Collins, W. J., Kramer, R. J., et al.: Effective radiative forcing from emissions of reactive gases and aerosols – a multi-model comparison, *Atmos. Chem. Phys.*, 21, 853–874, <https://doi.org/10.5194/acp-21-853-2021>, 2021.
- Thorpe, A. K., Green, R. O., Thompson, D. R., et al.: Attribution of individual methane and carbon dioxide emission sources using EMIT observations from space, *Science Advances*, 9, <https://www.science.org/doi/abs/10.1126/sciadv.adh2391>, 2023.
- Tullos, E. E., Stokes, S. N., Cardoso-Saldaña, F. J., et al.: Use of Short Duration Measurements to Estimate Methane Emissions at Oil and Gas Production Sites, *Environ. Sci. Technol.*, 8, 463–467, <https://doi.org/10.1021/acs.estlett.1c00239>, 2023.
- Turner, A. J., Frankenberg, C., Wennberg, P. O., and Jacob, D. J.: Ambiguity in the causes for decadal trends in atmospheric methane and hydroxyl, *Proceedings of the National Academy of Sciences of the United States of America*, 114, 5367–5372, <https://doi.org/10.1073/pnas.1616020114>, 2017.
- Tzompa-Sosa, Z. A., Mahieu, E., Franco, B., et al.: Revisiting global fossil fuel and biofuel emissions of ethane, *J. Geophys. Res. Atmos.*, 122, 2493–2512, <https://doi.org/10.1002/2016JD025767>, 2017.
- UNEP: Global Methane Pledge, Climate & Clean Air Coalition Secretariat, <https://www.globalmethanepledge.org/resources/global-methane-pledge>, 2023.
- UNFCCC: Greenhouse Gas Inventory Data Interface, http://di.unfccc.int/detailed_data_by_party, 2022.
- Varga, T., Fisher, R. E., France, J. L., et al.: Identification of Potential Methane Source Regions in Europe Using $\delta^{13}\text{C}(\text{CH}_4)$ Measurements and Trajectory Modeling, *JGR: Atmospheres*, 126, <https://doi.org/10.1029/2020JD033963>, 2021.
- Varon, D. J., McKeever, J., Jervis, D., et al.: Satellite discovery of anomalously large methane point sources from oil/gas production, *Geophys. Res. Lett.*, 46, 13 507–13 516, <https://doi.org/10.1029/2019GL083798>, 2019.

- Waldmann, P.: Development and First Deployment of an Innovative Airborne $\delta^{13}\text{C}(\text{CH}_4)$ In Situ Measurement Setup, Ludwig-Maximilian-Universität, München, Master's thesis, 2022.
- Weiss, A. I., King, J., Lachlan-Cope, T., and Ladkin, R.: On the effective aerodynamic and scalar roughness length of Weddell Sea ice, *J. Geophys. Res.-Atmos.*, 116, <https://doi.org/10.1029/2011JD015949>, 2011.
- Werle, P., Mücke, R., and Slemr, F.: The limits of signal averaging in atmospheric trace-gas monitoring by tunable diode-laser absorption spectroscopy (TDLAS), *Appl. Phys. B*, 57, 131–139, <https://doi.org/10.1007/BF00425997>, 1993.
- Werner, R. A. and Brand, W. A.: Referencing strategies and techniques in stable isotope ratio analysis, *Rapid Commun. Mass Spectrom.*, 15, 501–519, <https://doi.org/10.1002/rcm.258>, 2001.
- Whiticar, M. J., Faber, E., and Schoell, M.: Biogenic methane formation in marine and fresh-water environments: CO_2 reduction vs. acetate fermentation-Isotope evidence, *Geochimica et Cosmochimica Acta*, 50, 693–709, [https://doi.org/10.1016/0016-7037\(86\)90346-7](https://doi.org/10.1016/0016-7037(86)90346-7), 1986.
- Winterstein, F., Tanalski, F., Jöckel, P., et al.: Implication of strongly increased atmospheric methane concentrations for chemistry–climate connections, *Atmos. Chem. Phys.*, 19, 7151–7163, <https://doi.org/10.5194/acp-19-7151-2019>, 2019.
- WMO: Meteorology—A three-dimensional science, vol. 16, WMO bull, 1957.
- WMO: 20th WMO/IAEA Meeting on carbon dioxide, other greenhouse gases, and related measurement techniques (GGMT-2019), GAW Report No. 255, 2020.
- Worden, J. R., Bloom, A. A., Pandey, S., et al.: Reduced biomass burning emissions reconcile conflicting estimates of the post-2006 atmospheric methane budget, *Nature Communications*, 8, <https://doi.org/10.1038/s41467-017-02246-0>, 2017.
- Xiao, Y., Logan, J. A., Jacob, D. J., et al.: Global budget of ethane and regional constraints on U.S. sources, *J. Geophys. Res. Atmos.*, 113, <https://doi.org/10.1029/2007JD009415>, 2008.
- Yacovitch, T. I., Herndon, S. C., Roscioli, J. R., et al.: Demonstration of an Ethane Spectrometer for Methane Source Identification, *Environ. Sci. Technol.*, 48, 8028–8034, <https://doi.org/10.1021/es501475q>, 2014.
- Yacovitch, T. I., Daube, C., and Herndon, S. C.: Methane Emissions from Offshore Oil and Gas Platforms in the Gulf of Mexico, *Environ. Sci. Technol.*, 54, 3530–3538, <https://doi.org/10.1021/acs.est.9b07148>, 2020.
- Yu, X., Millet, D. B., Wells, K. C., et al.: Top-down constraints on methane point source emissions from animal agriculture and waste based on new airborne measurements in the U.S. upper Midwest, *J. Geophys. Res. Biogeoscience*, 125, <https://doi.org/10.1029/2019JG005429>, 2020.
- Zavala-Araiza, D., Alvarez, R. A., Lyon, D. R., et al.: Super-emitters in natural gas infrastructure are caused by abnormal process conditions, *Nat. Commun.*, 8, <https://doi.org/10.1038/ncomms14012>, 2017.

- Zavala-Araiza, D., Omara, M., Gautam, R., et al.: A tale of two regions: methane emissions from oil and gas production in offshore/onshore Mexico, *Environ. Res. Lett.*, 16, <https://doi.org/10.1088/1748-9326/abceeb>, 2021.
- Zhang, Y., Jacob, D. J., Lu, X., et al.: Attribution of the accelerating increase in atmospheric methane during 2010–2018 by inverse analysis of GOSAT observations, *Atmos. Chem. Phys.*, 21, 3643–3666, <https://doi.org/10.5194/acp-21-3643-2021>, 2021.
- Zhang, Z., Poulter, B., Feldman, A. F., et al.: Recent intensification of wetland methane feedback, *Nature Climate Change*, 13, 430–433, <https://doi.org/10.1038/s41558-023-01629-0>, 2023.
- Zhao, J., Saunio, M., Bousquet, P. Lin, X., et al.: On the role of trend and variability in the hydroxyl radical (OH) in the global methane budget, *Atmos. Chem. Phys.*, 20, 13 011–13 022, <https://doi.org/10.5194/acp-20-13011-2020>, 2020.

Danksagung

An dieser Stelle möchte ich mich ganz herzlich bei Professor Dr. Markus Rapp dafür bedanken, dass er die Rolle des Doktorvaters übernommen hat und mir damit die Möglichkeit gegeben hat, am DLR und an der LMU zu promovieren. Sein Feedback und seine Unterstützung auf den letzten Metern dieser Arbeit waren sehr hilfreich. Ich möchte mich außerdem bei meiner Betreuerin Dr. Anke Roiger bedanken, die mich in Ihre Nachwuchsgruppe "Atmosphärische Treibhausgase" aufgenommen hat und mich an dieses interessante Forschungsthema herangeführt hat. Sie war stets eine Unterstützung, fachlich wie auch emotional.

Mein herzlicher Dank gilt auch Professor James Lee, der sich bereit erklärt hat, der Zweitkorrektor dieser Arbeit zu werden, sowie allen Weiteren, die an der Messkampagne in der südlichen Nordsee und deren Auswertung beteiligt waren (Grant Allen mit Team, Eric Kort mit Team und Stefan Schwietzke).

Ich möchte meinen Dank Julian Kostinek und Alina Fiehn für ihre sehr kompetente Betreuung aussprechen, sowohl bei der wissenschaftlichen Analyse als auch auf Seiten des Instruments bei der Arbeit mit dem DLR-QCLS. Außerdem danke ich Max Eckl, der die Rolle von Julian übernommen hat und immer sehr hilfsbereit als Ansprechpartner bereit stand. Ich danke besonders Anke, Max, Alina und Helmut Ziereis für das ausführliche Korrekturlesen dieser Arbeit. Ich möchte mich bei allen Kolleg*innen der Abteilung für die sehr positive und humorvolle Arbeitsatmosphäre bedanken, die nicht nur das Arbeiten am Institut, sondern jede Messkampagne zu einem spannenden und geselligen Abenteuer macht. Insbesondere danke ich allen, die an den beiden Messkampagnen MAGIC und MTGA beteiligt waren, wie Klaus-Dirk Gottschaldt, Heidi Huntrieser und Lisa Eirenschmalz. Außerdem möchte ich Paul Stock und Michael Lichtenstern dafür danken, dass sie jederzeit bei allen technischen Fragen zur Verfügung standen.

Zu guter Letzt möchte ich mich bei meiner Familie und Josef (Sepp) bedanken, die mir bei allen Hochs und Tiefs motivierend und unterstützend zur Seite standen.